IASJ
المجلات الاكاديمية العراقية

KJPS
AL-Kitab Journal For Pure Sciences

AL-Kitab Journal For Pure Sciences

Volume : 7 (2023)

Issue: 2

ISSN: 2617-1260 (print)

ISSN: 2617-8141 (online)

DOI: http://10.32441/kjps

Deposit number at the Notional House of Books and Archives, Iraq, 2271 in 2017

Al-Kitab Journal for Pure Science

KJPS

ISSN: 2617-1260 (print), 2617-8141(online)
DOI: http://10.32441/kjps
https://isnra.net/index.php/kjps

An Academic Semi-Annual Journal

Volume: 7 Issue: 2 Dec. 2023

University Website: **www.uoalkitab.edu.iq**
Journal Website: **https://isnra.net/index.php/kjps**
E-mail: **kjps@uoalkitab.edu.iq**

KJPS
AL-Kitab Journal For Pure Sciences

Editorial Board

Editor-in-chief

Ayad Ghany Ismaeel
Academic degree: Dr.
Title: Professor
Al-Kitab University

Editor-in-chief

Sameer Saadoon Algburi / Managing Editor
Academic degree: Dr.
Title: Professor
Al-Kitab University
sameer.algburi@uoalkitab.edu.iq

Aims and Scope

The Al-Kitab Journal for Pure Sciences aims to provide an international forum for the publication and dissemination of original work that contributes to the understanding of the principal and related disciplines of science. Al-Kitab Journal for Pure Sciences publishes two peer-reviewed issues per year, an online and print journal, which publishes innovative research papers, literature reviews, and technical notes on the fields of Biology, Computer Sciences, Chemistry, Physics, and Mathematics.

Authors Guidelines

Rules and Instructions for Publication in Al-Kitab Journal for Pure Sciences

First: General requirements

1. The paper is submitted to the Editorial Secretariat directly in four copies with CD-ROM or E-mail of the magazine in MS Word and PDF files.
2. Research before being sent to scientific evaluators is subject to the quotation Turnitin program.
3. Research shall be accepted for publication after being judged by scientific evaluators and according to the rules.
4. The publication fee is (50$) for researchers from Iraqi Universities and (free of charge) for foreign researchers.

Second: To prepare research for publication, authors must follow the following procedures.

1. **The article:**

   The article needs to be typed on one side of A4 paper (Right margin =2.5 cm, left margin =2.5 cm, and 2cm for the top and bottom) with 1.5 space, and the pages must be numbered.

2. **The content organization:**

   MS Word is to be used as follows: "Simplified Arabic" font for the Arabic articles, and "Times New Roman" for the English articles. The Size of the title is 18 bold. The names of the authors will be typed in 11 bold in Arabic and 11 bold in English. Abbreviations, keywords, the main headings, the reference, and the acknowledgment will be typed in 14. Subheadings will be in 12 bold. The abstract will be size 12. The body of the article/paper is in size 12. The order of the paper's content will be as follows:

The article heading, the names of authors and their addresses, and the abstract (Both in Arabic and English).

3. **Research paper title:**

The title must be as short as possible and indicate the contents of the subject together with the name (names) of the authors. The names of the authors to whom correspondence is to be made should be indicated with (*) and show his / her email.

4. **The size:**

The paper should contain no more than 15 pages of journal pages including charts and diagrams. Extra pages will be charged at (3$) each.

5. **Abstract:**

The abstract should include the purpose and the means of the founding results and the conclusions. It should also contain the knowledge values of the subject of research. It is meant to be no more than 250 words. It should also emphasize the content of the subject and include the keywords used throughout the paper.

6. **Diagrams:**

Figures and diagrams must be given following the explanation referring to the diagram. Each diagram must contain its title below the diagram at the first size of 12. The diagram should be editable in terms of enlargement or reduction within the margins of the paper size. The parts of each diagram must be grouped into drawing parts.

7. **Tables:**

The tables should follow the parts of the main body and should be located below the indicated part of the text. Tables must have titles with a text size of 12. The text used inside the tables should be of size 12 and kept within the cells of the table.

8. **References:**

The references used in the paper must be given in order and their numbers given inside the square bracket **[ ]**. The following instructions are to be followed:

If the reference is a book, the First name of the reference must be given first followed by the other names. Then the title (bold and Italic) of the book, edition, year of publication, the publisher, and place of publication (year of publication).

Example: **[1]** P. Ring and P. Schuck, "**The Nuclear Many-Body Problem**", First Edition, Springer-Verlag, New York (1980).

(b) If the reference is a research paper or an article in a journal: The name of the author must be given first, the title of the article, the name of the journal, the volume (issue), page (Year). **Example:** **[1]** Ali H. Taqi, R. A. Radhi, and Adil M. Hussein,

"Electroexcitation of Low-lying Particle-Hole RPA States of ^{16}O with WBP Interaction", Communication

Theoretical Physics, 62(6), 839 (2014).

c) If the reference is an M.Sc. or Ph.D. thesis, the name of the anther must be written with the first name first followed by the surname, title of the thesis, the name of the university, and Country (Year).

Example: [1] R. A. Radhi, **"Calculations of Elastic and Inelastic Electron Scattering in Light Nuclei with Shell-Model Wave Functions**", Ph.D. Thesis, Michigan State University, USA (1983).

(d) If the reference is from the conference. Authors Name, "**Paper Title**", Conference, Country, Publisher, volume, page (Year).

Example: [1] Ali H. Taqi and Sarah S. Darwesh, **"Charge-Changing Particle-Hole Excitation of ^{16}N and ^{16}F Nuclei"**, 3rdInternational Advances in Applied Physics and Materials Science Congress, Turkey, AIP Conf. Proc., 1569, 27 (2013)

Third: Privacy Statement

1. The names and e-mail addresses entered into the journal's website will be used exclusively for the purposes stated in this journal and will not be provided for any other purpose or to any other party.
2. The editor of the journal has the right to change any statement or phrase of the research content he may find necessary to express the work suitable to the general style of the journal.
3. After publishing the paper and its presentation on the journal page, the editors' team will destroy all the scrap papers. The author has no right to ask for them in any case.

Fourth: Modernity of sources:

The percentage of modern references used in the research should not be less than 50% of the total references used in the research. Modernity is measured within the last ten years of the year of submission of the research. For example, when submitting the research in 2018, the references should be from 2008 upwards and not less than 50%. The journal prefers to have at least one of the reference types of research published in the previous journal issues.

Note: For more information, visit:

Al-Kitab University Website: www.uoalkitab.edu.iq

Or Journal Website: https://isnra.net/index.php/kjps

The Journal can also be e-mailed to kjps@uoalkitab.edu.iq

Table of Contents

Volume: 7 Issue: 2 Dec. 2023

Al-Kitab Journal for Pure Sciences (2023); 7(2):1-15.
https://doi.org/10.32441/kjps.07.02.p1

Al-Kitab Journal for Pure Sciences
ISSN: 2617-1260 (print), 2617-8141(online)

https://isnra.net/index.php/kjps

Using Genetic Algorithms to Segment Images: A Review

Rasha Talib Gdeeb
University of Baghdad, Iraq.
*Corresponding Author: rasha.talib@coeng.uobaghdad.edu.iq

Citation: Gdeeb RT. Using Genetic Algorithms to Segment Images: A Review. Al-Kitab J. Pure Sci. [Internet]. 2023 Aug. 25 [cited 2023 Aug. 25];7(2):1-15. https://isnra.net/index.php/kjps/article/view/946. DOI:https://doi.org/10.32441/kjps.07.02.p1.

Keywords: Segmentation, Genetic Algorithm, Artificial intelligence, Artificial Neural, Network, Image Processing.

Article History
Received 05 July. 2023
Accepted 02 Aug. 2023
Available online 25 Aug. 2023

Abstract:

The genetic algorithm plays a pivotal role in image processing, particularly in the critical stage of image segmentation. The process of segmenting photographs is an essential method in the field. Identifying objects, extracting features for object recognition, and classifying are integral components of image processing. However, the effectiveness of these activities relies on the quality of the operations performed. The work at hand in the domain of image processing is notably arduous and intricate. The segmentation of photos cannot be consistently achieved through the utilization of a singular approach. Nevertheless, it is not possible to consistently classify photos into extensive categories. The complexity inherent in the image segmentation task necessitates careful consideration when determining a suitable set of parameters to employ. The arduous task of selecting picture parameters the picture segmentation problem encompasses various factors that contribute to the complexity of the selection process. An optimization problem is employed to efficiently locate the global maximum inside a given search space, with the problem being formulated as a Genetic Algorithm. Subsequently, the task of determining the most suitable segmentation criteria for an image is successfully overcome. The primary objective of this study was to investigate the viability of employing genetic algorithms within the domain of image segmentation.

Keywords: Segmentation, Genetic Algorithm, Artificial intelligence, Artificial Neural Network, Image Processing.

استخدام الخوارزميات الجينية لتقسيم الصور: مراجعة

رشا طالب غضيب

جامعة بغداد كلية الهندسة، العراق.

rasha.talib@coeng.uobaghdad.edu.iq

الخلاصة:

تلعب الخوارزمية الجينية دورًا محوريًا في معالجة الصور، خاصة في المرحلة الحرجة من تجزئة الصورة. تعد عملية تجزئة الصور الفوتوغرافية طريقة أساسية في هذا المجال. يعد تحديد الكائنات واستخراج ميزات التعرف على الكائنات وتصنيفها مكونات أساسية لمعالجة الصور. ومع ذلك، فإن فعالية هذه الأنشطة تعتمد على جودة العمليات المنفذة. العمل الجاري في مجال معالجة الصور شاق ومعقد بشكل خاص. لا يمكن تحقيق تجزئة الصور بشكل متسق من خلال استخدام نهج فردي. ومع ذلك، ليس من الممكن تصنيف الصور باستمرار إلى فئات واسعة النطاق. يتطلب التعقيد الكامن في مهمة تجزئة الصورة دراسة متأنية عند تحديد مجموعة مناسبة من المعلمات لاستخدامها. المهمة الشاقة المتمثلة في اختيار معلمات الصورة تشتمل مشكلة تجزئة الصورة على عوامل مختلفة تساهم في تعقيد عملية الاختيار. يتم استخدام مشكلة التحسين لتحديد موقع الحد الأقصى العالمي بكفاءة داخل مساحة بحث معينة، مع صياغة المشكلة كخوارزمية جينية. وبعد ذلك، تم التغلب بنجاح على مهمة تحديد معايير التجزئة الأكثر ملاءمة للصورة. كان الهدف الأساسي من هذه الدراسة هو دراسة جدوى استخدام الخوارزميات الجينية في مجال تجزئة الصورة.

الكلمات المفتاحية: التجزئة، الخوارزمية الجينية، الذكاء الاصطناعي، الشبكة العصبية الاصطناعية، معالجة الصور.

1. INTRODUCTION:

Image segmentation is a technique utilized to partition a digital image into multiple sections composed of pixels **[1]**. Please note that picture segmentation should not be mistaken for image partitioning both edge detection and region extraction techniques were employed to generate these regions. Upon undergoing division, the distinct elements comprising an image maintain their original color and texture properties. The outcome comprises several discrete segments that, when integrated, form the entirety of the visual representation. Identifying a reliable approach capable of accurately segmenting all photographs can pose a significant challenge. The task of determining the most suitable strategy for segmentation is also complex and demanding. The applicability of these technologies, originally designed for a certain image type, is limited when applied to different types of photographs. The categorization of segmentation techniques can be classified into three groups, as outlined in reference **[2]:**

A- Traditional algorithms refer to algorithms that are based on mathematical or methodological principles.
B- Approaches about artificial intelligence .

C- Methods for achieving optimal performance.

The conventional procedures encompass several techniques such as utilization thresholds to identify unique histograms, performing region expansion or extraction, detecting edges and boundaries, and employing relaxation methods. The utilization of segmentation is derived from the discipline of artificial intelligence, wherein methodologies including Artificial Neural Networks are employed. This paper discusses the utilization of a Genetic Algorithm (GA) in optimization tactics. The parameters of segmentation algorithms and pixel-level segmentation have been modified due to the substantial impact of genetic algorithms on picture segmentation **[3].** In the context of segmentation analysis, the utilization of genetic algorithms (GA) can facilitate the determination of an optimal number of segments to consider for attribute selection, including heuristic thresholds.

2. Related Works

Image segmentation can be done using a variety of algorithms. However, owing to various constraints, finding the best solution is difficult. **[4]** classifies the pixels' belonging and then uses area expansion to obtain the piece. **[5]** suggested linking the region details and color histogram for creating video databases based on artifacts. A genetic algorithm-based segmentation method was proposed in **[6]** to alter image characteristics triggered by variable environmental conditions. **[7]** describes a two-step approach to image segmentation. The authors suggested a graph-based approach in **[8].**

3. Image Segmentation

In the process of segmentation, the input image is divided into regions that do not overlap with one another **[9].** Every region is the same and is linked together. When all the pixels conform to the homogeneity criterion, the areas are the same.

If there is a path between any two pixels that are located within the zone, then the zone is said to be connected. Using this method, an image can be divided into sections that have consistent and consistent features. The goal of picture segmentation is to reduce the complexity of an image's representation by converting it into a form of meaning that can be easily analyzed **[10, 11].**

3.1.Image Segmentation Using Gas

A proposed approach for estimating the solution area involves the utilization of a distance function that incorporates both local and global compute segments. This approach employs a genetic algorithm (GA).

To develop a proficient genetic algorithm (GA) for picture segmentation, it is imperative to focus on two main considerations as highlighted in previous research **[12,13].**

1- Identify the optimal symbol to symbolize each solution.
2- Establishing an optimal fitness posture depending on weight and health. Image segmentation algorithms typically include customizable parameters, which enable users to exert more precise control over the resulting output. The gas method can be broadly characterized as outlined in reference **[14].**

At the point when the seed supply is prepared for utilization, three factors come into play. The initial stage of the genetic cycle, as seen in **Fig.1.**

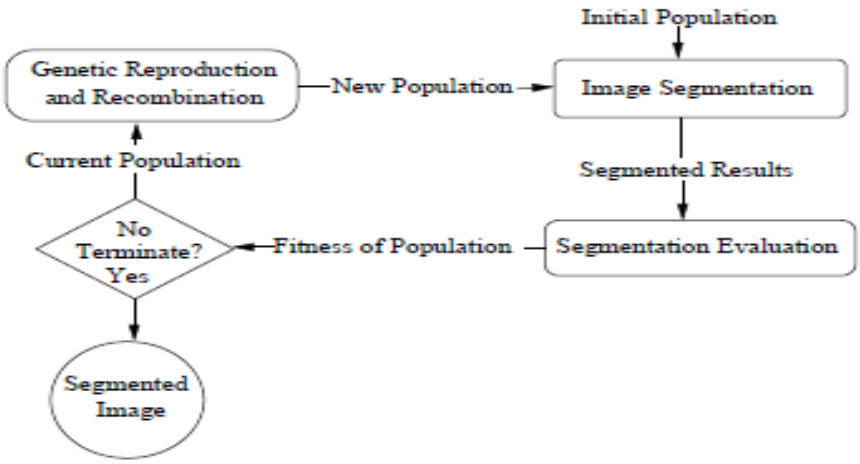

Fig1. Flow Chart of the Based Segmentation Method

The evaluation process assesses the quality of the result for each category of factors. If the maximal efficiency for the present population exceeds the previously indicated value, it is recommended to discontinue the method **[15].**

If the performance standards are not satisfied, the purpose of the genetic operators will be altered. Individuals who possess a significant degree of physical strength are considered suitable candidates for this endeavor. Within a given population, this phenomenon leads to the emergence of a subsequent generation of offspring that exhibits enhanced performance. Following the application of a revised population for the second iteration to divide the image, the cycle recommences. The term "generation" encompasses various stages within the iterative process, namely "Crossover," "Segmentation-Fitness," and "Mutation." **Fig. 1** illustrates the ongoing process will persist until all requisite requirements have been fulfilled **[16,17].**

The measurement of distance position in this context is contingent upon the number of pixels and is influenced by both distress and spatial location. This interplay of factors contributes to the generation of similarity, as depicted in **Fig. 2.**

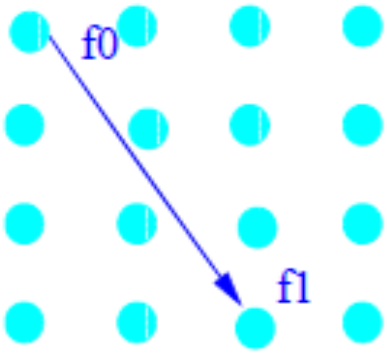

Fig2. The graph and the distance function

3.2.Genetic Algorithm Methodology

During a genetic algorithm, a collection of strings, often referred to as chromosomes, which represent potential solutions to an optimization problem, undergoes a progressive evolution towards improved solutions. In many cases, the phenomenon of evolution commences with a cohort of individuals that have arisen through autonomous reproductive actions, thereafter, progressing across successive generations. The generation of a new population is achieved through a process of random selection of individuals from the existing population, with the likelihood of selection influenced by their respective fitness levels. These selected individuals are then subjected to modifications, specifically through crossover and mutation techniques **[18].** Each successive cohort assesses the overall adaptability of everyone within the populace. Subsequently, the algorithm integrates the revised population in the future iteration. Typically, the termination of the process occurs when either the maximum number of generations has been attained or when the population has attained a satisfactory level of health. If the algorithm terminates when reaching a specific cumulative number of generations **[19-21],** it is uncertain whether a feasible solution has been obtained at that stage.

4. Segmentation Of the Image Using Genetic Algorithm

Farmer and Sugars **[22]** split the genetic algorithms used to segment images into two key groups for image segmentation.

1. Selection of parameters, where genetic algorithms are used to change the parameters of an existing system of image segmentation to maximize its performance.
2. Segmentation at the pixel level, using genetic algorithms to perform area marking.

Most methods of image segmentation have several parameters that need to be refined, and the first approach is therefore used more frequently**[23,24].**

5. Different Soft Computing Techniques Used for Image Segmentation

5.1. Fuzzy Clustering

Data points are divided into homogenous classes or clusters using clustering, which aims to make the items in the same cluster as similar as feasible and the items in separate classes as unlike as possible. Distance, connection, and intensity are a few variables that may be utilized as similarity indicators. In non-fuzzy or hard clustering, information is separated into distinct clusters, each of which contains exactly one data point. In fuzzy clustering, the data points may belong to many clusters, and for each point, membership grades that describe the degree to which the data points are a part of each cluster are assigned. An item can belong to many classes in variable degrees (referred to as memberships) according to the primary principle of fuzzy clustering. Numerous benefits may be seen in the membership produced by the fuzzy clustering method [25].

5.2. Possibility Fuzzy C Mean

The partition should exhibit two key characteristics: intra-cluster homogeneity, which implies that the data within each cluster should be as similar as possible, and inter-cluster heterogeneity, which implies that the data across different clusters should be as diverse as possible.

The assumption is made that the degree of typicality of a point within a fuzzy set (or cluster) is absolute. This degree is defined by the membership values assigned to that point among the other clusters existing in the domain under consideration [26]. The process of grouping is referred to as a probabilistic approach. In contrast, several clustering techniques employ a probabilistic constraint that mandates the summation of membership values for a given point to equal one. According to this constraint, it is stipulated that a given point can exclusively be assigned to a single cluster at any given moment. The PCM methodology diverges from other methods by not assuming probabilistic constraints. The Probabilistic Constraint Model (PCM) is founded on the concept of relaxing the probabilistic constraint [27], enabling the interpretation of the membership function or degree of typicality in a probabilistic fashion.

5.3. Artificial Neural Network

An artificial neural network (ANN) is a kind of information processing that emulates the operations of biological neural systems, such as the human brain. The narrative structure of the data processing system assumes a vital role within this paradigm. The system has numerous interconnected processing units, commonly referred to as neurons, which collaborate to address a diverse range of problems. An artificial neural network (ANN) can be tailored to suit specific applications, such as pattern recognition or data categorization, by undergoing a process of

learning [28]. Neural networks possess the ability to acquire novel talents through the process of monitoring and assimilating pre-existing ones. Autonomous systems lack the capacity for programming, rendering them impervious to instruction. It is imperative to use caution and thoughtful deliberation while choosing samples to prevent time wastage and, more significantly, to avert potential network malfunctions resulting from subpar input. The presence of a disadvantage compels the network to independently seek a resolution to the issue, potentially yielding unanticipated outcomes.

5.3.1 Supervised approach

For segmentation, supervised methods require expert human input. As a result, human professionals carefully choose the training data that will be utilized to segment the photos. Su-prevised approaches are based on the manual selection of training pictures by operators or people with competence.

Divide them up into n regions. Using the chosen photos as training images, the suggested architecture is trained by assigning labels to each area. After that, the technique may segment comparable pictures. Regions are given labels based on the knowledge contained in the neural network architecture that is being.

5. 3.2. Unsupervised procedures

Semi- or completely automated unsupervised approaches are available. The findings should be independent of humans; however, user intervention may be required at some point in the process to enhance the effectiveness of the approach. Without the help of an operator, an unsupervised approach mechanically divides the pictures. The technique divides the picture into k smaller parts, and then automatically labels each of those sections [29].

6. Technique Of Genetic Algorithm

The objective of a Genetic Algorithm is to identify the optimal solution to an optimization problem through the iterative improvement of a population of strings (chromosomes) that represent potential solutions to the problem. Evolution generally initiates with the formation of novel social collectives and proceeds across subsequent generations [30]. The process of determining the fitness of everyone in a population involves randomly selecting multiple individuals from the current population, applying crossover and mutation operations to these individuals to generate a new population in each generation, and subsequently calculating the average fitness of these individuals. The algorithm's future iterations incorporate the newly obtained demographic data. The termination of the method occurs when either a specific threshold for population fitness is attained or a predetermined number of generations have been

generated [31] The determination of whether a viable solution has been obtained is contingent upon the algorithm's termination due to reaching its maximum number of generations.

Genetic or evolutionary algorithms employ the fundamental principles of natural evolution to effectively choose the optimal resolution for a Solver problem. In the context of a genetic algorithm, the problem at hand is typically represented as a series of bit strings. However, in an evolutionary algorithm, the problem is approached by directly utilizing the choice variables and problem functions to find a solution. Both algorithms are classified as "algorithms." On evolutionary algorithms, many commercial Solver products are built. There are a few ways in which "evolutionary" optimization techniques differ from "classical" methods [25]. Operations That Are Random vs. Deterministic Population Compared to Single Ideal Response Utilizing "Survival of the Fittest" to choose the best solutions, creating new solutions through mutation, combining solutions through crossover, and so on. Five phases comprise basic GA (Fig. 3):

Start with a population of N chromosomes that was produced at random, where N represents the population's size and l represents the chromosome x's length. Find the fitness value of each chromosome x in the population by calculating its function (x). Continue doing this until N progeny are produced: Using the value of the fitness function, choose a pair of chromosomes at random from the current population. Create an offspring with the crossover and mutation operations, where i = 1, 2, ..., Fresh population should replace the existing one. Move on to step 2 in 5. As shown in Fig. 3, a straightforward GA process.

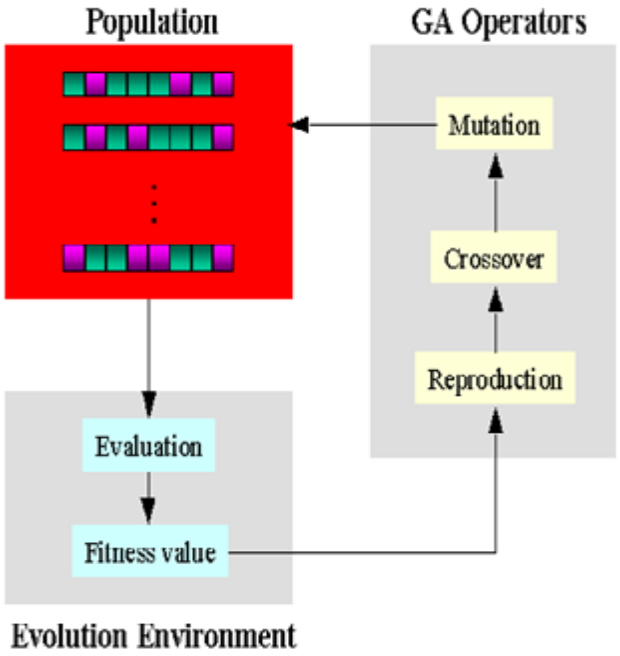

Fig 3: Genetic Algorithm process

a. Mutation

Periodically, an evolutionary algorithm will introduce random mutations or other modifications to a subset of the population. Consequently, a new set of alternatives for resolving the issue will arise. The formulation of this technique was derived from the examination of how DNA mutations contribute to the natural evolution of organisms. This phenomenon may be perceived positively or negatively about the existing population. There exist numerous potential approaches for implementing a "mutation," and the Evolutionary Solver utilizes three separate mutation protocols. The Evolutionary Solver employs a strategy known as "repair" to address issues by iteratively incorporating minor modifications into the algorithm. In instances where the probable outcome of a mutation appears unlikely, there exists a method that may, on occasion (but not consistently), render it conceivable. There exist numerous potential mutation operators, a few of which are outlined below:

1. Flipping.
2. Exchanging.
3. Reversing.

b. Crossover

An evolutionary algorithm attempts to combine components of existing solutions to generate a new solution with some of the traits of each "parent"; this attempt is motivated by the function of sexual reproduction in the development of biological organisms. In a "crossover" procedure that is motivated by the crossover of DNA strands that takes place during the reproduction of biological organisms, the components of current solutions are mixed. The Evolutionary Solver uses various variants of two separate crossover techniques since there are numerous alternative ways to do a crossover operation, much like with mutation, some of which are significantly better than others. The numerous crossing methods include:

- .Crossover at a single point,
- Crossover at two points.
- Multipoint/N-point crossover.
- Consistent crossover.
- Three-point crossover

The word "crossover probability" denotes a statistical measure employed to ascertain the frequency at which crossover operations are performed. In the absence of genetic recombination between parental sets, offspring can be seen as exact replicas of their parents in terms of genetic composition. If there is a genetic exchange between two individuals, the resulting progeny will possess chromosomes derived from both parental sets. If the probability of genetic recombination is 100%, then the offspring will exhibit identical traits. If the population size

reaches zero, all the chromosomes present will be utilized to generate a new generation. The process of chromosome crossing over is undertaken with the anticipation that the resultant chromosome will exhibit superiority over its parental counterparts, owing to the incorporation of beneficial segments from the original chromosomes **[26].**

c. Selection

The evolutionary algorithm undergoes a selection process wherein individuals deemed to possess higher fitness levels are retained within the population, while those with lower fitness levels are eliminated. The influence exerted by natural selection on the process of evolution served as a source of inspiration for the development of this technique. In the context of addressing a constrained optimization issue, the efficacy of a solution is contingent upon its adherence to the problem's constraints, as well as its alignment with the value of the problem's objective function. The process of selection guides the evolutionary algorithm towards progressively enhanced solutions as it traverses the search space. The subsequent examples illustrate prevalent techniques employed in the process of selection.

- Tournament entry.
- Randomly choosing.
- Boltzmann selection
- Stochastic unbiased sampling
- Picking a rank.
- Choice of the roulette wheel.

Using a competitive neural network is a superior approach to fuzzy clustering approaches when comparing the aforementioned 5 ways of picture segmentation. The use of genetic algorithms is another alternative method for segmenting images. The complexity of the problem is decreased using genetic algorithms. of image segmentation, genetic algorithms are employed as function optimizers to change the parameters of already-existing segmentation algorithms. GAs are probabilistic and casualty tools, but they may not evolve in the same way when used on the same issue. More system knowledge and more fuzzy logic and ANN approaches were required. More mathematics as compared to GAs **[27].**

Therefore, based on a comparison of all available soft computing techniques, genetic algorithms are the most accurate way to segment a picture since they can handle complicated color images, which is extremely helpful nowadays as most photographs are colorful.

d. Randomness

First, it uses some random sampling. It is therefore nondeterministic, and even if your model hasn't changed, different executions of the procedure may have slightly different results. The linear, nonlinear, and integer Solvers, which are also part of the Premium Solver, are

deterministic techniques; they consistently provide the same answer if you begin with the same values in the decision variable cells.

e. Population

Moreover, in contrast to conventional optimization methods that often retain only the best solution obtained thus far, an evolutionary algorithm maintains a population of viable solutions. While it is possible to identify a single or a limited number of options as the "best," the rest of the population serves as "sample points" in different areas of the search space. These points may contribute to the emergence of a more optimal solution in the future. The utilization of a population of solutions in the evolutionary algorithm serves the purpose of circumventing the potential entrapment at the present local optimum, enabling the algorithm to explore the possibility of a superior optimum that may lie beyond the scope of the current solution.

7. Method of Genetic Algorithm

The Genetic Algorithm consists of the steps below **[32]:**

Step 1: Pick an initial population of people.
Step 2: Assess everyone's health in that population.
Step 3: Repeat before termination of this generation (time limit, satisfactory fitness attained, etc.):

a-Select the best-fit reproductive individuals.
b-Breeding new individuals to give birth to offspring via crossover and mutation operations.
c-Evaluating the individual health of new people.
d-Substitute new people into the least-fit population.

The fact that GA tries to solve problems through evolution is both a benefit and a drawback. Natural life moves away from unfavorable situations rather than toward a good solution, therefore evolution is not unidirectional. It can lead to a species' evolution reaching a stalemate. We may be unaware that GA is providing a sub-optimal answer. A big phenomenon is the convergence principle. in GA For example, to begin a GA search by providing user input and receiving results, certain values are retrieved that are the best answer at the time. This proved to be a significant setback as well **[33]**. However, the produced result may not be optimum, and better outcomes in real life may be achievable. circumstance the reason for this is that there may be a local optimal point in a GA search process, and if you descend to that point, you won't be able to search for the global optimal. Which is exactly what we need. Convergence is the property of descent inside the local optimum space. This is a flaw in the GA search mechanism. **[34-36].**

8. Conclusion

The utilization of the Genetic Algorithm offers numerous advantages when seeking the optimal solution. This essay aims to elucidate the advantages associated with the implementation of hybrid algorithms. Numerous studies have consistently demonstrated that this strategy is the most effective method for optimizing a wide range of variables. The evolutionary algorithm streamlines the process of conducting a comprehensive search for the optimal solution across a multitude of criteria. Besides the fitness function, other parameters like as the chromosomal encoding scheme and the incorporation of genetic operators may influence the outcome of the optimization process. Conversely, by selecting the parameters judiciously, it is possible to enhance the quality of the image segmentation. Considerable discourse has transpired over the comparative advantages of non-conventional image segmentation algorithms, such as fuzzy, competitive neural networks, and evolutionary algorithms, in contrast to their more established counterparts. When comparing fuzzy and competitive neural networks, it becomes evident that fuzzy neural networks demonstrate superiority in the context of picture segmentation, whereas competitive neural networks are more effective for fuzzy clustering. Another viable option for image segmentation is the utilization of genetic algorithms. Genetic algorithms are employed to mitigate the intricacy of an issue that might otherwise pose significant challenges in its resolution. Genetic algorithms are widely recognized as function optimizers due to their application in refining the parameters of pre-existing segmentation algorithms, hence playing a crucial role in the image segmentation procedure. Furthermore, this study proposes the utilization of hybrid algorithms, such as genetic algorithms (GAs) and artificial neural networks (ANNs), to enhance the aesthetic quality of segmentation results and reduce processing durations.

9. References

[1] Ganesh M, Vilas M. Some Studies on Forming Optimization with Genetic Algorithm. An International Journal of Optimization and Control: Theories & Applications. 2012;2(2):105–12.

[2] Oliveira P, Yamanaka K. Image Segmentation Using Multilevel Thresholding and Genetic Algorithm": An Approach. In: Proceedings of the 2018 2nd International Conference on Data Science and Business Analytics (ICDSBA). Changsha, China; 2018. p. 21–3.

[3] Abbasi M, Rafiee M, Khosravi MR, Jolfaei A, Menon VG, Koushyar JM. An efficient parallel genetic algorithm solution for vehicle routing problem in cloud implementation of the intelligent transportation systems". Journal of cloud Computing. 9(6).

[4] Alkhafaji BJ, Salih MA, Nabat ZM, Shnain SA. Segmenting video frame images using genetic algorithms. Periodicals of Engineering and Natural Sciences. 2020;8(2):1106–14.

[5] Mohn CE, Stølen S, Kob W. Predicting the structure of alloys using genetic algorithms. Mater Manuf Process [Internet]. 2011;26(3):348–53. Available from: http://dx.doi.org/10.1080/10426914.2011.552021.

[6] Breje M. Object localization and border detection criteria design in edge-based image segmentation: automated learning from examples". IEEE Transactions on medical image. 2000;19(10).

[7] Wang S, Siskind JM. Image segmentation with ratio cut. IEEE Trans Pattern Anal Mach Intell [Internet]. 2003;25(6):675-690–4. Available from: http://dx.doi.org/10.1109/tpami.2003.1201819.

[8] Orlando J, Rui S. Image Segmentation by Histogram Thresholding Using Fuzzy Sets". IEEE Transactions on Image Processing. 2002;11(12):1457–65.

[9] Farmer ME, Shugars D. Application of genetic algorithms for wrapper-based image segmentation and classification. In: 2006 IEEE International Conference on Evolutionary Computation. IEEE; 2006.

[10] Artificial Intelligence: Artificial Intelligence for Humans". Artificial Intelligence: Artificial Intelligence for Humans. 2016.

[11] Mitra K. Color image segmentation: A state-of-the-art survey". Proceedings of Indian National Science Academy (INSA-A). 2001;67:207–21.

[12] Naemura M, Fukuda A, Mizutani Y, Izumi Y. Morphological segmentation of sport scenes using color information". IEEE Transactions on broadcasting. 2000;46.

[13] Breje M, Sonka M. Object localization and border detection criteria design in edge-based image segmentation: automated learning from examples". IEEE Transactions on medical image. 2000;19(10).

[14] Wang S, Siskind S. Image segmentation with ratio cut". IEEE Transaction on pattern analysis and machine intelligence. 2003;25.

[15] Farmer M, Shugars D. "Application of genetic algorithms for wrapper-based image segmentation and classification". In IEEE Congress on Evolutionary Computation. 2006;1300–7.

[16] Tabassum M, Mathew K. A genetic algorithm analysis towards optimization solutions". International Journal of Digital Information and Wireless Communications (IJDIWC). 2014;4:124–42.

[17] Mirjalili S, Dong JS, Sadiq AS, Faris H. Genetic algorithm: Theory, literature review, and application in image reconstruction". In: Nature-Inspired Optimizers. Cham: Springer.

[18] Jedlicka P. Genetic algorithm application in image segmentation". Pattern Recognin Image Anal. 2016;26:497–501.

[19] Gabrie. j, l" Artificial Intelligence: Artificial Intelligence for Humans". Artificial Intelligence: Artificial Intelligence for Humans. 2016.

[20] Oliveira A, Braga P, Lima R, Cornélio M. GA-based method for feature selection and parameters optimization for machine learning regression applied to software effort estimation". Information and Software Technology. 2010;52:1155–66.

[21] Yuce B, Fruggiero F, Packianather MS, Pham DT, Mastrocinque E, Lambiase A, et al. Hybrid Genetic Bees Algorithm applied to single machine scheduling with earliness and tardiness penalties". Computer Ind Eng. 2017.

[22] Jedlicka P, Ryba T. Genetic algorithm application in image segmentation". Pattern Recognit. Image Anal. 2016;26:497–501.

[23] Catalin Amza" A Review on Neural Network -Based Image Segmen- tation Techniques. In: Mechanical and Manufac- turing Engg. United Kingdom; p. 1–23.

[24] Sowmya B. Sheela Rani "Color Image Segmentation using Fuzzy Clustering techniques and Competitive Neural Network." Applied Soft Computing. 2011;11(3):3170–8.

[25] Adnan J, Minhat M. Using genetic algorithm to optimize machining parameters in turning operation ". International Journal of Scientific and Research Publications. 2013;3(5).

[26] Udhaykumar P. Task Scheduling of AGV in FMS using Non-Traditional Methods". International Journal of SimulationModeling. 2010;1:28–39.

[27] Bailey DG. Design for embedded image processing on FPGAs. John Wiley & Sons; 2011.

[28] Cheddad A, Condell J, Curran K, Mc Kevitt P. Digital image steganography: Survey and analysis of current methods. Signal Processing [Internet]. 2010;90(3):727–52. Available from: http://dx.doi.org/10.1016/j.sigpro.2009.08.010

[29] Zaitoun NM, Aqel MJ. Survey on image segmentation techniques. Procedia Compute Sci [Internet]. 2015;65:797–806. Available from: http://dx.doi.org/10.1016/j.procs.2015.09.027.

[30] Fraz MM, Remagnino P, Hoppe A, Uyyanonvara B, Rudnicka AR, Owen CG, et al. Blood vessel segmentation methodologies in retinal images-a survey. Computer methods and programs in biomedicine. 2012;108:407–33.

[31] Alsaidi BK, Al-Khafaji BJ, Wahab SAA. Content Based Image Clustering Technique Using Statistical Features and Genetic Algorithm. Engineering. Technology & Applied Science Research. 2019;9:3892–5.

[32] Muren, Wu J, Zhou L, Du Z, Lv Y. Mixed steepest descent algorithm for the traveling salesman problem and application in air logistics. Transp Res Part E: Logist Trans Rev [Internet]. 2019;126:87–102. Available from: http://dx.doi.org/10.1016/j.tre.2019.04.004

[33] Menon VG, Prathap J. Vehicular fog computing: challenges applications and future directions. In: fog computing: breakthroughs in research and practice. IGI global; 2018. p. 220–9.

[34] Lima AAM, de Barros FKH, Yoshizumi VH, Spatti DH, Dajer ME. Optimized artificial neural network for biosignals classification using genetic algorithm. J Control Autom Electr Syst [Internet]. 2019;30(3):371–9. Available from: http://dx.doi.org/10.1007/s40313-019-00454-1.

[35] Arif MH, Li J, Iqbal M, Liu K. Sentiment analysis and spam detection in short informal text using learning classifier systems. Soft Compute [Internet]. 2018;22(21):7281–91. Available from: http://dx.doi.org/10.1007/s00500-017-2729-x.

[36] Ghosh N, Agrawal S, Motwani M. A Survey of Feature Extraction for Content-Based Image Retrieval System". Lecture Notes in Networks and Systems. 2018;34:305–13.

Al-Kitab Journal for Pure Sciences (2023); 7(2):16-29.
https://doi.org/10.32441/kjps.07.02.p2

Al-Kitab Journal for Pure Sciences
ISSN: 2617-1260 (print), 2617-8141(online)

https://isnra.net/index.php/kjps

Study of the optical and spectral properties of Phosphor Tellurite Semiconducting Oxide Glasses

Hazhar.Kh.Omer*, Manaf.A.Hassan

Department of physics, faculty of education of pure sciences, University of Kirkuk, Kirkuk, Iraq

*Corresponding Author: hazharkhalid515@gmail.com

Citation: Omer HKH, Hassan MA. Study of the optical and spectral properties of Phosphor Tellurite Semiconducting Oxide Glasses. Al-Kitab J. Pure Sci. [Internet]. 2023 Sep. 10 [cited 2023 Sep. 10];7(2):16-29. https://isnra.net/index.php/kjps/article/view/951. https://doi.org/10.32441/kjps.07.02.p2.

Keywords: Optical energy gap. Urbach energy, X-ray, SEM, Glass system, DSC.

Article History

Received	20 July. 2023
Accepted	15 Aug. 2023
Available online	10 Sep. 2023

Abstract:

A systematic series of binary Phosphor tellurite glasses in the form [(90-X%)TeO2-(X%)V2O5] in mol%, where X = (10,20,25,30,35) have been successfully prepared in standard method (melt quenching), The effect of adding (V2O5) have been discussed. The X-Ray diffraction spectrum shows that the glass composite had no sharp peaks, The absence of abroad hump at (2θ=25-30o) indicates the presence of (L.R.O) long-range structural was disorder. The glass network structure was discussed through IR and Raman spectroscope and that showed the glass network is built of (TeO3 and TeO4) units. From the UV-visible spectrum, the edge of absorption the optical energy gap (Eopt) Urbach energy (Eo), and refractive index (n), have been determined. The results show that (Eopt) decreased with the increase of (V2O5) concentration, and Urbach energy (Eo) decreased with the increase of (V2O5) content, the refractive index (n) increased with the increase of (V2O5) concentration. The thermal parameters such as transition temperature (Tg), thermal stability (S), and thermodynamic fragility (F) are calculated by differential scanning calorimetry (DSC). Structural analysis of the glass system was identified by scanning electron microscopy (SEM).

Keywords: Optical energy gap. Urbach energy, X-Ray, SEM, Glass system, DSC.

دراسة الخصائص البصرية والطيفية لزجاجيات أوكسيد الفوسفور والتيليريوم الشبه الموصلة

هژار خالد عمر ، مناف عبد حسن

جامعة كركوك كلية التربية للعلوم الصرفة–قسم الفيزياء، العراق
hazharkhalid515@gmail.com

الخلاصة:

تم تحضير سلسلة من عينات الزجاجية شبه الموصلة من أوكسيد التيليريوم الثنائي و أوكسيد الفوسفور الخماسي حسب المعادلة [X] $TeO2-(X)\%V2O5$ $\%(90-$ حيث قيم $X = (10\square20\square25\square30\square35$) حيث تم تحضيرها بنجاح باستخدام الطريقة التقليدية في تحضير الزجاج (التبريد بالذوبان)، وتمت مناقشة تأثير إضافة ($V2O5$) ويبين طيف حيود الأشعة السينية أن المركب الزجاجي لا يحتوي على قمم حادة، ويشير وجود هالة عريضة عند ($\theta=25\text{-}30^{o}$٢) إلى عدم وجود ترتيب بنيوي طويل المدى.(LRO) كذلك تمت مناقشة بنية الشبكة الزجاجية من خلال مطيافية الأشعة تحت الحمراء و مطيافية رامان والتي أظهرت أن الشبكة الزجاجية متكونة من وحدات ($TeO3$ & $TeO4$)، ومن خلال الطيف المرئي للأشعة فوق البنفسجية تم تحديد حافة الامتصاص البصري وفجوة الطاقة الضوئية ($Eopt$) وطاقة اورباخ (Eo) ومعامل الانكسار(n))، وأظهرت النتائج أن قيم (($Eopt$) تنخفض مع الزيادة في تركيز ($V2O5$) وقيم (Eo) أيضاً، ومع الزيادة في تركيز ($V2O5$) نلاحظ ازدياداً في قيم معامل الانكسار(n)، المعاملات الحرارية مثل درجة حرارة الانتقال الزجاجيTg ، والاستقرار الحراري S والهشاشة الثرموديناميكيةF المقاسة عن طريق المسعر الحراري التفاضلي(DSC)، وتم التعرف على التحليل التركيبي للنظام الزجاجي عن طريق المسح المجهري الإلكتروني(SEM).

الكلمات المفتاحية: فجوة الطاقة البصرية، طاقة اورباخ، حيود الأشعة السينية، المجهر الماسح الإلكتروني، المسعر الحراري التفاضلي.

1. INTRODUCTION:

Specific optical properties make this glass particularly suitable for equipment in different laboratories [1]. Tellurium-containing glass melts quickly and is therefore considered a promising material due to its optical properties [2]. Transition materials have been used because they have more than two valence states that affect the optical parameters of the glass [3,4]. Vanadium pentoxide (V2O5) doped with a divalent ratio of {V+4/V+5} is an n-type semiconductor [5]. Tellurite glasses have gained importance in the optical instrumentation industry due to their high transparency in the visible and infrared spectrum [6]. The topology of tellurium-containing glasses is based on the presence of different types of TeO4 and TeO3 units [7]. The structural and optical properties of tellurite glasses have been studied [9,10,11,]. Glasses can be formed when tellurium dioxide (TeO2) is mixed with many different oxides from groups III, IV, and V of the periodic table. The triangular bipyramid (TeO4) transforms into (TeO3) and forms an alkali metal oxide [8]. Tellurium dioxide-based glasses have weak Te-O bonds

that are easily broken and are therefore suitable for accommodating metal oxide ions [9]. This study aimed to investigate the effect of (V2O5) on the optical, thermal, and structural properties of tellurite glass systems.

2. Experimental work

Ternary glasses of the type [(90-X%)TeO2-(X%)V2O5] were prepared from (V2O5-TeO2) by use of the standard (melt-quenching) technique. The appropriate amounts of reagents were mixed in alumina crucibles in an electric furnace kept at (850-950Co). then the series of melts was poured on the stainless plate at 450 Co The glass samples had a thickness (1mm). The structure of the glasses was checked by X-ray diffraction (XRD) using (PANalytical) radiation. Scanning electron microscopy (SEM) measured by (KYKYEM3200) images were acquired from the surfaces of glass samples. The IR and Raman spectroscopy of the glass system was recorded at room temperature in the 400-4000 cm-1 wave number range. The optical properties measurements by (UV-Visible-Biomte5) with wavelength range from 100-900nm. Thermal parameters investigated by (DSC) were glass transition temperature (Tg), thermal stability (S) and thermodynamic fragility (F) have been calculated.

3. Results and discussion

3.1 X-ray diffraction

X-ray diffraction spectra of (TeO_2-V_2O_5) glass samples were recorded at an angle of 2° in the range of 80° ≥ Θ ≥ 10°. **Figure (1)** shows that the XRD spectrum has no discrete or continuous peaks. The absence of sharp peaks and hillocks at (~27o) indicates the presence of long-range structural faults [10]. Since no sharp line spectrum was obtained in the XRD spectrum, it can be assumed that there is no evidence of a crystalline phase in the glass sample. The broad hump pattern indicates that the as-prepared glass samples are amorphous.

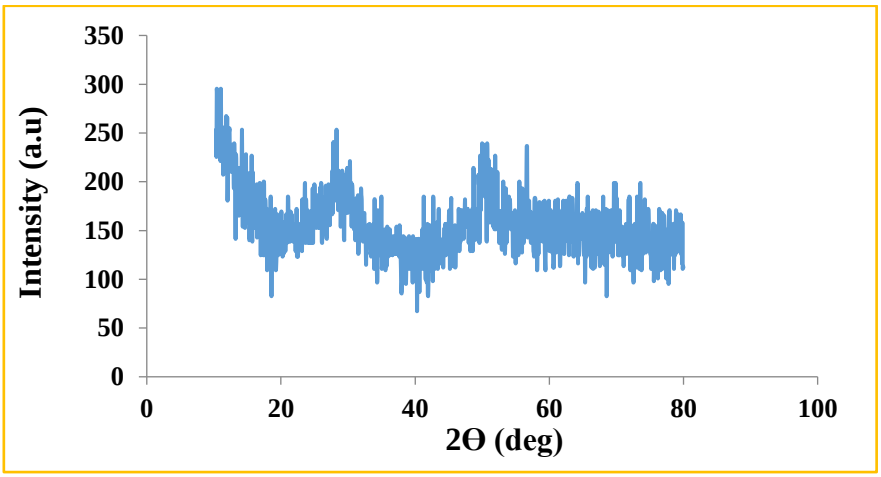

Figure 1: XRD pattern of TeO_2-V_2O_5

3.2 Infrared Absorption Spectra

TeO_2-V_2O_5 glasses were used to study the infrared absorption spectra, which are displayed in **Figure (2)**.

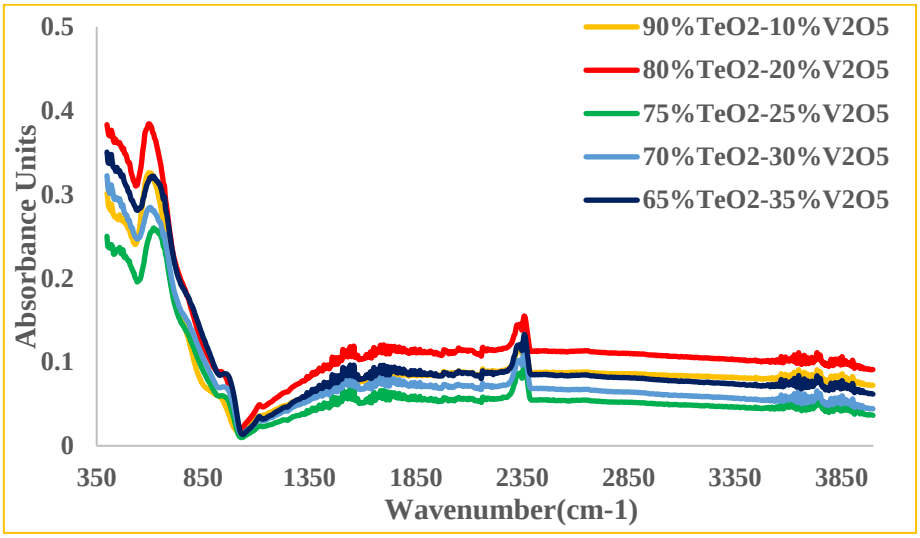

Figure 2: IR spectra of all the studied glass samples

We notice from **Table (1)** that there are many bands in different regions of the infrared range with an increase in the percentage of (V_2O_5), The presence of a band at (541-531) cm-1 could indicate a bend in the Te-O-Te bonds and the triangular expansion of TeO_4 with oxygen bonds, while the bands at (925-928) cm-1 could be due to such vibrations in the bonds V-O where V_2O_5 has strong vibrations in this spectral range **[11]**, while the presence of bands at (1013-1037)cm-1 indicates the vibrations of isolated vanadium groups V=O in (VO_5) trigonal, and the presence of bands at (1582-1642)cm-1 Refers to vibrations in the hydroxyl groups (OH) in the sample, where the bends of the O-H vibrations appear at this spectral range in the form of broadband, while the beams at (3662) cm-1 are due to the retention of water molecules within the structure of the sample **[12]**.

Table 1: Band positions of IR spectra of the studied glass sample

V_2O_5 Content	Band Position (cm^{-1})				
	500	900	1000	1500	3000
10	531		1013	1582	3662
20	532		1014	1585	3662
25	541	925	1030	1642	3662
30	540	925	1035		3661
35	541	928	1037		3662

3.3 Raman spectroscopy

Raman spectra were measured for the glass compound (TeO_2-V_2O_5) and all percentages (V_2O_5) at room temperature. **Figure (3.3)** shows the locations of the absorption bands for the Raman spectra. **Table (3)** also shows the values of the absorption bands for the Raman spectra for the glassy compound (TeO_2-V_2O_5).

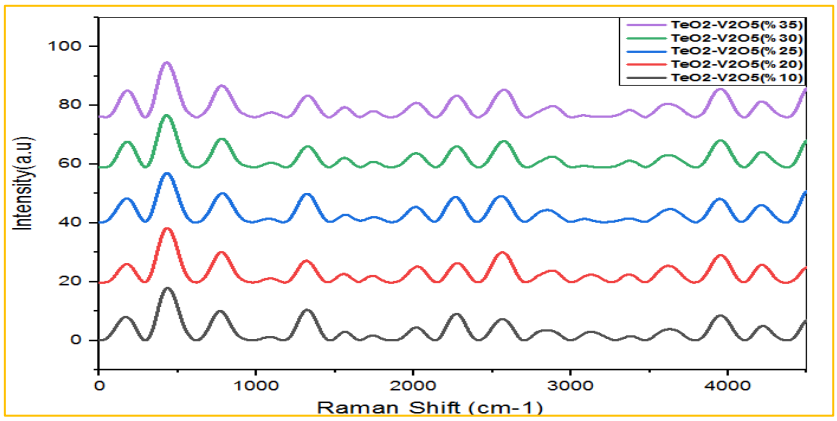

Figure 3: Raman spectra for the glassy compound (TeO_2-V_2O_5)

Table (2) shows the values of the Raman bands for all ratios of (V_2O_5), as we note that there is a band at (433-425) cm-1, which is due to the vibrations in the Te-O-Te bonds in the structural units of TeO_4, and this band represents the peak of the Te-O bonds and V-O vibrations **[12]**, while the bands at (781-768) cm-1 can indicate vibrations in the O-V-O and V=O bonds. When the concentration of V_2O_5 increases, we notice an overlap in the Te-O, V-O bonds, and finally the bands at (1322-1319)cm-1 It indicates the increase of O-V-O and V-O-V groups and the breaking of TeO_2 chains to be replaced by V_2O_5 as the basic network in the glassy group **[13]**.

Table 2: The values of the absorption bands of the Raman spectra for all ratios (V_2O_5) in the glassy compound (TeO_2-V_2O_5)

V2O5 Content	Raman Shift (cm-1)		
10	433	768	1319
20	430	775	1317
25	428	781	1319
30	428	778	1322
35	425	778	1322

3.4 Optical absorption edge

Ultraviolet and visible absorbance measurements were made for the semiconductor glass (TeO_2-V_2O_5) and all percentages (V_2O_5) as a function of wavelength as shown in **Figure (4).**

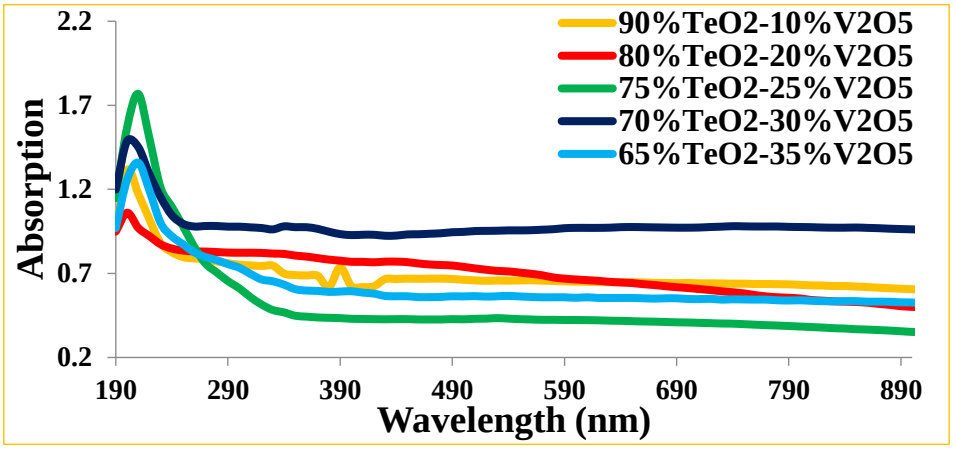

Figure 4: Absorption spectra for all the studied samples

The value of the optical energy gap (E_{opt}) was calculated from the **Figure (5).** The energy of the tail beam (Eo) was calculated from the graph **Figure (6)** between the logarithm of the absorption coefficient (Lnα) with the energy of the incident photon (ħω). the refractive index (n), of the semiconductor glass (TeO_2-V_2O_5) and the absence of sharp absorption edges from the UV-visible absorption spectra confirm the amorphous nature of the glass samples **[14]**.

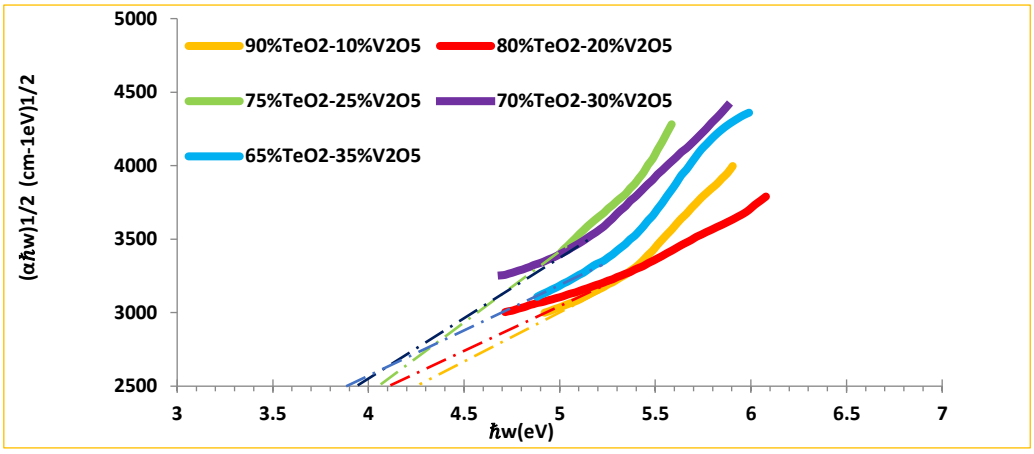

Figure 5: Quantity of $(\omega\hbar\alpha)^{1/2}$ as a function of photon energy in the glassy compound (TeO_2-V_2O_5)

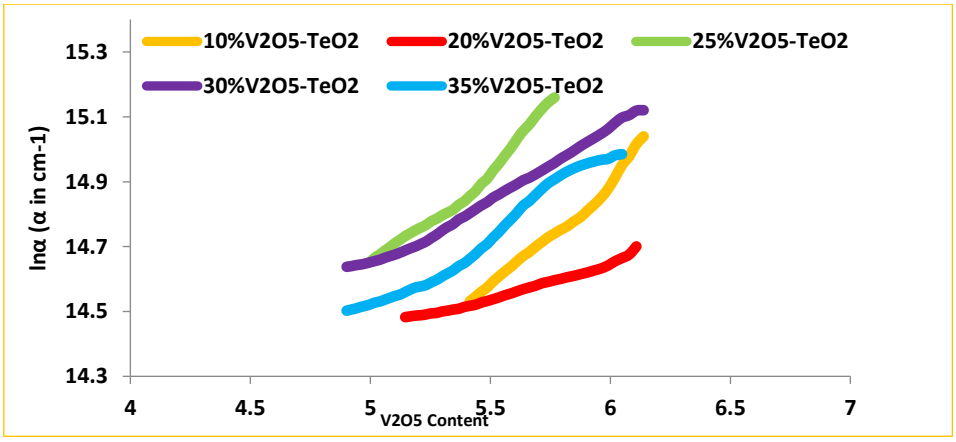

Figure 6: The quantity (lnα) as a function of the photon energy in the glassy compound (TeO_2-V_2O_5)

With the increase in the concentration of (V_2O_5), we notice a decrease in the optical gap energy (E_{opt}) values (4.23-3.93 eV) through the transformation of TeO_2 units into TeO_3 and TeO_4 units, and the establishment of bridging bonds of oxygen as shown in **Figure (7) [15]**, as well as with an increase The concentration of (V_2O_5) in the glass compound, we notice a decrease in the value of the energy of the tail of the band (E_o) (1.5-0.84 Ev), causing a sharp decrease in the long-term arrangement of atoms through the presence of the Te-O-V bridge bonds, which leads to an increase in the number of oxygen bonds, as indicated by The amorphous nature of the glass is consistent with the (XRD) results, which indicate the presence of a periodic three-dimensional network in the glass samples as shown in **Figure (8) [16]**.

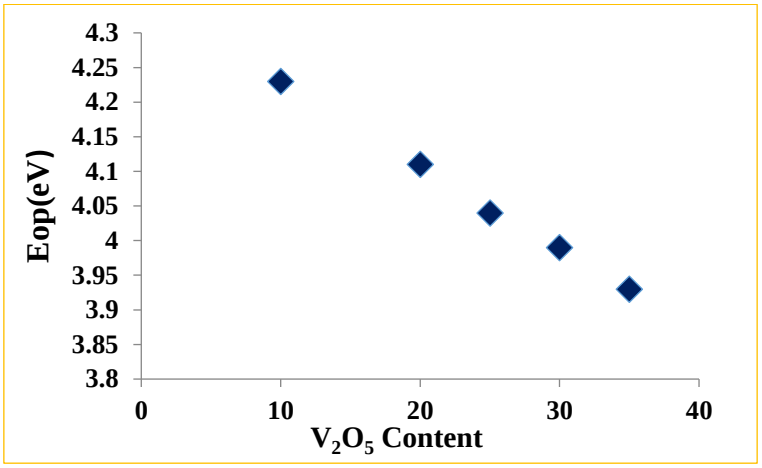

Figure 7: Optical gap energy as a function of (V_2O_5) content in the glass compound (TeO_2-V_2O_5)

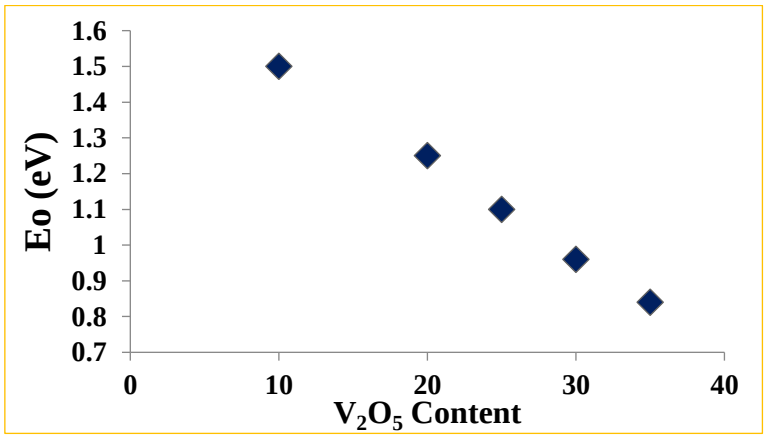

Figure 8: The tail energy of the beam as a function of (V_2O_5) content in the glassy compound (TeO_2-V_2O_5)

Figure (9) shows the increase in the refractive index with an increase in the concentration of (V_2O_5) from (1.80-1.83), as this can be linked to a decrease in unbridged oxygen bonds and an increase in the density of glass samples **Table (3)** shows all Parameters was calculated from UV-Visible spectrum **[17]**.

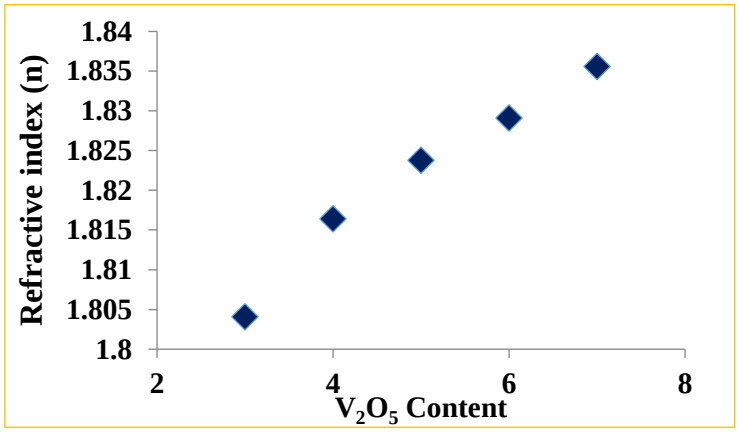

Figure 9: Refractive index as a function of the (V_2O_5) content in the glass compound (TeO_2-V_2O_5)

Table (3) The values of the optical gap energy, band tail energy, and refractive index for all (V_2O_5) content in the glassy compound (TeO_2-V_2O_5)

V205 Content	Eop(Ev)	Eo(Ev)	Refractive Index (n)
10	4.23	1.5	1.804
20	4.11	1.25	1.816
25	4.04	1.1	1.823
30	3.99	0.96	1.829
35	3.93	0.84	1.835

3.5 Differential scanning calorimetry (DSC)

DSC measurements were made for the glassy semiconductor compound (TeO_2-V_2O_5) and all percentages of (V_2O_5) in the compound as shown in **Figure (10)**, where the heat coefficients shown in **Table (4)** were found from the (DSC) curves.

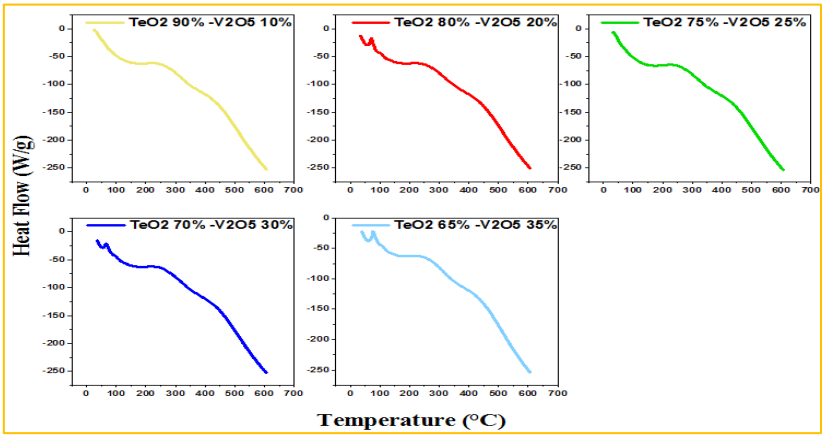

Figure 10: DSC curves for the glass compound (TeO_2-V_2O_5)

Table (4) shows the value of glass transition temperature (Tg), crystallization (Tc), melting temperature (Tp), thermal stability coefficient (ΔT), thermal stability (S), and thermodynamic brittleness (F) for the glass compound (TeO_2-V_2O_5)

V2O5 Content	Tg	Tc	Tp	ΔT	F	S
10	240	355	440	115	0.266247379	40.72916667
20	247	356	442	109	0.237109641	37.951417
25	252	360	444	108	0.226455231	36
30	258	363	448	105	0.199482743	34.59302326
35	266	368	450	102	0.161437701	31.44360902

Table (4) shows an increase in the value of the glass transition temperature (Tg) from 240C° to 266C° with an increase in the percentage of (V_2O_5) in the glass compound from 10mol% to 35mol% as shown in **Figure (11)** where it can be attributed to the increase in (Tg) The V-O bonds contain a higher heat content (644Kj/mol) compared to the heat content of the Te-O bonds (376Kj/mol) and also the arrangement of V_2O_5 atoms inside the glass lattice **[18]**, causing a decrease in the lattice hardness., the increase in (Tc) (368-355)C° with the increase in the concentration of (V_2O_5) is due to the decrease in the spacing between the V_2O_5 atoms, and the values of the thermal stability coefficient (ΔT) range between (102-115)C°, **Figure (12)**, which indicates The prepared glass is good for uses in optical techniques and devices, as the higher (ΔT) the better the quality of the formed glass **[19]**.

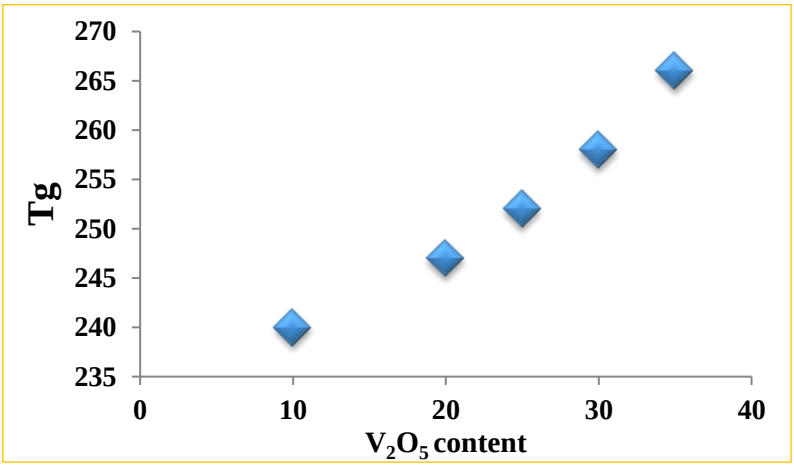

Figure 11: The change in the value of (Tg) as a function of (V_2O_5) content in the glass compound (TeO_2-V_2O)

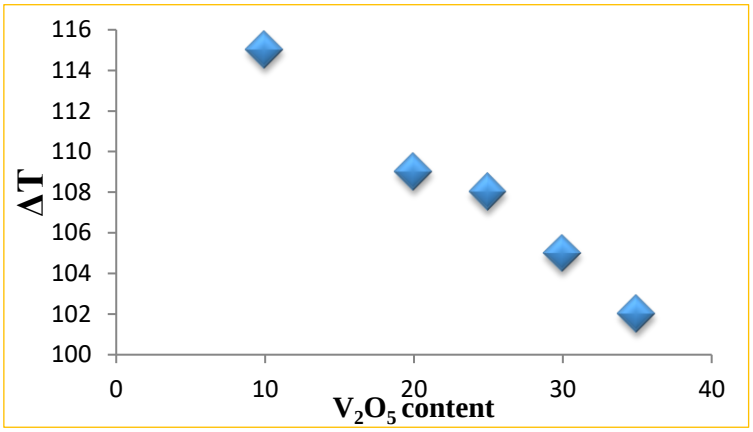

Figure 12: The change in the value of (ΔT) as a function of (V2O5) content in (TeO_2-V_2O_5) composite

The values of the thermal stability coefficient (S) decrease from 40.72 to 31.44 with the increase in the concentration of (V_2O_5) as shown in **Figure (13)**, and the thermodynamic fragility also decreases from 0.266 to 0.161 with the increase in the concentration of (V_2O_5) as shown in the **Figure (14)** due to the formation of bonds of bridging oxygen, which causes more openness in the vitreous lattice with less disturbances **[20].**

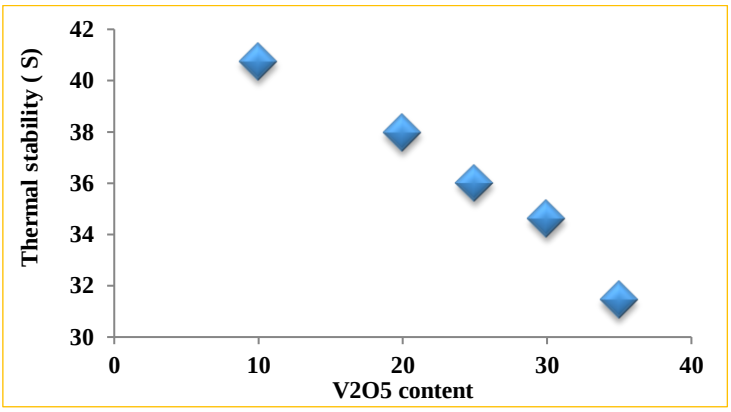

Figure 13: Variation of (S) values as a function of (V_2O_5) content in the glass compound (TeO_2-V_2O_5)

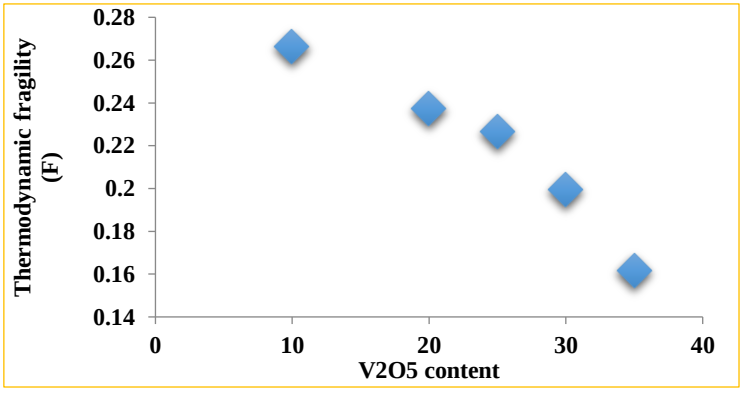

Figure 14: Variation of (F) values as a function of (V_2O_5) content in the glass compound (TeO_2-V_2O_5)

3.6 Scanning electron microscopy (SEM)

Scanning electron microscope measurements were made for the semi-conductive glass compound (TeO_2-V_2O_5) and all ratios (V_2O_5) and with different scales. The samples were measured individually for all scales, but we will suffice in our study with one image for each sample, as shown in **Figure (15)**.

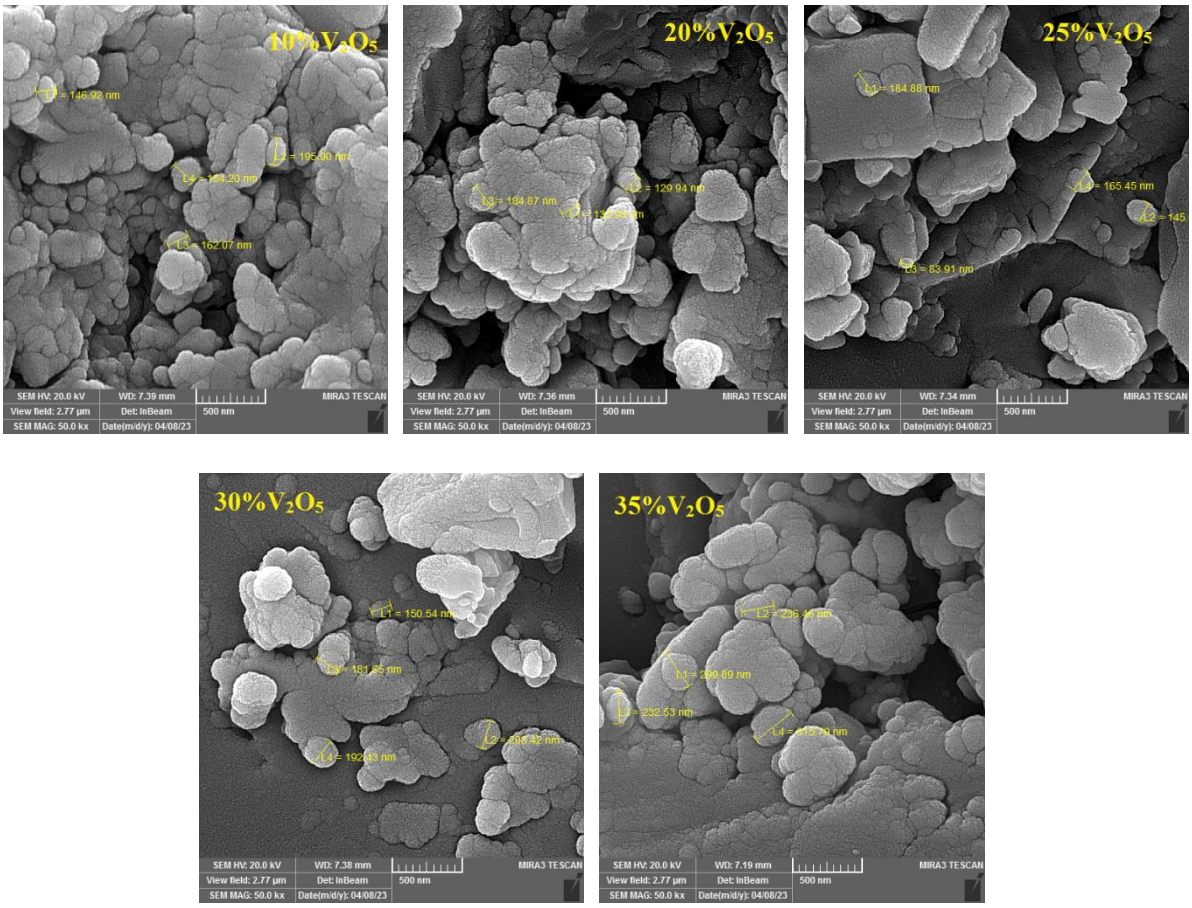

Figure 15: SEM images of all ratios of (V_2O_5) in the glass compound (TeO_2-V_2O_5)

(SEM) images show the glass samples in different shapes and sizes, including nanoparticles, which are shown in a network-shaped structure with ramified structures that extend over the surface of the sample [21]. It is well integrated after heat treatment and melting of the material and its fusion is ideal, forming a three-dimensional porous structure that extends over the entire sample distance, and The nanostructure consists of granules well connected and randomly arranged inside the sample, which confirms the amorphous nature of the banned glass [22,23].

4-Conclusion

The X-Ray phase shows that the glass system (TeO_2-V_2O_5) was non-crystalline which mean it is amorphous. The DSC spectra show that the (Tg), and (Tc), increase with rising content of

V_2O_5 from (5% to 25%), thermal stability and thermodynamic fragility decrease with rising content of V_2O_5, and the results of UV-Visible measurements show the following:

1-The (E_{opt}) decreased from (4.23 - 3.93) eV with increasing of V_2O_5 content.

2-The Urbach energy (Eo) decreased from (1.5 - 0.84) eV with increasing of V_2O_5 content.

3-The refractive index (n) is increasing from (1.804 - 1.835) with increasing of V_2O_5 content.

Raman and IR spectrum considered the amorphous structure of glass system (TeO_2-V_2O_5) from the band position and peaks.

5. References

[1] Sreedhar VB, Ramachari D, Jayasankar CK. Optical properties of zincfluorophosphate glasses doped with Dy3+ ions. Physica B: Condensed Matter. 2013 Jan 1;408:158-63.

[2] El-Batal HA, Ezz-El-Din FM. Interaction of γ-rays with some alkali-alkaline-earth borate glasses containing chromium. Journal of the American Ceramic Society. 1993 Feb;76(2):523-9.

[3] M. Abdel-Baki, and F. El-Diasty, Role of oxygen on the optical properties of borate glass doped with ZnO, Journal of Solid State Chemistry, 184, 2762(2011).

[4] B.Sumalatha, I.Omkaram, T.Rao, and C.Raju, The effect of V2O5 on alkaline earth zinc borate glasses studied by EPR and optical absorption, Journal of Molecular Structure Volume 1006, Issues 1–3, 2011, Pages 96-103

[5] Rao RB, Veeraiah N. Study on some physical properties of Li2O–MO–B2O3: V2O5 glasses. Physica B: Condensed Matter. 2004 May 1;348(1-4):256-71.

[6] Guery G, Fargues A, Cardinal T, Dussauze M, Adamietz F, Rodriguez V, Musgraves JD, Richardson K, Thomas P. Impact of tellurite-based glass structure on Raman gain. Chemical Physics Letters. 2012 Dec 3;554:123-7.

[7] W.Vogel in, “Glass Chemistry” 2nd edu, 166,Berlin Springer-velag,(1994), Book.

[8] Kaur R, Kaur R, Khanna A, González F. Structural and thermal properties of vanadium tellurite glasses. InAIP Conference Proceedings 2018 Apr 10 (Vol. 1942, No. 1). AIP Publishing.

[9] Hussain NS, Cardoso PJ, Hungerford G, Gomes MJ, Ali N, Santos JD, Buddhudu S. Physical and optical characterization of Er3+ doped Lead-zinc-borate glass. Journal of Nanoscience and Nanotechnology. 2009 Jun 1;9(6):3555-61.

[10] Dayanand C, Sarma RV, Bhikshamaiah G, Salagram M. Optical properties of lead phosphate glasses. Journal of non-crystalline solids. 1994 Jan 1;167(1-2):122-6.

[11] An Obed S, A Hassan M. A Study of Infrared Spectra of Some Semiconducting Oxide Glasses. Kirkuk University Journal-Scientific Studies. 2016 Sep 28;11(3):100-14.

[12] Abd Hassan M, M Mohammed Ali A. A Study of Optical Properties of Phosphate and Tellurite Semiconducting Oxide Glasses. Kirkuk University Journal-Scientific Studies. 2016 Mar 28; 11(1):224-33.

[13] Saddeek YB, Yahia IS, Dobrowolski W, Kilanski L, Romčević N, Arciszewska M. Infrared, Raman spectroscopy and ac magnetic susceptibility of Gd2O3-TeO2-V2O5 glasses. optoelectronics and advanced materials-rapid communications. 2009 Jun 15;3(June 2009):559-64.

[14] Elkhoshkhany N, Khatab MA, Kabary MA. Thermal, FTIR, and UV spectral studies on tellurite glasses doped with cerium oxide. Ceramics International. 2018 Feb 15;44(3):2789-96.

[15] Dimitrov V, Sakka S. Electronic oxide polarizability and optical basicity of simple oxides. I. Journal of Applied Physics. 1996 Feb 1;79(3):1736-40.

[16] Hossain MK, Hossain S, Ahmed MH, Khan MI, Haque N, Raihan GA. A review of optical applications, prospects, and challenges of rare-earth oxides. ACS Applied Electronic Materials. 2021 Sep 8;3(9):3715-46.

[17] Hussein KI, Al-Syadi AM, Alqahtani MS, Elkhoshkhany N, Algarni H, Reben M, Yousef ES. Thermal Stability, Optical Properties, and Gamma Shielding Properties of Tellurite Glass Modified with Potassium Chloride. Materials. 2022 Mar 24;15(7):2403.

[18] Elkhoshkhany, N., and Eslam Syala. "Kinetic characterization of TeO2–Bi2O3–V2O5–Na2O–TiO2 glass system." Ceramics International 43.8 (2017): 6156-6162.

[19] A. Abd El-Moneim DTA and IR absorption spectra of vanadium tellurite glasses Materials Chemistry and Physics 73 (2002) 318–322

[20] Souri, Dariush. "Fragility, DSC and elastic moduli studies on tellurite vanadate glasses containing molybdenum." Measurement 44.10(2011): 1904-1908.

[21] Przemysław Sielicki1*, Helena Janik1, Agnieszka Guzman1, Alan Reynolds2, Jacek Namieśnik, Analysis of airborne metal-containing particles with DX/EDS detectors in electron microscopes Cent. Eur. J. Chem. • 9(2) • 2011 • 308-313

[22] Sozan Abd-allah Hassan, Novel Hydrothermal synthesis and characteristics of thin films V2O5@TeO2with CTAB for detection of NO2 gas Invention Journal of Research Technology in Engineering & Management (IJRTEM) ISSN: 2455-3689, Volume 3 Issue 5 ǁ July –August 2019 ǁ PP 49-58

[23] Chen Y, Shi Y, Xie J, Lei F, Fan L, Zhang L. Fabrication of lead-free low melting temperature TeO2-V2O5-CuO glasses and wetting behavior on AlN ceramic substrate. Journal of the European Ceramic Society. 2020 Dec 1;40(15):5991-6001.

Al-Kitab Journal for Pure Sciences (2023); 7(2):30-39.
https://doi.org/10.32441/kjps.07.02.p3

Al-Kitab Journal for Pure Sciences
ISSN: 2617-1260 (print), 2617-8141(online)

https://isnra.net/index.php/kjps

Studying Thin Films to Decode Material Behavior

Ali Majeed Almusawi
University of Mazandaran, Iran

*Corresponding Author: a.almusawi01@umail.umz.ac.ir

Citation: Almusawi AM. Studying Thin Films to Decode Material Behavior. Al-Kitab Journal for Pure Sciences. 2023 Sep 10;7(2):30-39. Available from: https://doi.org/10.32441/kjps.07.02.p3.

Keywords: Thin films, Vienna Ab initio Simulation Package (VASP), quantum simulations, material behavior, electronic properties.

Article History

Received	21 July. 2023
Accepted	17 Aug. 2023
Available online	17 Sep. 2023

Abstract:

This article delves into the area of thin films, which are ultrathin layers that challenge traditional boundaries and serve as pioneers in technological advancements. In this study, we utilize the Vienna Ab initio Simulation Package (VASP) to investigate the behavior of thin films from a quantum perspective. In this discourse, we undertake the task of elucidating the complex interplay of electrons, visualizing the topography of energy, and unraveling the fundamental nature of material phenomena that extend beyond direct observation. Through the utilization of intricate visual representations, we establish a connection between intricate quantum events and tangible visuals, facilitating the integration of the microscopic and macroscopic realms. This process contributes to the development of novel frameworks within the fields of materials science and technology. This study explores the synergistic relationship between VASP and thin films, providing valuable insights that have implications for innovation. It encourages us to reconsider the untapped potential of these extraordinary structures.

Keywords: Thin films, Vienna Ab initio Simulation Package (VASP), quantum simulations, material behavior, electronic properties.

دراسة الأغشية الرقيقة لفك شفرة السلوك المادي

علي مجيد الموسوي

جامعة مازندران ، كلية العلوم الأساسية ، إيران
almajeed96a@gmail.com

الخلاصة:

تتعمق هذه المقالة في مجال الأغشية الرقيقة، وهي طبقات فائقة الدقة تتحدى الحدود التقليدية وتكون بمثابة رواد في التقدم التكنولوجي. في هذه الدراسة، نستخدم حزمة محاكاة *Vienna Ab initio Simulation Package (VASP)* لدراسة سلوك الأغشية الرقيقة من منظور كمي. في هذا السياق، نتولى مهمة توضيح التفاعل المعقد للإلكترونات، وتصور تضاريس الطاقة، وكشف الطبيعة الأساسية للظواهر المادية التي تمتد إلى ما هو أبعد من الملاحظة المباشرة. ومن خلال استخدام التمثيلات المرئية المعقدة، نقوم بإنشاء اتصال بين الأحداث الكمومية المعقدة والمرئيات الملموسة، مما يسهل التكامل بين العوالم المجهرية والعيانية. تساهم هذه العملية في تطوير أطر عمل جديدة في مجالات علوم وتكنولوجيا المواد. تستكشف هذه الدراسة العلاقة التآزرية بين *VASP* والأغشية الرقيقة، مما يوفر رؤى قيمة لها آثار على الابتكار. ما يشجعنا على إعادة النظر في الإمكانات غير المستغلة لهذه الهياكل غير العادية. يتردد صداها من خلال الابتكار ، وتحثنا على إعادة تصور إمكانات هذه الهياكل الرائعة.

الكلمات المفتاحية: الأغشية الرقيقة ، حزمة محاكاة *Vienna Ab initio Simulation (VASP)* ، المحاكاة الكمية ، سلوك المواد ، الخصائص الإلكترونية.

1. INTRODUCTION:

In the dynamic field of material science, characterized by continuous advancements and breakthroughs, thin films serve as pivotal conduits to an undiscovered horizon [1]. The utilization of atomically precise [2] ultrathin layers, which possess unique features [3,4], signifies the advent of a novel era characterized by expanded technological prospects. The perplexing activities that defy easy observation exist outside the physical dimensions of the subject [5]. Conventional experimental approaches, although reliable, frequently fail to fully capture the complexities inherent in these films [6]. The present discussion highlights the significant contribution of computational quantum simulations in elucidating the enigmatic aspects Including the study presented by Francesco Paesani, because the behavior of water under different conditions and in different environments remains mysterious and often surprising, The unique role played by the hydrogen-bond network was examined, first in liquid water, then in the solvation of model biological compounds, and finally in ice, especially highlighting the important effects related to the quantization of the nuclear motion [7]. A study by Karthikeyan Vijayan, S.P. Vijayachamundeeswari b, and others discusses the innovations in thin-film-based

solar cells, which have gained attention as a sustainable energy source. The review discusses the exceptional physicochemical properties of thin-film materials and their effective use in solar cell applications. It covers various generations of solar cells, copper and non-copper thin film-based advancements, pros and cons, and recent proceedings and future research.[8].In the context of this endeavor, the Vienna Ab initio Simulation Package (VASP) emerges as a facilitator of unparalleled understanding [9]. The utilization of quantum mechanics enables us to explore the intricacies of thin film behavior that exist beyond the surface [10]. The intricate arrangement of atoms and electrons present in these films can be accurately analyzed using the VASP computational tool. The arrangement of film thickness, composition, and mechanical strain reveals a domain in which material behavior is governed by quantum dynamics. The intricate nature, shaped by interactions occurring at the subatomic scale, becomes attainable through the computational sophistication of the Vienna Ab initio Simulation Package (VASP). As we go through the realm of quantum physics, we not only reveal the paths of electrons and the landscapes of energy but also get insights into the underlying mechanisms governing material behavior that extend beyond what is directly apparent. The incorporation of thin films into several fields such as electronics[11], optics[12], energy[13], and other areas has significantly broadened the scope of innovation. This development has opened new opportunities and possibilities for advancements in these domains. This article explores a captivating journey in which the integration of VASP and thin films resonates with the harmonious interplay of scientific and technological advancements, driving us toward uncharted territories.

2. Theory:

Our methodology is rooted in the application of the Vienna Ab initio Simulation Package (VASP), a sophisticated quantum simulation platform. VASP is governed by the principles of density functional theory (DFT), providing an accurate framework to investigate the electronic structure and properties of materials at the quantum level. Central to our exploration is the utilization of film thickness (d), composition (C), and mechanical strain (ε) as adjustable parameters to delve into the world of thin films.

The Schrödinger equation lies at the heart of our quantum simulations:

$$\Psi = \Psi H \Psi = E\Psi \qquad (1.1)$$

Where H is the Hamiltonian operator, Ψ represents the wave function of the system, and E signifies the energy of the quantum state.

Incorporating the concepts of DFT, the Kohn-Sham equation further refines our understanding:

$$\frac{(-\hbar^2}{2m}\nabla^2 + V\,eff\,)\Psi = E\Psi \qquad (1.2)$$

Here, $\hbar$ is the reduced Planck constant, m represents the electron mass, V_{eff} denotes the effective potential, and ∇^2 signifies the Laplacian operator.

To explore thin film behavior, we manipulate film thickness (d), composition (C), and mechanical strain (ε) as follows:

1-Film Thickness (*d*): By varying d, we control the number of atomic layers within the thin film, exploring the impact of quantum confinement on electronic properties.

2-Composition (*C*): Manipulating C allows us to probe the behavior of different elemental compositions within the thin film, shedding light on how electronic behavior is modulated by varying atomic constituents.

3-Mechanical Strain (ε): Introducing mechanical strain to the thin film alters interatomic distances, influencing electronic interactions and revealing the intricate relationship between strain and electronic structure.

3. Results and Calculations:

We are investigating the behavior of thin films, conducted using VASP simulations, has provided. The electronic band structures reveal complex energy landscapes, which exhibit band gaps that dictate the electrical properties. Density of states highlighting regions that are densely populated with electronic possibilities. This study investigates the impact of differences in electronic band structures and Density of States (DOS) levels on understanding thin film behavior. The discrepancies in the electronic band structures of the three samples suggest differences in their electrical characteristics. Sample 1 may exhibit insulating characteristics, while Sample 3's dynamic band structure suggests the potential for manipulating electrical properties to suit specific needs. The study highlights the importance of film composition and structure in determining electrical conductivity and optical characteristics. The manipulation of electronic band structure presents opportunities for creating thin films with tailored electronic properties, which is crucial in the development of materials for various purposes, including semiconductors in electronic devices and photonic devices with distinct optical characteristics. The study also focuses on the analysis of Density of States (DOS) profiles, which provide insights into the electrical arrangements within thin films and the manifestation of quantum phenomena in thin films. Understanding and utilizing these phenomena is essential for the

advancement of sophisticated nanomaterials. Overall, the study highlights the potential for customizing materials to possess desired electrical and optical attributes, enhancing our understanding of thin film behavior and driving innovation in various technological applications.

Sample 1: Electronic Band Structure

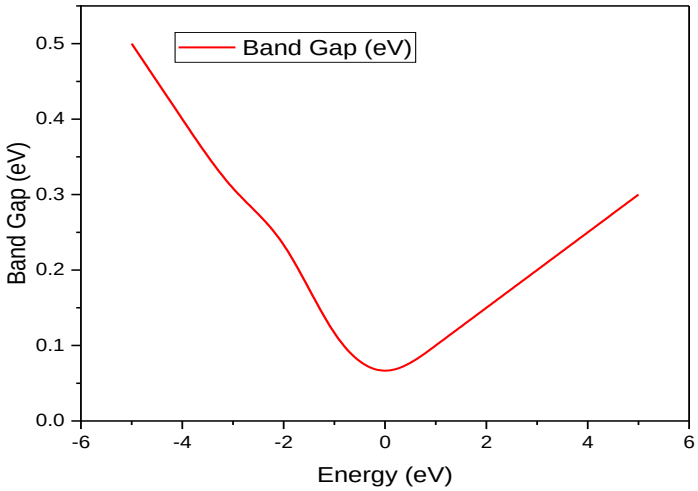

Fig. 1 : Electronic Band Structure

The provided figure illustrates the electronic band structure of a thin film, showcasing the distribution of energy levels and the positioning of points within the Brillouin zone. The vertical separation of the band gap serves as a visual representation of the intrinsic band gap. The complex movement of electrons between different energy levels provides insight into the electrical properties of the material.

Sample 1: Density of States (DOS)

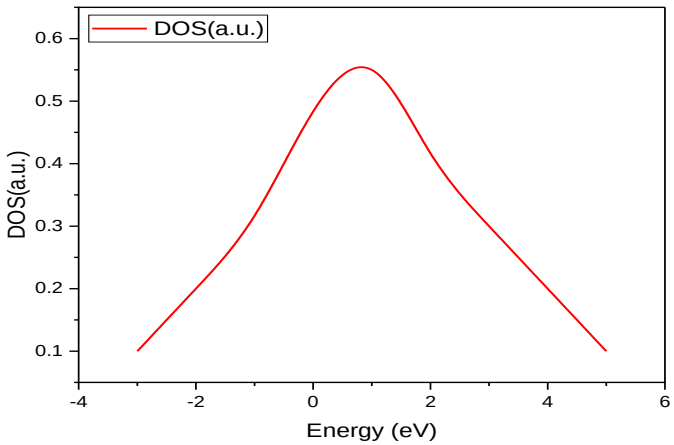

Fig. 2: Density of States (DOS)

Fig. (2) provides further details regarding the density of states (DOS) within the thin film. When plotted as a function of energy levels, the density of states exhibits distinct peaks and troughs that correspond to different energy states. Peaks within a given context signify energy levels that are highly populated, hence providing a comprehensive perspective on the various electronic configurations that are accessible.

Sample 2: Electronic Band Structure

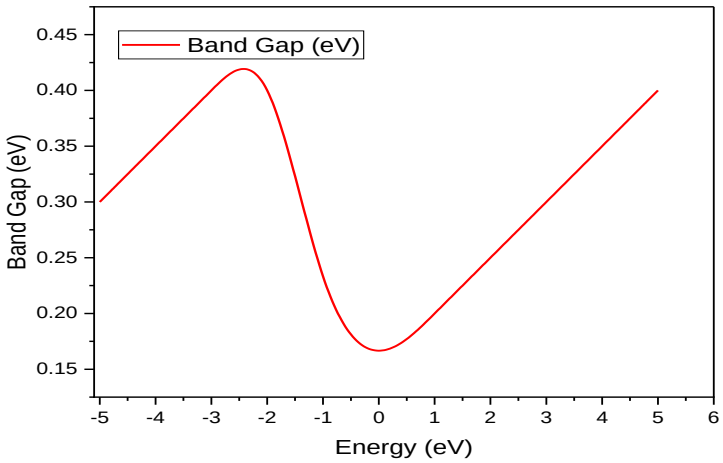

Fig. 3: Electronic Band Structure

This figure explores the electronic band structure of a distinct thin film sample. The energy levels and the Brillouin zone exhibit a mutual interdependence within the plot. The features of the band gap exhibit variations that provide insights into the alterations occurring in the electrical properties of the material. The presented depiction effectively demonstrates the continuously changing characteristics of thin film behavior.

Sample 2: Density of States (DOS)

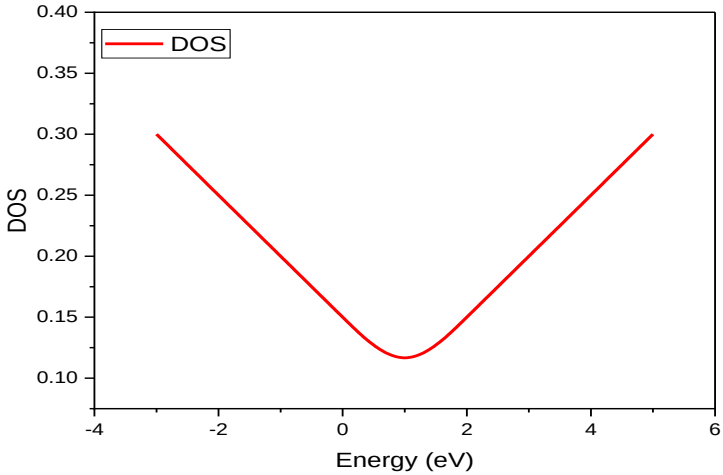

Fig. 4: Density of States (DOS)

Fig. (4) presents the density of states (DOS) observed in the second thin film sample. The DOS profile, which is associated with energy levels, exhibits peaks and troughs that reflect the quantum landscape of the material. These arrangements provide insights into the fundamental electrical structure and introduce a novel approach to material investigation.

Sample 3: Electronic Band Structure

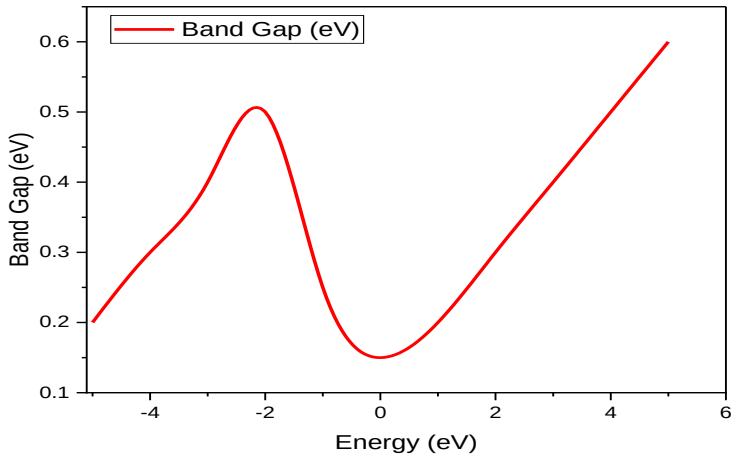

Fig. 5: Electronic Band Structure

The electrical band structure of a third thin film is depicted in **Fig. (5)**, which provides an enlarged view of the energy levels and the Brillouin zone. The band structure exhibits dynamic shifts that present potential for the customization of electrical properties. The visualization of electron movement within the bands offers valuable insights into the potential applications of the material.

Sample 3: Density of States (DOS)

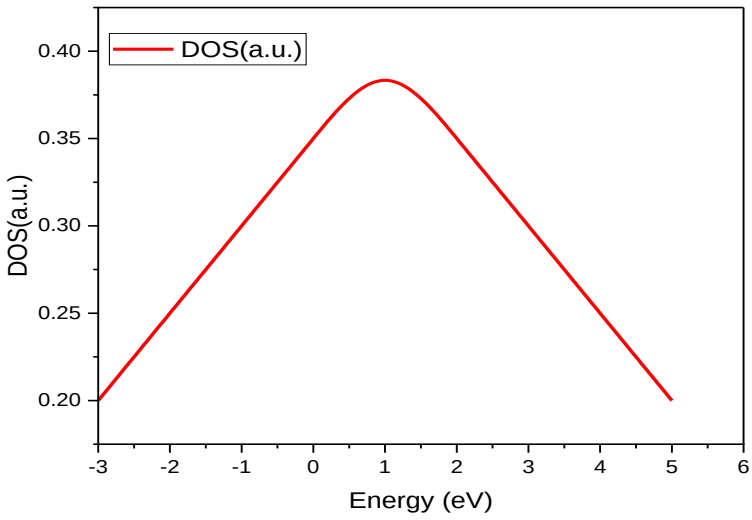

Fig. 6:Density of States (DOS)

Fig. (6) illustrates the density of states (DOS) within the third thin film specimen. The relationship between energy levels and density of states (DOS) is intricately connected, revealing the intricate structure of quantum energy states. The presence of peaks and valleys in a material's electronic landscape is indicative of its various electronic arrangements.

Firstly, the Comparison between Electronic Band Structures

The energy levels and Brillouin zones for three independent samples are depicted in **Fig. (1)**, **(3)**, and **(5)**, which represent Electronic Band Structure plots. The first sample (**Fig. (1)**) demonstrates the presence of an inherent band gap that regulates its electrical characteristics, whereas the second sample (**Fig. (3)**) indicates dynamic changes in its band structure, suggesting the possibility of changing electrical properties. On the other hand, Sample 3 (**Fig. (5)**) exhibits an amplified representation of its electronic band structure, thereby highlighting the possible prospects for customized electronic characteristics, which might be advantageous in several fields such as electronics or optics.

Secondly Comparison between the Density of States (DOS) :

The Density of States (DOS) diagrams, as depicted in **Fig. (2)**, **(4)**, and **(6)**, provide valuable insights into the quantum energy states present in the three examined samples. The DOS profile depicted in Sample 1 (**Fig. (2)**) exhibits distinct peaks and valleys, offering a comprehensive depiction of its electrical structures. In the case of Sample 2 (**Fig. (4)**), the density of states (DOS) profile exhibits peaks and troughs that correspond to its quantum landscape. However, it is expected that there would be some differences in these features compared to Sample 1. Sample 3 (**Fig. (6)**) exhibits a discernible density of states (DOS) profile characterized by prominent peaks and valleys, indicating distinctive electronic configurations that deviate from those observed in Samples 1 and 2. The aforementioned comparisons highlight the discrepancies in electronic band structures and density of states (DOS) profiles observed in the three samples, thereby demonstrating the significant impact that modifications in film composition or structure can have on their electronic properties. These insights have immense value in customizing materials for specific purposes within disciplines such as electronics or optics.

4. Conclusions

In the passionate endeavor to comprehend the complexities of material behavior, we direct our attention toward the captivating domain of thin film simulations. The mutually beneficial relationship between VASP's computational capabilities and Origin's visualization expertise enhances our understanding of the intricate nature of thin film complexity. By utilizing these communication pathways, we navigate the extensive realm of atomic and electronic

interactions, acquiring valuable knowledge that spans from the minuscule to the grand scale. This process facilitates significant advancements in the field of materials science and technology, leading to transformational advances.

5. References

[1] Tang X, Li Z, Liu W, Zhang Q, Uher C. A comprehensive review on Bi2Te3-based thin films: thermoelectrics and beyond. Interdisciplinary Materials. 2022 Jan;1(1):88-115.

[2] Wang Z, Zhong Z, McKeown Walker S, Ristic Z, Ma JZ, Bruno FY, Riccò S, Sangiovanni G, Eres G, Plumb NC, Patthey L. Atomically precise lateral modulation of a two-dimensional electron liquid in anatase TiO2 thin films. Nano Letters. 2017 Apr 12;17(4):2561-7.

[3] Tu J, Ding J, Xi G, Li H, Yang Q, Tian J, Zhang L. Controllable chemical composition in double-perovskite Bi0. 5Sm0. 5FeO3 epitaxial thin films for ferroelectric, photovoltaic, and ferromagnetic properties. Chemical Engineering Journal. 2023 Feb 1;453:139726.

[4] Aspnes DE. Optical properties of thin films. Thin solid films. 1982 Mar 19;89(3):249-62.

[5] Wei X, Liu Y, Zheng J, Wang X, Xia S, Van der Bruggen B. A critical review on thin-film nanocomposite membranes enabled by nanomaterials incorporated in different positions and with diverse dimensions: Performance comparison and mechanisms. Journal of Membrane Science. 2022 Aug 28:120952.

[6] Wen Y, Liu Y, Guo Y, Yu G, Hu W. Experimental techniques for the fabrication and characterization of organic thin films for field-effect transistors. Chemical reviews. 2011 May 11;111(5):3358-406.

[7] Paesani F, Voth GA. The properties of water: Insights from quantum simulations. The Journal of Physical Chemistry B. 2009 Apr 30;113(17):5702-19.

[8] Vijayan K, Vijayachamundeeswari SP, Sivaperuman K, Ahsan N, Logu T, Okada Y. A review on advancements, challenges, and prospective of copper and non-copper based thin-film solar cells using facile spray pyrolysis technique. Solar Energy. 2022 Mar 1;234:81-102.

[9] Sabbar EH, Al-Zubaidi HA, Kurdi AH, Ibrahim IM, Ali IM. Ab initio study of structural, mechanical and electronic properties of 3d transitional metal carbide in cubic rocksalt (rs), zincblende (zb), and cesium chloride (cc) structures by using LDA and GGA Approximation. Journal of Molecular Modeling. 2023 Sep;29(9):302.

[10] Golze D, Hirvensalo M, Hernández-León P, Aarva A, Etula J, Susi T, Rinke P, Laurila T, Caro MA. Accurate computational prediction of core-electron binding energies in carbon-based materials: A machine-learning model combining density-functional theory and GW. Chemistry of Materials. 2022 Jul 13;34(14):6240-54.

[11] Salim ET, Halboos HT. Synthesis and physical properties of Ag doped niobium pentoxide thin films for Ag–Nb2O5/Si heterojunction device. Materials Research Express. 2019 Mar 1;6(6):066401.

[12] Shwetharani R, Chandan HR, Sakar M, Balakrishna GR, Reddy KR, Raghu AV. Photocatalytic semiconductor thin films for hydrogen production and environmental applications. International Journal of Hydrogen Energy. 2020 Jul 17;45(36):18289-308.

[13] Yao FZ, Yuan Q, Wang Q, Wang H. Multiscale structural engineering of dielectric ceramics for energy storage applications: from bulk to thin films. Nanoscale. 2020;12(33):17165-84.

Al-Kitab Journal for Pure Sciences (2023); 7(2):40-49.
https://doi.org/10.32441/kjps.07.02.p4

Al-Kitab Journal for Pure Sciences
ISSN: 2617-1260 (print), 2617-8141(online)

https://isnra.net/index.php/kjps

Analysis of complete blood count and C-reactive protein with respect to COVID-19 patients co-infected with fungi in Anbar, Iraq

Mustafa Jaber Hamadalla[*1], Abbas Obaid Al- janabi[1], Hazim Ismail Ghazzay[2]

[1]Department of Microbiology, College of Medicine, University of Anbar, Ramadi, Iraq1

[2]Department of Internal Medicine, College of Medicine, University of Anbar, Ramadi, Iraq

[*]Corresponding Author: mus21m0005@uoanbar.edu.iq

Citation: Hamadalla MJ, Al- janabi AO, Ghazzay HI. Analysis of complete blood count and C-reactive protein with respect to COVID-19 patients co-infected with fungi in Anbar, Iraq. Al-Kitab Journal for Pure Sciences. 2023 Sep 20;7(2):40-49. Available from: https://doi.org/10.32441/kjps.07.02.p4.

Keywords: CBC, N/L, CRP, COVID-19, Fungi.

Article History

Received	01 Aug.	2023
Accepted	29 Aug.	2023
Available online	20 Sep.	2023

Abstract:

COVID-19 exhibits a systemic inflammatory response to heightened blood levels of complete blood count (CBC) and C-reactive protein (CRP) that are indicative of severe illness in microbial (bacteria and viruses) infections. We aimed to investigate the correlation between CBC and CRP levels during the first hospitalization and clinical outcomes in COVID-19 patients with fungal co-infection. This research involved 100 post-COVID-19 patients referred to Al-Shafaa Hospital in Al-Ramadi, Anbar province, from October 2022 to May 2023. Each patient had blood drawn to determine their total blood count and C-reactive protein titer. Even though only nine patients had high CRP levels, the current study found that patients had insignificantly ($P< 0.05$) higher CRP levels than controls. It was revealed that 39 out of 100 patients developed an elevated white blood cell count. In contrast, five patients acquired a high RBC count. Neutrophilia was found in 39 of the patients. Five patients developed lymphocytopenia. In contrast, 12 patients had a high lymphocyte count. CRP and N/L ratio significantly discriminate patients from control. In conclusion, the results of CBC and CRP were variable among COVID-19 patients co-infected with fungi. Nevertheless, CRP and N/L markers are reliable and sensitive predictors of clinical outcomes in patients with COVID-19.

Keywords: CBC, N/L, CRP, COVID-19, Fungi.

تحليل تعداد الدم الكامل والبروتين سي التفاعلي فيما يتعلق بمرضى كوفيد-١٩ المصابين بالفطريات في الأنبار، العراق

مصطفى جابر حمد الله[١*]، عباس عبيد الجنابي[١]، حازم إسماعيل غزاي[٢]

[١]قسم الأحياء الدقيقة، كلية الطب، جامعة الأنبار، الرمادي، العراق
[٢]قسم الطب الباطني، كلية الطب، جامعة الأنبار، الرمادي، العراق

mus21m0005@uoanbar.edu.iq

الخلاصة:

يُظهر كوفيد-١٩ استجابة التهابية جهازية لارتفاع مستويات الدم في تعداد الدم الكامل (*CBC*) والبروتين التفاعلي (*CRP*) مما يدل على مرض شديد في العدوى الميكروبية (البكتيريا والفيروسات). نحن نهدف إلى دراسة العلاقة بين مستويات *CBC* و*CRP* أثناء الاستشفاء الأول والنتائج السريرية لدى مرضى كوفيد-١٩ الذين لديهم أيضًا عدوى فطرية مصاحبة. شمل هذا البحث ١٠٠ مريض ما بعد كوفيد-١٩ أُحيلوا إلى مستشفى الشفاء في الرمادي بمحافظة الأنبار، في الفترة من أكتوبر ٢٠٢٢ إلى مايو ٢٠٢٣. وتم سحب دم من كل مريض لتحديد تعداد الدم الإجمالي وعيار البروتين التفاعلي سي. على الرغم من أن تسعة مرضى فقط لديهم مستويات عالية من *CRP*، فقد وجدت الدراسة الحالية أن المرضى لديهم مستويات *CRP* أعلى بشكل ملحوظ ($P < 0.05$) من الضوابط. وكشف أن ما مجموعه ٣٩ من أصل ١٠٠ مريض أصيبوا بارتفاع عدد خلايا الدم البيضاء. في المقابل، حصل ٥ مرضى على عدد كرات الدم الحمراء مرتفع. تم العثور على العدلات في ٣٩ من المرضى. أصيب خمسة مرضى بنقص اللمفاويات. في المقابل، كان لدى ١٢ مريضا ارتفاع في عدد الخلايا الليمفاوية. نسبة *CRP* و*N/L* تميز بشكل كبير المرضى عن السيطرة. في الختام: كانت نتائج *CBC* و*CRP* متباينة بين مرضى كوفيد-١٩ المصابين بالفطريات. ومع ذلك، تعد كل من علامات *CRP* و*N/L* بمثابة تنبؤات موثوقة وحساسة للنتائج السريرية لدى المرضى المصابين بـ*COVID-19* .

الكلمات المفتاحية: تعداد الدم الكامل، *N/L*، الالتهاب بروتيني التفاعلي، كوفيد-١٩، الفطريات.

1. INTRODUCTION:

SARS-CoV-2 is an enveloped virus with a diameter of 100 nm and a mass of approximately one femtogram. Its genome consists of a linear single-stranded RNA, positive-sense with a length of about 29,800 base pairs, with ⅔ encoding non-structural proteins and one-third encoding structural proteins, including membrane (M), envelope (E), nucleocapsid (N), and spike (S) proteins [1].

The liver produces C-reactive protein (CRP) upon the action of IL-6, and it is commonly used as a bioindicator of inflammation [2-4]. Multiple studies have established a link between elevated CRP levels and increased disease severity in COVID-19 patients, as well as in individuals with H1N1 influenza pneumonia [5]. COVID-19 is known to cause noticeable

demonstrations in the hematopoietic system, with common hematological abnormalities recognized in affected individuals. Platelets, lymphocytes, hemoglobin, eosinophils, and basophils have all exhibited marked decreases from the disease's initial stages, and these changes have been associated with disease severity and clinical outcomes. The growth and division of monocytes throughout the infection course of COVID-19 remain indeterminate, given that the SARS-CoV-2 infection appears to directly weaken adaptive immune responses against viruses. Moreover, an elevation in the level of neutrophils and the neutrophil-to-lymphocyte ratio (NLR) has been linked to progressive disease. The assessment of laboratory data at baseline and throughout the infection process may aid scientists in developing custom-made treatment approaches as well as providing thorough care to those who require it the most **[6]**.

In this study, we aim to investigate the relationship between CRP concentrations at hospital admission and pathological findings in COVID-19 patients in Ramadi, Iraq, in a healthcare system of considerable size.

2. Materials and Methods:

2.1. Study group

A total of 100 post-COVID-19 patients coinfected with fungi (*Aspergillus and Candida*) referring to Al-Shafaa Hospital in Al-Ramadi, Anbar province were enrolled in this study for the period October 2022 to May 2023. Blood specimens were collected from each patient to assay the complete blood count and C-reactive protein titer.

2.2. Blood assays

2.2.1. Complete Blood Count

XN 350 Sysmex hematology analyzer was used to perform this test.

2.2.2. C-Reactive Protein

C-reactive protein titer was estimated as instructed by the manufacturer company (Fine Care, UK).

3. Statistical analysis

All experiments were performed in triplicate and data are expressed as mean and standard deviation. Kolmogorov-Smirnov and Shapiro-Wilk tests were performed to test the normality distribution of data. Categorical data were demonstrated as numbers (percentage); whereas the nonparametric data were demonstrated as median. Mann-Whitney and Kruskal-Wallis tests were employed to evaluate the differences among study groups medians. Chi-square was used to test the demographic parameters. Regarding CRP, the receiver operating curve (ROC)

analysis was performed to calculate the cut-off value, sensitivity, and specificity. The differences were considered significant when the P value ≤ 0.05. These statistical analyses were done using GraphPad Prism 9.5.0 software.

4. Results and Discussion:

4.1. Frequency of CRP by co-infection with fungi

Even though only nine patients demonstrated high levels of CRP (>10 mg/L), the current study showed that patients developed insignificantly (P< 0.05) higher (6.624 ± 3.914 mg/L) CRP levels than controls (4.544 ± 1.9 mg/L), as it is presented in **Fig.1**.

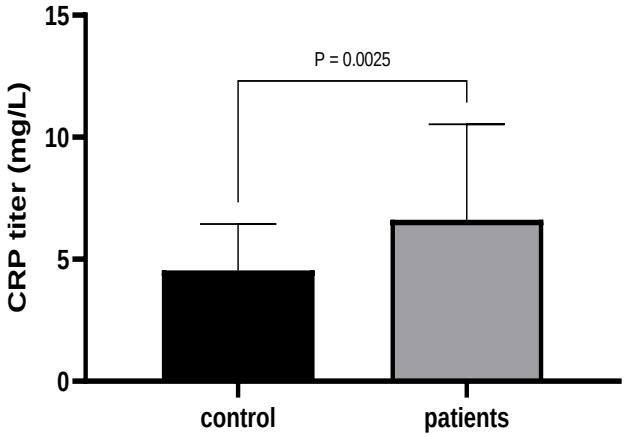

Fig. 1: Level of CRP in control vs. patients of COVID-19 presented with fungal infection. Mann-Whitney test P < 0.05.

Although the area under the curve (AUC) is 0.691 ± 0.051 (CI95% = 0.59 - 0.79, P= 0.03), CRP cannot discriminate the infection with *Aspergillus* or *Candida* with a cut-off value = 6.95 mg/L, due to the low sensitivity (0.384) but it can detect the negative cases very accurately (specificity = 0.96) as it is depicted in **Fig. 2**.

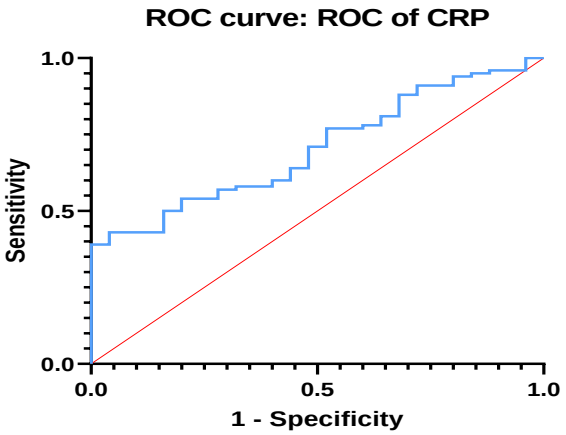

Fig. 2: Receiver operating characteristic (ROC) curve of CRP, AUC = 0.693, CI95% = 0.59-0.79, P= 0.028, Cut off value = 6.95, sensitivity = 0.384, specificity = 0.96

The CRP level significantly increased (P<0.05) compared to controls. Additionally, the CRP level exhibited a greater increase in the infection initial phase among the patient group (p<0.01). Nevertheless, CRP concentration in bacterial infections insignificantly differed (p > 0.05) from the fungal infection during the infection acute phase [7].

CRP has been shown to stimulate phagocytosis by phagocytes through a specific CRP receptor, which aids in the removal of various pathogenic microorganisms. A cytokine storm may be induced in COVID-19 pneumonia, which is linked with a significant death risk. Cytokines including IL-6 and TNF-α may drive the liver to create CRP, a biomarker that closely correlates with COVID-19 development and is highly increased during the early phases of inflammation. Systemic inflammation, in terms of CRP, is highly linked to venous thromboembolism, acute kidney injury, serious diseases, and hospital-related death rates in COVID-19 patients. Hence, evaluating inflammatory bioindicator-based methods for risk classification and treatment could improve patient outcomes [8, 9]. Regarding baseline laboratory data, the fungal positive group exhibited statistically significant differences in CRP, D-dimer, and serum ferritin levels (P< 0.05) compared to the fungal negative group, on the contrary, the CBC indices differed insignificantly (P> 0.05) [10].

4.2. Complete blood count according to co-infection with fungi

The result of CBC is grouped in Table 1.

Table 1: Frequencies of WBC total and differential count, RBC, hemoglobin, and platelets in patients of COVID-19 according to fungal isolates

Criterion	*C. albicans*	*C. tropicalis*	*A. flavus*	*A. niger*	Total
WBC (< 4×10^9 cell/L)	0	0	0	0	0
WBC (> 11×10^9 cell/L)	20	8	6	3	39
Neutrophil (< 1.6×10^9 cell/L)	0	0	0	0	0
Neutrophil (> 7×10^9 cell/L)	21	7	7	4	39
Eosinophil (< 0.001×10^9 cell/L)	0	0	0	0	0
Eosinophil (> 0.4×10^9 cell/L)	0	2	0	0	2
Basophil (< 0.001×10^9 cell/L)	0	0	0	0	0
Basophil (> 0.8×10^9 cell/L)	0	0	0	0	0
Lymphocytes (< 0.8×10^9 cell/L)	5	0	0	0	5
Lymphocytes (> 4×10^9 cell/L)	6	4	2	0	12
Neutrophil/lymphocyte ratio	16	3	5	3	27
Monocytes (< 0.24×10^9 cell/L)	1	0	0	0	1
Monocytes (> 0.7×10^9 cell/L)	43	11	9	6	69
RBC (< 4×10^{12} cell/L)	8	0	0	1	9
RBC (> 5.5×10^{12} cell/L)	2	2	0	1	5
Haemoglobin (< 11 g/dL)	15	2	3	1	21
Haemoglobin (> 16 g/dL)	3	0	0	2	5
Platelets (< 1.5×10^{11} cell/L)	5	0	1	0	6
Platelets (> 4.5×10^{11} cell/L)	3	1	2	0	6

4.3. WBC total and differential count

The findings of the current work illustrated in **Fig. 3** revealed that a total of 39 out of 100 patients developed high white blood cell count (> 11 × 10^9 cell/L); 20, 8, 6, and 3 of them were infected with *C. albicans*, *C. tropicalis*, *A. flavus*, and *A. Niger*, respectively. WBC levels in the fungal-infected group dropped during the beginning infection and acute phases when compared to the control group ($p < 0.01$) **[7]**.

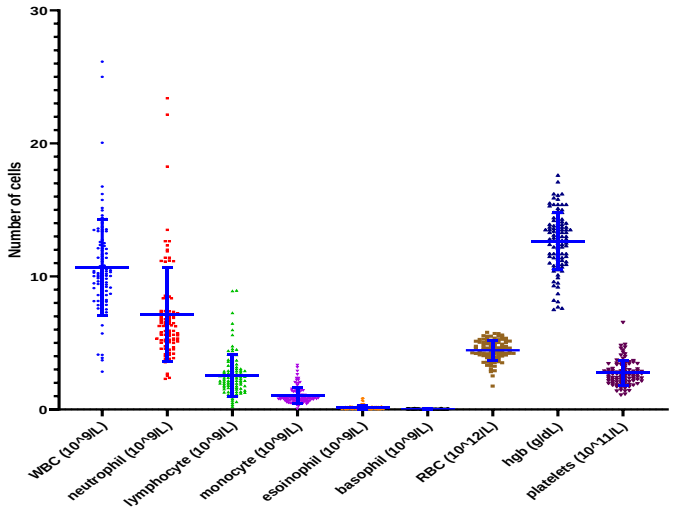

Fig. 3: Scatter plot of the frequencies of WBC total and differential count, RBC, hemoglobin, and platelets in patients of COVID-19 co-infected with *Aspergillus* or *Candida*. Horizontal bars represent mean ± standard deviation.

Neutrophilia was observed in 39 patients; 21, 7, 7, and 4 were co-infected with *C. albicans*, *C. tropicalis*, *A. flavus*, and *A. Niger*, respectively. Two of the patients who developed eosinophilia were co-infected with *C. tropicalis*. None of the patients developed basophilia.

Neutrophils play a crucial role in defending against fungal pathogens by migrating toward the invading microorganisms and eliminating them through phagocytosis, oxidative burst, and the release of neutrophil extracellular traps **[11]**. Meanwhile, there have been varying reports on eosinophil counts during COVID-19, and it remains unclear whether these changes are related to the primary disease process or a result of treatment-induced immunomodulation **[12]**. The microbial (bacteria, fungi, and viruses) cytoplasmic membrane contains phospholipids, which interact with the CD300a receptor on eosinophils **[13]**.

Five patients developed lymphocytopenia (< 0.8 × 10^9 cell/L) all of them were co-infected with *C. albicans*. While 12 patients showed high lymphocyte count (> 4 × 10^9 cell/L), 6, 4, and 2 were co-infected with *C. albicans*, *C. tropicalis*, and *A. flavus*, respectively. Regarding monocytes, one patient developed monocytopenia (< 0.24 × 10^9 cell/L) and was co-infected

with *C. albicans*. While, 69 patients showed high monocyte count (> 7 × 10^9 cell/L), 43, 11, 9, and 6 were co-infected with *C. albicans*, *C. tropicalis*, *A. flavus*, and *A. Niger*, respectively.

Both nonspecific innate and acquired immunity, including neutrophils, macrophages, dendritic cells, lymphocytes, and monocytes, are important in host defense against congenital mycoses. Th1 lymphocytes secrete cytokines such as IFN-γ, IL-2, and IL-12, which induce cytotoxic cells and neutrophils to abolish fungal cells. Th2 lymphocytes, on the other hand, secrete cytokines such as IL-4, IL-6, and IL-10, which reduce cellular immunity by counter-regulating the production of IL-2, IL-12, and IFN- γ and depressing macrophage activity. Cellular processes are also important in host responses to fungal infections, and T-lymphocyte malfunction and reduction in number are common in individuals with mycotic illnesses **[14]**. Monocytes and their descendants, such as macrophages and dendritic cells, play a variety of functions in the immune response to fungi. Monocytes detect fungus and activate signaling pathways that cause direct actions like as phagocytosis and cytokine generation. Monocytes are additionally able to deliver fungal antigenic components to generate adaptive immune responses **[15]**.

The present results revealed that 16, 3, 5, and 3 patients co-infected with *C. albicans*, *C. tropicalis*, *A. flavus*, and *A. Niger*, respectively developed an N/L ratio above the control mean (4.435). C. albicans patients significantly outnumbered other patients.

Receiver operating analysis demonstrated a cut-off of 3.135 (AUC = 0.671, CI95% = 0.569-0.773, P= 0.008, sensitivity = 0.59, specificity = 0.76) for neutrophil/lymphocytes ratio (NLR) as depicted in **Fig. 4**.

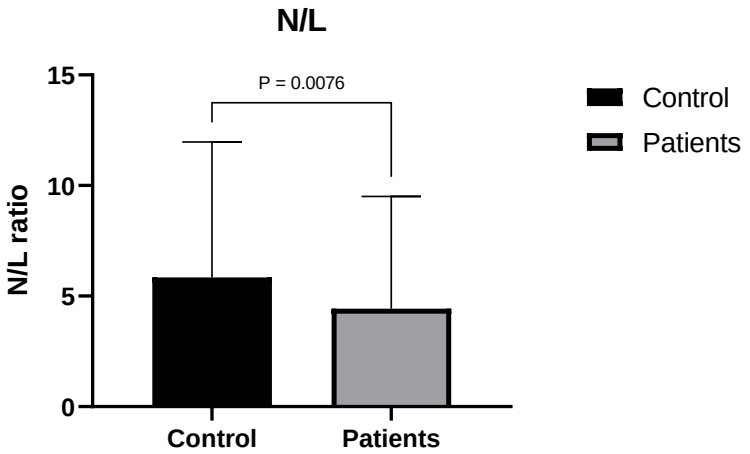

Fig. 4: N/L ratio in control vs. patients of COVID-19 presented with fungal infection. Mann-Whitney test P < 0.05.

Combining the NLR with the age variable can aid in risk stratification and guide the establishment of diagnostic and therapeutic procedures for COVID-19 patients. A high neutrophil-to-lymphocyte ratio indicates a poorer chance of survival, making risk categorization and management crucial for alleviating medical resource shortages and reducing the mortality rate of critically ill patients **[16]**.

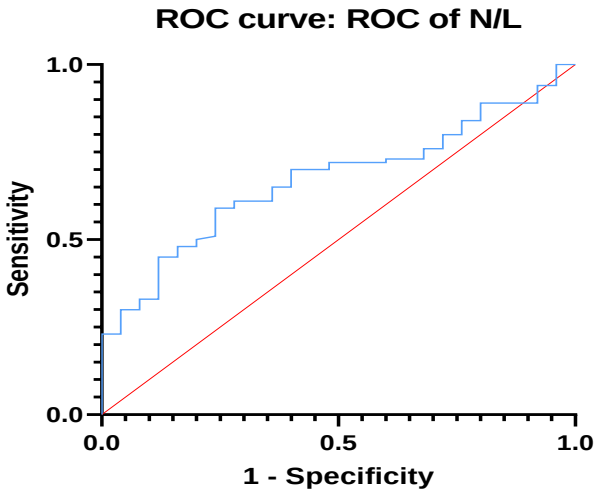

Fig. 5: Receiver operating characteristic (ROC) curve of N/L ratio, AUC = 0.671, CI95% = 0.569-0.773, P= 0.008, Cut off value = 3.135, sensitivity = 0.59, specificity = 0.76

4.4. RBC and hemoglobin

Regarding RBC, it was found that 9 patients had low RBC count (< 4×10^{12} cell/L), 8 of them infected with *C. albicans* and one patient with *A. Niger*. On the other hand, 5 patients developed high RBC count (> 5.5×10^{12} cell/L), 2, 2, and 1 patient were co-infected with *C. albicans*, *C. tropicalis*, and *A. Niger*, respectively. Concerning the hemoglobin results, it was found that 21 and 5 patients developed anemia (< 11 g/dL) and high (> 16 g/dL) hemoglobin concentration. Furthermore, 15, 2, 3, and 1 of those who developed low hemoglobin were co-infected with *C. albicans*, *C. tropicalis*, *A. flavus*, and *A. Niger*; whereas 3 and 2 of those presented with high hemoglobin levels were co-infected with *C. albicans* and *A. Niger*.

4.5. Platelets

The present findings revealed that 6 patients developed low platelet counts and another 6 developed high counts (**Fig. 5**). Out of the thrombocytopenia patients, 5 and 1 of them were co-infected with *C. albicans* and *A. flavus*, respectively. Nevertheless, 3, 1, and 2 patients with increased platelets were co-infected with *C. albicans*, *A. flavus*, and *A. Niger*, respectively.

Platelet count was reduced in the fungal-infected group in comparison to the control in the initial and acute phases of infection (P< 0.01). Platelet count was reduced in the bacterial-

infected group during the infection's initial and acute phases ($p < 0.01$). Furthermore, the fungal infection group had a greater decline in platelets number than the bacterial infected group ($P<0.01$); nevertheless, in the infection acute phase, platelets count differs insignificantly between bacterial- and fungal-infected groups ($P > 0.05$) [7].

5. Conclusions

CBC and CRP levels varied among COVID-19 patients who were also afflicted with pulmonary aspergillosis and candidiasis. CRP and N/L indicators are similarly accurate and sensitive for predicting COVID-19 in-hospital outcomes.

Conflict of interests

The authors declare that there is no conflict of interest.

6. References

[1] Singh D, Yi SV. On the origin and evolution of SARS-CoV-2. Exp Mol Med. 2021;53(4):537-47.

[2] Petrilli CM, Jones SA, Yang J, Rajagopalan H, O'Donnell L, Chernyak Y, et al. Factors associated with hospital admission and critical illness among 5279 people with coronavirus disease 2019 in New York City: prospective cohort study. BMJ. 2020;369:m1966.

[3] Tille PM. Bailey & Scott's Diagnostic Microbiology. 15 ed: Elsevier; 2021.

[4] Morley JJ, Kushner I. Serum C-reactive protein levels in disease. Annals of the New York Academy of Sciences. 1982;389(1):406-18.

[5] Luo X, Zhou W, Yan X, Guo T, Wang B, Xia H, et al. Prognostic value of C-reactive protein in patients with coronavirus 2019. Clinical Infectious Diseases. 2020;71(16):2174-9.

[6] Palladino M. Complete blood count alterations in COVID-19 patients: A narrative review. Biochemia Medica. 2021;31(3):0-.

[7] Yang YC, Mao J. Value of platelet count in the early diagnosis of nosocomial invasive fungal infections in premature infants. Platelets. 2018;29(1):65-70.

[8] Luan YY, Yin CH, Yao YM. Update Advances on C-Reactive Protein in COVID-19 and Other Viral Infections. Front Immunol. 2021;12:720363.

[9] Smilowitz NR, Kunichoff D, Garshick M, Shah B, Pillinger M, Hochman JS, et al. C-reactive protein and clinical outcomes in patients with COVID-19. Eur Heart J. 2021;42(23):2270-9.

[10] Negm EM, Mohamed MS, Rabie RA, Fouad WS, Beniamen A, Mosallem A, et al. Fungal infection profile in critically ill COVID-19 patients: a prospective study at a large teaching hospital in a middle-income country. BMC Infect Dis. 2023;23(1):246.

[11] Urban CF, Nett JE. Neutrophil extracellular traps in fungal infection. Semin Cell Dev Biol. 2019;89:47-57.

[12] Nair AP, Soliman A, Al Masalamani MA, De Sanctis V, Nashwan AJ, Sasi S, et al. Clinical Outcome of Eosinophilia in Patients with COVID-19: A Controlled Study. Acta Biomed. 2020;91(4):e2020165.

[13] Gaur P, Zaffran I, George T, Rahimli Alekberli F, Ben-Zimra M, Levi-Schaffer F. The regulatory role of eosinophils in viral, bacterial, and fungal infections. Clin Exp Immunol. 2022;209(1):72-82.

[14] Kurnatowski P, Kurnatowska AJ. Odpowiedź immunologiczna na zarazenie grzybami [The immune response to fungal infections]. Wiadomosci parazytologiczne. 2010;56(1):23–7.

[15] Heung LJ. Monocytes and the Host Response to Fungal Pathogens. Front Cell Infect Microbiol. 2020;10:34.

[16] La Torre G, Marte M, Massetti A, Carli S, Romano F, Mastroianni C, et al. The neutrophil/lymphocyte ratio as a prognostic factor in COVID-19 patients: a case-control study. European review for medical and pharmacological sciences. 2022;26(3):1056-64.

Al-Kitab Journal for Pure Sciences (2023); 7(2):50-61.
https://doi.org/10.32441/kjps.07.02.p5

Al-Kitab Journal for Pure Sciences
ISSN: 2617-1260 (print), 2617-8141(online)
https://isnra.net/index.php/kjps

Analysis of the properties of the topological Index using (analysis tools)

Batool S. Hattawi *, Nabeel E. Arif

College of Computer Science and Mathematics Department of Mathematics,
Tikrit University, Iraq.

*Corresponding Author: Batoolsatwan@gmail.com

Citation: Hattawi BS, Arif NE. Analysis of the properties of the topological Index using (analysis tools). Al-Kitab Journal for Pure Sciences. 2023 Oct 01;7(2):50-61. Available from: https://doi.org/10.32441/kjps.07.02.p5.

Keywords: Index, Dendrimers, Core, Stage, PAMAM, Graph.

Article History

Received	12 Aug. 2023
Accepted	29 Sep. 2023
Available online	01 Oct. 2023

Abstract:

Graph G has two sets of information: the vertices, V(G), and the edges, E(G). The definitions for the Connectivity, Geometric Arithmetic, Atomic Bond, and Sum Connectivity Indices of G:

- The Connectivity index: $X(G) = \sum_{u,v\in E(G)} \frac{1}{\sqrt{deg(u).deg(v)}}$
- The Geometric Arithmetic Index: $GA(G) = \sum_{u,v\in E(G)} \frac{2\sqrt{deg(u).deg(v)}}{deg(u)+deg(v)}$
- The Atom bond connectivity index: $ABC(G) = \sum_{u,v\in E(G)} \sqrt{\frac{deg(u)+deg(v)-2}{deg(u).deg(v)}}$
- The Sum connectivity index: $X(G) = \sum_{u,v\in E(G)} 1/(\sqrt{(deg\ (u) + deg\ (v)\ )}\ )$

were deg(u), deg(v) are a degree of vertices. Dendrimers are synthetic, man-made molecules that are composed of monomers organized in a branching structure. in this article, we calculate Connectivity, Geometric Arithmetic, Atom Bond Connectivity, and Sum Connectivity Index for the PAMAM, POPAM, and HACN1J dendrimers.

Keywords: Index, Dendrimers, Core, Stage, PAMAM, Graph.

تحليل خصائص المؤشر الطوبولوجي باستخدام (أدوات التحليل)

بتول سطوان حتاوي*، نبيل عزالدين عارف

قسم الرياضيات كلية علوم الحاسوب والرياضيات ، جامعة تكريت ، العراق
Batoolsatwan@gmail.com

الخلاصة:

الرسم البياني يحتوي على مجموعتين، مجموعة الرؤوس التي يرمز لها بالرمز $V(G)$ ومجموعة الحواف $E(G)$. نعرف Connectivity, Geometric Arithmetic, Atomic Bond, and Sum Connectivity Indices والتي تعرف كالتالي:

- $X(G) = \sum_{u,v \in E(G)} \frac{1}{\sqrt{deg(u).deg(v)}}$ $GA(G) = \sum_{u,v \in E(G)} \frac{2\sqrt{deg(u).deg(v)}}{deg(u)+deg(v)}$
- $ABC(G) = \sum_{u,v \in E(G)} \sqrt{\frac{deg(u)+deg(v)-2}{deg(u).deg(v)}}$
- $X(G) = \sum_{u,v \in E(G)} 1/(\sqrt{(deg\,(u) + deg\,(v)\,)}\,)$

عندما deg(u)، deg(v) هما درجة الرؤوس. المتشعبات عبارة عن جزيئات اصطناعية من صنع الإنسان تتكون من مونومرات منظمة في بنية متفرعة. في هذه المقالة سيتم إيجاد صيغ فهارس تبلوجية خاصة Connectivity, Geometric Arithmetic, Atom Bond Connectivity, Sum Connectivity Index لكل من متشعبات ال PAMAM, POPAM وHACN1J. حتى نجد نتائج فهارس هذه التشعبات غير المنتهية التفرع بشكل أسرع وأسهل.

الكلمات المفتاحية: الفهرس ، تشعبات ، المركز ، المرحلة ، *PAMAM* ، الرسم البياني.

1. INTRODUCTION:

A. Balaban (1982) [1], A. Graovac (2010) [2], M. Randi (1975) [3], and N. Trinajsti) (2018) [4] all contributed significantly to the development of chemical graph theory, an essential area of mathematical chemistry. Physical properties, chemical reactions, and biological activities can all be better comprehended with the help of topological indices. From this vantage point, the topological index plays a crucial part in reducing the complexity of the tested molecule to a single real number. Moreover, we graphically present our findings. These visual representations of topological indices highlight the reliance on a specific underlying structure, Graphs can be used to depict chemical substances, A topological descriptor of a graph is a number (or combination of numbers) that quantifies some aspect of the graph. The physicochemical qualities of substances can be investigated with the use of such a descriptor, called a topological index, if it correlates with a certain molecular feature [5]. Recent years have

seen extensive research on the analytical and structural features of topological indices in mathematical chemistry. Topological indices are of theoretical and practical significance because they have become a useful tool for investigating a wide range of real-world issues in fields like physics and computer science. In general, graph isomorphism has no effect on topological indices, which are numerical numbers derived from the molecular graph of a chemical compound. There is a class of indices called degree-based topological indices that can be used to highlight and characterize specific aspects of chemical compounds; these indices are calculated by looking at the degrees of the molecular graph. The M-polynomial also has an important role here since it may be used to derive closed-form formulas for degree-based topological indices. The fields of QSPR and QSAR make heavy use of topological indices. Numerous topological indices have been described so far; these indices are crucial to the research of QSPR/QSAR, which in turn aids in the prediction of various physiochemical properties and bioactivity, which is useful in the drug discovery process. It's noteworthy because of all the ways it can be used, including in nano science, biotechnology, and other areas. This receives the attention of researcher's world **[6,7]**. It is helpful to know approximate expressions when topological indices are not feasible. Mathematical characteristics of topological indices have been studied by a Researchers as of late **[8-12]**. The importance of the research from a theoretical point of view is that we find results for these indexes for infinitely branched dendrimers, but from a practical point of view, it is to help medical and analytical researchers in how to use these dendrimers in the field of analysis and pharmacy.

2. The basic concepts:

1- **Definition of the graph:** A simple graph G is vertex-transitive if, for any two vertices of G, there is an automorphism of G that maps one to the other **[13]**.

2- **Definition distance:** the distance between two vertices in a graph is the number of edges in the shortest path connecting them **[14].**

3- Definition degree: The degree of a vertex v in a graph G, denoted deg(v) is the number of proper edges incident on v plus twice the number of self-loops **[15]**.

4- **The definition topological index** is the numerical result of any graph invariant **[16]**.

5- **Definition of dendrimer:** dendrimers represent a unique class of branched polymers, As the generation increases, the external free ends of the previous generation are further branched to produce an exponentially increasing number of new monomers **[17]**.

6- Let G be a graph **the Connectivity index of G [13]**, signified by X(G) is:

$X(G)= \sum_{u,v \in E(G)} \frac{1}{\sqrt{deg(u).deg(v)}}$, where deg(u),deg(v) are degree of vertices .

7- Let G be a graph, **the Geometric Arithmetic Index of G [18]**, signified by GA(G) is:

GA(G)= $\sum_{u,v \in E(G)} = \frac{2\sqrt{deg(u).deg(v)}}{deg(u)+deg(v)}$, where deg(u),deg(v) are degree of vertices .

8- Let G be a graph ,**the Atom bond connectivity index of G [19]**, signified by ABC(G) is : ABC(G)= $\sum_{u,v \in E(G)} \sqrt{\frac{deg(u)+deg(v)-2}{deg(u).deg(v)}}$, where deg(u),deg(v) are degree of vertices.

9- Let G be a graph **the Sum connectivity index of G [13]**, signified by X(G) is:

X(G) =$\sum_{u,v \in E(G)} = \frac{1}{\sqrt{deg(u)+deg(v)}}$, where deg(u),deg(v) are degree of vertices

3. Results:

In this section, we will calculate Connectivity, Geometric Arithmetic, Atom Bond Connectivity, Sum Connectivity Index for some of the PAMAM, POPAM, and HACN1J dendrimers. We simply refer to this PAMAM by PD, POMAM by POD2, and HACN 1J by HD1, as will be seen in the shapes that will be presented, and each shape will have several stages of growth of its own. Applications may be mentioned. Farahani MR, Kulli V, Akbari M., Rehman M, Nazeer W, Saleh EA-K, Hameed Jasim T, Raoof AG, Jassim TH in studying some indexes for some manifolds in **[8-12]**. It is known that a graph can be described by a connection **Table (1)**, a series of numbers, a matrix, a polynomial, or a derived number.

1- we consider type of PAMAM dendrimer, denoted by PD3**[3]**, **Figure (1)** shows that.

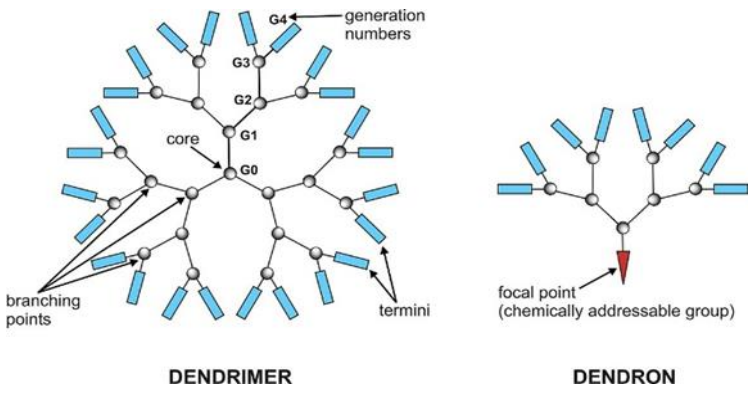

Figure 1. PAMAM dendrimers with 3-developmental stages PD3[3].

Remark 1: |v(PD3[n])|=16×2n+2-467

|E(PD3[n])|= 16×2n+2-468

Table 1: values of (dij) in PD3[n] , (i , j)= (1,3) , (3,3) and steps n= (0,1,2,3)

Stage / di,j	0	1	2	3	n
$d_{1,3}$	3	6	12	24	3×2^n
$d_{3,3}$	0	3	9	21	$3\times2^n-3$

Theorem 1: Let $PD_3[n]$ be PAMAM dendrimers with n developmental stages and n={0,1,2,……..}. Then the Connectivity Index of $PD_3[n]$ is given by $X(G)=(1\sqrt{3})(3\times2^n)+(1\3)(3\times2^n-3)$.

Proof: for nano star $PD_3[n]$ with contributed (1,3) and (3,3) edge; the formula of Connectivity Index is reduced to: $X(G)=(1\sqrt{3})(d_{13})+(1\3)(d_{33})$ Using simple calculation; one can show that by remark 1. In each stage, the PAMAM dendrimers PD3[n] edge set can be partitioned into four subsets. Thus, d13 and d33 are the two distinct classes of edges. **Figure (1)** depicts the initial stage graph of PD3[n] (n=0) This is the core of PD3[n]. There are d13 edges and d33 edges totalling 3×2^n and 3×2^n -3. **Table (1)** displays the values of dij for the cases when (I,j)=(1,3),(3,3) and n=0,1,2,3.,there for we obtain $X(G)=(1\sqrt{3})(3\times2^n)+(1\3)(3\times2^n-3)$.

Theorem 2: Let $PD_3[n]$ be PAMAM dendrimers with n developmental stages and n={0,1,2,...}. Then the Geometric Arithmetic Index of $PD_3[n]$ is given by $GA(G)=(\sqrt{3}\2)[3\times2^n]+[(3\times2^n)-3]$.

Proof: The formula for the Geometric Arithmetic Index of a nano star PD3[n] with a contributed (1,3) and (3,3) edge is reduced to $GA(G)=(\sqrt{3}\2)[d_{13}]+[d_{33}]$ By calculation, can show that by remark 1. In each step, the edge set of PAMAM dendrimers PD3[n] can be partitioned into four partitions. Thus, d13 and d33 are the two distinct classes of edges. The centre of PD3[n] corresponds to the graph of the first stage of PD3[n] (n=0) as depicted in **Figure (1)**. There is 3×2^n and 3×2^n -3 edges, respectively, of types d13 and d33. **Table (1)** displays the values of dij where (I,j) = (1,3),(3,3) and n = 0,1,2,3; hence, we get $GA(G)=(\sqrt{3}\2)[3\times2^n]+[(3\times2^n)-3]$ □

Theorem 3: Let $PD_3[n]$ be PAMAM dendrimers with n developmental stages and n={0,1,2...}. Then the Atom Bond Connectivity Index of $PD_3[n]$ is given by

$ABC(G)=\sqrt{2\3}(3\times2^n)+(2\3)(3\times2^n-3)$.

Proof: for nano star $PD_3[n]$ with contributed (1,3) and (3,3) edge; the formula for Atom Bond Connectivity Index is reduced to $ABC(G)=\sqrt{2\3}(d_{13})+(2\3)(d_{33})$ Using elementary mathematics, it is possible to demonstrate this using remark 1. The PAMAM dendrimers PD3[n] have four distinct partitions along their edge set. Thus, d13 and d33 are the two distinct classes of edges. The core stage of PD3[n] (n=0) is represented by the graph shown in **Figure (1)**. There are d13 edges and d33 edges totalling 3×2^n and 3×2^n -3. **Table (1)** displays the values of dij for the cases when (I,j)= (1,3),(3,3) and n=0,1,2,3 there for we get $ABC(G)=\sqrt{2\3}(3\times2^n)+(2\3)(3\times2^n-3)$.

Theorem 4: Let PD3[n] be PAMAM dendrimers with n developmental stages and n={0,1,2..}. Then the Sum Connectivity Index of PD3[n] is $X(G)=(1\backslash 2)(3\times 2^n)+(1\backslash\sqrt{6})(3\times 2^n-3)$.

Proof: for nano star $PD_3[n]$ with contributed (1,3) and (3,3) edge; the formula of the Sum Connectivity Index is reduced to $X(G)=(1\backslash 2)(d_{13})+(1\backslash\sqrt{6})(d_{33})$ Using elementary mathematics, it is possible to demonstrate this using remark 1. The PAMAM dendrimers PD3[n] have four distinct partitions along their edge set. Thus, d13 and d33 are the two distinct classes of edges. The initial stage of PD3[n] (n=0) is represented by the graph shown in **Figure (1)**. There are d13 edges and d33 edges totalling 3×2^n -3and3×2^n . **Table (1)** displays the values of dij for the cases when (I,j)=(1,3)(3,3) and n=0,1,2,3 there for we get $H(G)=1\backslash 2(d_{13})+1\backslash 3(d_{33})$.

2-Now, we consider POPAM dendrimers, denoted by $POD_2[n]$. As can be shown in **Figure (2)**, POPAM dendrimers $POD_2[n]$ of generation G_n with three developmental stages.

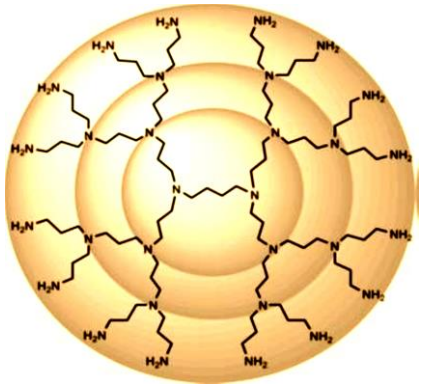

Figure 2: POPAM dendrimer of generations G_n with 3-developmental stages, $POD_2[3]$

Remark 2: $|v(POD_2[n])|=16\times 2^{n+3}-394$

$|E(POD_2[n])|= 16\times 2^{n+3}-395$

Table 2: values of (d_{ij}) in $POD_2[n]$, (i , j) = (1,2),(2,2)and(2,3) and steps n = 1,2,3

Stage / di,j	1	2	3	n
$d_{1,2}$	4	8	16	2×2^n
$d_{2,2}$	11	27	59	$8\times 2^n-5$
$d_{2,3}$	6	18	42	$6\times 2^n-6$

Theorem 5: Let $POD_2[n]$ be POPAM dendrimers with n developmental stages and n={0,1,2,…..}. Then the Connectivity index of $POD_2[n]$ is given by $X(G)=(1\backslash\sqrt{2})(2\times 2^n)+(1\backslash 2)(8\times 2^n-5)+ (1\backslash\sqrt{6})(6\times 2^n-6)$.

Proof: Connectivity index formula for nano star POD2[n] with (1,2), (2,2), (2,3) edge contributions is $X(G)=(1\sqrt{2})(d_{23})+(1\2)(d_{22})+(1\sqrt{6})(d_{12})$. A quick calculation shows this; see remark 2. In each stage, the POPAM dendrimers' edge set POD2[n] can be partitioned into three subsets. So, we have d12, d22, and d23 edges. The core stage of POD2[n] (n=0) is represented by the graph in **Figure (2)**. The number of edges of types d12, d22, and d23 is 2×2^n, (8×2^n)-5 and (6×2^n)-6. Values of dij are shown in **Table (2)** for the cases where (I,j) = (1,2),(2,2),(2,3), and n = 1,2,3, respectively. then we get $X(G)=(1\sqrt{2})(2\times2^n)+(1\2)(8\times2^n-5)+(1\sqrt{6})(6\times2^n-6)$.

Theorem 6: Let $POD_2[n]$ be POPAM dendrimers with n developmental stages and n={0,1,2...}. Then the Geometric Arithmetic Index of $POD_2[n]$ given to $GA(G)=(2\sqrt{2}\3)[2\times2^n]+(8\times2^n-5)+(2\sqrt{6}\5)[(6\times2^n)-6]$.

Proof: for nano star $POD_2[n]$ with contributed (1,2),(2,2) and (2,3) edge ; the formula of Geometric Arithmetic Index is reduced to $GA(G)=(2\sqrt{2}\3)[d_{23}]+[d_{22}]+(2\sqrt{6}\5)[d_{12}]$. A quick calculation demonstrates this; see remark 2. In each stage, the POPAM dendrimers' edge set POD2[n] can be partitioned into three subsets. So, we have d12, d22, and d23 edges. The initial stage of POD2[n] (n=0) is represented by the graph in **Figure (2)**. The number of edges of types d12, d22, and d23 is 2×2^n , (8×2^n)-5 and (6×2^n)-6. Values of dij are shown in **Table (2)** for the cases where (I,j)=(1,2),(2,2),(2,3), and n=1,2,3, respectively. then we get $GA(G)=(2\sqrt{2}\3)[2\times2^n]+(8\times2^n-5)+(2\sqrt{6}\5)[(6\times2^n)-6]$.

Theorem 7: Let $POD_2[n]$ be POPAM dendrimers with n developmental stages and n={0,1,2,..}. Then the Atom Bond Connectivity Index of $POD_2[n]$ is given by $A\ B\ C(G)=\sqrt{1\2}(16\times 2^n-11)$.

Proof: Atom Bond Connectivity Index formula reduced for nano star POD2[n] with contributed (1,2), (2,2), and (2,3) edge $ABC(G)=\sqrt{1\2}[d_{12}+d_{22}+d_{23}]$. Using simple mathematics; this is demonstrated by remark 2. The POPAM dendrimers POD2[n] edge set can be partitioned into three parts at each phase. Therefore, there are three varieties of edges: d12, d22, and d23. The core of POD2[n] represents the graph of the initial stage, which is POD2[n] (n=0) as shown in **Figure (2)**. There are2×2^n edges of type d12, (8×2^n)-5 edges of type d22, and (6×2^n)-6 edges of type d23. **Table (2)** displays the values of dij when (I,j) = (1,2),(2,2), and (2,3) and n = 1,2,3; consequently, we obtain $ABC(G)=\sqrt{1\2}(16\times 2^n-11)$.

Theorem 8: Let $POD_2[n]$ be POPAM dendrimers with n developmental stages and n={0,1,2...}.

Then the Sum Connectivity index of $POD_2[n]$ is given by $X(G)=(1\backslash\sqrt{3})(2\times 2^n)+(1\backslash 2)(8\times 2^n-5)+(1\backslash\sqrt{5})(6\times 2^n-6)$.

Proof: for nano star $POD_2[n]$ with contributed (1,2), (2,2) and (2,3) edge; the formula of Sum Connectivity index is reduced to $X(G)=(1\backslash\sqrt{3})[d_{12}]+(1\backslash 2)[d_{22}]+(1\backslash\sqrt{5})[d_{23}]$. Remark 2 demonstrates this via simple calculation. In each stage, the edge set of POPAM dendrimers POD2[n] can be partitioned into three partitions. As a result, we have three sorts of edges: d12, d22, and d23. The core of POD2[n] represents the graph of the first stage, POD2[n] (n=0), as seen in **Figure (2)**. There is 2×2^n, (8×2^n)-5 and (6×2^n)-6 edges of types d12, d22, and d23, respectively. **Table (2)** displays the values of dij where (I,j)= (1,2), (2,2), and (2,3) and n=1,2,3. there for we get $X(G)=(1\backslash\sqrt{3})(2\times 2^n)+(1\backslash 2)(8\times 2^n-5)+(1\backslash\sqrt{5})(6\times 2^n-6)$.

3-Lastly, we consider HACN1J dendrimers, denoted by $HD_1[n]$. **Figure (3)** shows that HACN1J dendrimers $HD_1[n]$ of generation G_n with five growth stages.

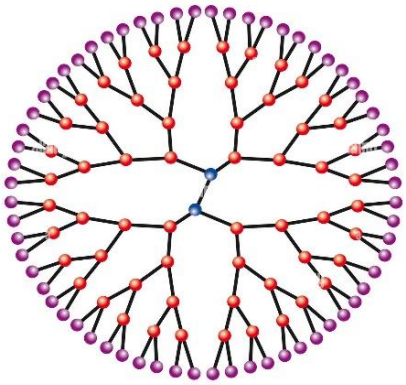

Figure 3: HACN1J dendrimer of generations G_n with 5- developmental stages, $HD_1[5]$

Remark 3: $|v(HD_1[n])|=16\times 2^{n+2}-386$

$|E(HD_1[n])|= 16\times 2^{n+2}-387$

Table 3: The value of dij in HACN1J where (i , j)=(1, 3)and(3,3) and steps n=1,2,3,4,5

Stage / di,j	1	2	3	4	5	n
$d_{1,3}$	4	8	16	32	64	2×2^n
$d_{3,3}$	1	5	13	29	61	$2\times 2^n-3$

Theorem 9: Let $HD_1[n]$ be HACN1J dendrimers with n developmental stages and n={0,1,2….}. Then the Connectivity index of $HD_1[n]$ is given by $X(G)=(1\backslash\sqrt{3})(2\times 2^n)+(1\backslash 3)(2\times 2^n-3)$.

Proof: for nano star HD[n] with contributed (1,3) and (3,3) edge; the formula of Connectivity index is reduced to X(G)=(1\√3)(d_{13})+(1\3)(d_{33}). Using easy math; this can be shown in remark 3. In each step, the edge set of HACN1J dendrimers can be split into five parts. So, d13 and d33 are two kinds of edges. **Figure (3)** shows that the core of HACN1J is the curve of the first stage, which is HD1[n] (n=1). There are (2×2^n) and (2×2^n)-3 edges of type d13 and d33. **Figure (3)** shows the values of dij when (I,j)= (1,3) and (3,3) and n = 1,2,3 so we have X(G)=(1\√3)(2×2^n)+(1\3)(2×2^n-3).

Theorem 10: Let $HD_1[n]$ be HACN1J dendrimers with n developmental stages and n={0,1,2...}. Then the Geometric Arithmetic Index of $HD_1[n]$ is given by GA(G)=(√3 \2) [2×2^n] +(2×2^n-3).

Proof: fore nanosat HD[n] with contributed (1,3) and (3,3) edge; the formula of the Geometric Arithmetic Index is reduced to GA(G)=(√3 \2) [d_{13}] +[d_{33}]. Using elementary calculations; this is demonstrated by remark 3. In each stage, the edge set of HACN1J dendrimers can be divided into five partitions. Therefore, there are two categories of edges: d13 and d33. **Figure (3**) depicts the nucleus of HACN1J, which depicts the graph of the first stage, HD1[n] (n=1). There are (2×2^n) and (2×2^n)-3 edges of d13 and d33, respectively **Figure (3)**, shows the values of dij when (I,j) = (1,3) and (3,3) and n = 1,2,3 then we have GA(G)=(√3 \2) [2×2^n] +(2×2^n-3).

Theorem 11: Let $HD_1[n]$ be HACN1J dendrimers with n developmental stages and n={0,1,2...}. Then the Atom Bond Connectivity Index of $HD_1[n]$ is given by ABC(G)= $\sqrt{2\backslash3}$ (2×2^n)+$2\sqrt{1\backslash9}$(2×2^n-3).

Proof: for nano star $HD_1[n]$ with contributed (1,3) and (3,3) edge ; the formula of Sombor index is reduced to ABC(G)= $\sqrt{2\backslash3}$[d13]+$2\sqrt{1\backslash9}$[d_{33}]. Using mathematical consider and by remark3. edges of HACN1J dendrimers can be partitioned into five subsets at each stage. So, there are two distinct kinds of edges: d13 and d33. **Figure (3)** depicts the first stage HD1[n] (n=1) graph near the core of HACN1J(n=1). There are (2×2^n) and (2×2^n)-3 edges of type d13 and d33. **Table (3)** displays the values of dij for the cases where (I,j)=(1,3) and (3,3) and n=1,2 ,3, respectively. there we have ABC(G)= $\sqrt{2\backslash3}$ (2×2^n)+$2\sqrt{1\backslash9}$(2×2^n-3).

Theorem12: Let $HD_1[n]$ be HACN1J dendrimers with n developmental stages and n={0,1,2...}. Then the Sum Connectivity index of $HD_1[n]$ is given by X(G)=(1\2)(2×2^n)+(1\√6)(2×2^n-3).

Proof: for nano star $HD_1[n]$ with contributed (1,3) and (3,3) edge; the formula of Sum Connectivity index is reduced to X(G)=(1\2)[d_{13}]+(1\√6)[d_{33}]. A quick calculation

demonstrates this; see remark 3. In each stage, the HACN1J dendrimer edge set can be partitioned into five subsets. Thus, d13 and d33 are the two distinct classes of edges. As can be seen in **Figure (3)**, the core of HACN1J is represented by the graph of the initial stage, HD1[n] (n=1). The number of edges of types d13 and d33 is (2×2^n) and (2×2^n)-3. When n=1, 2, 3, we get the values of dij shown in **Figure (3)** for (I,j)=(1,3) and (3,3), then we have $X(G)=(1\backslash2)(2\times2^n)+(1\backslash\sqrt{6})(2\times2^n-3)$.

4. Conclusions:

In this research, we have looked at the topological index of several different types of dendrimers, including PAMAM dendrimers, POPAM dendrimers, and HACN1J dendrimers. Topological indexes for various classes of dendrimers are calculated using closed formulas. Our long-term goal is to learn about and calculate topological indices for different classes of dendrimers and nanostructures.

5. Recommendations and future studies :

In this paper, I presented finding new index formulas for new dendrimers, as explained as follows:

1- Finding a new Connectivity index formula special for PD3[n] dendrimer

$$X(G) = (1\backslash\sqrt{3})(3 \times 2^n) + (1\backslash3)(3 \times 2^n-3).$$

2- Finding a new Connectivity index formula special for POD2[n]dendrimer

$$X(G) = (1\backslash\sqrt{2})(2 \times 2^n) + (1\backslash2)(8 \times 2^n-5) + (1\backslash\sqrt{6})(6 \times 2^n-6).$$

3- Finding a new Connectivity index formula special for HD1J dendrimer

$$X(G) = (1\backslash\sqrt{3})(2 \times 2^n) + (1\backslash3)(2 \times 2^n-3).$$

4- Finding a new Geometric Arithmetic index formula special for PD3[n] dendrimer

$$GA(G) = (\sqrt{3}\backslash2)\,[3 \times 2^n] + [\,(3 \times 2^n) - 3].$$

5- Finding a new Geometric Arithmetic index formula special for POD2[n]dendrimer

$$GA(G) = (2\sqrt{2}\backslash3)\,[2 \times 2^n] + (8 \times 2^n-5) + (2\sqrt{6}\backslash5)\,[\,(6 \times 2^n) - 6].$$

6- Finding a new Geometric Arithmetic index formula special for HD1J dendrimer

$$GA(G) = (\sqrt{3}\backslash2)\,[2 \times 2^n] + (2 \times 2^n-3).$$

7- Finding a new Atom bond connectivity index formula special for PD3[n] dendrimer

$$ABC(G) = \sqrt{2\backslash3}\,(3 \times 2^n) + (2\backslash3)(3 \times 2^n-3).$$

8- Finding a new Atom bond connectivity index formula special for POD2[n]dendrimer

$ABC(G)=\sqrt{1\backslash 2}\,(16\times 2^{n}-11)$.

9- Finding a new Atom bond connectivity index formula special for HD1J dendrimer

$ABC(G)=\sqrt{2\backslash 3}[d13]+2\sqrt{1\backslash 9}[d_{33}]$.

10- Finding a new Sum connectivity index formula special for PD3[n] dendrimer

$S(G)=(1\backslash 2)(3\times 2^{n})+(1\backslash\sqrt{6})(3\times 2^{n}-3)$.

11- Finding a new Sum connectivity index formula special for POD2[n]dendrimer

$S(G)=(1\backslash\sqrt{3})(2\times 2^{n})+(1\backslash 2)(8\times 2^{n}-5)+(1\backslash\sqrt{5})(6\times 2^{n}-6)$.

12- Finding a new Sum connectivity index formula special for HD1J dendrimer

$S(G)=(1\backslash 2)(2\times 2^{n})+(1\backslash\sqrt{6})(2\times 2^{n}-3)$.

6. References

[1] Balaban AT. Highly discriminating distance-based topological index. Chemical physics letters. 1982;89(5):399-404.

[2] Furtula B, Graovac A, Vukičević D. Augmented zagreb index. Journal of mathematical chemistry. 2010;48:370-80.

[3] Taherpour AA, Zolfaghar N, Jamshidi M, Jalilian J, Rezaei O, Shahri Z. Structural distortions of fullerene C60n (n= 0 to− 6) by first principle density functional theory. Journal of Molecular Structure. 2019;1184:546-56.

[4] Trinajstic N. Chemical graph theory: Routledge; 2018.

[5] Nawaf AJ, Mohammad AS. Some Topological Indices and (Hosoya and Schultz) Polynomial of Subgroup intersection graph of a group Z_r. Journal of Al-Qadisiyah for computer science and mathematics. 2021.

[6] Mitić B, Milovanović E, Matejić M, Milovanović I. Some properties of the inverse degree index and coindex of trees. Filomat. 2022;36(7):2143-52.

[7] Balasubramanian K. Topological peripheral shapes and distance-based characterization of fullerenes C20-C720: Existence of isoperipheral fullerenes. Polycyclic Aromatic Compounds. 2022;42(4):1649-67.

[8] Farahani MR. Some Connectivity index of an infinite class of Dendrimer Nanostars. Journal of Applied Physical Science International. 2015;3(3):99-105.

[9] Kulli V, Akhbari M. Multiplicative atom bond connectivity and multiplicative geometric-arithmetic indices of dendrimer nanostars. Annals of Pure and Applied Mathematics. 2018;16(2):429-36.

[10] Rehman M, Nazeer W. New definition of atomic bond connectivity index to overcome deficiency of structure sensitivity and abruptness in the existing definition. Scientific Inquiry and Review. 2019;3(4):01-20.

[11] Saleh EA-K, hameed Jasim T. N-Micro topological spaces. Samarra Journal of Pure and Applied Science. 2020;2(4):126-34.

[12] Raoof AG, Jassim TH. A Double Intuitionistic Compact Space in Intuitionistic Topological Spaces. Samarra Journal of Pure and Applied Science. 2022;4(4):78-87.

[13] Bouwer I. Vertex and edge transitive, but not 1-transitive, graphs. Canadian Mathematical Bulletin. 1970;13(2):231-7.

[14] Gutman I. Distance of thorny graphs. Publ Inst Math(Beograd). 1998;63(31-36):73-4.

[15] Goudar VM, Ashalatha K, Muddebihal M. On the Geodetic Number of Line Graph. Int J Contemp Math Sciences. 2012;7(46):2289-95.

[16] Schwerdtfeger P, Seth M. Encyclopedia of computational chemistry. John Wiley & Sons, Ltd; 1998.

[17] Cai C, Chen ZY. Rouse Dynamics of a Dendrimer Model in the ϑ Condition. Macromolecules. 1997;30(17):5104-17.

[18] Vukičević D, Furtula B. Topological index based on the ratios of geometrical and arithmetical means of end-vertex degrees of edges. Journal of mathematical chemistry. 2009;46:1369-76.

[19] Cui Q, Qian Q, Zhong L. The maximum atom-bond connectivity index for graphs with edge-connectivity one. Discrete Applied Mathematics. 2017;220:170-3.

Al-Kitab Journal for Pure Sciences (2023); 7(2):62-77.
https://doi.org/10.32441/kjps.07.02.p6

Al-Kitab Journal for Pure Sciences
ISSN: 2617-1260 (print), 2617-8141(online)
https://isnra.net/index.php/kjps

Isolation and Identification of Bacteria and Fungi Correlated with Mastitis in Breastfeeding Women in AI-Anbar Governorate/West of Iraq

Yasmeen Kateb Ahmed[1*], Abbas Obaid Al-janabi[1], Amer Fakhri Mizban[2]

[1]Department of Microbiology, College of Medicine, University of Anbar, Iraq
[2]Department of Surgery, College of Medicine, University of Anbar, Iraq

[*]Corresponding Author: yas20m0018@uoanbar.edu.iq (orcidory000-0001-6533-3875)

Citation: Ahmed YK, Al-Janabi AO, Mizban AF. Isolation and Identification of Bacteria and Fungi Correlated with Mastitis in Breastfeeding Women in AI-Anbar Governorate/West of Iraq. Al-Kitab Journal for Pure Sciences. 2023 Oct 04;7(2):62-77. Available from: https://doi.org/10.32441/kjps.07.02.p6.

Keywords: Mastitis, Breastfeeding, Staphylococcus aureus, Candida spp.

Article History

Received	15 Aug. 2023
Accepted	30 Sep. 2023
Available online	04 Oct. 2023

Abstract:

Mastitis is a common phenomenon experienced by a lot of breastfeeding women. Lactational mastitis, commonly occurs because of prolonged milk duct engorgement, which allows bacteria to enter through breaks in the skin, resulting in an infection. Mastitis can occur at various stages of lactation, although it is most observed within the second and third weeks following childbirth. For isolation and identification of bacteria associated with mastitis, Blood agar medium, MacConkey agar, and mannitol salt agar were used, whereas Sabouraud Dextrose Agar (SDA) was used for fungal isolation. Different biochemical test has been performed for bacterial isolates including gram stain, catalase, coagulase, and Vitec 2 compact. For fungal isolates, KOH treatment and lactophenol cotton blue test were performed. Fungal DNA was extracted then PCR was used for the detection ITS Gene of candida spp. Using gel electrophoresis of PCR product on 2% agarose. The study revealed Staphylococcus aureus, Klebsiella pneumoniae, and Candida spp. as significant bacteria that are commonly related to mastitis in women. The prevalence of Staphylococcus aureus was seen to be high, with a notable manifestation of lesions. Additionally, both Staphylococcus aureus and Klebsiella pneumoniae were shown to be associated with the presence of redness. Candida albicans had a notable

prominence, displaying a heightened prevalence in the regions of the nipple. Furthermore, it demonstrated a correlation with the presence of lesions and redness. The presence of redness was observed as a notable sign in cases linked with Candida tropicalis. This study provides insights into the microbial diversity linked to mastitis mainly in breastfeeding women, highlighting the prevalence of Staphylococcus aureus, Klebsiella pneumoniae, and Candida spp.

Keywords: Mastitis, Breastfeeding, Staphylococcus aureus, Candida spp.

عزل وتشخيص البكتيريا والفطريات المرتبطة بالتهاب الضرع عند النساء المرضعات في محافظة الأنبار/غرب العراق

ياسمين كاتب أحمد[1*]، عباس عبيد الجنابي[1]، عامر فخري مزبان[2]

[1]قسم الأحياء الدقيقة، كلية الطب، جامعة الأنبار، العراق.
[2]قسم الجراحة، كلية الطب، جامعة الأنبار، العراق.
yas20m0018@uoanbar.edu.iq

الخلاصة:

إن التهاب الثدي هو ظاهرة شائعة تصيب اغلب النساء المرضعات. تنتج هذه الإصابة من تورم في القنوات اللبنية والذي بدوره يسمح للبكتريا بالدخول خلال الثغرات في الجلد ومن ثم حدوث العدوي قد تحدث تلك الإصابة خلال مراحل مختلفة من الرضاعة، ولكن يحدث غالبا في أول ثلاث أسابيع تلي الولادة. ولأجل عزل وتعريف البكتريا المتعلقة بالتهاب الثدي تم استخدام وسائط مثل وسط الدم (*Blood agar*)، ووسط ماككونكي (*MacConkey agar*)، ووسط ملح مانيتول (*Mannitol salt agar*)، في حين تم استخدام وسط سابورود ديكستروز أجار (*Sabouraud Dextrose Agar - SDA*) لعزل الفطريات. تم عمل اختبارات كيميائية مختلفة لعوامل البكتيريا المعزولة، بما في ذلك اختبار صبغة جرام (*Gram stain*)، واختبار الكاتالاز (*Catalase*)، واختبار الكواجيوليز (*Coagulase*)، ونظام فيتيك ٢ كومباكت (*Vitek 2 compact*). أما بالنسبة لمجموعة الفطريات فقد تم إجراء اختبار هيدروكسيد البوتاسيوم (*KOH treatment*) واختبار اللاكتوفينول كوتون بلو (*Lactophenol cotton blue test*). ثم عمل استخلاص الحمض النووي للفطريات ثم عمل (*PCR*) لاكتشاف جين *ITS* لجنس الكانديدا (*Candida spp*). وبعد ذلك تم عمل (*gel electrophoresis*) لفحص منتج *PCR* على ٢٪جل أجاروز، أظهرت نتائج الدراسة ارتباط عدد من البكتريا والفطريات بالتهاب الثدي ء. وكان أبرزها (*Staphylococcus aureus*) (*Klebsiella pneumoniae*) وأنواع من الفطريات من جنس الكانديدا (*Candida spp.*).كان *Staphylococcus aureus* مرتبطا بتكون التقرحات، ولكن وجود *Staphylococcus aureus* مع *Klebsiella pneumonia* كان مرتبطا بالاحمرار، ولكن وجود فطر *Candida albicans* كان مرتبطا بأعراض الاحمرار والتقرحات وخاصة في منطقة الحلمة. ووجد أن وجود الاحمرار كان علامة بارزة على وجود فطر *Candida tropicalis*. تقدم هذه الدراسة رؤي مختلفة حول التنوع الميكروبي المرتبط بالتهاب الثدي خاصة في النساء المرضعات وتسلط الضوء على انتشار *Staphylococcus aureus* ، و*Klebsella pneumoniae* وكذلك *Candida spp*.

الكلمات المفتاحية: التهاب الثدي, الرضاعة الطبيعية, بكتريا ستافيلوكوكس, فصائل فطر الكانديدا.

1. INTRODUCTION:

Breastfeeding is critical in maintaining the proper development of the brain and in preventing the simultaneous appearance of malnutrition, infectious illnesses, and mortality [1]. Furthermore, regardless of the country's economic situation, it provides long-term benefits by lowering the chance of obesity and chronic illnesses during maturity [2]. Breastfeeding, in addition to providing passive immunity, promotes active communication between the immune systems of mothers and newborns [3]. Furthermore, women pass on microbial elements to their offspring via breast milk [4].

When infants under the age of 12 months and young children between the ages of 12 and 36 months receive breast milk from their mothers through the act of breastfeeding, they have the best chance of survival, growth, and optimal development [5]. This is partly because breastfeeding is a dynamic intervention activity, and breast milk contains unique living qualities that contribute to these favorable results [6,7].

Breastfeeding women often encounter a condition known as lactational mastitis, which manifests as inflammation in the breast tissue.[8] This discomfort arises due to factors like nipple fissures and milk stasis, which can disrupt the otherwise harmonious experience of breastfeeding [9]. Due to a decline in their defense ability, bacteria through the milk ducts retrograde into the mammary gland, leading to infection [10].

In the initial stage, patients commonly exhibit symptoms such as breast redness, swelling, tenderness, and inadequate milk discharge [11]. As the condition advances, the formation of a lump becomes more pronounced, accompanied by additional symptoms including fever, chills, fatigue, headaches, and other manifestations [12]. Most often, S. aureus colonizes the skin and is one of the most important causes of locational mastitis [13,14]. Methicillin-resistant Staphylococcus aureus (MRSA) may also become a risk factor for this infection [15,16].

Mastitis is intimately associated with bacterial growth, a state where the mastitis-causing microbiota increases while the normal mammary microbiota diminishes [13]. Also, Klebsiella pneumonia has been reported as one of the organisms related to mastitis [16,17]. Fungal infections affecting the nipple and breast may be experienced by breastfeeding women. It is caused by Candida albicans, a prevalent fungal organism responsible for various thrush infections [18,19]. Inflammatory processes and pain may be sparked by the co-existence of Candida spp. in the lactating nipple and breast, including Staphylococcus aureus (S. aureus), Candida albicans, and another Candida spp.

Another possibility is that this syndrome could be caused by multiple organisms. Co-infection with Staphylococcus aureus, Candida albicans, and other Candida spp. in the lactating nipple and breast may lead to inflammation and pain [20].

There are many organisms involved in mastitis in breastfeeding women, so this study aimed to isolate and identification of microorganisms related to mastitis in breastfeeding women, determine the relation between mastitis symptoms and organisms, and assess between microorganisms and mastitis source.

2 .Materials and Methods:

2.1 .Study Design and Sampling: It is a cross-sectional study consisting of 100 patients with skin infections with mastitis who were recruited from AL-Ramadi Teaching Hospital in Anbar Governorate, Iraq. From the mother and her child, the sample was collected between November 2022 and March 2023. Samples were obtained from a mother with mastitis and her baby. The step in collecting samples is to use sterile cotton swabs, where a swab is taken from the mother from the site of lesion or redness located on the nipple and breast, and a swab is also taken from the mother's milk and her baby's mouth.

2.2 .Identification of Bacterial Isolates: The blood Agar media used for isolation. 4.25-gram agar was dissolved in 100 ml dis.H2O and sterilized in an autoclave for 15 minutes at 121, cooled to 45 C then 10% V/V sterile defibrinated blood was added aseptically, plates were inoculated and incubated at 37 C for 48 hr [21].

Mannitol salt agar medium also was used to test the ability of the organisms to ferment mannitol, 11.1 gram of the media was dissolved in 100 ml dis H2O and sterilized in an autoclave for 15 minutes at 121 C. Cooled, poured in Petri dishes, and plated were inoculated then incubated for 48h at 37C [22].

Subculture on MacConkey agar was performed by dissolving 5.5 grams of medium in 100 ml dis. H2O was sterilized in an autoclave at 121C for 15 minutes poured onto plates, inoculum was spread on the surface of the plates, and incubated for 48h at 37 C. Gram stain test was carried out to characterize the isolates [23].

A 3% solution of hydrogen peroxide (H2O2) was created by diluting a stock solution (15%) in a dark bottle, then a few drops were added to culture on the slide and on blood agar to do catalase test [24] coagulase test was performed in a glass tube containing a few milliliters of citrated plasma, few drops of bacterial suspension were added, then the tube was incubated for 24 hours in the oven [25] and Vitek 2 were done by using (Gram-positive Vitek-2, Gram-negative Vitek-2) kits acquired from BioMerieux, France.

2.3 .Identification of fungal isolates: Sabouraud Dextrose Agar (SDA) (Oxide, United Kingdom) was prepared and inoculated by swabs and then incubated for 24 hr at 37C. For the KOH test, 10 grams of potassium hydroxide were dissolved in 80 mL dis.H2O. Drops of KOH solution were added to the specimen, a coverslip was placed over the specimen after 10 minutes **[26]**. Lactophenol cotton blue **[27]** and Germ tube tests were performed for fungal isolates **[28].**

2.4 .Molecular study of fungal isolates: Fungal DNA was extracted by using the Fungi/Yeast Genomic DNA Isolation Kit Provided by Norgen Biotech, PCR was used for the detection ITS Gene of candida spp. The primers were designed based on the National Centre for Biotechnology Information (NCBI) and provided by the BioOneer Company **Table (1)** .
To detect the ITS gene of Candida spp., PCR protocol was employed in **Table (2)**.

Table 1: Sequence of PCR primer [29]

Sequence of forward and reverse
F /TCCGTAGGTGAACCTGCGG
R /TCCTCCGCTTATTGATATGC

After PCR amplification, gel electrophoresis of PCR product was done on 2% agarose.
The investigation encompassed a statistical analysis of the data concerning the types of microorganisms found in each sample, together with the observed variances in symptoms linked with them. The analysis was properly carried out using SPSS Version 25.0 software. The data underwent extensive preprocessing and validation procedures to guarantee its quality and dependability.

Table 2: PCR amplification protocol [30]

Step	Temperature	Time	Cycle
Initial denaturation	94	5min	1
Denaturation	94	45 S	35
Annealing	52	1 min	
Extension	72	1 min	
Extension	72	7min	1
Hold Temperature	4	4min	----

3. Results and discussion:

3.1 Bacterial isolation and biochemical identification: For isolation of Staphylococcus aureus, the differential media blood agar was used, and the colonies appeared on the plate after 24 h (**Figure 1. A**). Gram stain test revealed that it is gram-positive bacteria which is a main character of Staphylococcus aureus. Also, it produced blurred edges and completely clear zones which indicates that beta-hemolysis took place. **Figure 1. B**

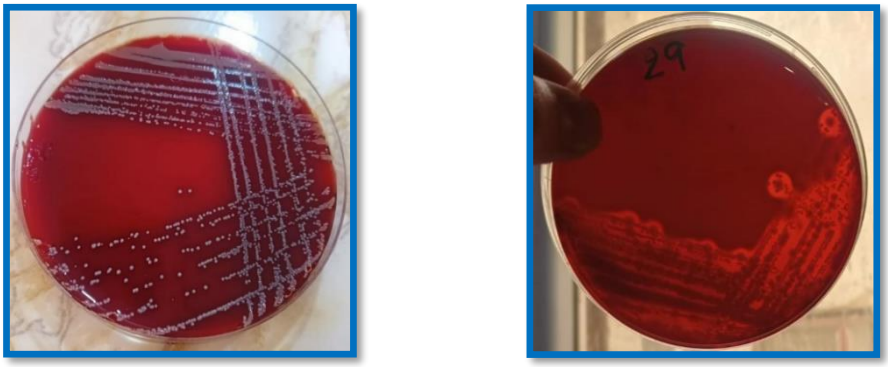

A) Growth of Staphylococcus aureus. B) Beta-hemolysis of Staphylococcus aureus on blood agar

Figure 1: Staphylococcus aureus on blood agar medium.

Small yellow colonies appeared on mannitol salt agar due to mannitol fermentation by producing an acid that causes the red color of phenol to turn yellow and this is a character of Staphylococcus aureus. **Figure (2)**.

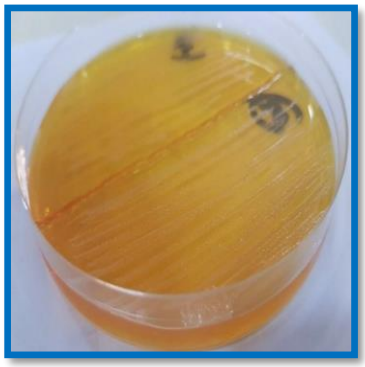

Figure 2: positive mannitol fermenter Staphylococcus aureus.

Staphylococcus aureus is characterized by being catalase positive as it transforms hydrogen peroxide (H2O2) to water and oxygen this test was done on both blood agar and on the slide. **Figure (3).**

A. On blood agar B. On slide

Figure 3: Catalase test positive of staphylococcus aureus

Staphylococcus aureus cells clumped together within 10 seconds in comparison to the control because of staphylococcus aureus being coagulase positive. **Figure (4)**.

Vitek 2 was done and with all results biochemical tests showed that the isolate was Staphylococcus aureus.

Figure 4 Coagulase test positive for staphylococcus aureus

The identification of Klebsiella pneumoniae using MacConkey agar is based on the ability of this organism to ferment lactose as Klebsiella pneumoniae is a lactose-fermenting bacterium so pink mucoid colonies are present on the MacConkey agar plate. **Figure (5)**. Gram stain test of the isolate showed that it is a gram-negative bacterium, which is consistent with Klebsiella pneumoniae. The Vitek 2 compact system confirmed the identification of the isolate as Klebsiella pneumoniae.

Figure 5: Klebsiella pneumonia growing on MacConkey agar medium

3.2 .Biochemical identification of fungi: Candida spp. grew on SDA medium which is differential media for pathogenic fungi including different species of Candida. **Figure (6)**.

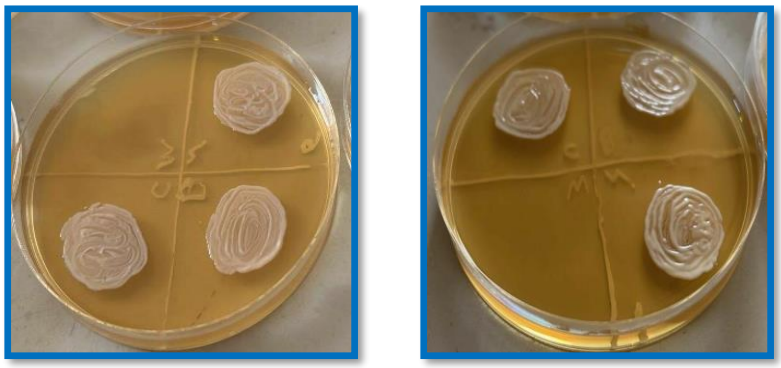

Figure 6: Macroscopic examination for candida spp. on SDA

Upon microscopic examination of isolates treated with potassium hydroxide (KOH), the result may exhibit a combination of hyphae, pseudohyphae, and budding yeast cells **Figure (7)**.

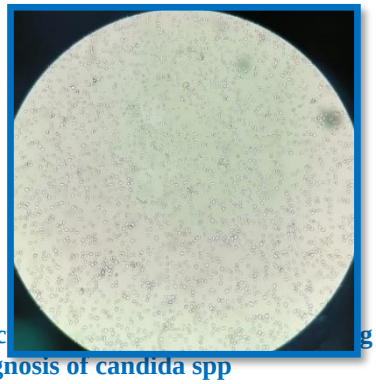

Figure 7: Direc g 10% KOH for diagnosis of candida spp

Morphology of Candida spp. become obvious after LPCB staining. LPCB staining is a useful method for the visualization and identification of fungal structures and spores, including those of Candida spp **Figure (8)**.

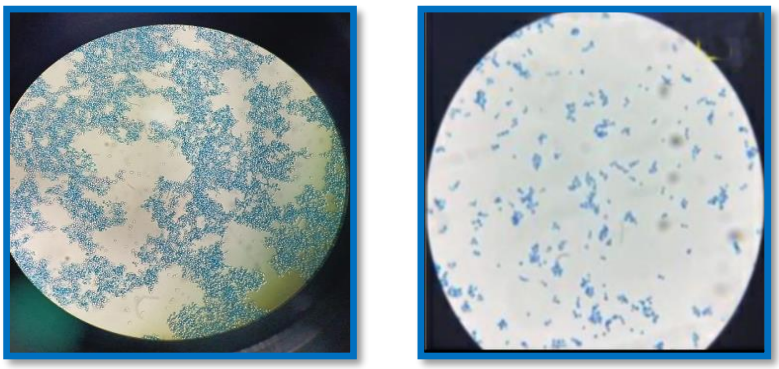

Figure 8 Microscopic examination of fungal spores and other fungal structures with lactophenol cotton blue (candida)

Germ tubes appeared after 3, 6, and 9 hours indicating that the Candida spp. isolates are likely Candida albicans **Figure (9)**.

Figure 9: Germ tube test for candida identification, it tested after 3 h, tested again after 6 h and after 9 h.

3.3 .Molecular study of fungi: Gel electrophoresis has been performed on genomic DNA extracted from Candida spp and the presence of DNA bands on the gel indicates the presence of genomic DNA in the sample **Figure (10)**.

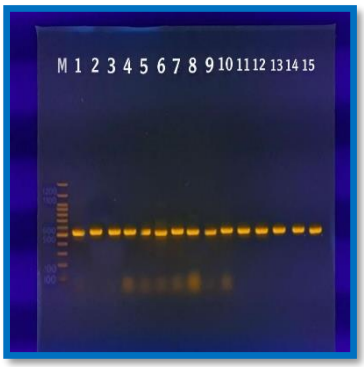

Figure 10 Gel electrophoresis of genomic DNA extraction, 1% agarose gel.

PCR was used for the detection of the ITS Gene of candida spp. After PCR amplification, gel electrophoresis of PCR product was done on 2% agarose. The target gene was found, and its band size is 550 bp **Figure (11)**

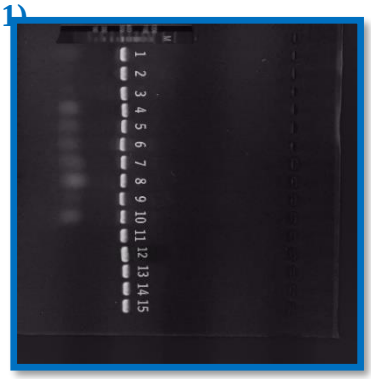

Figure 11 Gel electrophoresis showing PCR product with a band size of 550 bp. N: DNA ladder (1000 plus)

3.4 .The association between the type of organism and the mastitis occurrence and symptoms in women: Percentage of various organisms (Staphylococcus aureus, Klebsiella pneumonia, and Candida albicans) found in various sources (nipples, breast, and kid oral cavity) among women with mastitis. The presence of Candida albicans in different sources with a higher percentage than Staphylococcus aureus & Klebsiella pneumonia **Table (4)**.

Table 4: Type of microorganisms and mastitis occurrence

	Staphylococcus aureus	*Klebsiella pneumonia*	*Candida albicans*	χ^2	*P* value
Nipples	38 %	20 %	90%	3.324	0.1897
breast	50%	20%	73%		
Nipples	38 %	20 %	90%	0.009	0.995
Child oral cavity	37%	20%	90%		
Breast	50%	20%	73%	3.661	0.16
Child Oral Cavity	37%	20%	90%		

Different microorganisms are linked to distinct mastitis symptoms. Staphylococcus aureus and Candida albicans appear to be linked to the symptom of lesions, whereas Staphylococcus aureus, Klebsiella pneumonia, and Candida albicans appear to be linked to redness. Cases involving Candida albicans alone, on the other hand, have a higher prevalence of the combination of redness and lesions. Finally, Candida tropicalis is associated with redness as a symptom **Table (5)**.

Table 5: Type of microorganisms and symptoms of mastitis correlation

	Symptoms		
	Redness	Lesions	Redness& Lesions
Staphylococcus aureus & Candida albicans	8%	30%	0%
Staphylococcus aureus & & Klebsiella pneumonia & Candida albicans	32%	0%	0%
Candida albicans	0%	0%	20%
Candida tropical	10%	0%	0%

4. Discussion:

The bacterial isolate was Staphylococcus aureus as resulted from the biochemical tests performed which included growth on blood agar and making beta-hemolysis, and mannitol fermentation as these are characteristics of Staphylococcus aureus as reported **[31]**. Also gram-positive, catalase-positive **[32],** and the positive result of the coagulase test **[31]** support that it is Staphylococcus aureus. Vitek 2 results align with other biochemical tests and the demonstrated characteristics of Staphylococcus aureus **[33].**

For Klebsiella pneumoniae, the identification tests conducted are going with characters of it which had mentioned in previous studies. Vitek2 **[33]**, lactose fermentation on MacConkey agar **[34]**, being gram-negative **[35]**. According to the Clinical and Laboratory Standards Institute (CLSI), gram stain testing is a rapid and reliable method for the preliminary identification of bacterial isolates **[36].**

In the context of fungi, Candida spp. characters found in previous studies are the same results obtained from the biochemical tests. Growing on Sabouraud Dextrose Agar (SDA) which contains antibiotics such as chloramphenicol and cycloheximide that inhibit the growth of bacteria and other fungi, thereby allowing for the selective growth of Candida spp. **[37]**. The presence of a combination of hyphae, pseudohyphae, and budding yeast cells after KOH treatment **[38]** and Morphology of Candida spp. after LPCB staining **[39, 40]** are recognized as characteristic attributes frequently linked to Candida spp. Germ tube is also used for the

Identification of a Candida as albicans or non-albicans species depending on the presence or absence of germ tubes [41]. A molecular study was also done to detect the ITS gene of Candida using PCR and a single band of 550 bp was found [42]. The ITS region (Internal Transcribed Spacer) is a highly conserved region found in the rDNA gene of fungi, including Candida spp. This region has been widely used as a target for molecular identification of fungal species using PCR-based techniques, including PCR amplification and agarose gel electrophoresis [43].

Many studies have studied the relation between type of microorganisms and mastitis. One study reported that Staphylococcus aureus, Streptococcus agalactiae, and Mycoplasma spp. are the most common pathogens that cause mastitis [44]. A study in 2022 demonstrated that Staphylococcus aureus and Klebsiella pneumonia were found at lower proportions in mastitis cases. Staphylococcus aureus is a common pathogen in cases of mastitis, but it may not be as common as Candida albicans [45]. In a case-control study, women with mastitis were more likely than women in the control group to have Staphylococcus aureus in their breast milk [46]. According to research performed in Germany, the pathogens most found in mastitis instances can differ. Coliform infections like E. coli were discovered to be the most common pathogens in severe episodes of mastitis [47].

A lot of studies investigated the relation between the mastitis symptoms' and microorganism's type. Staphylococcus aureus and Candida albicans: an investigation reported that these germs are linked to lesions. Women with Staphylococcus aureus plus Candida albicans in their breast milk may have more lesions than those with Candida albicans [46]. Both bacteria have been linked to the symptoms of breast tissue lesions. These bacteria and their link to the development of breast lesions emphasize the necessity of appropriate cleanliness and efficient preventive measures during breastfeeding [48].

Staphylococcus aureus, Klebsiella pneumonia, and Candida albicans: This combination of bacteria is linked to redness as a mastitis symptom according to a study performed in China [49]. Redness is associated with Staphylococcus aureus, Klebsiella pneumoniae, and Candida albicans [50].

Candida albicans: Cases involving Candida albicans alone had a higher frequency of redness and lesions due to an investigation [51,52]. When Candida albicans causes an infection without the presence of other microbes, it may generate a more prominent inflammatory response, including redness [50].

Candida tropicalis: This bacterium has been related to redness as a mastitis symptom as mentioned [53]. When Candida tropicalis infects breast tissue, it can cause mastitis or breast

inflammation. The affected area may exhibit redness, swelling, and discomfort as part of the inflammatory response **[54].**

5 .Conclusion:

This study utilized a range of microbiological and molecular methodologies to identify the microorganisms accountable for mastitis in women. The investigation also analyzed the correlation between bacteria and the incidence and manifestations of mastitis. Candida albicans had a significant prevalence, namely in the nipple. The findings of the research demonstrated that various microorganisms exhibit unique symptom profiles.

6 .References:

[1] Victora CG, Bahl R, Barros AJ, França GV, Horton S, Krasevec J, Murch S, Sankar MJ, Walker N, Rollins NC. Breastfeeding in the 21st century: epidemiology, mechanisms, and lifelong effect. The Lancet. 2016 Jan 30;387(10017):475-90.

[2] Bode L, Raman AS, Murch SH, Rollins NC, Gordon JI. Understanding the mother-breastmilk-infant "triad". Science. 2020 Mar 6;367(6482):1070-2.

[3] Christian P, Smith ER, Lee SE, Vargas AJ, Bremer AA, Raiten DJ. The a need to study human milk as a biological system. The American journal of clinical nutrition. 2021 May;113(5):1063-72.

[4] Rollins NC, Bhandari N, Hajeebhoy N, Horton S, Lutter CK, Martines JC, Piwaz EG, Richter LM, Victora CG. Breastfeeding 2: why invest, and what it will take to improve breastfeeding practices. Lancet. 2016;387(10017):491-504.

[5] Horta BL, Rollins N, Dias MS, Garcez V, Pérez-Escamilla R. Systematic review and meta-analysis of breastfeeding and later overweight or obesity expands on previous study for World Health Organization. Acta Paediatrica. 2023 Jan;112(1):34-41.

[6] Miller EM. Beyond Passive Immunity: Breastfeeding, milk, and collaborative mother-infant immune systems. InBreastfeeding 2017 Dec 22 (pp. 26-39). Routledge.

[7] Williams JE, Carrothers JM, Lackey KA, Beatty NF, Brooker SL, Peterson HK, Steinkamp KM, York MA, Shafii B, Price WJ, McGuire MA. Strong multivariate relations exist among milk, oral, and fecal microbiomes in mother-infant dyads during the first six months postpartum. The Journal of Nutrition. 2019 Jun 1;149(6):902-14.

[8] Wilson E, Woodd SL, Benova L. Incidence of and risk factors for lactational mastitis: a systematic review. Journal of Human Lactation. 2020 Nov;36(4):673-86.

[9] Moyo GP. Breast Pathologies and Inadequate Breastfeeding Practices: A Survey Among a Group of Newly Delivered Women in Yaounde, Cameroon. Journal of Family Medicine and Health Care. 2020;6(3):87-90.

[10] Barker M, Adelson P, Peters MD, Steen M. Probiotics and human lactational mastitis: A scoping review. Women and birth. 2020 Nov 1;33(6):e483-91.

[11] Li D, Li J, Yuan Y, Zhou J, Xiao Q, Yang T, Li Y, Jiang L, Gao H. Risk factors and prognosis of acute lactation mastitis developing into a breast abscess: A retrospective longitudinal study in China. Plos one. 2022 Sep 1;17(9):e0273967.

[12] Abramowitz C, Deutch A, Shamsian E, Musheyev Y, Ftiha F, Burnstein S, Deutsch AL. Red Cabbage: A Novel Treatment for Periductal Lactational Mastitis. Cureus. 2022 Dec 31;14(12).

[13] Tao YN, Tong XK, Qian C, Wan H, Zuo JP. Microbial quantitation of colostrum from healthy breastfeeding women and milk from mastitis patients. Ann Palliat Med. 2020 Jul 1;9(4):1666-80.

[14] Rimoldi SG, Pileri P, Mazzocco MI, Romeri F, Bestetti G, Calvagna N, Tonielli C, Fiori L, Gigantiello A, Pagani C, Magistrelli P. The role of Staphylococcus aureus in mastitis: A multidisciplinary working group experience. Journal of Human Lactation. 2020 Aug;36(3):503-9.

[15] Blackmon MM, Nguyen H, Mukherji P. Acute Mastitis.

[16] Jena P, Duggal S, Gur R, Kumar A, Bharara T, Dewan R. Staphylococcus aureus in breast abscess-major culprit besides others. Indian Journal of Medical Sciences. 2019 Oct 19;71(1):40-4.

[17] Lin XR. Study on the pathogenesis of maladjustment of lactating mastitis microflora. Journal of Hainan Medical University. 2019;25(3):83-6.

[18] Al-Dafay AM, AL-Ruaby KJ, AlQushawi AA. Detection of Phospholipase and Asparty1 Protaines gens in Candida Species Isolated From Mammary Candidiasis in Lactating Women. Indian Journal of Forensic Medicine & Toxicology. 2021 Jun 2;15(3):5428-35.

[19] Mitchell KB, Johnson HM, Eglash A, Academy of Breastfeeding Medicine. ABM Clinical Protocol# 30: breast masses, breast complaints, and diagnostic breast imaging in the lactating woman. Breastfeeding Medicine. 2019 May 1;14(4):208-14.

[20] Amir LH, Cullinane M, Garland SM, Tabrizi SN, Donath SM, Bennett CM, Cooklin AR, Fisher JR, Payne MS. The role of micro-organisms (Staphylococcus aureus and Candida albicans) in the pathogenesis of breast pain and infection in lactating women: study protocol. BMC pregnancy and childbirth. 2011 Dec;11(1):1-1.

[21] Parija SC. Staphylococcus. InTextbook of Microbiology and Immunology 2023 Mar 17 (pp. 339-354). Singapore: Springer Nature Singapore.

[22] Omotosho O, Ukatu S, Okandeji M, Okunlade O, Adeola A, Emikpe B. Antimicrobial Resistance Profile of Aerobic Nasal Microflora of Nigerian Indigenous Pigs. Alexandria Journal for Veterinary Sciences. 2023 Jan 1;76(1).

[23] Iida R, Hashimoto K, Hirata K, Matsuoka K, Yokoyama S. Detection System of Gram Types for Bacteria from Gram Stained Smears Images. InICPRAM 2020 (pp. 477-484).

[24] Sapkota J, Sharma M, Jha B, Bhatt CP. Prevalence of staphylococcus aureus isolated from clinical samples in a tertiary care hospital: A descriptive cross-sectional study. JNMA: Journal of the Nepal Medical Association. 2019 Nov;57(220):398.

[25] Rakotovao-Ravahatra ZD, Randriatsarafara FM, Milasoanjara RN, Ranaivosoa MK, Rakotovao AL, Rasamindrakotroka A. Assessment of the coagulase test in the identification of Staphylococcus aureus strains. Journal of Biotechnology and Biomedicine. 2019;2(3):105-11.

[26] Venugopal D, Husain K, Mustafa SA, Sabeen S. Epidemiology, risk factors and antimicrobial profile of Vulvovaginal Candidiasis (VVC): A study among women in the central region of Saudi Arabia. Journal of Medical Mycology. 2021 Jun 1;31(2):101049.

[27] Sulmiyati S, Said NS, Fahrodi DU, Malaka R, Maruddin F. The Characteristics of Yeast Isolated from Commercial Kefir Grain, Indonesia. Hasanuddin Journal of Animal Science (HAJAS). 2019 May 30;1(1):26-36.

[28] Hidayati Y, Asnaily A, Jumaisal A, Simanjuntak JP. Comparison of Several Types of Plasma as Media in the Germ Tube Test for Identification of Candida Albicans. Jurnal Teknokes. 2023 Apr 13;16(2).

[29] Xie J, Fu Y, Jiang D, Li G, Huang J, Li B, Hsiang T, Peng Y. Intergeneric transfer of ribosomal genes between two fungi. BMC Evolutionary Biology. 2008 Dec;8(1):1-7.

[30] Petti CA, Bosshard PP, Brandt ME, Clarridge JE, Feldblyum TV, Foxall P, Furtado MR, Pace N, Procop G. Interpretive criteria for identification of bacteria and fungi by DNA target sequencing; approved guideline. Clinical and Laboratory Standards Institute (CLSI) Documents. 2008;28:19087-898.

[31] Tille P. Bailey & Scott's diagnostic microbiology-E-Book. Elsevier Health Sciences; 2015 Dec 28.

[32] Koneman EW, Allen SD, Janda WM, Schreckenberger PC, Winn WC. Diagnostic microbiology. The nonfermentative gram-negative bacilli. Philadelphia: Lippincott-Raven Publishers. 1997:253-320.

[33] Lupetti A, Barnini S, Castagna B, Capria AL, Nibbering PH. Rapid identification and antimicrobial susceptibility profiling of Gram-positive cocci in blood cultures with the Vitek 2 system. European journal of clinical microbiology & infectious diseases. 2010 Jan;29:89-95.

[34] Iqbal Z, Mumtaz MZ, Malik A. Extensive drug-resistance in strains of Escherichia coli and Klebsiella pneumoniae isolated from pediatric urinary tract infections. Journal of Taibah University Medical Sciences. 2021 Aug 1;16(4):565-74.

[35] Amraei S, Eslami G, Taherpour A, Hashemi A. The role of ACT and FOX genes in Klebsiella pneumoniae strains isolated from hospitalized patients. Micro Nano Bio Aspects. 2022 Aug 1;1(2):18-25.

[36] Wayne PA. Clinical and Laboratory Standards Institute: Performance standards for antimicrobial susceptibility testing: 20th informational supplement. CLSI document M100-S20. 2010.

[37] Acharya T, Hare J. Sabouraud agar and other fungal growth media. InLaboratory Protocols in Fungal Biology: Current Methods in Fungal Biology 2022 Feb 3 (pp. 69-86). Cham: Springer International Publishing.

[38] Thammahong A, Kiatsurayanon C, Edwards SW, Rerknimitr P, Chiewchengchol D. The clinical significance of fungi in atopic dermatitis. International journal of dermatology. 2020 Aug;59(8):926-35.

[39] Larone DH. Medically important fungi: a guide to identification, ASM Press. Washington, DC.[Google Scholar]. 2011.

[40] Singh S. Microbial assay techniques. Medical Microbiology. 2022 Apr 4:177.

[41] Saeed AS, Saadullah AA. Isolation, Identification and Antifungal Susceptibility Testing of Candida Species from Dermatologic Specimens in Duhok Province. ZANCO Journal of Pure and Applied Sciences. 2019 Sep 10;31(4):1-8.

[42] Zhu Y, O'Brien B, Leach L, Clarke A, Bates M, Adams E, Ostrowsky B, Quinn M, Dufort E, Southwick K, Erazo R. Laboratory analysis of an outbreak of Candida auris in New York from 2016 to 2018: impact and lessons learned. Journal of clinical microbiology. 2020 Mar 25;58(4):e01503-19.

[43] Chu H, Duan Y, Lang S, Jiang L, Wang Y, Llorente C, Liu J, Mogavero S, Bosques-Padilla F, Abraldes JG, Vargas V. The Candida albicans exotoxin candidalysin promotes alcohol-associated liver disease. Journal of Hepatology. 2020 Mar 1;72(3):391-400.

[44] Cullinane M, Amir LH, Donath SM, Garland SM, Tabrizi SN, Payne MS, Bennett CM. Determinants of mastitis in women in the CASTLE study: a cohort study. BMC Family Practice. 2015 Dec;16(1):1-8.

[45] Castro I, García-Carral C, Furst A, Khwajazada S, García J, Arroyo R, Ruiz L, Rodríguez JM, Bode L, Fernández L. Interactions between human milk oligosaccharides, microbiota, and immune factors in milk of women with and without mastitis. Scientific Reports. 2022 Jan 25;12(1):1367.

[46] Kvist LJ, Larsson BW, Hall-Lord ML, Steen A, Schalén C. The role of bacteria in lactational mastitis and some considerations of the use of antibiotic treatment. International breastfeeding journal. 2008 Dec;3:1-7.

[47] Fredebeul-Krein F, Schmenger A, Wente N, Zhang Y, Krömker V. Factors associated with the severity of clinical mastitis. Pathogens. 2022 Sep 24;11(10):1089.

[48] Berens PD. Breast pain: engorgement, nipple pain, and mastitis. Clinical obstetrics and gynecology. 2015 Dec 1;58(4):902-14.

[49] Li D, Li J, Yuan Y, Zhou J, Xiao Q, Yang T, Li Y, Jiang L, Gao H. Risk factors and prognosis of acute lactation mastitis developing into a breast abscess: A retrospective longitudinal study in China. Plos one. 2022 Sep 1;17(9):e0273967.

[50] Amir LH, Donath SM, Garland SM, Tabrizi SN, Bennett CM, Cullinane M, Payne MS. Does Candida and/or Staphylococcus play a role in nipple and breast pain in lactation? A cohort study in Melbourne, Australia. BMJ open. 2013 Jan 1;3(3):e002351.

[51] Merad Y, Derrar H, Belkacemi M, Drici A, Belmokhtar Z, Drici Sr AE. Candida albicans mastitis in breastfeeding woman: an under recognized diagnosis. Cureus. 2020 Dec 11;12(12).

[52] Kaski K, Kvist LJ. Deep breast pain during lactation: a case-control study in Sweden investigating the role of Candida albicans. International breastfeeding journal. 2018 Dec;13:1-9.

[53] Hanna L, Cruz SA. Candida mastitis: a case report. The Permanente Journal. 2011;15(1):62.

[54] Krukowski H, Saba L. Bovine mycotic mastitis. Folia Vet. 2003;47:3-7.

Al-Kitab Journal for Pure Sciences (2023); 7(2):78-88.
https://doi.org/10.32441/kjps.07.02.p7

Al-Kitab Journal for Pure Sciences
ISSN: 2617-1260 (print), 2617-8141(online)
https://isnra.net/index.php/kjps

Study of the electronic properties of pure nanostructured hexagonal Zinc Oxide by DFT method

Randa Saad Ahmed, Issa Zain Al-Abidin Hassan

Kirkuk University, Iraq

*Corresponding Author: ww55ggfcc@gmail.com

Citation: Ahmed RS, Hassan IZ. Study of the electronic properties of pure nanostructured hexagonal Zinc Oxide by DFT method. Al-Kitab Journal for Pure Sciences. 2023 Oct 04;7(2):78-88. Available from: https://doi.org/10.32441/kjps.07.02.p7.

Keywords: h-ZnO, density function theory (DFT), approximation (GGA-PBE), CASTEP program, electronic properties of pure hexagonal Zinc Oxide, hybrid approximation (HSE03).

Article History

Received	21 Aug. 2023
Accepted	03 Oct. 2023
Available online	10 Oct. 2023

Abstract:

(ZnO) Zinc oxide is considered a semiconducting material from the family of transparent conductive oxide materials. Our study aims to study the electronic properties of pure Nano-sized hexagonal zinc oxide using the DFT method using the (GGA-PBE) approximation and the (HSE03) approximation, as we demonstrated through our study on the unit cell In the large cell (3×3×3) and the small cell (1×1×1), zinc oxide has a direct energy gap in the (GGA-PBE) approximation, and its value is (e V) 1.74) and in the (HSE03) approximation, the value of the energy gap is (e V2.79). The difference in the two approximations is very clear, and it is evidence that when using the (GGA-PBE) approximation for the DFT method, it reduces the value of the energy gap for zinc oxide, and when using the (HSE03) approximation, the energy gap increases because it is more mathematically accurate, even though it takes more time to calculate.

Keywords: h-ZnO, density function theory (DFT), approximation (GGA-PBE), CASTEP program, electronic properties of pure hexagonal Zinc Oxide, hybrid approximation (HSE03).

دراسة الخواص الإلكترونية لأوكسيد الزنك السداسي النقي النانوي بطريقة *DFT*

رنده سعد احمد، عيسى زين العابدين حسن

جامعة كركوك، العراق
ww55ggfcc@gmail.com

الخلاصة:

(*Zn O*) أوكسيد الزنك يعتبر مادة شبه موصلة من عائلة مواد الأكاسيد الشفافة الموصلة .الهدف من دراستنا هو دراسة الخواص الإلكترونية لأوكسيد الزنك السداسي النقي النانوي بطريقة *DFT* باستخدام تقريب(*GGA-PBE*) وتقريب (*HSE03*) ،حيث أثبتنا من خلال دراستنا على وحدة الخلية الكبيرة(٣×٣×٣) والخلية الصغيرة (١×١×١)، إن أوكسيد الزنك يملك فجوة طاقة مباشرة في تقريب(*GGA-PBE*) وتبلغ قيمته *1.74 (e V)* وفي تقريب (*HSE03*) يبلغ قيمة فجوة الطاقة (*e V2.79*). إن الفرق في التقريبين واضح جدا وهو دليل على أنه عند استخدام تقريب(*GGA-PBE*) لطريقة *DFT* فانة يقلل من قيمة فجوة الطاقة لأوكسيد الزنك وعند استخدام تقريب (*HSE03*) تزداد فجوة الطاقة لكونها أكثر دقة حسابيا رغم أنها تستغرق وقت أكثر في الحساب .

الكلمات المفتاحية: h-ZnO، نظرية الكثافة الدالية (DFT)، التقريب (GGA-PBE)، برنامج CASTEP، الخواص الإلكترونية لأكسيد الزنك السداسي النقي، تقريب (HSE03) الهجين.

1. INTRODUCTION:

Since graphene appeared in the headlines and was rediscovered in 2004-2005, there has been and continues to be an increase in interest in isolating and using other new two-dimensional materials. Two-dimensional materials such as hexagonal zinc oxide (h-ZnO) and graphene possess a set of properties that are used in a large number of scientific disciplines and on a wide industrial scale for manufacturing across many fields in the search for significantly improved device performance, starting with sensing **[1]**. Through energy storage and generation and carbon-based molecular electronics **[2] [3]**semiconductors with hexagonal transition elements **[4-12]** (II-VI) in the periodic table crystallize in a hexagonal close-packed (HC) system and can Zinc oxide (ZnO) exists in nature in the form of a powder or solid crystal **[13]** and depending on the conditions of preparation. It features a wide direct n-type bandgap at 300K°. The benefit of the large bandgap is to withstand large electric fields with the added benefit of low electrical noise. The strong correlation energy (60mev) is also distinguished by the fact that it can be used to make an energy-based laser **[6 ,14]** with wonderful physical properties, which makes it one of the most widely used materials in various fields such as photoelectrons and photovoltaic cells. Researchers have been interested in Zinc oxide is currently used for its uses in various electronic **[15]**, industrial, military, medical, chemical, physical, biomedical, and other fields.

Hexagonal zinc oxide is characterized by high electron mobility, a non-toxic nature, and excellent photocatalytic activity by ultraviolet radiation. (Zn-O) leads to the fact that (sp^2) hybridization in the two-dimensional graphene-like honeycomb structure is stronger than (sp^3) hybridization in bulk zinc oxide crystals. In addition, hexagonal zinc oxide is highly resistant to strong radiation and shows remarkable photoluminescence **[16 ,17]**.

2. Method for calculating electronic properties:

The electronic properties of pure hexagonal zinc oxide were studied using First Principle Calculations **[18]** using Density Functional Theory (DFT), Generalized Gradient Approximation (GGA), and using the Perdew – Burke approximation. Ernzerhof (PBE) for the possibility of exchange correlation energy and also used the hybrid HSE03 approximation **[19, 20]** hybrid functional based on a screened Coulomb potential to be more mathematically accurate for the energy gap in the program **[21]** (CASTAP) and it was used to describe the electronic valence structure of Zinc Oxide Pure hexagon($Zn - 3d^{10}\,4S^2$, $O - \ 2S^2\ 2P^4$).

3. Results and Calculations:

3.1. Bond length of pure nanoparticle hexagonal zinc oxide:

The calculations were carried out on the small unit cell (1×1×1), the large unit cell (3×3×3), (3×3×1), and the large unit cell (4×4×1), and it gives the same results whether the large cell is taken or not. The small cell was taken (1×1×1). Zinc oxide consists of 8 atoms of oxygen and 30 atoms of zinc, which are the lattice parameters (a, b, c). (a=b= 3.525 Aº) in the plane (X, Y). As for the value of (c), which represents the distance between each two layers, it was chosen (c=5.025 Aº) (in the direction of the Z axis).) This large distance was chosen for calculation purposes as it is possible in this case, the interaction between the layers is neglected, so that the calculated properties of zinc oxide with one layer (layer) only and not the bulk (bulk), the length of the bond according to practical measurements, the original length of the bond is (1.501 Aº) and after the Geometry Optimization procedure it became (1.976 Aº) as shown in **Figure (1-a)**. The primitive cell unit consists of the original lattice constants (a=b=2.600, c=30.00 Aº). The first Berlion region is set at point k. (11×11×2) as for the angle between the atoms bonded to each other for zinc and oxygen (Zn-O-Zn)، it is equal to (120°) as shown in **Figure (1-b)**. Also, the lattice parameters (a, b, c). (a=b= 3.525 Aº) in the plane, only one, as in this case the interaction between the classes can be neglected.

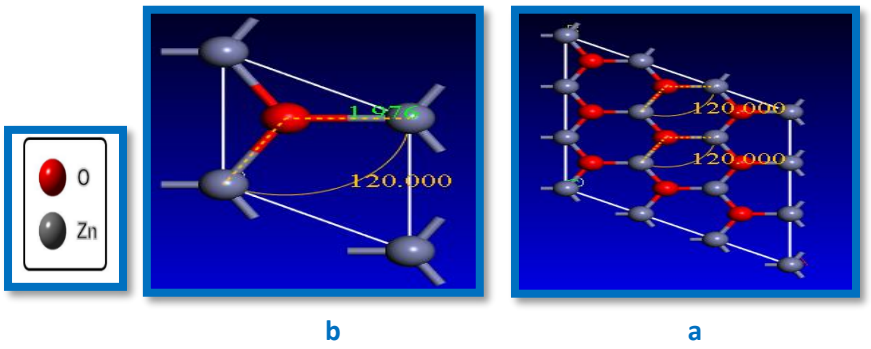

Figure 1: Hexagonal Pure Zinc Oxide cell after Conditioning and the Value of the angle between (Zn-O-Zn).

3.2. Electronic properties of hexagonal zinc oxide sheets:

3.2.1. Calculate energy packets using the (GGA-PBE) approximation:

The band gap is defined as the energy required to excite (transfer) electrons from the top of the valence band to the conduction band. It is called forbidden because it is a place free of electronic states and in which electrons do not settle in pure semiconductors. The energy gap allows one to distinguish between insulators. Semiconductors, metals, and conductors. The value of the energy gap for pure hexagonal zinc oxide is calculated through the values of the difference between the two closest points in the conduction band and the valence band, and determining whether the gap is direct or indirect .I calculated the electronic properties of zinc oxide, including the band structures, and determined the samples of the first Berlion region at the k point (11×11×2) of the lattice using (GGA-PBE) calculations for a pure hexagonal zinc oxide sheet. From the results, we notice an energy gap of 1.742 eV directly at Point (K) as shown in **Figure (2)**. It is known that the (GGA-PBE) approximation using DFT theory generally underestimates the band gap in pure hexagonal zinc oxide, and the reduction of the energy gap occurs in the (GGA) approximation in ZnO, so we used (HSE03) approximates the hybrid, which will be explained later in detail.

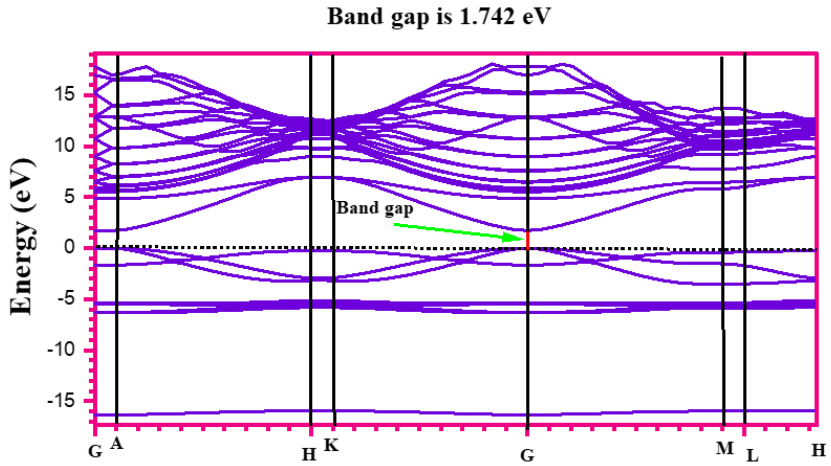

Figure (2) Structures of the electronic states (band gap) of pure hexagonal zinc oxide sheet using the (GGA-PBE) approximation.

3.2.2. Calculate energy packages using approximation (HSE03)

The hybrid (HSE03) approximation can describe the electron self-interaction better than the (GGA-PBE) approximation، and the calculation results are closer to the experimental values, although it is time and computationally expensive. **Figure (3)** shows the beam structures using the (HSE03) approximation. The points were taken at the K point (4×4×1) using the (HSE03) approximation for a pure hexagonal zinc oxide plate on the small cell (1×1×1) because it gives the same results as the large cell calculations. To calculate the band gap، we take the difference between the two closest points in the conduction and valence bands. We notice when performing the calculations that the energy gap is (2.794 eV) at point (K)، which is a direct energy gap، meaning that the energy gap has changed and become wider than it was when it was calculated. In the (GGA-PBE) approximation (GGA-PBE) and an approximation to the results of experimental calculations **[22, 23]**, these types of the broad bandgap of (2D ZnO) have the potential to be implemented in nanoscale UV-optoelectronics via nonstructural engineering. The direct and indirect band gap can be compared. If the band gap is direct, the electron releases its energy in the form of a photon. If the band gap is indirect, it releases its energy in the form of a phonon. The transfer of electrons between the conduction and valence bands is useful in several applications, the most important of which are solar cell, lasers, masers, and light diodes. **Table (1)** shows a comparison between the current study and previous studies of 2D hexagonal ZnO for the lattice, energy gap, approximation, and device used.

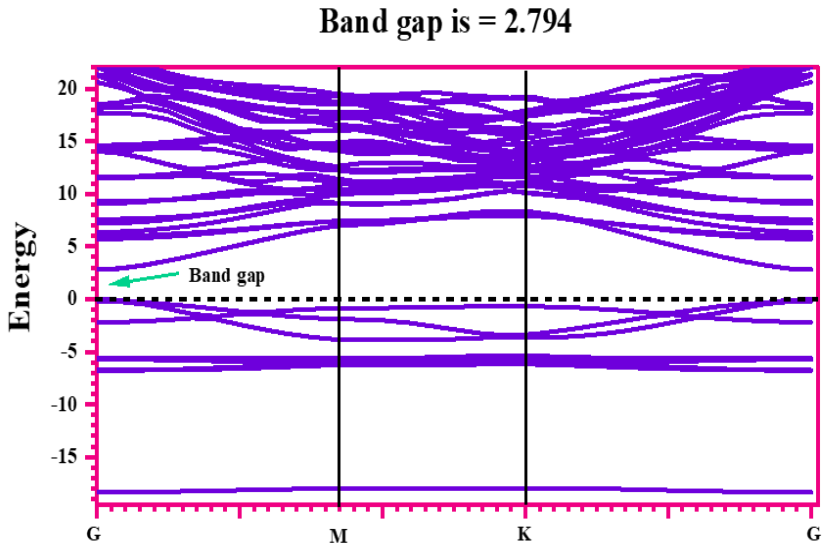

Figure (3) shows the structures of the electronic states (band gap) of a pure hexagonal zinc oxide sheet using the (HSE03) approximation.

Table (1) shows a comparison between the current study and previous studies of two-dimensional hexagonal zinc oxide for the lattice, energy gap, approximation, and device used.

Material	Structure	Bandgap (eV)	XC functional	Program	Ref
	Hexagonal	4.48 eV 4.20 eV	HSE03	DFT	[22 ,23]
2D-Zn O	Hexagonal	1.75 e V	PW91 sRef. 26d	CASTAP	[24]
	Hexagonal	1.68eV	GGA	DFT	[25]
	Hexagonal	1.742 eV	GGA-PBE	CASTAP	in this study
	Hexagonal	2. 794 eV	HSE03	CASTAP	in this study

4. Total density of states (TDOS)

4.1. Total density of states using the GGA-PBE approximation

Density of states in materials physics. The condensed state describes the proportion of states that the system must occupy at each energy. The total density of states is obtained by summing the peaks of all the bands. I calculated the density of states. I took the density of states at the point k (1 x 1 x 1) using (GGA- PBE) **Figure (4)** represents the energy changes in terms of energy, where we notice the density of states in the extended field (0-18.6 (eV)) representing the conduction band, and this means that there is a critical temperature at which the density of states is high and a noticeable change appears at (3.5 e\eV). This was done. A high density of states was also recorded in the extended field.

((-16.6) - 0 (eV)) which represents the valence band region and the presence of the first peak in the extended field ((-16.8)-(-15.3 e\ eV)) which is estimated at (3.4 e \eV) after which the density of states disappears. The second peak in the extended field ((-6.87)-(-4.63eV)), which is estimated at ((11.6(e\eV)) and then disappears, the density of states is high for zinc for the 2p orbital) in the beam The valence band is rich in electrons with the ability to move, and at this energy, the ability to move the electrons is for the conduction band. It can be noted that the valence band near the Fermi level is dominated by O-2p with a small contribution from the Zn-3d states, and the conduction band mainly contributed to the states (O-2p, Zn-4s). The third peak in the valence band is in the extended field ((-3.94)-0.06(e\ eV)) the density is estimated at (2.87 e\ eV) in the valence band region. The density of electronic states is symmetric for both spin and spin. The symmetrical electron density causes the magnetic moment of this material to be zero, which indicates that zinc oxide is a non-magnetic semiconductor material.

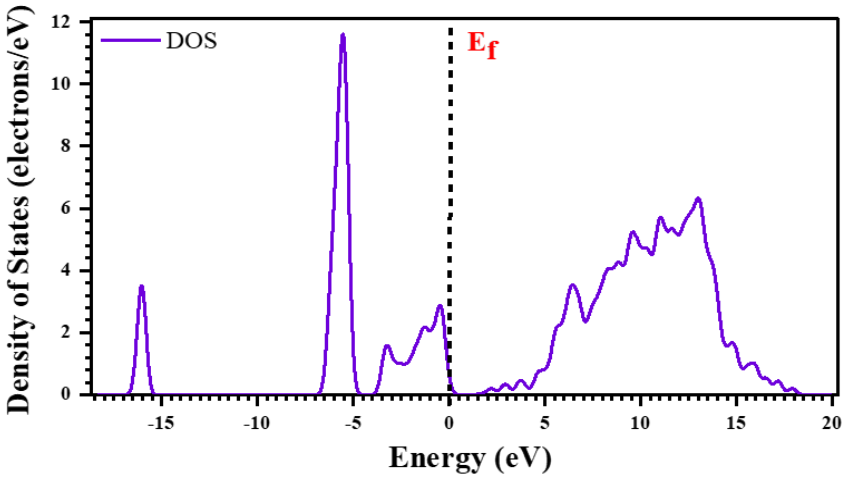

Figure (4) shows the electronic state structures (total density) of pure hexagonal zinc oxide sheets using the (GGA-PBE) approximation.

4.2. Total density of states using the approximation (HSE03)

To know the extent of the effect of the hybrid (HSE03) approximation on the overall density of states of the GGA-PBE approximation, we note that the energy field extending from (0- 21 (e V)) In **Figure (5)** is called the conduction band. We notice a noticeable change from (0.5-18 (e V)) where the density of states varies because of the high temperatures in these areas of energy. The highest density of states is recorded in the conduction region at energy (10.1 eV) and reaches (5.1). The valence band is the energy field extending from (0-(-20) e V). We notice a first peak extending from ((-20.1)-(-22.8) (e V)) after which there is no density. The states are a result of the possibility of the electrons not being transferred. We notice in the energy range from ((-17.1)-0.67(e V)) the occurrence of different density states in the energy values and peaks, which means that they are rich in electrons that can move freely between energy levels. We note that the regions near The Fermi level are where the density of states for the conduction and valence bands decreases due to the lack of electrons in them. It becomes clear to us from the density of states in the regions of the conduction band and the valence band that the regions in which electrons are present, i.e., rich in electrons, have peaks of state density in which there are no electrons, i.e., poor in electrons. We notice that there is not a significant difference in the overall density of states for both the (GGA) approximations and the hybrid (HSE03) approximation.

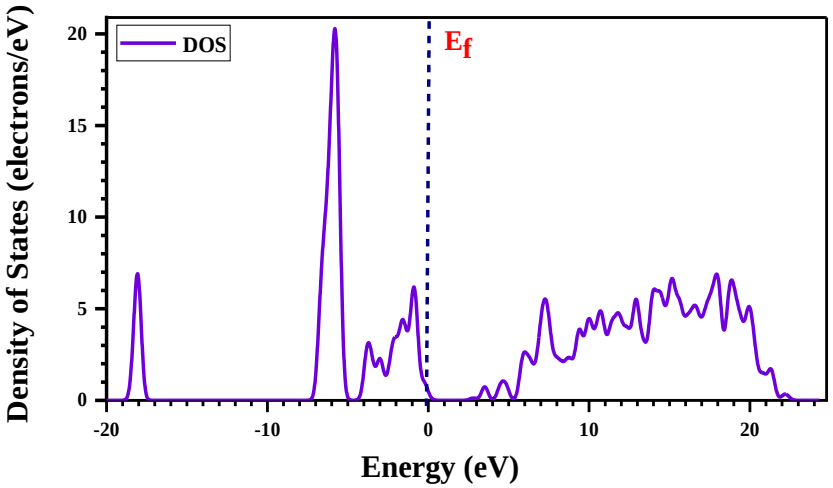

Figure (5) shows a pure hexagonal zinc oxide sheet's electronic state structures (total density) using the HSE03 approximation.

5. Conclusions

The purpose of the research is to study the electronic properties of pure Nano-hexagonal zinc oxide using the DFT method. We found that when calculating the electronic structures (densities of total and partial states) using the generalized gradient approximation (GGA), where the density of states in the extended field (0-18.6 (eV)) this region represents the conduction band This means that there is a high temperature, meaning there are many conductive electrons, the density of states is high, and a noticeable change appears at (3.5 e\eV). This is due to the lack of transfer of electrons that cannot break the Coulomb potential barrier. We found that if we modify and prepare the geometry of the zinc oxide network, the length of the bond increases from the original length (1.501 A ˚ - 1.97 A ˚) and that the resulting increase does not affect the structure of the network. When calculating the beam structures using the generalized gradient approximation (GGA-PBE), we found that it is equal to (1.74e V), and it turns out that the energy beams fall on the same values of (K) at the first Brillion point, meaning that the energy gap is direct band gap. When calculating the beam structures, we found that the energy gap using the hybrid (HSE03) approximation, which is equal to (2.79 e V) at point (K), is that the energy gap is direct. We found out through our theoretical calculations in the CASTAP program and using DFT theory that the energy gap lies at the same values as (K), which is a direct band gap using the two approximations, the (GGA-PBE) approximation and the (HSE03) hybrid approximation. Now the hybrid approximation does not reduce the value of the band. The range of pure hexagonal zinc oxide nanoparticles, in contrast to the (GGA-PBE) approximation, shows us that hexagonal zinc oxide has a wide bandgap. It is a semiconductor material and is used in electronics applications and energy electron emitters.

6 .References:

[1] Slate AJ, Karaky N, Whitehead KA. Antimicrobial properties of modified graphene and other advanced 2D material coated surfaces. 2018.

[2] Novoselov KS, Geim AK, Morozov SV, Jiang D-e, Zhang Y, Dubonos SV, et al. Electric field effect in atomically thin carbon films. science. 2004;306(5696):666-9.

[3] Chung K, Lee C-H, Yi G-C. Transferable GaN layers grown on ZnO-coated graphene layers for optoelectronic devices. Science. 2010;330(6004):655-7.

[4] Janotti A, Van de Walle CG. Fundamentals of zinc oxide as a semiconductor. Reports on progress in physics. 2009;72(12):126501.

[5] Pearton S, Norton D, Ip K, Heo Y, Steiner T. RETRACTED: Recent progress in processing and properties of ZnO. Progress in materials science. 2005;50(3):293-340.

[6] Özgür Ü, Alivov YI, Liu C, Teke A, Reshchikov MA, Doğan S, et al. A comprehensive review of ZnO materials and devices. Journal of Applied Physics. 2005;98(4).

[7] Tsukazaki A, Ohtomo A, Onuma T, Ohtani M, Makino T, Sumiya M, et al. Repeated temperature modulation epitaxy for p-type doping and light-emitting diode based on ZnO. Nature materials. 2005;4(1):42-6.

[8] Repins I, Contreras MA, Egaas B, DeHart C, Scharf J, Perkins CL, et al. 19· 9%-efficient ZnO/CdS/CuInGaSe2 solar cell with 81· 2% fill factor. Progress in Photovoltaics: Research and applications. 2008;16(3):235-9.

[9] Morkoç H, Özgür Ü. Zinc oxide: fundamentals, materials and device technology: John Wiley & Sons; 2008.

[10] Klingshirn C. ZnO: From basics towards applications. physica status solidi (b). 2007;244(9):3027-73.

[11] Guo H, Lu N, Dai J, Zeng XC, Wu X, Yang J. Electronic structure engineering in chemically modified ultrathin ZnO nanofilms via a built-in heterointerface. RSC Advances. 2014;4(36):18718-23.

[12] Behera H, Mukhopadhyay G. Strain-tunable band parameters of ZnO monolayer in graphene-like honeycomb structure. Physics Letters A. 2012;376(45):3287-9.

[13] Rahal A. Elaboration des verres conducteurs par déposition de ZnO sur des verres ordinaires. UNIVERSITE D'ELOUED. 2013.

[14] Topsakal M, Cahangirov S, Bekaroglu E, Ciraci S. A First-Principles Study of Zinc Oxide Honeycomb Structures. Bulletin of the American Physical Society. 2010;55.

[15] Pan Q, Liu BH, McBriarty M, Martynova Y, Groot I, Wang S, et al. Reactivity of ultra-thin ZnO films supported by Ag (111) and Cu (111): a comparison to ZnO/Pt (111). Catalysis letters. 2014;144:648-55.

[16] Freeman CL, Claeyssens F, Allan NL, Harding JH. Graphitic nanofilms as precursors to wurtzite films: theory. Physical review letters. 2006;96(6):066102.

[17] Tusche C, Meyerheim H, Kirschner J. Observation of depolarized ZnO (0001) monolayers: formation of unreconstructed planar sheets. Physical review letters. 2007;99(2):026102.

[18] Freysoldt C, Grabowski B, Hickel T, Neugebauer J, Kresse G, Janotti A, et al. First-principles calculations for point defects in solids. Reviews of modern physics. 2014;86(1):253.

[19] Niraula PR. Density functional theory study of two-dimensional boron nitride films: City University of New York; 2020.

[20] Chakarawet K, Debus RJ, Britt RD. Mutation of a metal ligand stabilizes the high-spin form of the S2 state in the O2-producing Mn4CaO5 cluster of photosystem II. Photosynthesis Research. 2023:1-6.

[21] Rutter MJ. C2x: A tool for visualisation and input preparation for Castep and other electronic structure codes. Computer Physics Communications. 2018;225:174-9.

[22] Lee J, Sorescu DC, Deng X. Tunable lattice constant and band gap of single-and few-layer ZnO. The journal of physical chemistry letters. 2016;7(7):1335-40.

[23] Supatutkul C, Pramchu S, Jaroenjittichai A, Laosiritaworn Y, editors. Electronic properties of two-dimensional zinc oxide in hexagonal,(4, 4)-tetragonal, and (4, 8)-tetragonal structures by using Hybrid Functional calculation. Journal of Physics: Conference Series; 2017: IOP Publishing.

[24] Ma X, Wu Y, Lv Y, Zhu Y. Correlation effects on lattice relaxation and electronic structure of ZnO within the GGA+ U formalism. The Journal of Physical Chemistry C. 2013;117(49):26029-39.

[25] Tu Z. First-principles study on physical properties of a single ZnO monolayer with graphene-like structure. Journal of Computational and Theoretical Nanoscience. 2010;7(6):1182-6.

Al-Kitab Journal for Pure Sciences (2023); 7(2):89-98.
https://doi.org/10.32441/kjps.07.02.p8

Al-Kitab Journal for Pure Sciences
ISSN: 2617-1260 (print), 2617-8141(online)
https://isnra.net/index.php/kjps

Role of Phenolic Compounds in Allelopathic Activity

Iman Radha Jasim[*1], Hala Muzher Yaqub[1], Faten Khaleel Ibrahim[2]

[1]Department of Biology, College of Science, Mosul University, Mosul, Iraq.
[2]Department of Environmental Science, College of Environmental Science and Technology, University of Mosul, Iraq

*Corresponding Author: imsbio73@uomosul.edu.iq

Citation: Jasim IR, Yaqub HM, Ibrahim FK. Role of Phenolic Compounds in Allelopathic Activity. Al-Kitab Journal for Pure Sciences. 2023 Oct 14;7(2):89-98. Available from: https://doi.org/10.32441/kjps.07.02.p8.

Keywords: phenolic compound, secondary compounds, allelopathy.

Article History

Received	23 Aug. 2023
Accepted	04 Oct. 2023
Available online	14 Oct. 2023

Abstract:

Phenolic compounds are vital plant allelochemical groups in the ecology, multiple parts of plants contain a variety of phenolic compounds these natural compounds help plants defend themselves against predatory plants. Plants' acetic acid and shikimic metabolic pathways produce phenolic chemicals. Additionally, these compounds exhibit a wide variety of structural forms. In many commercial processes, phenolic compounds are utilized to create chemicals including insecticides, explosives, medicines, and colors. Phenolic chemicals are widely used as herbicides for crop protection in an allelopathic approach., insecticides, and fungicides. They are also employed in the bleaching stage of paper production. The major goal of this evaluation is to draw attention to the ability of phenolic chemicals to allelopathic, which can offer us solutions to a variety of ecological issues, particularly those related to the conservation of the environmentally friendly development of forests, farms, with other alternatives to current synthetic pesticides include bioactive plant secondary metabolites by releasing phytotoxic substances from plant cells.

Keywords: phenolic compound, secondary compounds, allelopathy.

دور المركبات الفينولية في الفعالية الاليلوباثية

إيمان رضا جاسم*[1]، حلا مزهر يعقوب[1]، فاتن خليل ابراهيم[2]

[1]قسم الأحياء، كلية العلوم، جامعة الموصل، الموصل، العراق.
[2]قسم العلوم البيئية، كلية العلوم والتكنولوجيا البيئية، جامعة الموصل، العراق

imsbio73@uomosul.edu.iq

الخلاصة:

الأحماض الفينولية مركبات كيميائية نباتية حيوية في البيئة، تحتوي أجزاء متعددة من النباتات على مجموعة متنوعة من المركبات الفينولية، وتساعد هذه المركبات الطبيعية النباتات في الدفاع عن نفسها ضد الممرضات النباتية وينتج حامض الأسيتيك ومسارات التمثيل الغذائي في النباتات مواد كيميائية فينولية وبالإضافة إلى ذلك تظهر هذه المركبات مجموعة واسعة التراكيب الكيميائية. في العديد من التجارب يتم استخدام المركبات الفينولية لإنتاج مواد كيميائية بما في ذلك المبيدات الحشرية والأدوية والألوان. تستخدم المواد الكيميائية الفينولية على نطاق واسع كمبيدات أعشاب لحماية المحاصيل ومبيدات حشرية، ومبيدات الفطريات. كما أنها تستخدم في مرحلة التبييض لإنتاج الورق. الهدف الرئيسي من هذه المقالة هو التعرف على قدرة المواد الكيميائية الفينولية ، والتي يمكن أن توفر لنا حلولاً لمجموعة متنوعة من القضايا البيئية، لا سيما تلك المتعلقة بالحفاظ على البيئة وتنمية الغابات والمزارع، مع بدائل أخرى تشمل المبيدات الاصطناعية الحالية والنباتات النشطة بيولوجيًا عن طريق إطلاق مواد سامة من الخلايا النباتية.

الكلمات المفتاحية: الأحماض الفينولية ، المركبات الثانوية، الاليلوباثي.

1. INTRODUCTION:

Allelopathic interactions are caused in different crops or plants via phenolics. It is necessarily important to identify the phenolic compounds and confirm their presence and persistence in the environment throughout time in amounts sufficient to damage plant species, to show the function of phenolic in allelopathy. Any allelopathic substance needs to have its major mode of action determined. Only when a thorough biotic and abiotic variable that influences phenolic toxicity is known can the allelopathic effects of phenolic be acknowledged [1]. Due to the long-term cultivation of the same plant species on the same site, phenolic compounds are one of the main categories of phytotoxic chemicals that induce soil sickness. Decomposed plant residues are their source. A young apple orchard with replant disease was found abundant in phenolic compounds [2]. The main cause of replanting issues in managed tree ecosystems is autotoxicity.

Plant phenolic may be a significant factor in allelopathy, according to the [3] *Ageratum conyzoides* contain p-coumaric, gallic, ferulic, and p-hydroxybenzoic all reported to exhibit

phytotoxic properties [4]. The natural evergreen broad-leaf trees did not exhibit any effects from the high soil phenolic levels when compared to leaves, bulbs' aqueous extract and volatile chemicals were far stronger inhibitors of germination and seedling development, seedlings of tested plants ' ability to germinate and thrive was hindered by the soil under the *Allium ursinum* that contained phenolic. both unbound as well as free forms of p-coumaric, ferulic, p-hydroxybenzoic, and vanillic acids found within allelopathic materials in solutions of leaves and buds. Furthermore, *Lantana camara* contains phenolic compounds with substantial allelopathic activity, including nopinene, eucalyptol, D-limonene, and triterpenoids called Lantadenes A and B [5]. These findings imply that *A. ursinum* affects the growth and germination of seeds in other herbaceous plants in the plant community by releasing volatile chemicals into the soil. Twenty-five substances were extracted and identified from the root exudates of rice, phenolic acids with the allelopathic potential of caffeic, p-coumaric, syringic, ferulic, and sinapic are some of the substances already present in oilseed radish [6, 7].

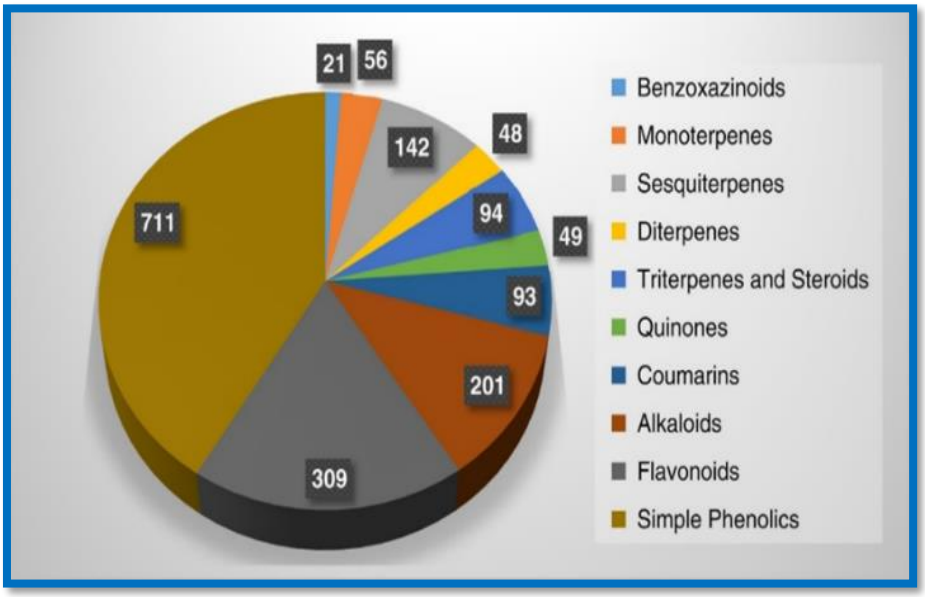

Fig. 1: Total publications in allele chemicals since 2007 [8]

- **Chemical composition**

Phenolics are composed of an aromatic hydrocarbon group and a straight hydroxyl group (-OH) relates to a benzene ring to form phenolic substances a class of chemicals that are essential and naturally occurring allelochemicals of plants within the environment [9]. The pentose-phosphate route is often where phenolic chemicals are produced. In the acetic acid and shikimic process of metabolism, condensation reactions between 4-phosphate erythrose and phosphoenolpyruvic acid, and 7-phosphate altoheptulose result in the production of phenolic chemicals [10].

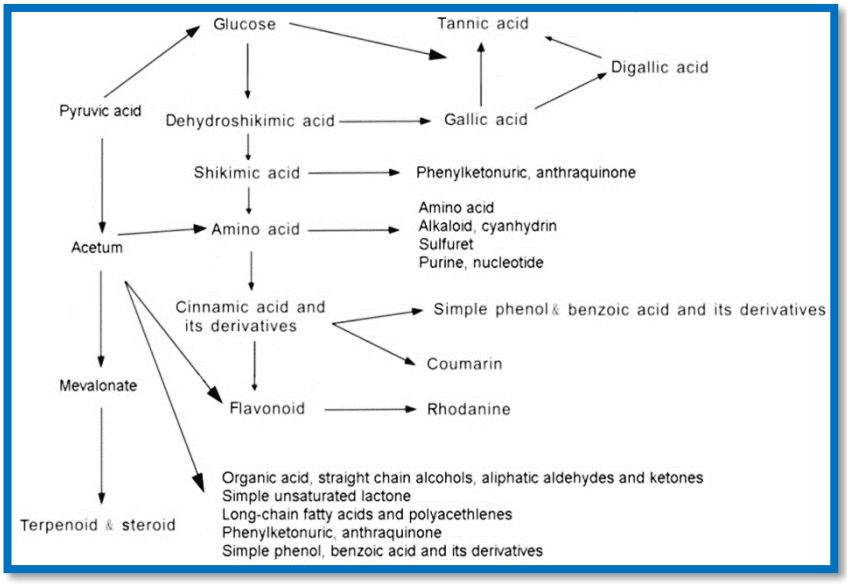

Figure. 2: Major allelopathic compounds' biosynthetic routes.

- **Phenolic effect on agriculture**

Allelochemicals such as vanillin and p-hydroxybenzoic, p-coumaric, ferulic, and caffeic in *Bidens pilosa*, covered by bioassays. Several substances in cover plant biomass, those of a phenolic character and produced through the malonic and shikimic acid pathways for plants, have allelopathic effects by decomposing residues that have been deposited on the soil surface, Secondary compounds are released due to plants towards the atmosphere. The method differs depending on the type of plant, kind of soil., and phenological stage **[11, 12]**. For instance, during the breakdown of its phytomass, rye releases a few substances with an allelopathic effect **[13]**, plants primarily create phenolic compounds for the goals of growth, development, and defense. These aromatic benzene ring molecules play an important role in the interactions between the biotic and abiotic stressors on the plant. They are an essential part of a plant's secondary metabolites and necessary for a variety of physiologic and mechanical functions.

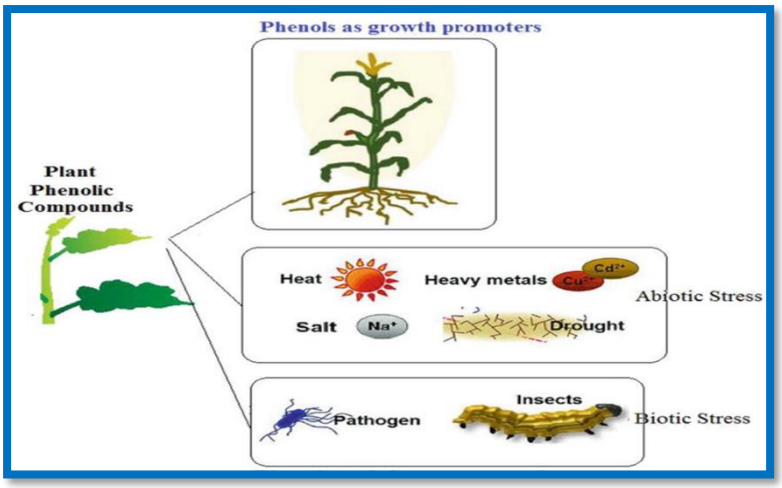

Fig. 3: phenols as defense compounds

Extracts of *Peganum harmala* leaf included Gallic acid, vanillic acid, 4-hydroxybenzoic acid, 3,4-dihydroxybenzoic acid, caffeic acid, syringic acid, and ferulic acid. In comparison to stem or root extracts, leaf extracts had a higher total phenolic acid concentration **[14]**.

Buckwheat's ability to control weed growth is attributed to a few phenolic acids and flavonoids **[15]**. Additionally, tomato and maize tissues had more phenolic compounds than buckwheat extracts **[16]**, showing analyze the primary phenolic substances with the potential to cause harm can be found in rye and oilseed radish shoots., The detrimental effects of such plants on weeds should be exploited for increasing crop production. Crop plants and natural vegetation containing phenols with detrimental effects should be screened for their capacity to suppress weeds. When describing the same species in the same experimental location **[16]**, Furthermore, it was discovered that higher levels of cinnamic acid in rye are related to lignification, the procedure that comes after plant leaching, volatilization, and dry matter degradation by soil microbes.

[17] In the phonological stage of plants, there may be interactions between bacteria, substances with an allelopathic potential, the nature of the soil, food for plants, pH, climate, and other factors. an impact on the phytotoxicity of those substances. It was also noted that the complete amount of phenols in a liquid extract of oilseed radish remains from a plant's stems and leaves was higher **[18]**, The main allelochemicals found in *T. procumbens* were phenolic compounds, which is similar to a recent study by **[19]** Vanillin was shown to be the main allelochemical in the current study's detection of phenolic acids in *Tridax procumbens*, with benzoic, ferulic, and ellagic. Vanillin, a phytotoxic substance, was also discovered in numerous other plants, including *Oryza sativa* **[20]**.

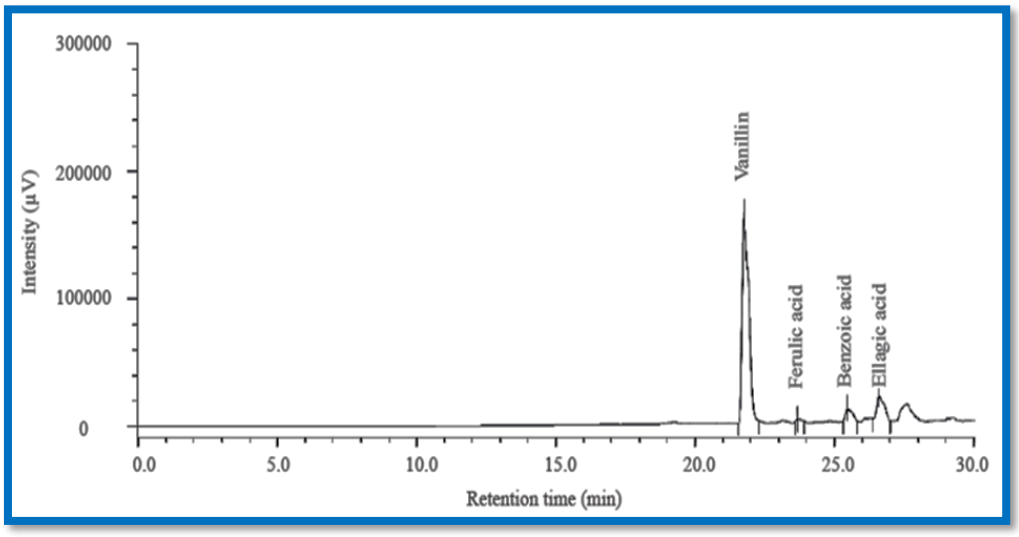

Fig. 4: High performance liquid chromatography used to identify phenolic acids in T. procumbens [20]

Cinnamic and benzoic acids, flavonoids, and terpenes are among the most allelochemicals and are phytotoxic. Allelochemicals harm the development of companion and succeeding crops in a few agroecosystems [21].

2. Physiological and Ecological Mechanisms:

Phenolic allelochemicals have been found both in naturally occurring and controlled environments, where have been shown to create a variety of ecological including losses in crop productivity due to soil disease, failures in natural forest regeneration, and difficulties with the orchard replanting. The biosynthesis and buildup of phenolic compounds are the results of well-controlled processes. The routes for phenolic compounds have evolved throughout time in several plant families. especially when these chemicals take on specific favorable activities [22].

2.1. Impacts on the Membrane Permeability and Regulations on Plant Nutrient Uptake

Plant tissue either slowly grows or dies due to the phenolic allelochemicals effect on cell membrane permeability, prevented from taking nutrients from their environment and have an impact on their regular growth [23], demonstrated a correlation between increases in membrane permeability and decreases in phenyl-ß-glucosyltransferase (PGT) activity and phenol glycosylation via Benzoic acid and cinnamic acid in cucumber (*Cucumis sativus*).

2.2. Impacts on the Photosynthesis and Respiration of Plants

The main effects on photosynthesis have been a decrease in the amount of chlorophyll and photosynthesis. Cucumber seedlings were raised in benzoic and cinnamic acid derivative-containing solutions in the study [24], demonstrating that intercellular CO_2 concentration stomatal conductance and leaf transpiration were all reduced. In seedlings, chlorogenic acid increased stomatal while ferulic acid decreased photosynthetic rate and stomatal, low, and intermediate chlorogenic acid concentrations reduced transpiration rate [25].

2.3. Impacts on the length, division, and structure of the cell

The ability of phenolic allelochemicals to impact the development and growth of plants by preventing the division of cells, elongation of the roots, and cell ultra-structure [26], discovered that coumarin decreased cellular activity and the quantity of Golgi bodies, increased cortex cell thickness, and slowed roots expansion of lettuce (*Lactuca sativa* L.) seedlings, Benzoic acid decreased the elongation of *Eutrema wasabi* roots after a 7-day treatment. Organelle structures were significantly harmed, and the root cells were organized erratically. Vanillic, caffeic, ferulic, coumaric, and chlorogenic acids are bioactive substances found in medicinal plants that have inhibitory activity [27], The reaction of seedlings of *Rhododendron delavayi* demonstrated

that biomass accumulation was restricted by three types of phenols—feru. acid, chlorogenic acid, and protocatechuic acid a rise in total Chl, Chl a, and Chl b, and carotenoid concentrations were stimulated. Stomatal opening, the ratio of stomatal openings, stomatal length, and stomatal width were all considerably suppressed by low doses of feru. acid.

2.4. Impact on the Function and Activities of Different Enzymes

Thanks to the cell membrane of a plant, phenolic allelochemicals enter and alter the function and activity of specific enzymes. At 0.1 mM, caffeine also increased reactive oxygen species (ROS) generation and significantly altered the activities of POD, which decreased rhizogenesis and inhibited root growth of mung bean. According to the findings of other investigations, ferulic acid treatment for 6 days decreased the maize (*Zea mays* L.) root's length and weight at the start of seedlings [21]. Additionally, there was a considerable decrease in the activity of hydrolase, maltase, phospholipase, and protease.

2.5. Impacts on Plant Endogenous Hormone Synthesis

DNA and RNA integrity may be compromised by any phenolic [29], phenolic compounds almost emerge as a mixture and not as a single component. Therefore, it is likely that no one chemical ever contributed to allelopathy in the case of phenolic substances [30].

3. Conclusions

These individual plant phenolic compounds affect several environmental species in opposing ways. It is also known that they have an impact on other plant metabolic processes. These phenolic substances take part in both the above- and below-ground defensive mechanisms of plants. They are created as root exudates and have an impact on the variety of the soil and the nearby plants. An overview of the functions of plant phenolic compounds as signaling, pigment, antibacterial, and defense agents in the plant kingdom is given in the current article.

4. References

[1] Einhellig FA. The physiology of allelochemical action: clues and views. In: Allelopathy, from Molecules to Ecosystems (Eds. Reigosa, M.J. and Pedrol, N.) pp.1-23, Science Publishers: Enfield, New Hampshire, 2002.

[2] Rehman F, Khan FA, Badruddin SM. Role of phenolics in plant defense against insect herbivory. Chemistry of phytopotentials: health, energy and environmental perspectives. 2012:309-13.

[3] Cheng F, Cheng Z. Research progress on the use of plant allelopathy in agriculture and the physiological and ecological mechanisms of allelopathy. Frontiers in plant science. 2015 Nov 17;6:1020.

[4] Batish DR, Kaur S, Singh HP, Kohli RK. Role of root-mediated interactions in phytotoxic interference of Ageratum conyzoides with rice (Oryza sativa). Flora-Morphology, Distribution, Functional Ecology of Plants. 2009 Jan 1;204(5):388-95.

[5] Gindri DM, Coelho CM, Uarrota VG. Physiological and biochemical effects of Lantana camara L. allelochemicals on the seed germination of Avena sativa L. Pesquisa Agropecuária Tropical. 2020 Aug 24;50.

[6] Rehman MU, Hussain M, Ali M, Mustafa CB, Shafi J, Iqbal F. Allelopathy of Brassica. A review. Scientia Agriculturae. 2013;8:222-9.

[7] Papetti A, Milanese C, Zanchi C, Gazzani G. HPLC–DAD–ESI/MSn characterization of environmentally friendly polyphenolic extract from Raphanus sativus L. var.“Cherry Belle” skin and stability of its red components. Food research international. 2014 Nov 1;65:238-46.

[8] Macías FA, Mejías FJ, Molinillo JM. Recent advances in allelopathy for weed control: From knowledge to applications. Pest management science. 2019 Sep;75(9):2413-36.

[9] Li ZH, Wang Q, Ruan X, Pan CD, Jiang DA. Phenolics and plant allelopathy. Molecules. 2010 Dec 7;15(12):8933-52.

[10] Wang Q, Ruan X, Li ZH, Pan CD. Autotoxicity of plants and research of coniferous forest autotoxicity. Sci. Sil. Sin. 2006;43:134–142.

[11] Rueda-Ayala V, Jaeck O, Gerhards R. Investigation of biochemical and competitive effects of cover crops on crops and weeds. Crop Protection. 2015 May 1;71:79-87.

[12] Sampaio BL, Edrada-Ebel R, Da Costa FB. Effect of the environment on the secondary metabolic profile of Tithonia diversifolia: a model for environmental metabolomics of plants. Scientific reports. 2016 Jul 7;6(1):29265.

[13] Tanwir F, Dionisio G, Adhikari KB, Fomsgaard IS, Gregersen PL. Biosynthesis and chemical transformation of benzoxazinoids in rye during seed germination and the identification of a rye Bx6-like gene. Phytochemistry. 2017 Aug 1;140:95-107.

[14] YILAR M, Bayar Y, Onaran A. Chemical composition and allelopathic effect of Origanum onites L. essential oil. Plant Protection Bulletin. 2019 Sep 9;59(3):71-8.

[15] VRCHOTOVA N, SERA B, Dadáková E. HPLC and CE analysis of catechins, stilbens and quercetin in flowers and stems of Polygonum cuspidatum, P. sachalinense and P. x bohemicum. Journal of the Indian Chemical Society. 2010;87(10):1267-72.

[16] Souza M, Comin JJ, Kurtz C, Lovato PE, Lima AP, Kuhnen S. Phenolic compounds with allelopathic potential of Secale cereale L. and Raphanus sativus L. grown under an agroecological no-tillage system. Planta Daninha. 2019 Sep 30;37.

[17] Oliveira RA, Brunetto G, Loss A, Gatiboni LC, Kurtz C, Muller VM, Lovato PE, Oliveira BS, Souza M, Comin JJ. Decomposição e liberação de nutrientes de plantas de cobertura e seus efeitos em atributos químicos do solo e produtividade da cebola. Rev Bras Cienc Solo. 2016;40:e0150105.

[18] Bergamaschi KB. Capacidade antioxidante e composição química de resíduos vegetais visando seu aproveitamento. Piracicaba: USP. 2010.

[19] Monquero PA, Amaral LR, Inácio EM, Brunhara JP, Binha DP, Silva PV, Silva AC. Effect of green fertilizers on the suppression of different species of weeds. Planta Daninha. 2009;27:85-95.

[20] Andriana Y, Xuan TD. Contribution of phenolic acids and dimethyl sulfone to the allelopathic effect of invasive Tridax procumbens. Pesquisa Agropecuária Tropical. 2021 Jan 18;50:e64792.

[21] Mahugo Santana C, Sosa Ferrera Z, Esther Torres Padrón M, Juan Santana Rodríguez J. Methodologies for the extraction of phenolic compounds from environmental samples: new approaches. Molecules. 2009 Jan 9;14(1):298-320.

[22] Politycka B. Phenolics and the activities of phenylalanine ammonia-lyase, phenol-β-glucosyltransferase and β-glucosidase in cucumber roots as affected by phenolic allelochemicals. Acta physiologiae plantarum. 1998 Dec;20:405-10.

[23] Li HH, Inoue M, Nishimura H, Mizutani J, Tsuzuki E. Interactions of trans-cinnamic acid, its related phenolic allelochemicals, and abscisic acid in seedling growth and seed germination of lettuce. Journal of Chemical Ecology. 1993 Aug;19:1775-87.

[24] Yu JQ, Ye SF, Zhang MF, Hu WH. Effects of root exudates and aqueous root extracts of cucumber (Cucumis sativus) and allelochemicals, on photosynthesis and antioxidant enzymes in cucumber. Biochemical systematics and ecology. 2003 Feb 1;31(2):129-39.

[25] Fu YH, Quan WX, Li CC, Qian CY, Tang FH, Chen XJ. Allelopathic effects of phenolic acids on seedling growth and photosynthesis in Rhododendron delavayi Franch. Photosynthetica. 2019 Apr 1;57(2).

[26] Li HH, Inoue M, Nishimura H, Mizutani J, Tsuzuki E. Interactions of trans-cinnamic acid, its related phenolic allelochemicals, and abscisic acid in seedling growth and seed germination of lettuce. Journal of Chemical Ecology. 1993 Aug;19:1775-87.

[27] Singh AA, Rajeswari G, Nirmal LA, Jacob S. Synthesis and extraction routes of allelochemicals from plants and microbes: A review. Reviews in Analytical Chemistry. 2021 Sep 9;40(1):293-311. https://doi.org/10.1515/revac-2021-0139

[28] Devi SR, Prasad MN. Effect of ferulic acid on growth and hydrolytic enzyme activities of germinating maize seeds. Journal of Chemical Ecology. 1992 Nov;18:1981-90.

[29] Devi SR, Prasad MN. Effect of ferulic acid on growth and hydrolytic enzyme activities of germinating maize seeds. Journal of Chemical Ecology. 1992 Nov;18:1981-90.

[30] Ni HW. Present status and prospect of crop allelopathy in China. Rice allelopathy. 2000:41-8.

Al-Kitab Journal for Pure Sciences (2023); 7(2):99-114.
https://doi.org/10.32441/kjps.07.02.p9

Al-Kitab Journal for Pure Sciences
ISSN: 2617-1260 (print), 2617-8141(online)
https://isnra.net/index.php/kjps

Using Universal Kriging for Spatiotemporal Data of Soil Pollution with Metals in Al Karama Industrial Area in Mosul City

Mai Hussein Ali *, **Ghanim Mahmood Dhahir**

Department of Mathematics, College of Education for Pure Sciences, University of Mosul, Mosul, Iraq.

*Corresponding Author: mustafamohamed40020@gmail.com

Citation: Ali MH, Dhahir GM. Using Universal Kriging for Spatiotemporal Data of Soil Pollution with Metals in Al Karama Industrial Area in Mosul City. 2023 Oct 30;7(2):99-114. Available from: https://doi.org/10.32441/kjps.07.02.p9.

Keywords: The Universal Kriging, the Covariance models, Spatiotemporal data, standards of error.

Article History

Received	03 Sep. 2023
Accepted	22 Oct. 2023
Available online	30 Oct. 2023

Abstract:

The current research tackles the performance of Spatiotemporal Interpolation Techniques using the Kriging Technique after relating it to time, which is introduced to the Prediction Process as the reliable mathematical formula to obtain the best performance of a proposed mathematical model. This study's main objective is to evaluate the best Unbiased Linear Prediction Technique with the slightest variance of error through mathematical equations that are derived and related to time.

In this study, the researcher used Spatiotemporal Data of Soil Pollution with minerals in the industrial zone in Mosul city with the actual locations. The data consists of (192) real observations of Arsenic (As) and Chrome (Cr) in the AL Karama Industrial Zone, and this data represents the depth with the actual locations. The Kriging Technique and Kriging Covariance through the mathematical formula are related to time in this research. A function for the place was applied, namely, the variogram function that represents the difference between the observations, as this function was determined for all the directions of the compass, and its parameters were estimated. Through the covariance and the standards of error, it was concluded that the ideas of the Mathematical Spatiotemporal model express the positivity of the proposed model amongst the models of the Covariance functions, such as the Spherical model and the

Exponential model, which are approximate models from the principal point of view to the characteristics of the Kriging mode. We also recommend entering three-dimensional data to obtain a proposed mathematical model or data for infectious diseases and atmospheric gas Pollution, using other Spatiotemporal Prediction methods and linking them with artificial intelligence and Fuzzy methods. All the calculations were conducted using the MATLAB Language.

Keywords: The Universal Kriging, the Covariance models, Spatiotemporal data, standards of error.

استخدام الكريكنك الشامل للبيانات الزمانية المكانية لتلوث التربة بالمعادن في منطقة الكرامة الصناعية في مدينة الموصل

مي حسين علي *، غانم محمود ظاهر
ghanim-hassod@uomosul.edu.iq ، mustafamohamed40020@gmail.com

قسم الرياضيات، كلية التربية للعلوم الصرفة، جامعة الموصل، العراق.

الخلاصة:

يتناول هذا البحث أداء تقنيات الاستكمال الزماني المكاني باستخدام تقنية كريكنك بعد ربطها بالزمن والتي تدخل في عملية التنبؤ على شكل صيغ رياضية معتمدة من أجل الحصول على أفضل أداء لنموذج رياضي مقترح. إن الهدف الرئيسي من هذه الدراسة هو تقييم أفضل لتقنية التنبؤ من أجل الحصول على أفضل تنبؤ خطي غير متحيز مع أقل تباين للخطأ من خلال معادلات رياضية مشتقة ومرتبطة بالزمن.

لقد تم الاعتماد في هذا البحث على بيانات زمانية ومكانية لتلوث التربة بالمعادن في منطقة صناعية في مدينة الموصل مع مواقعها الحقيقية حيث تتكون البيانات من (١٩٢) مشاهدة حقيقية لكل من معدني الزرنيخ (*As*) والكروم (*Cr*) في صناعة الكرامة وهذه البيانات تمثل العمق مع مواقعها الحقيقية. من خلال هذا البحث تم تطبيق تقنية كريكنك وتباين كريكنك من خلال الصيغ الرياضية المرتبطة بالزمن. وقد تم تطبيق دالة للموقع ودالة للزمن هي دالة الفاريوكرام والتي تمثل الفرق بين المشاهدات حيث تم احتساب هذه الدالة لجميع اتجاهات البوصلة وتقدير معلمات الدالة. وتم من خلال النتائج التوصل إلى أن تقنية كريكنك تظهر أداءً وتقديراً مميزاً وواقعياً وذلك من خلال صيغ التباين ومعايير صحة الخطأ. إن أفكار النموذج الرياضي الزماني المكاني المشترك يعبر عن إيجابية النموذج المقترح من بين نماذج دوال التغاير مثل النموذج الكروي والنموذج الأُسي وهما نموذجان متقاربان من حيث المبدأ لخصائص تقنية كريكنك. كما نوصي بإدخال بيانات ثلاثية الأبعاد للحصول على نموذج رياضي مقترح، أو بيانات لأمراض العدوى والتلوث بالغازات الجوية، واستخدام طرق تنبؤ زمكانية أخرى وربطها مع أساليب الذكاء الاصطناعي أو الأسلوب المضبب. تم إجراء الحسابات باستخدام لغة ماتلاب (*Matlab Language*).

الكلمات المفتاحية: الكريكنك الشامل، نماذج التغاير، بيانات زمانية مكانية، معايير الخطأ.

1. Introduction:

Kriging Technique gained this name after the name of the South African mining engineer D. G. Krige, who submitted specific ideas in his master's thesis in (1951), and these ideas were adopted by the famous French mathematician George Matheran and called the Kriging Technique for spatial prediction. Spatial prediction received significant attention in statistics as the forecast can potentially affect the values in unknown locations. Despite the long history of this subject, the uncertainty feature is related to the type of the most convenient prediction method. Sometimes, many researchers rely on the nature of the data (samples) and the decisions made when identifying the prediction criteria. When any vector is specified, a particular indicator can be measured by increasing the number of Kriging applications, and it is the Best Linear Unbiased Prediction (BLUP)m where the statistical characteristic is preferred repeatedly so that the chance is available to determine the mean as a model in Kriging Technique. Usually, the spatial technique is evaluated into two values: mean and residual. Here, the random data is related to the residual, and the Universal kriging (UK) becomes related to the mean. Several studies suggest a model estimate the level of air pollution explicitly by merging both the temporal and spatial dependent variables; spatial interpolation methods and their applications have been developed in various disciplines, such as mining engineering **[11]** and environmental sciences **[6]**, **[1]**, many studies have dealt with spatial prediction **[5]**, **[15]**, in health, pollution and precipitation **[16]**, in the field of soil data, its properties and groundwater **[3]**, **[2]**.

2. Method

2.1 Regionalized Random Variables:

If the random variable Z(s) is a spatial variable in the location s, and if $s = s_o$, then $Z^*(s_o)$ is the variable to be predicted in the location s_o. The random spatial variable (regional) is defined as a numerical function with a spatial distribution that is different from one location to another with the continuity of the phenomenon, but the spatial (regional) data is the information that describes objects and events in a location of the earth surface or near it or inside the earth or close to it. Usually, the spatial geographical data involves the information of the location (it includes coordinates on the ground, the feature or the event information, or certain phenomena) with the temporal information (time or age) that exists in the location, and the location is stable on the wide range. If Z(s) is a random spatial variable in the location (s), then the distribution data Z(s) has a prediction that is written with the following formula:

$$\mathbf{m(s) = E[Z(s)] = \int_{-\infty}^{\infty} x\, f_{Z(s)}(x)dx = \mu} \qquad \mathbf{, \forall\, s \in D} \qquad \mathbf{(1)}$$

his case is called First-Order Stationarity, but in Second-Order Stationarity, the random variable Z(s) is a second-order stationary variable if the prediction of the random variable is present and doesn't depend on the location (s). $\boldsymbol{E[Z(s)] = \mu \quad , \ \forall s \in D}$

If the variance exists, it is defined as $\mathbf{var\ [Z(s)] = \sigma^2_{Z(S)} = E[\{Z(s) - m(s)\}^2]}$

$$\mathbf{var\ [Z(s)] = \int_{-\infty}^{\infty} (x - m(s))^2\, f_{Z(s)}(x)\, dx}$$

For each pair of spatial random variables $[\boldsymbol{Z(s), Z(s+h)}]$ The covariance function is known and depends on lag only.

$$\mathbf{COV\ \big(Z(s), Z(s+h)\big) = E\big[\big(Z(s) - m(s)\big)\big(Z(s+h) - m(s+h)\big)\big] = \sigma\ (h)}$$

The second-order stationarity entails the presence of the covariance function and a specific finite variance function. The Intrinsic Stationary is more generalized than the previous stationarity in that the mathematical prediction exists and doesn't depend on the location (s).

$$\mathbf{E\ [Z(s)] = \mu}$$

The increase $[\mathbf{Z(s), Z(s+h)}\ ]$ has a finite variance and doesn't depend on the location (s).

$$\boldsymbol{var[Z(s), Z(s+h)] = E[(Z(s+h) - Z(s))^2] = 2\gamma(h)}$$

The function $2\gamma(h)$ is called a variogram function, while the stochastic process is called the random process, which is a group of random variables that depend on time. If we assume that there is the element (s) (sample space) for a random experiment (E), then the function:

$$\boldsymbol{Z = \{Z(t,s), t \in T, s \in S\}, T \subset R} \qquad \textbf{(2)}$$

It is called the random process or the stochastic process.$\big((t), (t,s)\big)$, where T is the parameter time, S is the space, and the sample (the case) (states space), as T might be countable (discontinuous values) or uncountable (continuous) ,and the same is with s [8], [13], [17].

2.2 Variogram Function:

Usually, the variogram function is defined as the function of the following probabilities:

$$\mathbf{2\gamma(h) = E[(Z(s) - Z(s+h))^2]} \qquad \textbf{(3)}$$

When dealing with the real data, the variogram function is estimated by the experimental variogram function in relation to the lag vector (h) as a set of observations that exist in the form of pairs with spaces between them lag(h) [4], [7], [9].

$$\boldsymbol{2\gamma^*(h) = \frac{1}{N(h)} \sum_{i=1}^{N(h)} (Z_i - Z_j)^2, j=1,2\ldots,N(h)} \qquad \textbf{(4)}$$

There are three parameters for the variogram function, they are:

- The range is symbolized with (a), and it represents the distance on the x coordinate or lag until the curve is stable.
- Sill, where the value of $\mathbf{c + c_o}$ Represents the variance.

- The Nugget Effect stands for the random errors in the measurement units, which is the nugget effect of the function at h = 0, and it is also called the nugget effect or discontinuity, as shown in **Figure (1)**:

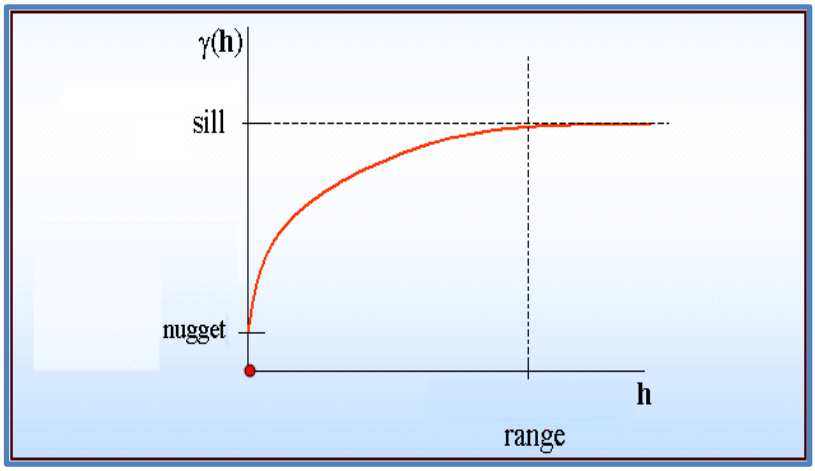

Figure (1): An illustration of the variogram function characteristics

Figure (1) shows the variogram drawing in general, where the x-axis is the lag(h) and the y-axis represents the semi-variogram function γ(h) with the parameters: (nugget effect) is the lack of continuity, (still) is the variance, and (range) is the lag. The variogram function has the following properties:

$$\boldsymbol{\gamma(h) = \gamma(-h)}$$
$$\boldsymbol{\gamma(0) = 0} \qquad \boldsymbol{, h = 0}$$
$$\boldsymbol{\frac{\gamma(h)}{\| h \|^2} \to 0} \qquad \textbf{when} \qquad \boldsymbol{\|h\| \to \infty}$$

For any real group $\{a_1, a_2, \dots\dots\dots, a_n\}$ that verifies $\sum_{i=1}^{m} \mathbf{a_i} = \mathbf{0}$ we get the following characteristics: $\boldsymbol{\Sigma_{i=1}^{m} \Sigma_{j=1}^{m} a_i \; a_j \; \gamma\left(s_i - s_j\right) \leq 0}$

Here, the process is isotropic, i.e., $\boldsymbol{\gamma(\mathbf{h}) = \gamma(\|h\|)}$**.** There is a relationship that connects the variogram and the covariance function, which $\boldsymbol{\gamma(\mathbf{h}) = \mathbf{C}(\mathbf{0}) - \mathbf{C}(\mathbf{h})}$, where γ(h) is Semi variogram function and C(0) is a Variance function and C(h) represents the Covariance function **[4] ,[7]** .

2.3 Spatiotemporal Random Function Model

Let $Z = \{Z(s,t), s \in S, t \in T\}$ be a group of spatiotemporal data or temporal data from a variable with spatial coordinates $(s_i, t_i), i = 1, \dots\dots, n$ within the spatial domain S for the time interval T. Assuming that this definition satisfies the stochastic spatiotemporal function $Z(s,t)$, predictions can be made $Z(s_o, t_o)$ For the unmeasurable spatiotemporal points **[6],** the model of the random function is given as follows:

$$\boldsymbol{Z^*(s,t) = m(s,t) + e(s,t)} \qquad \textbf{(5)}$$

Where m (s, t) is the deterministic part and e (s, t) is the stochastic residual part. The stability of the direction can be presumed in the time and place, and it can be allowed to change as a known function of covariates, and m represents the basic variance in the spatiotemporal process. The direction is developed by the regression-type model that connects the important variable z with the relevant covariates. The residual **e** represents the difference between the observations and predictions of the trend of the stationarity model of residuals for replication in Kriging processes results from removing the direction component, and they are distributed normally [7], [18], [17].

2.4 Spatiotemporal Variogram Function

The estimation of spatiotemporal direction is done by subtracting m(s) from the observations of the spatiotemporal level e(s, t), and the residual might be differences or correlations in space and time. The resulting residuals could be used in constructing the sample of the variogram function in time and space. The sample of the variogram function model diagram $2\gamma(h,u)$ is calculated as follows:

$$\boldsymbol{2\gamma(h,u) = \frac{1}{N(h,u)}\sum_{i=1}^{N(h,u)} [e(s,t) - e(s+h,t+u)]^2} \quad \textbf{(6)}$$

Where h is the distance separating the points in space and, u is the separation in the time, N(h, u) is the number of observations in Z that are separated by lag (h, u). The spatiotemporal structure of the variogram function is symbolized by 2γ(h, u), which is according to the distance or lag. Once the plot samples of the spatiotemporal variogram function model are calculated, a model with a few model variances can be modeled to estimate the spatiotemporal covariance and variance. The variogram function can represent the spatiotemporal variables. $\gamma_{S,T}(s,t)$ in the following formula:

$$\boldsymbol{\gamma_{S,T}(s,t) = \gamma_s(h) + \gamma_T(u) + \gamma_J\left(\sqrt{h^2 + (x,u)^2}\right)} \quad \textbf{(7)}$$

Where x represents the spatiotemporal variance when the spatiotemporal distances and the spatial distance are merged, and γ_J Are the spatiotemporal variogram functions [19], [21].

2.5 Universal Kriging

In this type of kriging, the data Z_i, i= 1, …, n, are unknown at the points *vi* where i= 1, …, n is interpreted as outcomes of a random field that can be decomposed as the sum of the deterministic components of a random field Z(s) is stationarity and has a mean of zero. This is supposed to be*:* $\mathbf{Z(s) = \sum_{j=1}^{p} \beta_j f_j(s) + R(s)}$

Where R is a zero mean of a random field, which is represented as a function *f*, which is assumed to be known, together with the variogram function of the random field R, the

coefficients β_j are secondary coefficients of the prediction. Under these assumptions, Universal Kriging (UK) can be defined as If we have s_o, then Universal Kriging overall estimate at a point s_o based on the spatial data $Z(s_i)$ where $i = 1, \ldots, n$ is defined as an unbiased linear estimate.

$$Z^*(s_0) = \sum_{i=1}^{n} \lambda_i Z(s_i)$$

With the most accurate squared predictive error. The Universal Kriging can be written in the following form: $\mathbf{Z = X\beta + R}$

Justifying the morphological similarity with the general linear estimation. The function to be minimized can be written in the case of a Universal Kriging as follows:

$\varphi(\lambda_1, \lambda_2, \ldots, \lambda_n, m_1, \ldots, m_p) = E[(Z(s_0) - \sum_{i=1}^{n} \lambda_i Z(s_i))^2] - 2\sum_{j=1}^{p} m_j(\sum_{i=1}^{n} \lambda_i f_j(s_0))$,Where $j = 1, \ldots, p$ and m_j Are Lagrangian multiples, repeating the derivation along the lines of the above leads to a linear system. $\Gamma U\, \lambda U = \gamma U$, where ΓU is a matrix, λU is a value, and γU is a value. The Universal Kriging Coefficients can be determined by solving the linear system. $\Gamma U\, \lambda U = \gamma U$, therefore: $\lambda U = \Gamma_U^{-1}\, \gamma U$.

Similarly, the squared prediction error can be calculated as in the case of Ordinary Kriging (OK) through the following equation [9], [10], [14].

$$\sigma_{UK}^2(v_0) = \lambda_U^T\, \gamma U = \gamma_U^T\, \Gamma_U^{-1}\, \gamma U \qquad (10)$$

2.6 Spatiotemporal Kriging Technique

In a similar way to the pure spatial case in the regression Kriging (RK), separate predictions are of the direction, and the remaining components are performed, and then they are added together once again. The techniques of applying the steps differ in terms of satisfying the Spatiotemporal Kriging Technique (STK) on the random residuals through the best unbiased linear prediction $e(s_o, t_o)$.

$$e^*(s_o, t_o) = \sum_{i=1}^{n} \lambda_i e(s_i, t_i) \qquad (9)$$

where; λ_i Represents the weights of the spatiotemporal Kriging technique that is determined by the spatiotemporal waste structure. Also, $e(s_i, t_i)$ Are the residual of the samples in the area that is neighboring the prediction location? The optimum weights of the spatiotemporal Kriging technique are obtained via the following relation:

$$\sum_{i=1}^{n} \lambda_j \gamma_{st}(s_i - s_j, t_i - t_j) + \mu = \gamma_{st}(s_i - s_o, t_i - t_o), \qquad \forall_j = 1, \ldots, n$$

$$\sum_{i=1}^{n} \lambda_i = 1$$

Where the Lagrange multiplier μ is the number of observations that are confined to the research area. The final spatiotemporal estimation in the location (s_o, t_o) It is given by the components that remain together.

$$\boldsymbol{Z^*(s_o, t_o) = m^*(s_o, t_o) + e^*(s_o, t_o)} \quad \textbf{(11)}$$

The prediction covariance is estimated by:

$$\boldsymbol{var(Z^* s_o, t_o) - Z(s_o, t_o)) = \sigma^2\left(m^*(s_o)\right) + \left(\sum_{i=1}^{n} \lambda_i\ \gamma_{s,t}(s_i - s_o, t_i - t_o) + m\right)}$$

The vector of the error component is given by:

$$\boldsymbol{\sigma^2\left(m^*(s_o)\right) = (x_o - x^T\ c^{-1}\ c_o)^T (x^T\ c^{-1}\ x)^{-1}\ (x_O - x^T\ c^{-1}\ c_O)} \quad \textbf{(12)}$$

Where *x* is the sample of the covariance matrix remaining in the research locations, c is the covariates in the research location, and x_o It is the vector of the variables [12], [20], [17].

2.7 Measures of The Predictive Performance with Time

The predictive performance for each model is accomplished by verifying the (Cross Validation) as the accuracy of prediction validity with the time factor by the mean absolute predictive error (MAPE), which equals:

$$\boldsymbol{MAPE = \frac{1}{N} \sum_i \sum_t \left| \frac{\gamma(s_i, t) - \gamma^*(s_i, t)}{\gamma^*(s_i, t)} \right| * 100} \quad \textbf{(13)}$$

Where N is the total number of available observations in the group, $\gamma(s_i, t)$ is the measurements of the pollution in the counter i and the unit of time in the group t, $\gamma^*(s_i, t)$ Represents the root mean square error (RMSE) can be found [20]:

$$\boldsymbol{RMSE = \sqrt{\frac{1}{N} \sum_i \sum_t \left(\gamma(s_i, t) - \gamma^*(s_i, t)\right)^2}} \quad \textbf{(14)}$$

3. Data Analysis

We relied on spatiotemporal data with their actual locations from research published in the College of Environmental Sciences by researcher Salem Rabie Zannad (2020), and the title of the research was "Industrial Pollution and Environmental Impact Assessment of Industrial Areas in the City of Mosul." University of Mosul.

3.1 The area of study

The area of the study is in Mosul city in the northern west part of Iraq, which is between the longitude 41 º - 44º to the east and latitude of (41º - 44º) to the east and latitude of (35º - 37º). The Al Karama industrial zone is in the eastern part of Mosul (the left bank of the city). The area of the study is famous for the factories and mills in addition to the repair and maintenance shops and garages that represent an important factor to the city. The real spatiotemporal data of the industrial zone in Mosul city is the data adopted in this research, and it consists of (192)

real values for Arsenic (As) and Chrome (Cr), which cause pollution to the soils of the industrial zone with the course of time and for three seasons: (Autumn, Winter, and Spring).

Table (1): Results of the variogram functions for Arsenic and Chrome metals for all the trends

Arsenic As							
G1	0.932	1.260	1.491	2.093	3.151	3.796	5.108
G2	7.096	14.640	18.552	21.829	22.486	16.377	30.059
G3	8.373	17.082	20.769	26.197	31.531	28.323	52.590
G4	6.243	13.054	16.192	18.917	17.085	9.182	12.410
G5	4.014	7.950	10.022	11.961	12.819	10.086	17.583
G6	7.308	15.068	18.480	22.557	24.308	18.753	23.500
Chrome Cr							
G1	0.364	0.322	0.270	0.380	0.602	0.481	0.656
G2	0.425	1.040	1.880	3.130	4.222	5.547	7.119
G3	0.618	1.336	2.521	4.126	5.326	6.718	7.507
G4	0.410	0.819	1.136	2.180	3.496	2.914	2.722
G5	0.848	1.340	1.968	2.957	3.888	5.075	6.580
G6	1.153	2.098	3.118	5.204	7.160	7.502	6.250

Table (1) below contains the results of the variogram function according to equation (1) for all the directions of the compass with the basic angles of the compass (θ=135°, 45°, 90°, 0°), where G1 represents the angle θ=0°, G2 represents the results at the angle θ=90° with lag (h), whereas G3 stands for the results at the angle θ=45° and G4 represents the results at the angle θ=135° with lag (h) of h = 1.414, 2.82, …, 9.898 for the case of Arsenic and Chrome metals. The results of the mean variogram function where the first row is G5 represents the mean of the two angles θ = 90°, 0° because the lag is equal when h =1, 2, …,7, the second row shows the mean of the two angles θ = 135°, 45° because the lag is equal in the case of the Arsenie and the Chrome metals.

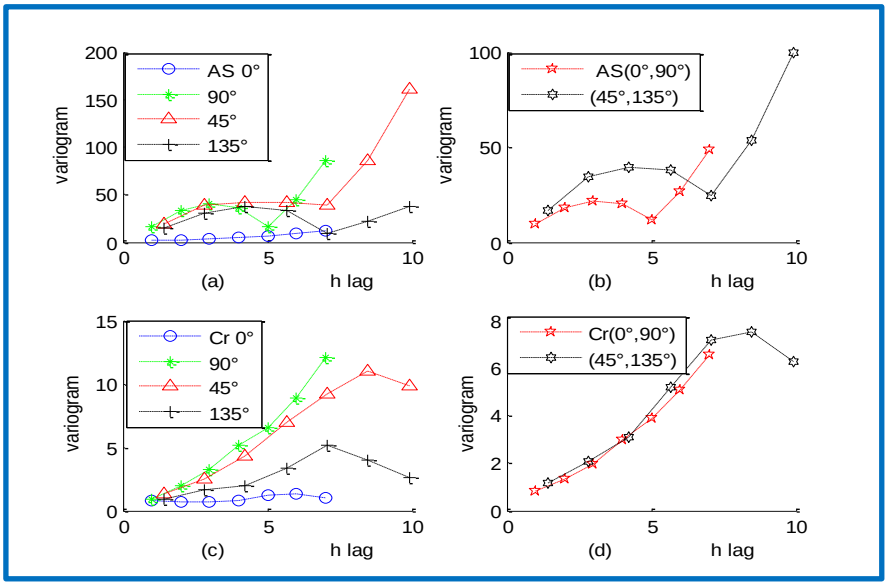

Figure (2): Curves of the variogram function for the Arsenic and Chrome metals

Figure (2) shows the curves of the variogram functions as the curves in (a) for all the angles: the blue curve is when θ=0°, the green curve is when θ = 90°, the red curve is when the angle is (θ=45°) and the discontinuous dots curve is when θ =135°. As for (b), it represents the mean of the two variogram functions at the angles (0°and 90°) represented by the red curve, and the black curve represents the angles (45° and 135°) for Arsenic (As). The same can be said for the curves in figure (c) for all the angles related to Chrome, and figure (d) represents the mean variogram function of Chrome.

Table (2): Results of the characteristics of the variogram function means for Arsenic and Chrome metals for all the angles.

Metal / Statistics	As		Cr	
	(0°,90°)	(45°,135°)	(0°,90°)	(45°,135°)
Min	4.014	7.308	0.848	1.154
Max	17.58	32.5	6.58	7.503
Mean	10.63	19.85	3.237	4.641
Median	10.09	18.75	2.958	5.204
Range	6	8.485	6	8.485

Table (2) shows the results of the variogram function for all the angles, where (Min) stands for the point of nugget effect, (Max) represents the variance, (Mean) represents the mean, (median) represents the median, and (Range) stands for the range in the case of Arsenic and Chrome metals.

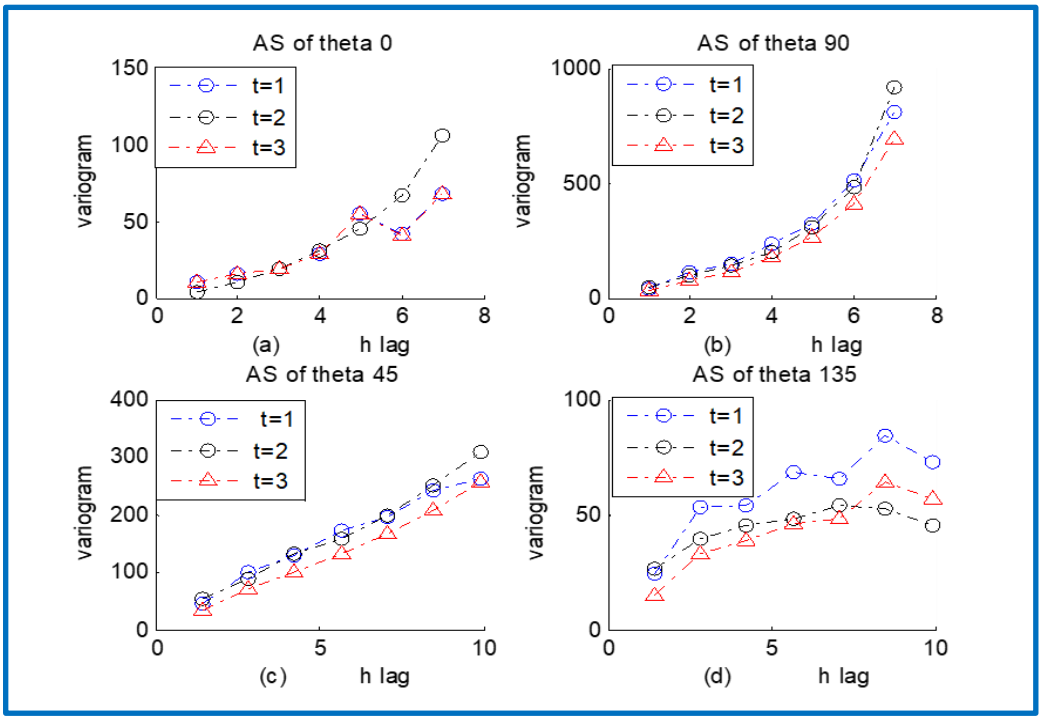

Figure (3): Results of variogram function of the spatiotemporal data of Arsenic and Chrome metals in all the directions of the compass

Figure (3) shows the variogram functions, where (a) represents the result of the variogram function at the angle (0^o) with time. Where (t =1, t=2, t=3) between the lag on the x-axis and the variogram function on the y-axis and the same is for the rest of the angles in the figure; (b), (c) and (d) for the angles 45, 90 and 125 ^{o} respectively. In **Figure (3)**, the curves of the functions (a) as (t=1, t=2, t=3) between the lag on the x-axis and the variogram function on the y-axis and the same for the rest of the angles in figures b, c and d for the angles (45°, 90°, and 135°) respectively.

Table (3): Results of the variogram function mean of Arsenic metal at (t=1, t=2, t=3)

G5 (T=1)	G6(T=2)	G7(T=3)
9.667	9.224	9.828
19.753	18.248	20.070
24.566	21.415	24.895
23.881	20.355	25.404
13.380	11.818	14.965
31.483	26.882	34.139
60.007	48.866	66.623

Table (3) shows the results of the variogram function mean, where G5 represents the results of the variogram function mean at (T=2), and G7 represents the variogram function mean at (T=3).

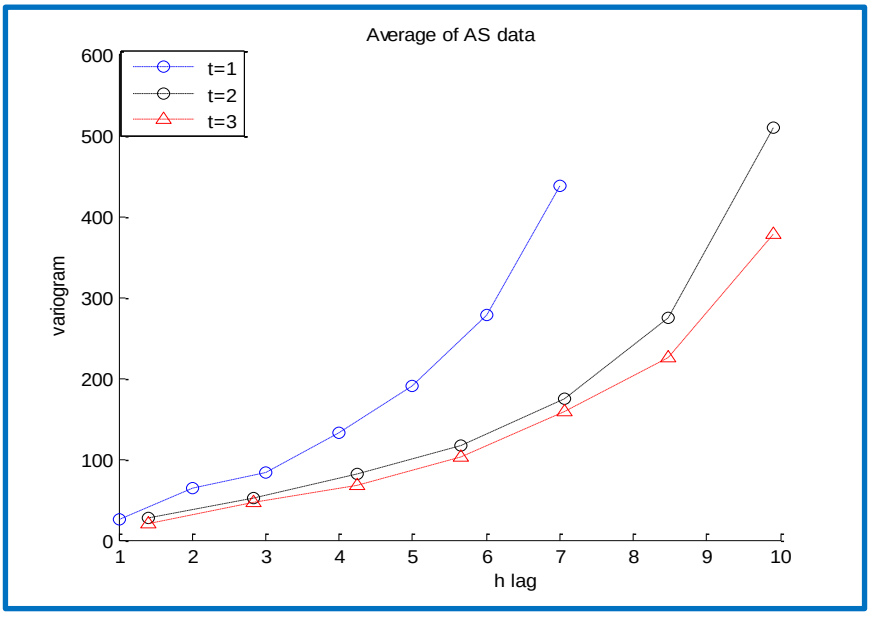

Figure (4): Results of variogram mean of the spatiotemporal data of Arsenic.

Figure (4) shows three curves of the variogram. The blue curve shows the average at (t=1), the red curve shows the average at (t = 2), and the black curve shows the average at (t=3).

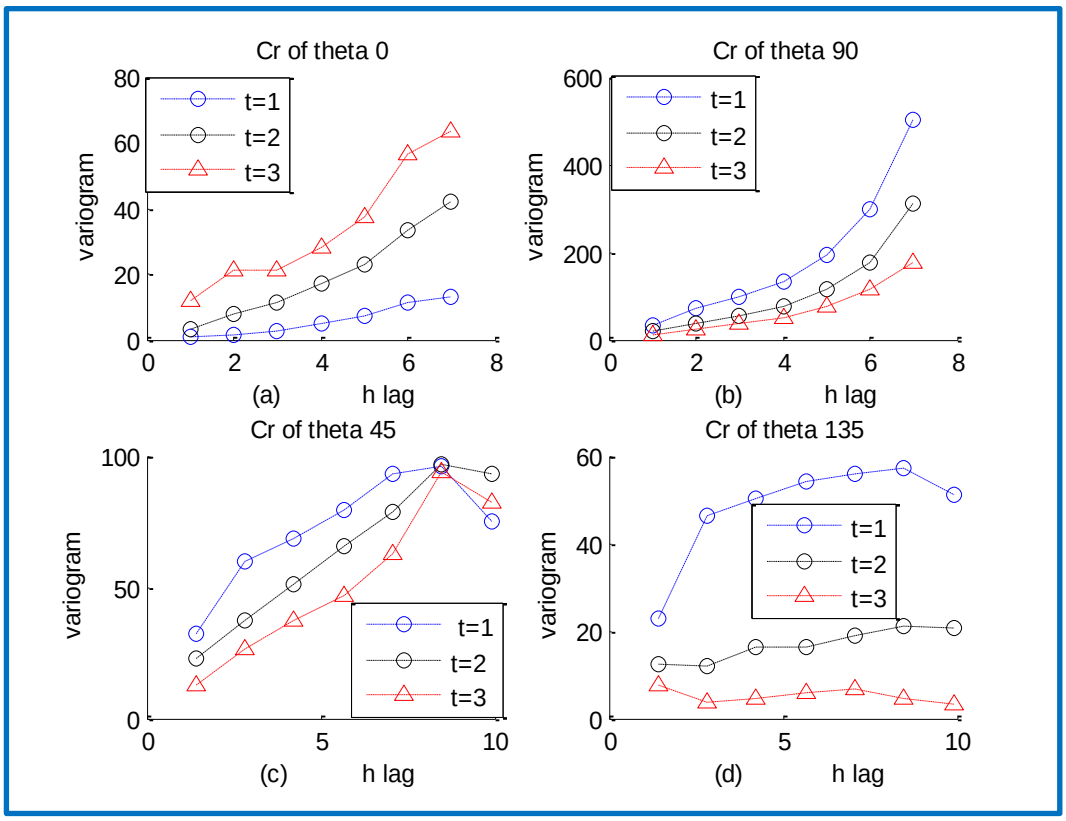

Figure (5): of the spatiotemporal data of Chrome in all the directions of the compass

Figure (5) shows the curves of the variogram functions. Part (a) represents the Results of the variogram function at the angle (0^o) with the times (t = 1, t = 2, t = 3) between the lag on the x-axis and the variogram function on the y-axis. The same is true for the rest of the angles in the parts (b), (c), and (d) in the figure for the angle.

Table (4): variogram function of the mean of Chrome.

G5 (t=1)	G6(t=2)	G7(t=3)
0.789	0.848	0.803
1.363	1.340	1.284
2.150	1.968	1.917
3.511	2.957	2.841
4.825	3.888	3.865
6.029	5.075	5.383
7.775	6.580	6.940

Table (4) represents the results of the mean variogram function at time (t = 1,2,3). G5 represents the mean of the angle (0^o), G6 represents the mean of the angle (90^o), and G6 represents the mean of the angle (45^o).

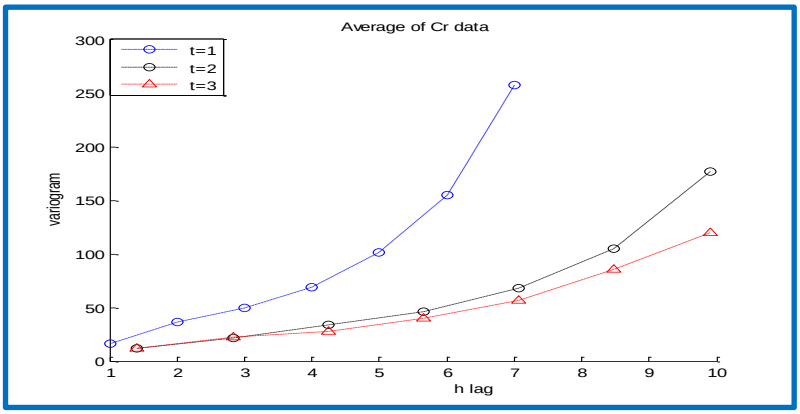

Figure (6): Results of an average of variogram function at (t=1, t=2, t=3) for Chrome

Figure (6) includes three curves of the mean variogram function for Chrome. The blue curve shows the mean at (t = 1), the black curve shows the mean at (t = 2), and the black curve shows the mean at (t = 3).

Table (5): Results of the variogram function characteristics for Arsenic and Chrome at (t=1, t=2, t=3)

Statistics \ Time	As			Cr		
	t=1	t=2	t=3	t=1	t=2	t=3
Min	25.73	26.64	20.06	16.01	12.21	11.96
Max	437.8	509.6	378.9	257.8	176.7	120
Mean	173	176.7	142.7	97.73	66.23	52.14
Median	132.3	116	102.3	68.67	46.39	39.49
Range	6	8.485	8.485	6	8.485	8.485

Table (5) shows the results of the variogram function characteristics for all the times (t=1, t = 2, and t=3) for the average of the variogram function for Arsenic and Chrome. Min represents the nugget effect point; Max represents the variance. Mean represents the average, Median, and Range.

Table (6): Parameters of variogram function of the spatiotemporal data of Arsenic and Chrome

Parameters \ Data	Metal	Model	Theta or Time	Sill (m^2)	Nugget Effect(m^2)	Range (m or month)
Space	As	Spherical	(0°,90°)	17.58	4.014	6
			(45°,135°)	32.5	7.308	8.485
Spatiotemporal	As	Spherical	t=1	60.01	9.668	6
			t=2	48.87	9.225	8.485
			t=3	66.62	9.829	8.485
Space	Cr	Exponential	(0°,90°)	6.58	0.848	6
			(45°,135°)	7.503	1.154	8.485
Spatiotemporal	Cr	Exponential	t=1	7.775	0.789	6
			t=2	6.58	0.848	8.485
			t=3	6.941	0.803	8.485

Table (6) shows the results of the variogram function parameters for the spatiotemporal data of Arsenic and Chrome. It demonstrates the model approximate to the covariance function through the characteristics of the variogram functions and their means in all the angles with the same lag as mentioned earlier, and it also shows the parameters of all the times (t =1, t =2 and t=3) of the mean of the variogram function of Arsenic and Chrome. The table shows the main parameters of the variogram function with the spatial pattern in the angles (0^o, 90^o) and (45^o,135^o) as the table includes the parameters of variogram parameters as (sill) stands for the variance, (nugget effect) represents the nugget effect, while (range) represents the range with (meter or month). As for the spatiotemporal, it shows (t = 1,2,3) for the data related to the time of the two metals (Arsenic and Chrome).

Table (7): Selected prediction values with the performance of prediction measures

MAPE	0.13244	0.1156	0.1002	0.3372
RMSE	0.1451	0.3219	0.2117	1.0089
Z*(s)	32.574	27.1918	18.2894	25.5074

Table (7) shows some values to be predicted as Z* represents the values to be predicted, and Z stands for the actual values with the standards of error (MAPE and RMSE). From the results, it is noticed that the standards of error are small in value, and this indicates the validity of the prediction process of the data about which prediction rests compared with the original data.

4. Conclusions:

The selection of the mathematical model and the evaluation of the impartiality of the models are necessary to improve the prediction by applying the spatiotemporal data and drawing the curves of the spatiotemporal distribution of arsenic and chromium data in soil pollution in the study area. From **Table (6)**, we notice that the variogram function has the aspherical model in the case of spatial data and spatiotemporal data for arsenic metal, while in the case of spatial and spatiotemporal data, the variogram function has an exponential model in the case of chromium metal. We note that there is a great similarity in the properties of the covariance functions(spherical model and exponential model) through forecasting and taking into account the criteria for the correctness of the prediction as well as the least variance and the conditions of the results obtained in obtaining covariance models with convergent parameters for the best prediction show us the property of uniform spatial distribution of data in all directions of the compass and through the application of the kriging technique, the results showed the correctness of the prediction and the completion methods showed similar performance between the kriging technique. Finally, the proposed model of the spherical curve and the exponential curve

approaches 91% of the model of covariance functions for common spatiotemporal data with very small error rates when forecasting.

Universal kriging (UK), the method of spatial or temporal multiple regression, is a model that divides a random function into a linear set of drift and a random element that is the remainder.

Through this research, we recommend using infection disease data and atmospheric gas pollution data and entering three-dimensional data to obtain a proposed mathematical model and other spatiotemporal forecasting methods and linking them to artificial intelligence methods and the fuzzy method.

5. References

[1] Burrough PA, McDonnell RA, Lloyd CD. Principles of geographical information systems. 3rd ed. London, England: Oxford University Press; 2015.

[2] Camana FA, Deutsch CV. Cokriging of Multiple Types of Drill Hole Data. CCG Annual Report. 2020;22.

[3] Caloiero T, Filice E, Coscarelli R, Pellicone G. A homogeneous dataset for rainfall trend analysis in the Calabria region (Southern Italy). Water. 2020;12.(٩)

[4] Cheng, H., Shen, R., Chen, Y., Wan, Q., Shi, T., Wang, J., ... and Li, X. Estimating

[5] heavy metal concentrations in suburban soils with reflectance

[6] spectroscopy. Geoderma. 2019; 336, 59-67.

[7] Chiles JP, Dilfiner P. Geostatistics: modeling spatial uncertainty. Vol. 713. John Wiley and Sons; 2012.

[8] Collins FC, Bolstad PV. A Comparison of Spatial Interpolation Techniques in Temperature Estimation. In: Proceedings of the 3rd International Conference/Workshop on Integrating GIS and Environmental Modeling. Santa Barbara, Santa Fe, NM; Santa Barbara, CA; 1996.

[9] Cseke B, Zammit-Mangion A, Heskes T, Sanguinetti G. Sparse approximate inference for spatio-temporal point process models. Journal of the American Statistical Association. 2016;111(516):1746–63.

[10] Farmer WH. Ordinary kriging as a tool to estimate historical daily streamflow records. Hydrology and Earth System Sciences. 2016;20(7):2721–35.

[11] Goovaerts P. Kriging and semivariogram deconvolution in the presence of irregular geographical units. Mathematical geosciences. 2008;40:101–28.

[12] Huang CL, Wang HW, Hou JL. Estimating spatial distribution of daily snow depth with kriging methods: combination of MODIS snow cover area data and ground-based observations. The Cryosphere Discussions. 2015;9(5):4997–5020.

[13] Journal AG, Huijbregts CJ. Mining Geostatistic. New York: Academic Press; 1978.

[14] Kilibarda M, Hengl T, Heuvelink GBM, Graler B, Pebesma E, Tadic MP, et al. Spatio-temporal interpolation of daily temperatures for global land areas at 1 km resolution. Journal of Geophysical Research: Atmospheres. 2014;119(5):2294–313.

[15] Kerry, R., Goovaerts, P., Rawlins, B. G., and Marchant, B. P. Disaggregation of legacy soil data using area to point kriging for mapping soil organic carbon at the regional scale. Geoderma. 2012;170, 347-358.

[16] Keskin, H., and Grunwald, S. Regression kriging as a workhorse in the digital soil mapper's toolbox. Geoderma. 2018;326, 22-41.

[17] Kumar V. Kriging of groundwater levels, case study. Journal of Spatial Hydrology. 2006;6:81–94.

[18] Tadić JM, Williams IN, Tadić VM, Biraud SC. Towards hyper- Dimensional variography using the product-sum covariance model. Atmosphere. 2019;10.(٣)

[19] Tan K, Ma W, Wu F, Du Q. Random forest-based estimation of heavy metal concentration in agricultural soils with hyperspectral sensor data. Envirosnmental monitoring and assessment. 2019;191:1–14.

[20] Varadhan R. Numerical optimization in R: Beyond optimization. Journal of Statistical Software. 2014;60:1–3.

[21] Wikle, C. K., Zammit-Mangion, A., and Cressie, N. Spatiotemporal statistics with R. CRC Press.2019 .

[22] Yoon SY, Ravulaparthy SK, Goulias KG. Dynamic diurnal social taxonomy of urban environments using data from a geocoded time use activity-travel diary and point-based business establishment inventory. Transportation Research Part A: Policy and Practice. 2014; 68:3–17.

[23] Zammit-Mangion A. FRK: An R package for spatial and spatiotemporal prediction with large datasets. 2017.

Al-Kitab Journal for Pure Sciences (2023); 7(2):115-129.
https://doi.org/10.32441/kjps.07.02.p10

Al-Kitab Journal for Pure Sciences
ISSN: 2617-1260 (print), 2617-8141(online)

https://isnra.net/index.php/kjps

Synthesis, Evaluation of anticancer and antimicrobial activities of some Schiff bases derivatives

Wijdan Amer Ibrahim, Wassan Baqir Ali, Mohammed Alwan Farhan*

Department of Chemistry, College of Science, Diyala University, Diyala, Iraq

*Corresponding Author: mohammed_alwan@uodiyala.edu.iq

Citation: Farhan MA, Ibrahim WA, Ali WB. Synthesis, Evaluation of anticancer and antimicrobial activities of some Schiff bases derivatives. Al-Kitab J. Pure Sci. [Internet]. 2023 Nov. 23 [cited 2023 Nov. 23];7(2):115-29. Available from: https://doi.or g/10.32441/kjps.07.02.p10.

Keywords: Schiff base, tartaric acid, Thio carbohydrazide, and Anti-cancer effects.

Article History

Received	05 Oct. 2023
Accepted	05 Nov. 2023
Available online	23 Nov. 2023

Abstract:

In this research, compound [1,2-Bis-(4-amino-5-mercapto-4H-[1,2,4]triazol-3-yl)-ethane-1,2-diol] was used as the starting material for the synthesis of different Schiff's Bases compounds. The fusion of tartaric acid with Thio carbohydrazide produced the compound (C1), Schiff's bases (C2-C4) were created through the condensation of substances (C1) with different substituted benzaldehydes in the presence of glacial acetic acid as a catalyst. Thin layer chromatography (TLC) was used to confirm the compounds' purity, and spectroscopic methods were used to infer the compounds' structures (FTIR) and magnetic nuclear resonance spectroscopy (1H-NMR and 13C-NMR). The agar well diffusion method was used to test synthesized compounds for their antibacterial activity against K. pneumonia and S. aureus, and the findings were inconsistent. Target substances were tested for their ability to kill human breast cancer at concentrations of 50 and 100 g/mL. Human muscle tissue HC normal cell line, human cervical cancer Hela cell line, and HePG2 cell line. The results showed that the chemicals had potential cytotoxic activity against the Hela cell line, particularly compound (C4), which had the greatest inhibition at doses of 100 mg/mL among the examined substances.

Keywords: Schiff base, tartaric acid, Thio carbohydrazide, and Anti-cancer effects.

تحضير وتقييم الفعالية المضادة للسرطان والمضادة للميكروبات لبعض مشتقات قواعد شيف

وجدان عامر إبراهيم، وسن باقر علي، محمد علوان فرحان*

wijdan.amer84@gmail.com, dr.wassan976@uodiyala.edu.iq , mohammed_alwan@uodiyala.edu.iq

قسم علوم الكيمياء، كلية العلوم، جامعة ديالى، ديالى، العراق

الخلاصة:

في هذا البحث استخدم المركب [١،٢--*BIS-(4-AMINO-5-MERCAPTO-4H-[1,2,4]TRIAZOL-3-YL)-ETHANE-1,2-DIOL*] كمادة يمكن من خلالها البدء بتحضير العديد من قواعد شيف. حضر المركب (*C1*) من خلال صهر حامض الترتريك *TARTARIC ACID* مع ثايوكربوهايدرازايد *THIOCARBOHYDRAZIDE* بينما المركبات (*C2 –C4*) حضرت من تفاعل المركب (*C1*) مع مركبات بنزالدهايد معوضة مختلفة بوجود حامض الخليك الثلجي كعامل مساعد. استخدمت كروموتوغرافيا الطبقة الرقيقة لتأكيد نقاوة المركبات، والطرائق الطيفية مثل مطيافية الأشعة تحت الحمراء (*FTIR*) والرنين النووي المغناطيسي *1H-MAGNETIC NUCLEAR RESONANCE SPECTROSCOPY)* (*NMR AND 13C-NMR*) لتأكيد تراكيب المركبات. استخدمت طريقة الانتشار في الوسط الزرعي لفحص الفعالية المضادة لبكتريا *K. PNEUMONIA AND S. AUREUS* اذ كانت النتائج غير متناسقة. كما استخدمت المركبات في هذا العمل لفحص قابلية قتل سرطان الثدي في خلايا النسيج العضلي المحدد بأنسجة العضلات البشرية ،وسرطان عنق الرحم البشري *HUMAN MUSCLE TISSUE HC NORMAL CELL LINE, HUMAN CERVICAL CANCER HELA CELL LINE, AND HEPG2 CELL LINE* عند تراكيز ٥٠ و١٠٠ ملي غرام / مليلتر. أثبتت هذه المركبات الفعالية الخلوية السمية ضد نوع *HELA CELL LINE* وبالأخص المركب (*C4*) والذي اعطى اعلى تثبيط عند التركيز ١٠٠ ملي غرام / ملليتر مقارنة بالمركبات الأخرى.

الكلمات المفتاحية: قواعد شف، حامض الترترك، ثايوكربوهايدرازايد، مضادات السرطان.

1. Introduction:

Kriging Synthesizing heterocyclic organic compounds is an important class that has been found to have many uses in medicinal chemistry. Most medicinally significant compounds with pharmacological actions ranging from antibacterial to anticancer contain nitrogen atoms in their heterocyclic structures **[1-3]**. An imine distinguishes Schiff bases. (C=N–) bond, commonly known as an azo methine compound, is typically made by easily condensing primary amines with carbonyl compounds, primarily aromatic aldehydes, and ketones. Schiff's bases are a great pharmacophore and are utilized as a starting material for the synthesis of several bioactive heterocyclic compounds. **[4-8]** for anti-inflammatory, anticancer, antibacterial, antifungal, antimalarial, antiviral, and antioxidant, Therapeutics that are cytotoxic, enzyme-inhibitory, and

anti-COVID-19 **[9, 10].** The azomethine group chemical is used as a synthetic intermediary in a variety of organic syntheses, including the preparation of 1,3-oxazepine by tricyclic addition with cyclic anhydride **[11].** The 1,2,4-triazoles and their derivatives are heterocyclic compounds having five members that include two carbon atoms and three nitrogen atoms. **[12].**

The 1,2,4-triazoles have a wide range of pharmacological possibilities, including antibacterial properties. Antifungal, anti-inflammatory, antioxidant, analgesic, and anticancer properties have garnered a great deal of interest during the past two decades, particularly. The biological significance of 1,2,4-triazole has led to the development of several techniques for the synthesis of this scaffold with biological activity **[13- 15]** and 1,2,4-triazoles have a unique position in the fields of medical and pharmaceutical chemistry as well as industrial **[16].**

2. EXPERIMENTAL SECTION:

2.1 Materials

All the chemicals and solvents utilized during the synthesis of the compounds were bought from a variety of different suppliers, including Merck, BDH, Sigma Aldrich, and Fulka They weren't further purified; they were used as obtained. TLC sheets were used to verify the purity of the produced compounds, and FTIR and ^{1}H NMR instruments were used to analyze their chemical structures. The glassware laboratory was used in this investigation as well as the uncorrected Gallen Kamp (MFB-600) melting point apparatus, which was used to determine the melting points of compounds. Compounds' FT-IR spectra were obtained using a KBr Disc and a Perkin Elmer Speactum-65 in the Chemistry Department of Diyala University. TMS was applied as the internal standard for the ^{1}HNMR spectra, and deuterated DMSO was used as a solvent on a Bruker 400 MHz spectrophotometer.

2.2 Procedure:

2.2.1 Synthesis of 1,2-Bis-(4-amino-5-mercapto-4H-[1,2,4]triazol-3-yl)-ethane-1,2-diol (C1)

By mixing tartaric acid (0.003 mol) and Thio carbohydrazide (0.006 mol), which were placed in a round-bottomed flask and heated in an oil bath until the contents of the flask melted, compound (C1) was created **Scheme 1.** When the product was finished cooling, sodium bicarbonate solution was applied to neutralize any carboxylic acid that may have remained unreacted. The product was then recrystallized from (Ethanol/water) to afford the title compounds after being rinsed with water and collected by filtration **[17, 18]. Table 1**. Lists the physical characteristics of the created chemical (C1).

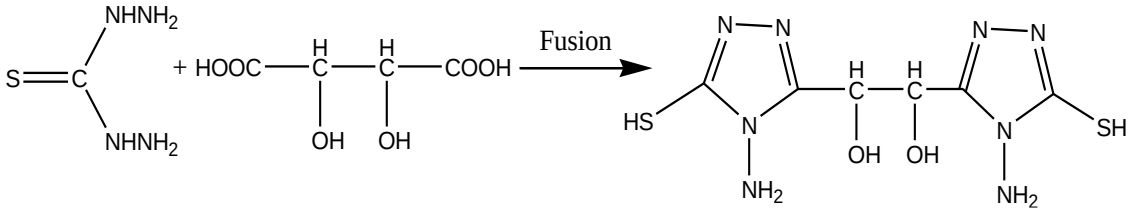

Scheme 1. Synthesis of compound C1

2.2.2 Synthesis of Schiff's bases (C2-C4)

The reaction of compound (C1) (0.01 mol) with several substituted benzaldehydes (0.02 mol) in absolute ethanol and (3–4 drops) of glacial acetic acid was refluxed for 6–8 hours to produce the Schiff bases **Scheme 2.** The precipitate was then cooled, filtered, and cleaned with diethyl ether before being recrystallized with the proper solvent **[19, 20]. Table 1**. Lists the synthetic compound's physicochemical characteristics (C2–C4).

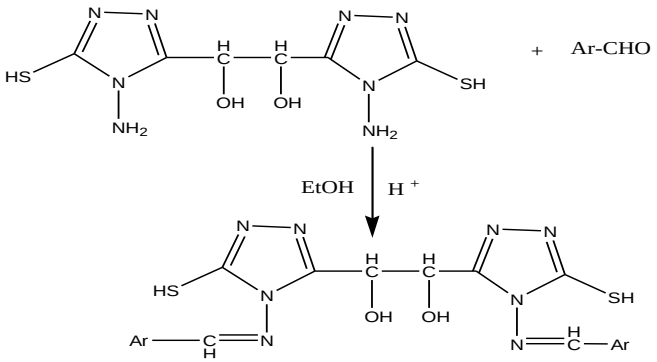

Scheme 2. Synthesis of compounds C2-C4

Ar = 4-dimethyl amino benzene,4-nitrobenzene, 2,4-dichlorobenzene

Table 1: Physical properties of the prepared derivatives (C1-C4)

Compound. No	M.P°C	Yield	Recrystal. solvent
C1	231-233	75%	Ethanol + water
C2	160-162	93%	Ethanol
C3	150-152	91%	Ethanol
C4	189-192	92%	Ethanol

2.3 Biological evaluation

2.3.1 Antimicrobial assay

On blood agar and Mannitol salt agar, Staphylococcus aureus was cultivated and identified. On MacConkey agar and Rosin Methylene blue, an isolated K. pneumonia was grown and identified. Because the Macfarlane turbidity standard provided by the manufacturer (Biomatrix) yields an approximation of 1.5 x 108 cells/ml, it was utilized to calibrate the number of bacterial

cells. The Muller Hinton agar medium was made by dissolving 38 grams in 1L of distilled water, sterilizing it in an autoclave at 121 °C under 15 pounds of pressure for 15 minutes, letting it cool, and then pouring it onto sterile dishes. These dishes were then maintained in the refrigerator until they were needed.

2.3.2 Analysing synthetic chemicals' antibacterial properties using the agar diffusion method.

To prepare the suspended bacteria and place it in tubes with brain heart infusion broth to activate the bacteria, a few bacteria colonies were conveyed via a loop. The tubes were incubated at 37 °C for (18–24) hours. The conventional McFarland solution (1.5 x 108) cells/ml and the bacteria in suspension were compared. After that, the miller hinted that agar-containing plates on which the bacteria suspension had been previously dispersed were left to dry for a time. Using a cork borer that had been sanitized, holes with a diameter of 5 mm were created in the culture medium. By using a micropipette, 100 µl of the substance was added to each hole separately. After that, incubate the dishes for 24 hours at 37 °C. The diameter of the inhibition zone surrounding each hole was measured to gauge the potency of each concentration **[21]**

2.3.3 Cytotoxicity Assay

The following three cell lines were used in this study: cancer of the human breast Human cervical carcinoma and the HePG2 cell line Hela. While the human muscle tissue HC is a normal cell line. These cell lines were acquired from the tissue culture unit at the Al-Mustansirah University in Baghdad, Iraq's Iraqi Centre for Cancer, and Medical Genetics Research (ICC MGR). The evaluation of a compound's solubility before an in vitro cytotoxicity test. The cytotoxicity experiment was performed using the Freshly (2012) technique and the crystal violate stain. To prepare varied concentrations ranging from (50,100) g/mL, the organic compounds were first dissolved in DMSO and then diluted with serum-free media (SFM). The tumour cells were plated in 96-well microplates (1 x 105 cells/mL) and incubated for 24 hours at 37 °C., A fresh serum-free medium (SFM) containing concentrations of each drug was then used to replace the old media. A humidified incubator at 37 °C with (5% CO_2) was used to incubate the plate for 24 hours. Following incubation, 100 mL of crystal violate was added to each well, and they were again incubated for 20 min at 37 °C with the culture medium removed. The following equation was used to compute the inhibition percentage: The following three cell lines were used in this study: cancer of the human breast Human cervical carcinoma and the HePG2 cell line Hela. While the human muscle tissue HC is a normal cell line. These cell lines were acquired from the tissue culture unit at the Al-Mustansirah University in Baghdad, Iraq's Iraqi Centre for Cancer, and Medical Genetics Research (ICC MGR). The evaluation of a

compound's solubility before an in vitro cytotoxicity test. The cytotoxicity experiment was performed using the Freshly (2012) technique **[22]** and the crystal violate stain. To prepare varied concentrations ranging from (50,100) g/mL, the organic compounds were first dissolved in DMSO and then diluted with serum-free media (SFM). The tumour cells were plated in 96-well microplates (1 x 105 cells/mL) and incubated for 24 hours at 37 °C., A fresh serum-free medium (SFM) containing concentrations of each drug was then used to replace the old media. A humidified incubator at 37 °C with (5% CO_2) was used to incubate the plate for 24 hours. Following incubation, 100 mL of crystal violate was added to each well, and they were again incubated for 20 min at 37 °C with the culture medium removed. The following equation was used to compute the inhibition percentage.

Percentage of cell inhibition = (absorbance reading of control cells - absorbance reading of treated cells for each concentration/absorbance reading of control cells) x 100

3. RESULTS AND DISCUSSION:

3.1 Chemistry results

Thio carbohydrazide was converted into 1,2-Bis-(4-amino-5-mercapto-4H- [1,2,4] triazol-3-yl)-ethane-1,2-diol (C1) through the cyclization of tartaric acid. **Scheme 1**. Schiff bases (C2-C4) were prepared by the condensation of compound (C1) with the appropriate aromatic aldehydes as shown in **Scheme 2.** The synthesized compounds' structures were established using ^{1}HNMR and FTIR spectroscopy. The product's TLC in each case revealed the existence of a single spot that was specific to that product.

3.2 FTIR spectroscopy for synthesis compounds [23, 24]

The compound (C1) was identified using FT IR, which displays distinctive bands in the following range. The bands at 3291-3190 cm^{-1}, which might be attributed to asymmetric and symmetric stretching vibration of (NH_2), absorption band at 3300 cm^{-1}, which was attributed to O-H group, 2936 cm^{-1} (C-H aliphatic), and 1617 cm-1 owing to (C= N) of triazole ring. The OH group was responsible for assigning the bands: (3159-33304 cm^{-1}) as the significant diagnostic bands of chemicals (C2-C4) in the FTIR spectra. About (3118-3136 cm^{-1}) is where the C-H aromatic stretching vibration bands of compounds (C2-C4) are found, The C-H aliphatic stretching vibration bands of these compounds at (2947-2955), whereas stretching vibration at 1633-1684 cm^{-1} was due to CH=N (imine), (1613-1628 cm^{-1}) for stretching vibration of C=N (triazole ring) and the disappearance stretching frequency of NH2 at 3291,3190 cm^{-1} is a good indicated to form Schiff bases compounds. Other bands of compound (C2-C4) are shown in **Table 2**.

Table 2: Compounds' FTIR measurements (C1-C4) FTIR spectrum characteristic bands (cm-1)

No	OH	SH	C-H Aromatic	C- H Aliphatic.	C=N	C=C Aromatic	Other
C1	3300	2660	-	2936	1617	-	NH2(3291,3190)
C2	3159	2688	3118	2947	1613	1591-1529	CH=N (1657)
C3	3271	2654	3136	2953	1618	1573-1485	CH=N (1633)
C4	3304	2680	3136	2955	1628	1584-1501	CH=N (1684)

3.3 NMR spectroscopy for the prepared compounds[25, 26]

The ^{1}H-NMR spectra were recorded in DMSO (dimethyl sulfoxide), with chemical shifts given in ppm and TMS (tetramethyl silane) used as the reference. The ^{1}H-NMR data for chemical (C1) revealed two protons of (SH) at 10.25 ppm in a single signal. Four (NH_2) group protons were identified by a singlet signal at 5.52 ppm. Signals that were detected at 5.22 ppm were attributed to protons of (2CH), while those at 4.51 ppm were related to two protons of (2OH), as shown in **Fig. 1.** The ^{1}H NMR data for compound (C2) in **Fig. 2**. Showed that two protons of (SH) were responsible for a single signal at 10.25 ppm. Two protons of the Schiff base group (CH=N) were identified by a singlet signal at 8.67 ppm. A signal that was detected in the range of 7.77 to 6.67 ppm was attributed to the aromatic ring proton. Signals at 5.31 ppm were attributed to protons of (2CH), those at 4.95 ppm to two protons of (2OH), and those at 3.10 ppm to a singlet signal of ($N(CH_3)_2$). While the single signals at 10.22 ppm in the ^{1}H NMR of compound (C3) **Fig. 3.** Were identified as the protons of (2SH). Two protons of the Schiff base group (CH=N) were identified by a singlet signal at 8.60 ppm. A signal that was visible in the range of (8.35-7.71) ppm was attributed to protons from aromatic rings. Protons of (2CH) were attributed to the signals that showed at 5.34 ppm, while two protons (2OH) were allocated to the signals at 4.32 ppm. The ^{1}HNMR results for compound (C4). **Fig. 4.** displays the chemical shifts in ppm: 10.25's, 2H, 2SH), 8.35's,2H,2 N=CH),8.01-7.40'm 6H,Ar),5.20 (d, 2H, 2CH), and 4.00 (d, 2H, 2OH). The ^{13}C NMR spectrum of compound (C1). Shows the following signals of carbon: 165.3, 150.4, 64.3. Whereas the ^{13}C NMR spectrum of compound (C2). Shows the following signals of carbon:166.8, 160.8, 152.3, 110.4 – 149.2, 64.9, and 60.6. The ^{13}C NMR spectrum of compound (C3). Shows the following signals of carbon: 169.2, 160.5, 159.6, 121.9 – 149.7, 64.8. Finally, the ^{13}C NMR spectrum of compound (C4). Shows the following signals of carbon:168.1, 160.7, 155.0, 127.3-149.8, 65.0.

3.4 Antimicrobial activity evaluation

The agar well diffusion method was used on Muller Hinton agar medium to test the antibacterial activity of novel compounds using 10 mg/ml of dimethyl sulfoxide (DMSO) as a

solvent, with McFarland turbidity as a reference solution. The studied drugs' zones of inhibition were measured in millimeters (mm). The results are reported in **Table 3**. According to the screening results, the compounds (C3- C4) have high activity against S. aureus bacteria at a concentration of 300 ppm, whereas compound C1 has no activity at a concentration (100, 200) ppm against both S. aureus and K. pneumonia. In vitro anticancer activity.

Three human cell lines—the human cervical cancer Hela cell line, the human breast cancer HePG2 cell line, and the human—were tested to determine whether each substance had any harmful effects in vitro. The human muscle tissue HC is a normal cell line that was exposed to two different concentrations—50 and 100 g/mL—for 24 hours at 37 degrees Celsius. Results showed that compound (C2) had the highest cytotoxic activity with the lowest inhibition rate (88.70%) at a concentration of 100 g/mL on the HePG2 cell line, compound (C4) had the lowest inhibition rate (76.16%) at the same concentration on the HePG2 cell line, and compound (C3) had the highest inhibition rate (79.67%) at the same concentration on the Hela cell line. While compound (C4) had the highest level of cytotoxicity on the Hela cell line, with an inhibition rate of (89.50%) at a dose of 100 g/mL. The other results are summarized in **Table 4** and **Fig. (9-15)**.

Table 3: The Biological activity compounds (C1-C4)

	S. aureus			*K. pneumonia*		
No	100 ppm	200 ppm	300 ppm	100 ppm	200 ppm	300 ppm
C1	-	-	12 mm	-	-	-
C2	-	11 mm	-	-	-	-
C3	11mm	14 mm	22mm	-	-	12 mm
C4	14 mm	13 mm	17 mm	-	-	12 mm

Table 4: The in vitro cytotoxicity of produced compounds on several cell lines at 50 and 100 g/mL following a 24-hour incubation at 37 °C.

No.	Inhibition ratio100% Normal Cell Line HC Con. µg/mL		Inhibition ratio100% Cell Line cancer HepG2 Con. µg/mL		Inhibition ratio100% Hela cell line Con. µg/mL	
	50	100	50	100	50	100
C1	18.40	19.70	69.47	78.43	78.65	89.48
C2	9.12	11.78	71.13	88.7	81.10	87.34
C3	8.11	13.57	57.45	78.53	67.55	79.67
C4	10.12	16.22	63.67	76.16	78.69	89.50

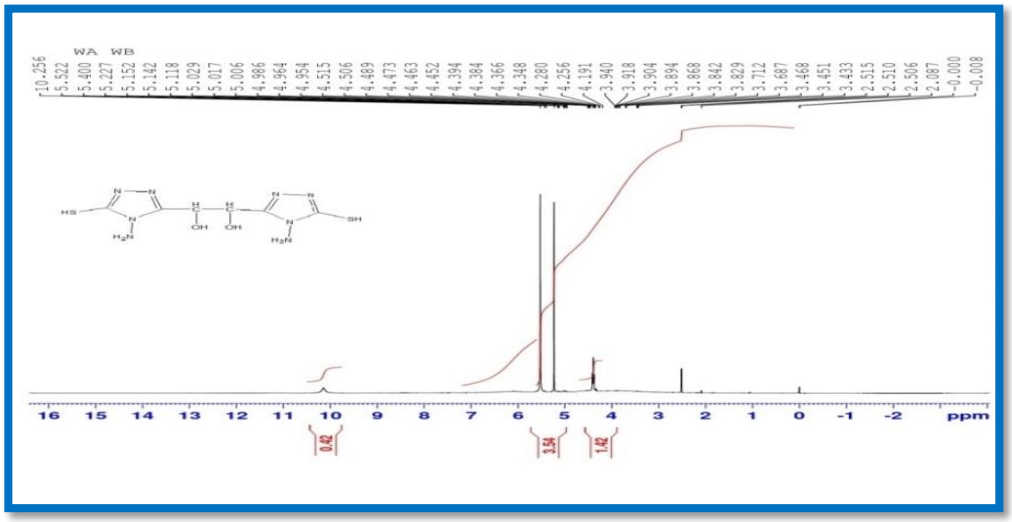

Fig. 1: The ^{1}H-NMR spectrum of the compound (C1).

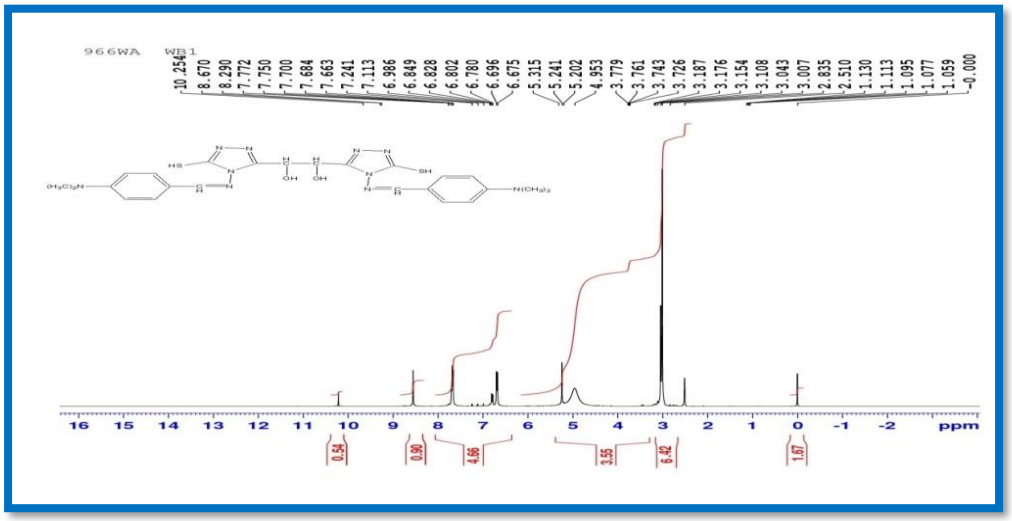

Fig. 2: The ^{1}H-NMR spectrum of the compound (C2).

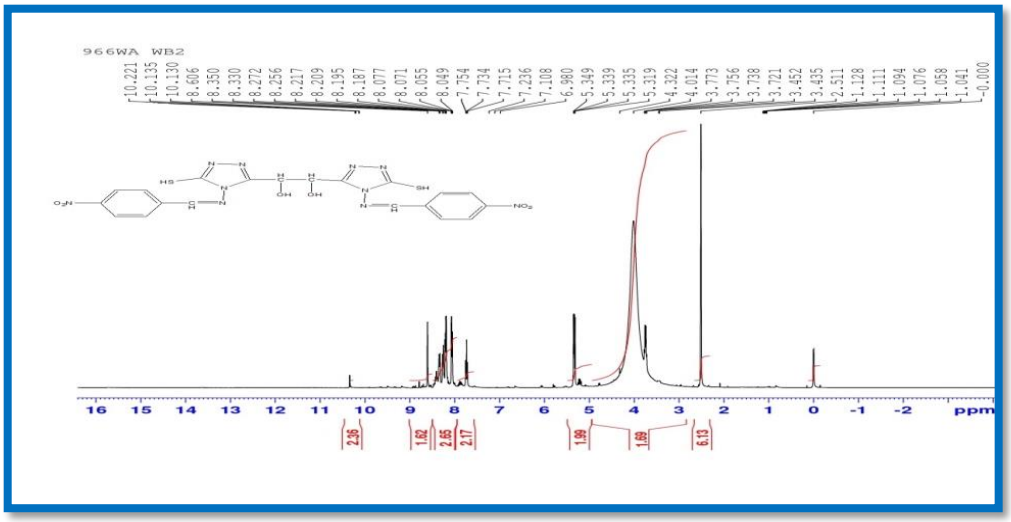

Fig. 3: The ^{1}H-NMR spectrum of the compound (C3).

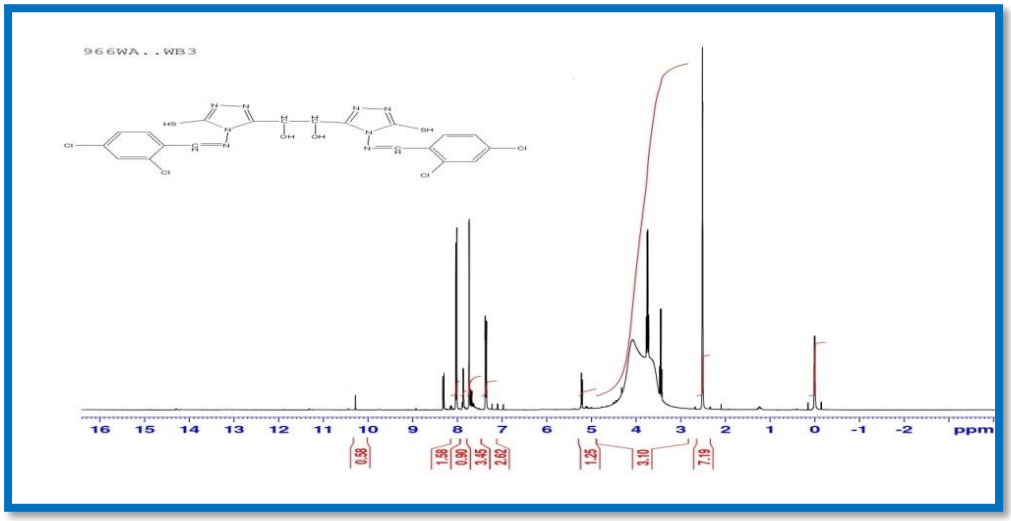

Fig. 4: The ^{1}H-NMR spectrum of the compound (C4).

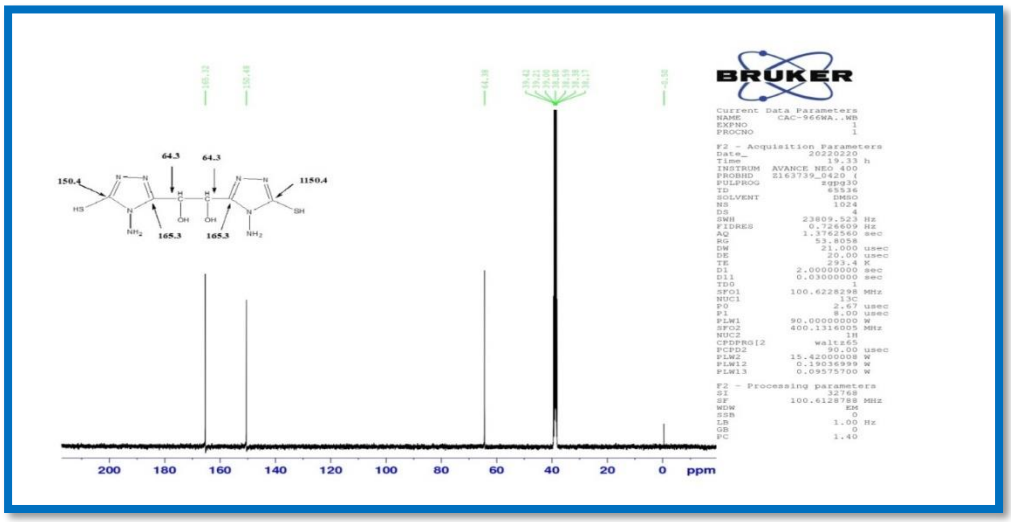

Fig. 5: The ^{13}C-NMR spectrum of the compound (C1).

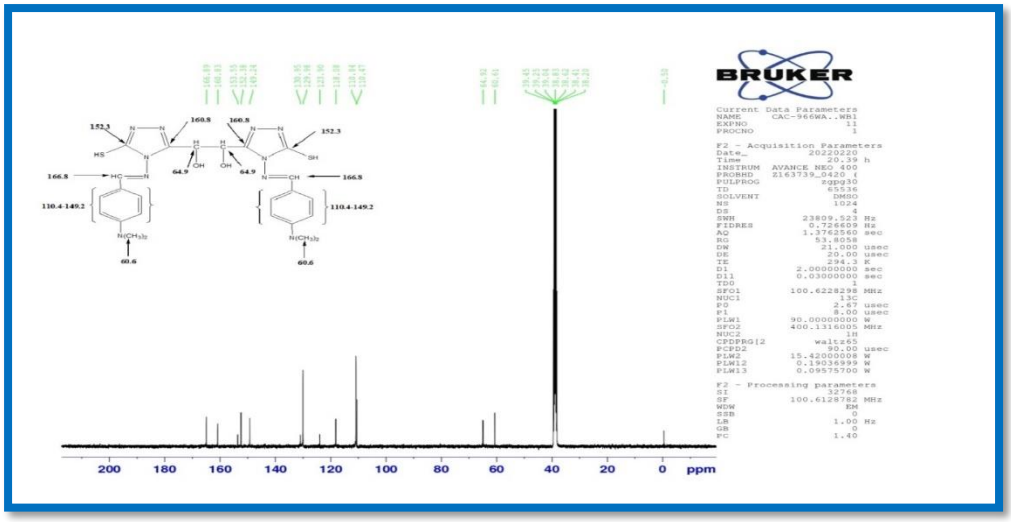

Fig. 6: The ^{13}C-NMR spectrum of the compound (C2).

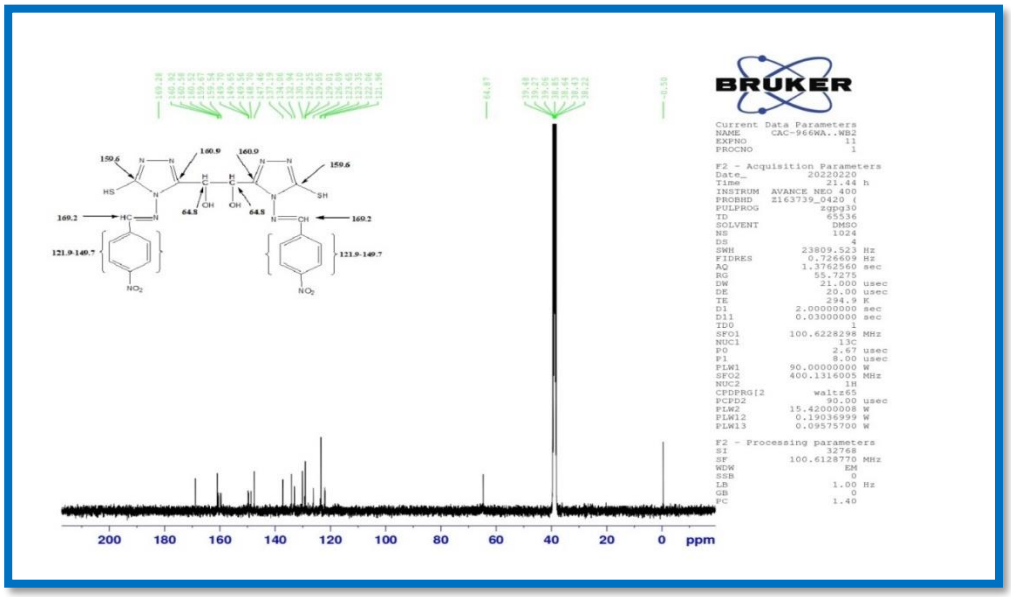

Fig. 7: The ^{13}C-NMR spectrum of the compound (C3).

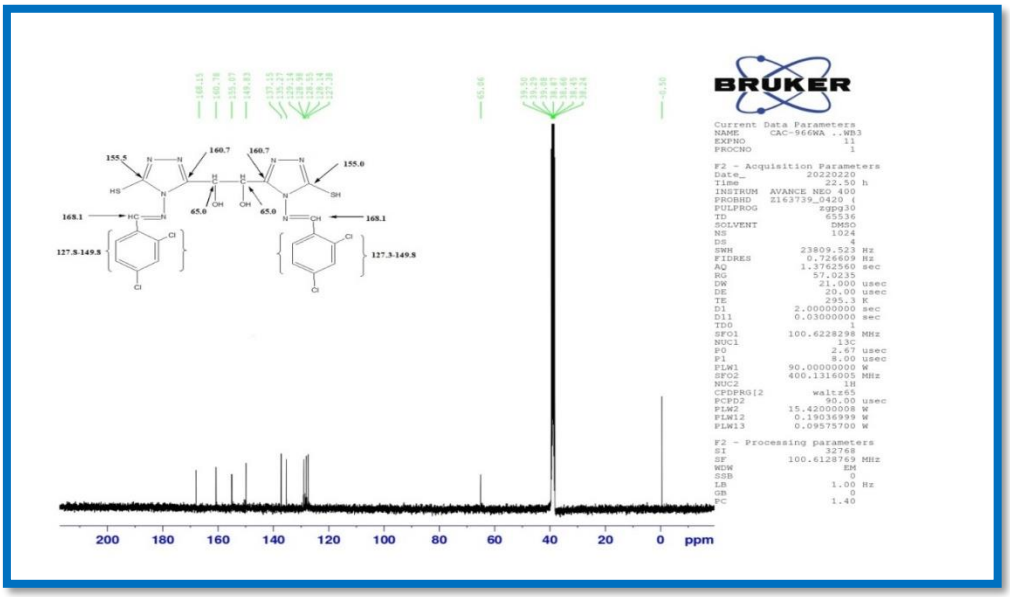

Fig. 8: The ^{13}C-NMR spectrum of the compound (C4).

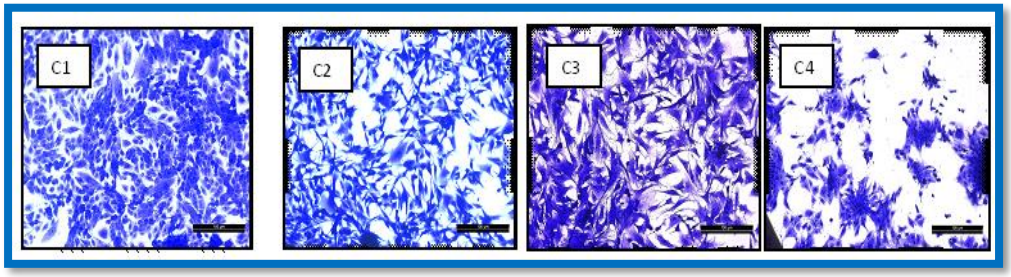

Fig. 9: The Inhibition of cell line (HepG2) by compounds C1-C4 in 50 µg/mL

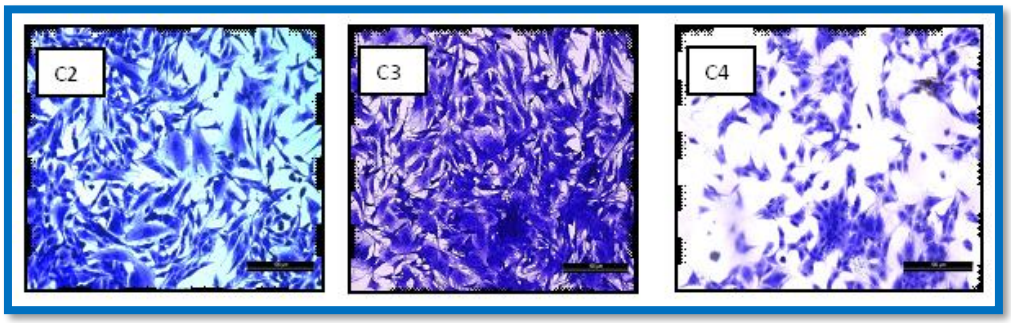

Fig. 10: The Inhibition of cell line (HepG2) by compounds C2-C4 in 100 µg/mL

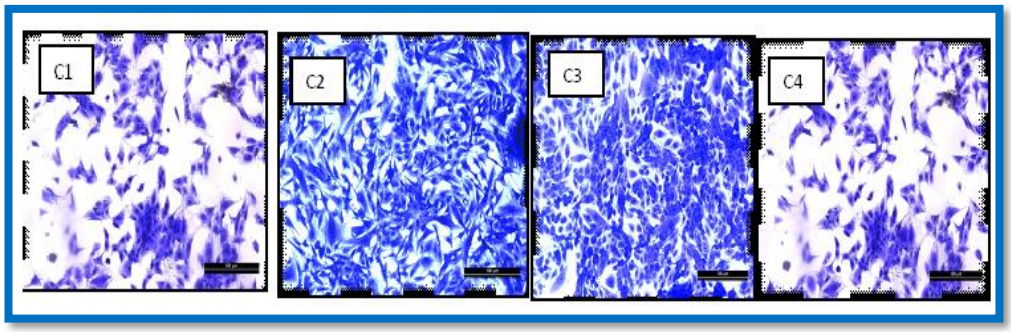

Fig. 11: The Inhibition of cell line (Hela) by compounds C1-C4 in 50 µg/mL

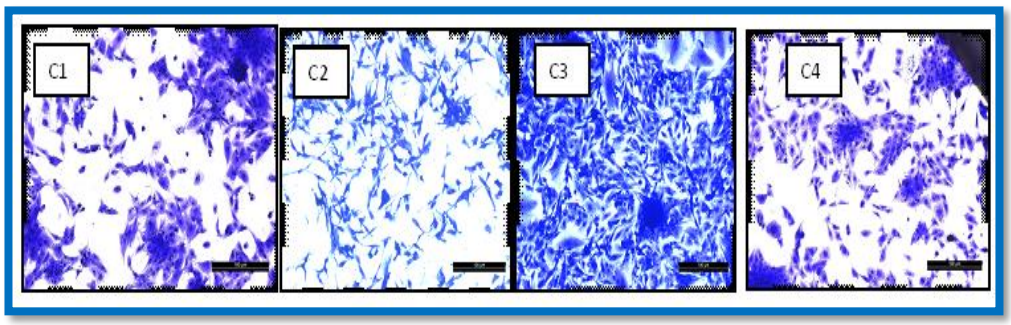

Fig. 12: The Inhibition of cell line (Hela) by compounds C1-C4 in 100 µg/mL

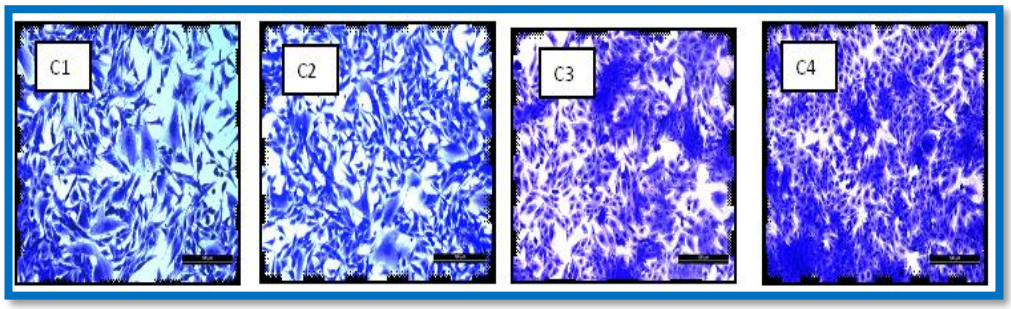

Fig. 13: The Inhibition of Normal cell line (HC) by compounds C1-C4 in 100 µg/mL

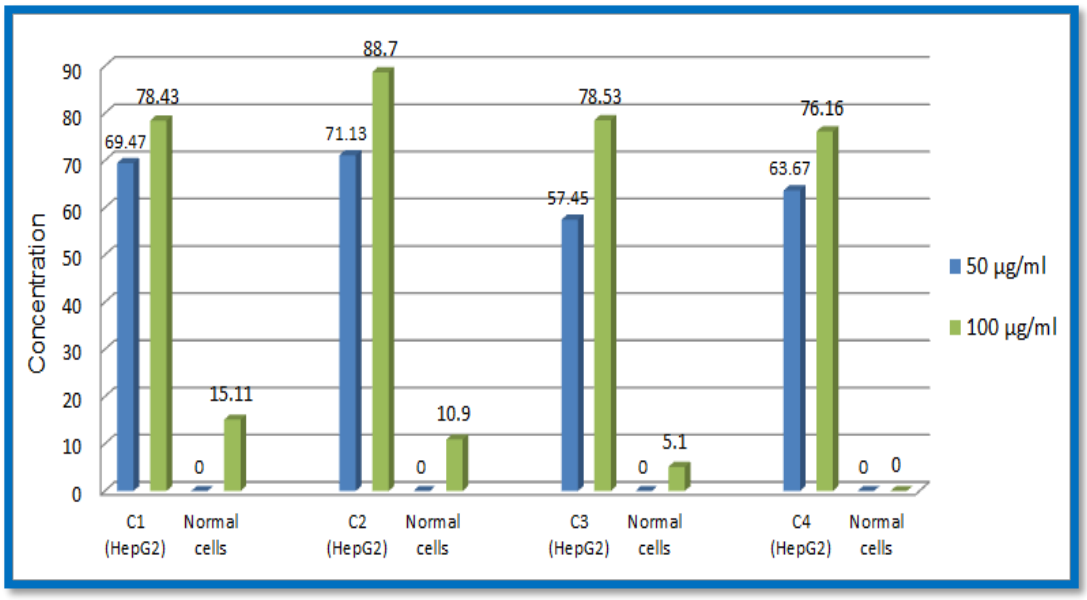

Fig. 14: The HepG2 and HC cell line treated with compounds C1-C4

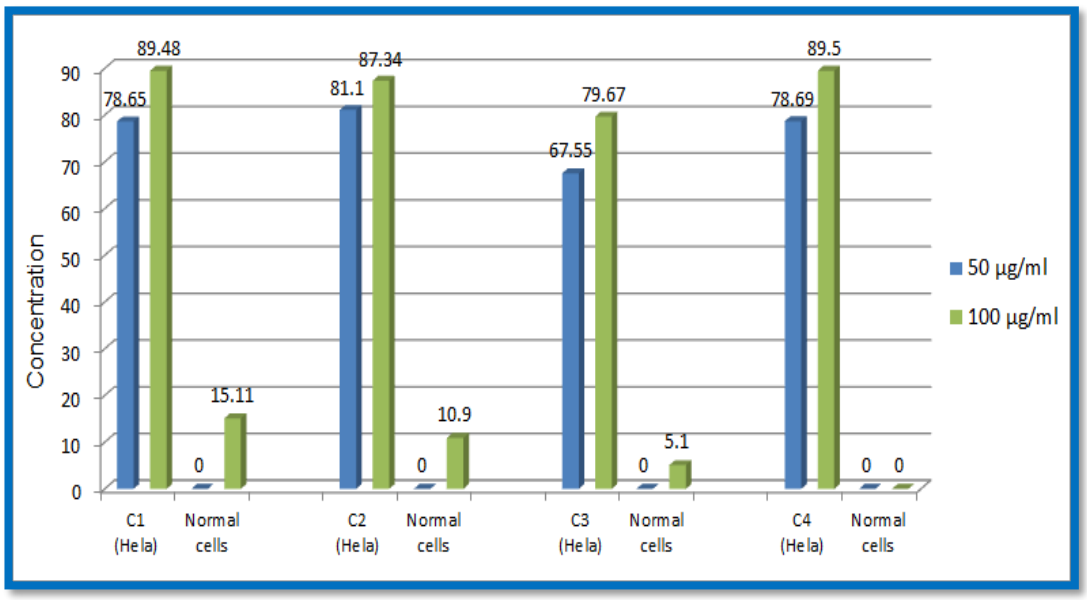

Fig. 15: The Heal and HC cell line treated with compounds C1-C4

4. CONCLUSION

Schiff bases compounds (C1 and C2) were prepared by earlier method describes by Sreenu,p.; et al [17]. while C3 and C4 Schiff bases were synthesized in the present work. Many techniques were used to characterize these new compounds such as FTIR, 1HNMR and 13CNMR. In addition to physical properties. Evaluated the produced compounds' antibacterial properties and found that they had good to acceptable antibacterial activity against the two species of bacteria used—K. Pneumonia, a gram-negative bacterium, and S. aureus, a gram-positive bug. The cytotoxic potential of a few title compounds was also tested against three

human cell lines: breast cancer in humans' cervical cancer in humans, HePG2 cell line Muscle from humans, and Hela cells In two distinct concentrations of 50 and 100 g/mL, the HC cell line is normal. The findings showed that chemical (C4) had the maximum level of cytotoxic action against the Hela cell line at a dose of 100 g/mL, with an inhibition rate of (89.50%).

5. References

[1] Issam AM, Mahmood A, Rabia I, Muhammad AQ, Riaz H. 1,3-oxazepine compounds derived from azomethine: Synthesis, characterization and antibacterial evaluation. Latin American Journal of Pharmacy. 2018 Feb 10;37(3):540–546.

[2] Nagaraju K, Lalitha G, Suresh M, Kranthi KG, Sreekantha BJ. A review on recent advances in nitrogen-containing molecules and their biological applications. Molecules. 2020 Apr 20;25(8):1-42.

[3] Emranul K, Monir U. A review on biological and medicinal impact of heterocyclic compounds. Results in Chemistry. 2022 Oct 26;4(1):1-11.

[4] Ali MA, Tagreed HA, Eid A, Abdel AQ. Synthesis and DFT Study of the Complexation of Schiff Base Derived Curcumin and L-Tyrosine with Al(III), Ag(I), and Pb(II) Metal Ions. Indonesian Journal of chemistry. 2021 Feb 22;21(3):708-724.

[5] Alina S, Alexandra B. Advanced and Biomedical Applications of Schiff-Base Ligands and Their Metal Complexes: A Review. Crystals. 2022 Oct 12;12(10):2-15.

[6] Hadeer MS, Ali TB, Hazim YA. Synthesis and Characterization of ZnO Nanoparticles via Thermal Decomposition for Zn(II) Schiff Base Complex. Indonesian Journal of chemistry. 2022. Jul 20;22(5);1396-1406.

[7] Mohammed AF, Olfat AN, Wassan BA. New photostabilizers for poly (vinyl chloride) derived from heterocyclic compounds. Eurasian Chemical Communication. 2022 Jun 22;4(6):525-543.

[8] Kawther AH, Naser S. Synthesis, Characterization, and Antibacterial Activity of Lanthanide Metal Complexes with Schiff Base Ligand Produced from Reaction of 4,4-Methylene Diantipyrine with Ethylenediamine. Indonesian Journal of chemistry. 2022 Jul 28;22(5):1365-1375.

[9] Ali MH, Ahmed OS, Bassem HH, Ahmed Y, Wael MA, Mohamed FM. Green Synthesis, Characterization, Antimicrobial and Anticancer Screening of New Metal Complexes Incorporating Schiff Base. American Chemical Society Omega. 2022 Sept 1;7(36):32418–32431.

[10] Satheesh CE, Raghavendra KP, Jayanna K, Suchetan PA, Sabine F, Devaraju S. Synthesis, structural characterization, and evaluation of new peptidomimetic Schiff bases as potential antithrombotic agents. Monatshefte fur Chemie. 2022 Jul 14;153(1):635–650.

[11] Ali KN, Sarah AM. Preparation, characterization and biological activity of some new seven-membered heterocyclic compounds. World Journal of Advanced Research and Reviews. 2022 Jul 28;15(1):662-678.

[12] Mukesh K, Sumit T, Balasubramanian N, Kalavathy R, Siong ML, Syed AA, Vasudevan M, Saloni K. Synthesis and biological evaluation of heterocyclic 1,2,4-triazole scaffolds as promising pharmacological agents. BMC Chemistry. 2021 Jan 1;15(1):1–16.

[13] Ali TB, Nada AR, Ahmed HS, Maryam EM, Mohammed IH, László T, Mohammed B. Synthesis, Structural Analysis and Thermal Behavior of New 1,2,4-Triazole Derivative and Its Transition Metal Complexes. Indonesian Journal of chemistry. 2022 Nov 14; 22(1):223-232.

[14] Meinaa JD, Athraa HM. Synthesis, Characterization and Antioxidant Evaluation of Some Tetrazole Derivatives. Indonesian Journal of chemistry. 2022 Oct 1;22(6):1596-1604.

[15] Ashraf AA, Alaa AH, Maysa MM, Stefan B. Chemistry and Biological Activities of 1,2,4-Triazolethiones—Antiviral and Anti-Infective Drugs. Molecules. 2020 Jul 3;25(10:1-54.

[16] Saadon AA, Abbas JA. Synthesis and Characterization of New 1 , 2 , 4- Triazole Derivatives Form 2-Naphthol. Journal of University of Babylon, Pure and Applied Sciences. 2018 Jan 1;26(6):234–252.

[17] Sreenu p, Krishnaiah v, Rajeshkumar k, Lieve N, Sandra L, Rajeswar RV. Bis coumarinyl bis triazolothiadiazinyl ethane derivatives: Synthesis, antiviral activity evaluation, and molecular docking studies. Synthetic Communications. 2018 Jan 1;48(12):1494–1503.

[18] Ashraf AA, Alan BB, Talaatt I, Ashraf MM, Mohamed R. Hydrazinecarbothioamide group in the synthesis of heterocycles. Arkivoc. 2009 Jul 1;(1):150–197.

[19] Moustafa AH, Haggam RA, Younes ME. DOUBLE-HEADED ACYCLO C-NUCLEOSIDE ANALOGUES. Functionalized 1,2-bis-(1,2,4-Triazol-3-yl)ethane-1,2-diol. Nucleosides, Nucleotides and Nucleic Acids. 2005 Jan 7;24(1):1885–1894.

[20] Carlos FGG. Introduction to infrared and raman-based biomedical molecular imaging and comparison with other modalities. Molecules. 2020 Nov 26;25(23):1-23.

[21] Wijdan AI, Mohammed AF, Marwah HA. Synthesis and evaluation of biological activity of some new salicylic acid derivatives. Biochemical and Cellular Archives. 2020 Nov 1;20(9):3727–3732.

[22] Freshney RI. Culture of animal cell. Sixth edition. 5th edition. New York. Wiley liss. 2012.

[23] Robert MS, Francis XW, David jk. Spectrometric identification of organic compounds. 7th ed. state university. new york. john Wiley. 2005.

[24] Mohammed AF, Zahraa S. Al-Garawi, Wassan BA, Olfat AN. A novel method for long-term preserving of urine microstructure using poly(vinyl chloride). Journal of Applied Polymer Science. 2023 Apr 20;140(26):1-9.

[25] Metin B. Basic 1H- and 13C-NMR spectroscopy. First ed. Ankara. Elsevier. 2005.

[26] Mohammed AF, Wassan BA, Olfat AN. Synthesis, Characterization and Biological Activity of Schiff Bases Derived from Heterocyclic Compounds. Teikyo Medical Journal. 2022 Feb 22;45(1):4781-4790.

Al-Kitab Journal for Pure Sciences (2023); 7(2):130-152.
https://doi.org/10.32441/kjps.07.02.p11

Al-Kitab Journal for Pure Sciences
ISSN: 2617-1260 (print), 2617-8141(online)

https://isnra.net/index.php/kjps

Diverse Applications of β-enaminone Ligands and their Metal Complexes: A Review Article

Enass J. Waheed[1], Ali M. Al-khazraji[*1], Awf A. Ahmed[2]

[1]Department of Chemistry, College of Education for Pure Sciences, Ibn -Al-Haitham, University of Baghdad, Adhamiya, Baghdad, Iraq.
[2]Ministry of Education/Directorate of Education, Rusafa First, Baghdad, Iraq

*Corresponding Author: ali.m.ak@ihcoedu.uobaghdad.edu.iq

Citation: Al-khazraji AM, Waheed EJ, Ahmed AA. Diverse Applications of β-enaminone Ligands and their Metal Complexes: A Review Article. Al-Kitab J. Pure Sci. [Internet]. 2023 Nov. 25 [cited 2023 Nov. 25];7(2):130-152. Available from: https://doi.or g/10.32441/kjps.07.02.p11.

Keywords: β-enaminone, diverse applications, complexes.

Article History
Received 10 Oct. 2023
Accepted 05 Nov. 2023
Available online 25 Nov. 2023

Abstract:

As they include both nucleophilic and electrophilic moieties on the same skeleton, enaminones are an important subclass of chemical compounds that contain conjugated NC=C-C=O fragments. These active sites aid in the production of organic molecules containing linear or cyclic heteroatoms. Enaminones and the chemica1 compounds produced from them are both biologically active against the most dangerous bacteria. As a result, they have been utilized as starting materials for the synthesis of anti-inf1ammatory, antibacteria1, anticonvulsant, anticancer, anti-urease, anti-malaria1, optically luminescent, corrosion inhibition, and antitumor agents. Their synthesis has usually a terrific deal of interest and a plethora of synthetic paths have been narrated, including Lewis's acids, P2O5/SiO2, Cu- nanoparticles, and heteropoly acid. Enaminone metal complexes have serval applications in industry and engineering. The definition, significance, and diverse applications of β-enaminone 1igands and their meta1 complexes are presented in this review study.

Keywords: β-enaminone, diverse applications, complexes.

التطبيقات المتنوعة لليكاندات بيتا – ايناميون ومعقداتها الفلزية: مقال مراجعة

إيناس جاسم وحيد[1], علي مضر عبد الكريم*[1], عوف عبد الرحمن احمد[2]

[1]قسم الكيمياء ، كلية التربية للعلوم الصرفة ابن الهيثم ، جامعة بغداد ، بغداد ، العراق.
[2]وازرة التربية، مديرية التربية، الرصافة الأولى، بغداد، العراق.

enass.j.w@ihcoedu.uobaghdad.edu.iq, ali.m.ak@ihcoedu.uobaghdad.edu.iq, awfphd69@gmail.com

الخلاصة:

نظرًا لأن الإيناميونات تشتمل على كل من الجزئين نيوكليوفيلي والكتروفيلي في نفس الهيكل التركيبي، فانها تعد مجموعة فرعية مهمة من المركبات الكيميائية التي تحتوي على أجزاء $NC=C-C=O$ مترافقة. تساعد هذه المواقع النشطة في إنتاج جزيئات عضوية تحوي ذرات مختلفة خطية او حلقية. إن الإيناميونات والمركبات الكيميائية المنتجة منها نشطة بيولوجيًا ضد أخطر أنواع البكتيريا. ونتيجة لذلك، فقد تم استخدامها كمواد أولية لتخليق مضادات الالتهاب، ومضادات البكتيريا، ومضادات الاختلاج، ومضادات السرطان، ومضادات اليورياز، ومضادات الملاريا، والإضاءة البصرية، ومثبطات التآكل، وعوامل مضادة للأورام. لقد حظي تركيبها بقدر كبير من الاهتمام، وقد تم ذكر عدد كبير من دورها في التحضير الصناعي، بما في ذلك أحماض لويس، و$P2O5/SIO2$، والجسيمات النحاسية، وحوامض البوليمرات المتغايرة. تحتوي معقدات بيتا-يناميون الفلزية على تطبيقات مهمة في الصناعة والهندسة أيضاً تم عرض تعريف وأهمية والتطبيقات المتنوعة لليكاندات بيتا-ايناميون ومعقداتها الفلزية في هذه الدراسة المراجعة.

الكلمات المفتاحية: بيتا – إناميون، تطبيقات، معقدات متنوعة.

1. Introduction:

Enaminones are compounds derived from –di-carbonyl compounds with the (N–C=C–C=O) system. Enaminones are a kind of organic chemical that may be easily produced by different processes such as condensation, adjunct, cleavage of hetero-cyclic, and acylation. -enaminon is a chemical that is employed in the production of chemicals, bioactive substances, medicines, anti-tumor, anti-microbial, antiepileptic, and other therapeutic activities. it is also utilized as an intermediate step (medium step) in the synthesis of numerous chemical compounds **[1-4]**. In fact, they are commonly employed as intermediates in the production of key medicinal compounds. Because of their chemical transformations and different chemica1 reactivity due to their electron amusing and electron flawed cores, these intriguing compounds are extremely important. One advantage of compounds with an enaminones organization in their building is that they are extremely steady molecu1es. They are easily created utilizing generally accessible and little-cost starting ingredients. Enaminones are also one of the greatest beginning resources for organic production strategies since they may be made utilizing inexpensive starting ingredients **[5-8]**, **Scheme l**.

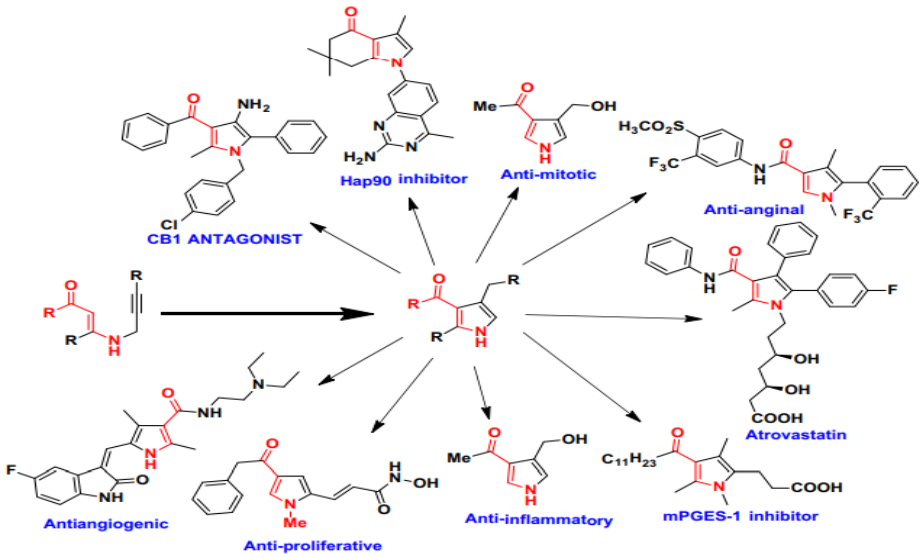

Scheme 1: Examples of bioactive b-enaminones

Enaminones and their complexes have some applications on a variety of grounds. Enaminones have received a lot of attention because of their capacity to system compounds (they are excellent poly-dentate ligands), since following complexation, the effectiveness, and characteristics of β-enaminones are much improved. Enaminone complexes exhibit a diverse range of living functions. A copper-based greenish-yellow comp1ex was produced utilizing a ferroceny1 enaminone, which is an excellent replacement for olefin polymerization catalysts. Zinc and iron enaminone complexes with antibacterial action have also been found. Various enaminone complexes have been found to have fungicidal and bactericidal activity critical to 8 kinds of bacteria and 3 kinds of fungi **[9-12]**. A review of the literature reveals the toxicity possible of the ligand β-enaminone and its CdII complex hostile to MCF7. Compounds of different ions with ligands β-enaminone have also been discovered to have remarkable anti-urease properties. Enaminones have grown in importance because they may be employed as effective chelating ligands for transition metals, and the anions they form are isoelectronic substitutes for cyclopentadieny1-based anions. **[13-16]**

Several techniques aimed at the production of β-enaminones employing Lewis acid reagents, including Bi(TFA), Er(OTf), and Yb(OTf), have been described in the literature. Furthermore, β-enaminones have been produced employing microwave and ultrasonic irradiation. All of these procedures, however, have their own downsides and restrictions, such as lengthier reaction times, the use of costly substances, the usage of hazardous solvents, and the employment of moisture-sensitive Lewis acids. The majority of these approaches relied heavily on secondary amines. In continuation of our ongoing research into novel synthetic methodologies for organic synthesis and the function of transition metal catalysts in such

synthesis, we present here the selective and efficient synthesis of β-enaminones utilizing Cu-nano-particles. Transition metal nanoparticles have been exploited as decent catalysts in a variety of synthesis carbon-based transformations in recent years due to their extraordinary volume ratio to surface area coordination places, which are primarily accountable for their catalyst activity. Copper- nano-particles are less expensive than typical catalysts and insist on just minor reaction settings to produce a high yield in reaction time **[17-20]**.

2. Theory: A literature review of the synthesis of β-enaminone ligands and their metal complexes

Using enaminone-directed Rh(III)-catalyzed CH coupling with alpha-diazo-alpha-phosphono acetate, a C-C de-phosphorylation reaction in the presence of fluoride was explored to form 4- hydroxy -l- naphthoates and (E) - selective alpha, Peta- unsaturated ester could be produced by performing intermolecular C-C coupling of alpha- phosphono acetate and Benz aldehyde **[21]**, **Scheme 2**.

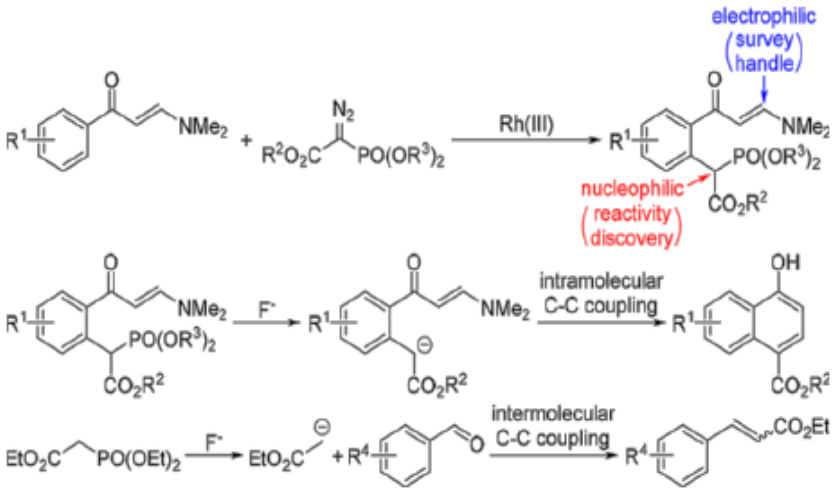

Scheme 2: β-enaminone compounds

Three new ligands for enaminone derived from the chemical compound benzidine were prepared: L_3 (c_1)= (z)-4-((4-amino-[1,1-bi phenyl]-4-yl)amino)pent-3-en-2-one , L_3 (d1)= (z)-5-((4'- amino-[1,1-bi-phenyl]-4-yl)amino)hept-4-en-3-one, and L_3 (e_1)= (z)-3-((4'-amino-[1,1-bi-phenyl]-4-yl)amino)-1-phenylbut-2-en-1-one of the important things that make this special lesson of β-enaminones has many important features and potential tenders that caught the attention of researchers is the bond between the two vinyl clusters in the p-position relative to NH_2 group. Also, the availability of NH_2 group greeneries room for more functionalization of our compounds. The use of a cheap, light, clean, and effective catalyst, which favors the chemistry approach, is one of the greatest significant advantages provided by this method **[22]**, **Scheme 3**.

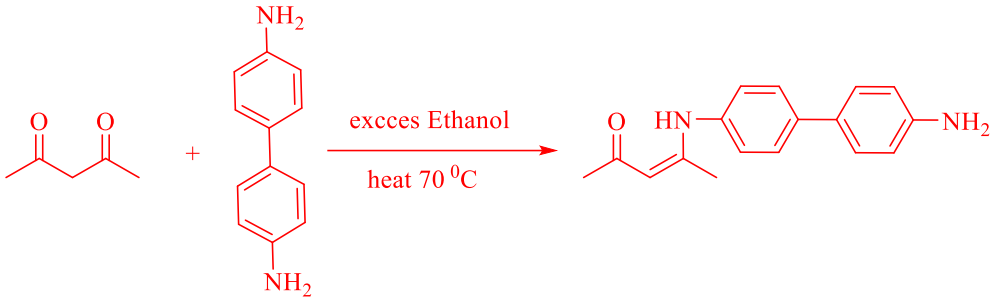

Scheme 3: Structure of L_1

Four enaminone compounds derived from the reaction of 5-formyl barbituric acid and selected specific amines were prepared with high productivity and efficiency. The prepared compounds were characterized by several spectroscopic methods, including FTIR, ^{1}H and ^{13}C NMR, and CHN. There was great agreement between the results obtained and the results mentioned for similar derivatives in the medical literature **[23]**, **Scheme 4**.

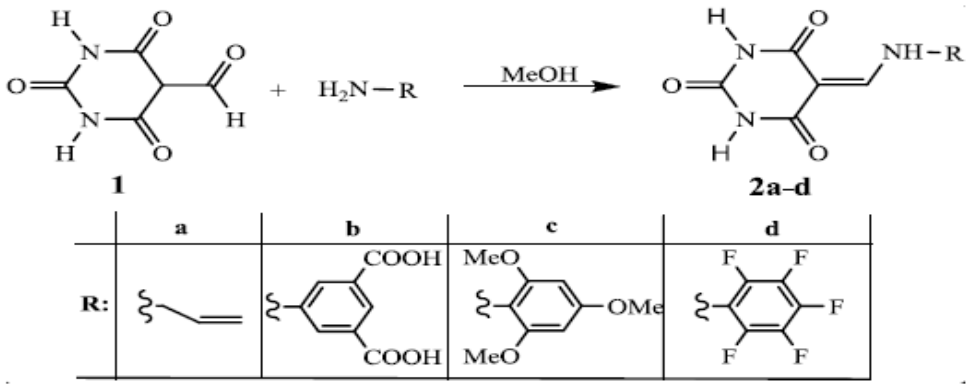

Scheme 4: Synthesis of Enaminone Derivatives

Prepared tetradentate ligands derived from 2 , 20- penaphthol and 2 ,20- diphenol, namely H_2L_1 (1)= 3, 30 - bis [((2,4,6- tri-methyl – phenyl) imino) methyl] - [1, 10] – bi- phenyl -2,20 –diol and H_2L_2 (3)= 3,30 –bis [((2,4,6- tri -methyl phenyl) imino) methyl] - [1, 10] –bi-naphthalenyl -2,20 -diol, which in turn reacted with cobalt acetate tetrahydrate to prepare Co [3,30 – bis - ((R) – imino methyl) - (1, 10) – bi-phenyl -2,20 - dioxo] 2 (2) and Co [3, 30 -bis-((R) – imino methyl) - (1, 10) –bi-naphthalenyl -2, 20 – dioxo]2 (4) (where R= 2, 4, 6-$Me_3C_6H_2$). The prepared compounds were characterized by several spectroscopic methods, including CHN, Mass spectra, FTIR, UV-Vis, magnetic measurement, and single-crystal X-ray diffraction analysis. The presence of tetrahedral structure for both 2 and 4 metal ions was diagnosed by X-ray crystallography. Synthesis of β-enaminone from 1, 3- di-carbonyl compounds and aliphatic amines under ambient conditions using metal complexes 2 and 4 successfully catalyzed the reaction **[24]**, **Scheme 5**.

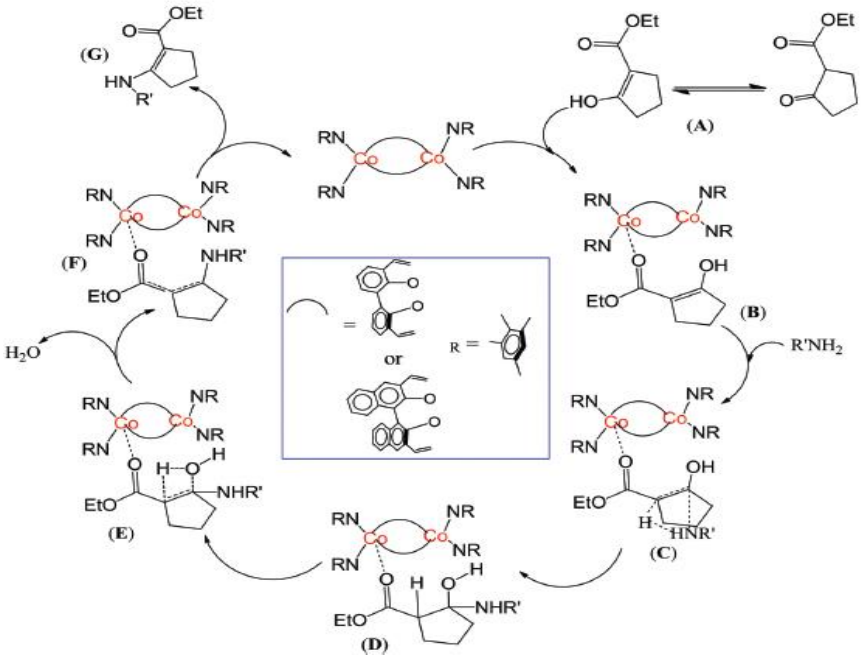

Scheme 5: Synthesis of di-nuclear cobalt complexes (2,4) by β – enaminones.

Three derivatives of trans enaminone, namely (non-brominated (TE), tri-brominated (Br_3-TE), and mono-brominated (Br-TE), were designed and prepared with aggregation-induced emission properties. With different fluorescence properties, two kinds of Br-TE quartzes B &G were obtained and through halogen bond formation their state (solid) fluorescence was improved. The higher products of Br-TE-G are due to stronger multiple intermolecular interactions that may restrict molecular movements, causing a lower decay rate (enhanced radioactive and non-radioactive), in addition to halogen bond interactions, and this was concluded through theoretical calculations and careful examination of single crystal data. To control the state (solid) production goods of luminous resources, specifically fluorescent resources, halogen bonding is rarely relied upon, which represents the interaction between molecules **[25]**, **Scheme 6**.

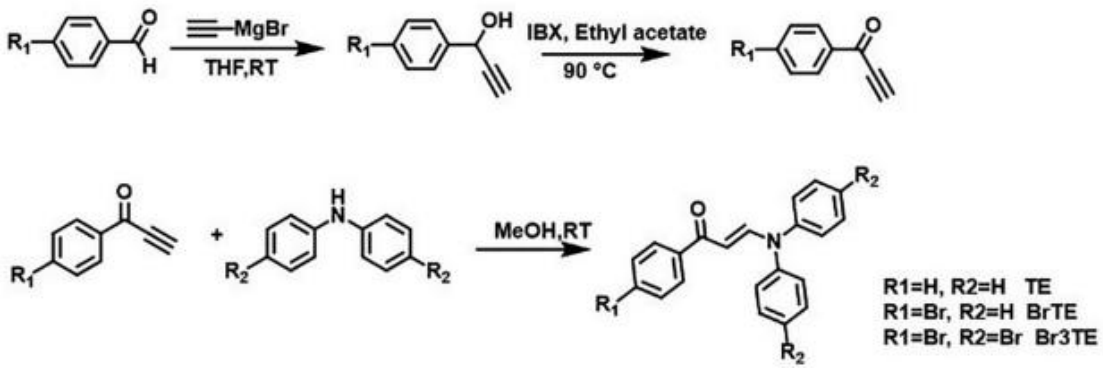

Scheme 6: Preparation of trans enaminone derivatives (TE, Br_3-TE and Br-TE)

In recent decades, there has been a surge in the chemistry of heterocycles. This has resulted in an astounding number of molecules with at least one heterocyc1e in their structure. In fact, more than two-thirds of the 65 million chemical molecules comprise a heterocyclic structure. Heterocycles are significant not only for their richness and exceptional diversity, but also for their biologica1, medica1 (vitamins, hormones, antibiotics, etc.), industria1, and technica1 applications (corrosion inhibitors, dyes, stabilizers, pesticides, herbicides, etc.). Many natural substances of plants, animals, or synthetic origin have nitrogenous structures among the many families of heterocyclic compounds. The pyrazo1o-enaminones are among them **[26]**, **Scheme 7**.

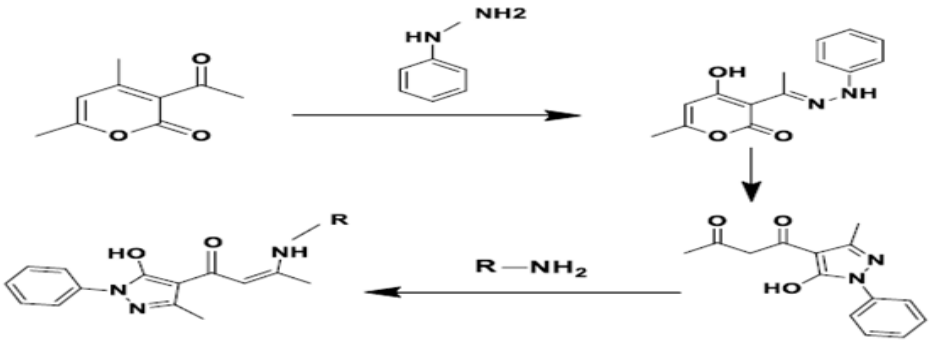

Scheme 7: Synthesis of pyrazole-enaminones

β-Enaminone compounds were prepared through a new one-pot procedure in the presence of the Pd-DNA catalyst, with the use of amino sources (NPr_3, NEt_3, and NBu_3). The method comprises sequential Sonogashira carbonyl coupling of a terminal alkyne to an aryl iodide and oxidative dealkylation of the tertiary amines. The catalyst was used in many subsequent tests with the same results after it was successfully recovered. On the basis of the activity of palladium nanoparticles, the reaction mechanism was proposed **[27]**, **Scheme 8**.

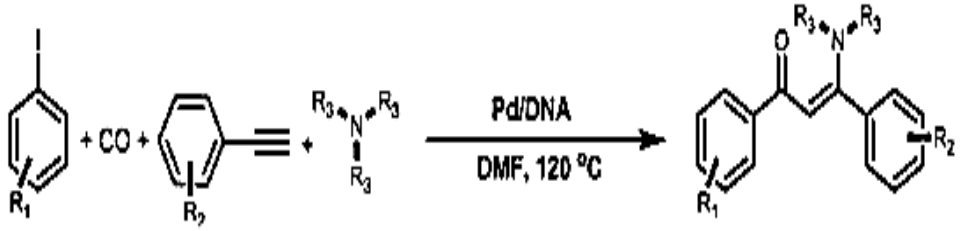

Scheme 8: Preparation of β-enaminone in the presence of palladium catalyst

By aza-Michael addition of aminoalkyl-, thio-aniline, and phenol- with ynones under metal-free conditions with high efficiency and chemical selectivity, the selective chemical preparation of β-enaminones was achieved with a yield of up to 99% in 31 examples. From β-enaminone, the novel dual-1,5-di-substituted tri-azole scaffold was prepared subsequently **[28]**, **Scheme 9**.

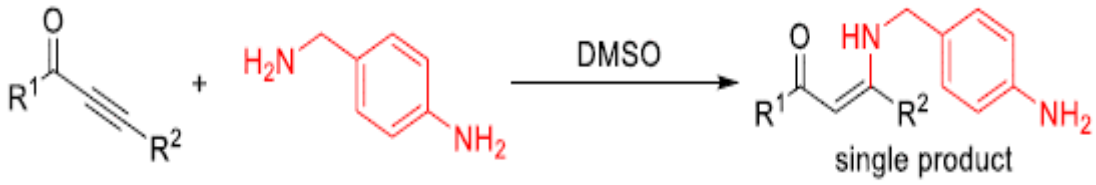

Scheme 9: Synthesis of β-enaminones

Relying on enaminone or 1,2-benzenediamine and on (S)-quinenamine as a chiral tertiary amine (as a hydrogen bond donor), twenty-four new organocatalysts were prepared. By transferring (S)-quininamine (9 examples) with the amination of N, N-dimethylanaminone, anemone-type catalysts were prepared., whereas the l,2-benzenediamine-type catalysts were created in three stages using (S)-quininamine and ortho-fluoronitrobenzene derivatives. Their interest in the Michae1 buildup of acetylacetone to trans nitro styrene seemed hazy. Up to 72 percent of enantioselectivities were reported **[29]**, **Fig. l**.

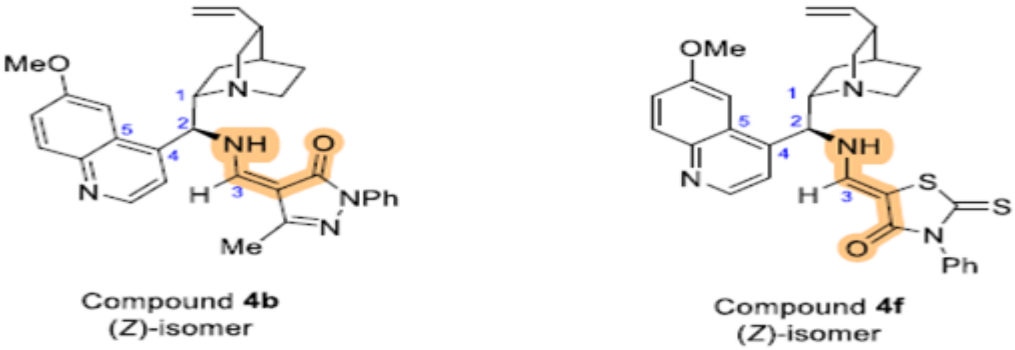

Fig. 1: Molecular structures of enaminones 4b (left) and 4f (right)

A transition-meta1-free technique for constructing 3-sub-stituted or 3,4-di-substituted quinolinyl from widely accessible N, N - di-methyl enaminones and o-amino benzyl alcohols is described. The explicit oxidant cyclol condensation route stands a comprehensive range of functional groups, admitting for the capable preparation of different quinolinyl in reasonable to appropriate product. During the oxidative cyclization route, a C(sp^3) - O bond cleavage, a C= N bind, and a C=C bond creation arise, and a mechanism has been postulated. Finally, we established an effortless technique for the preparation of 3- substituted or 3,4- di-substituted quinolines with adequate to good products utilizing wide accessible N, N- di-methy1 enaminones, and o-aminobenzy1 alcohols supported by Ts OH /$K_2S_2O_8$. This direct oxidative cyclocondensation route improved the approach for synthesizing quinolines from o-aminobenzy1 alcohols **[30]**, **Scheme 10**.

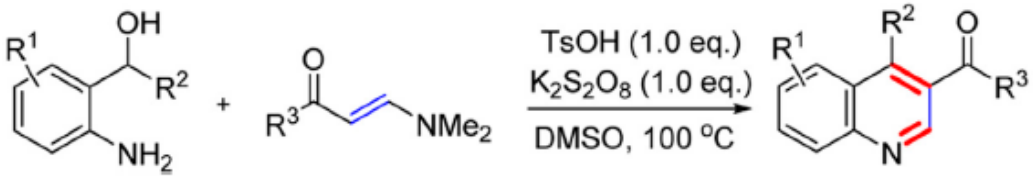

Scheme 10: Synthesis of quino1ines from β-enaminones

This research involves synthesizing one ligand and then complicating it with meta1s. The ligand (L_3) was created by combining the ligand (L_1) with 3-aminopheno1, rubbing it, and then melting it. Complexes of cobalt, nickel, copper, zinc, and cadmium ions with (L3) and 3-aminophenol were prepared by reacting meta1 salts with (L_3) and 3-aminophenol in ethanol. Physical and spectroscopic techniques of the fashioned ligands and complexes, such as electrical conductivity, magnetic sensitivity, melting points, UV-Vis spectrum, infrared (FTIR), and nuclear magnetic resonance spectra of the proton and carbon ($_1$HNMR), were used to establish the structures' validity (^{13}C-NMR) **[31]**, **Scheme 11**.

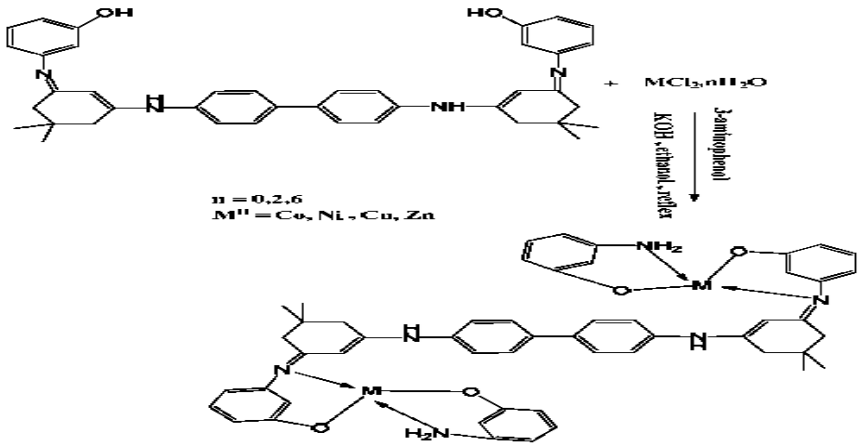

Scheme 11: Preparation of mixed 1igand (L^3) complexes

The aza-Michae1 additive and intramolecu1ar annu1ation of enaminones with anthranilic has been established as a ion - technology for the preparation of 3-acyl quinolones. Methanesulfonic acid (MSA) and sodium iodide (Sodium iodide) are also important components of the process. This ring-opening/reconstruction process is easy to use, wide substrate range, offers high products, and is very efficient. Finally, under transition metal ion-free conditions, a gentle and efficient mechanism for the preparation of a wide range of 3-acyl quinolines has been developed. By intra-molecular annulation and aza-Michael addition, the process made effective use of a range of enaminones and anthranils, giving a series of 3-acyl quinolines. Investigations of the mechanism indicated that there was no radical step in the pathway. It was noted that MSA and NaI were critical to the success of the transformation **[32]**, **Scheme l2**.

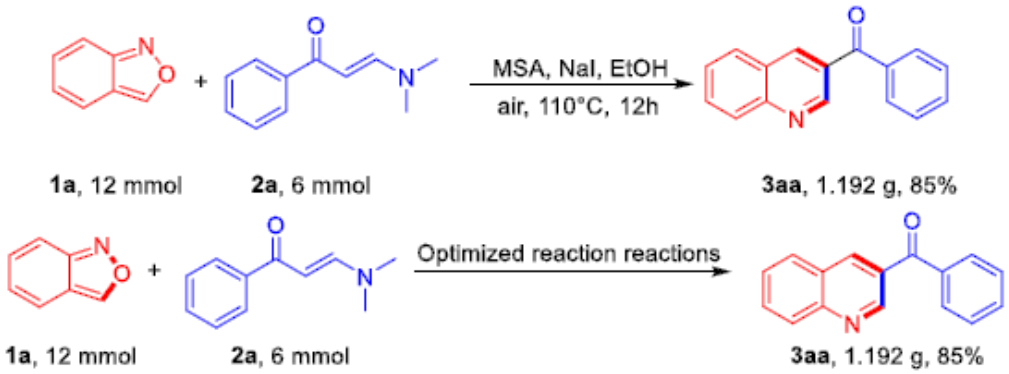

Scheme 12: Gram-scale reaction

Via Ru $^{(III)}$ - catalyzed C–H bond stimulation and successive intra-molecular C–C cyclization of β-enaminones and 1, 3 -di-carbonyl products, iso-coumarins were prepared. With a wide range of materials with high functional mass tolerance, selective cleavage of the enaminone C-C bond, and mild reaction conditions the synthetic protocol has been characterized. By reacting with $PhI(OAc)_2$, 1,3 –di-carbonyl products can generate in situ iodinium as a carbene precursor for the preparation of multi-cyclic scaffolds where bioactive skeletons and synthetic precursors have been prepared useful as an application of this method **[33]**, **Scheme l3**.

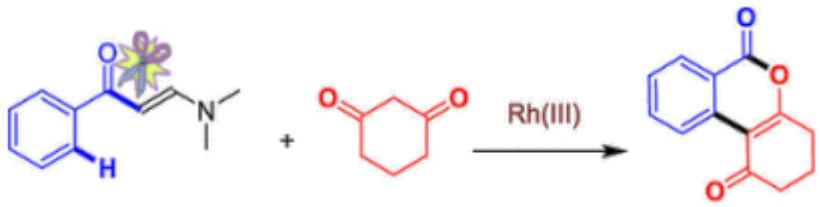

Scheme 13: Synthesis of isocoumarins

Complexes (Mix ligand) formula [(M)(L_1)(8.h.q)] were prepared where (L_1) represents a new ligand of β-enaminone and (8. h.q) represents (8-hydroxyquinoline) and (M) represents the ions of the following transition elements [Ni (II), Cu (II), Co (II), Zn (II) and Cd (II)]. The prepared products were diagnosed by various Devices, including; FT/IR, ^{1}H/ ^{13}C NMR, Uv/Vis, and CHNS, and through the results of the measurements, it was concluded that the ligand binds with metal ions by O and N atoms outside the ring, that is, it behaves like a bi-dentate ligand **[34] , Fig. 2.**

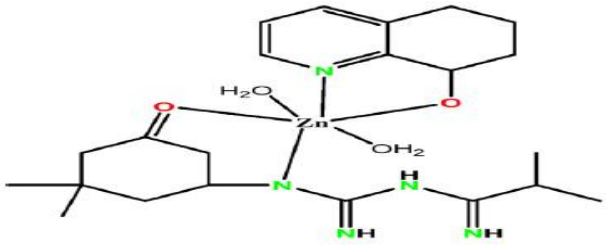

Fig. 2: Structure of Zn complex

3. Diverse applications of β-enaminone ligands and their metal complexes

3.1. Anti-cancer activity and docking studies.

Green chemistry and a stereospecific synthesis route were used to create (Z) - enaminones (amide substituted) as potential Pl_3K inhibitors and breast cancer medicines. Competitive EL1SA was used to evaluate Pl_3K inhibition. The anticancer potentia1 was evaluated using a panel of cancer cell lines including MCF-7 (breast cancer), G-36l (skin cancer), and HCT ll6 (colon cancer). In the Pl_3K experiment, 2(c and f) were indifferent to the suggested inhibitory activity, as shown by the obtained IC_{50} (>1.0 M). The $1C_{50}$ range (0.05 M) revealed that compounds 2a, 2b, and 2d have excellent activity potential, but compounds 2e and 2i have a moderate action potential $1C_{50}$ (0.l and 0.25) respectively. The docking study suggested that the hydrophobic interactions in the Pl3K binding small were completely overpowered by the binding attraction of the extremely powerful ligands (2a, 2d, and 2b: Ki = l8.l6, 56.l4 and 84.87 nM, respectively). The antipro1iferative activity dominance of chosen complexes (2a, 2b, and 2d) against MCF-7 was indicated by MTT test findings. The comparative activity of 2a, 2b, and 2d were equivalent to those of the standard, doxorubicin, at 84.56, 80.87, and 90.l2 percent, respectively (82.l6 percent). SAR tests revealed that (Z) - enaminones (amide substituted) are effective inhibitors of PI_3K for the treatment of breast cancer **[35]**, **Fig. 3**.

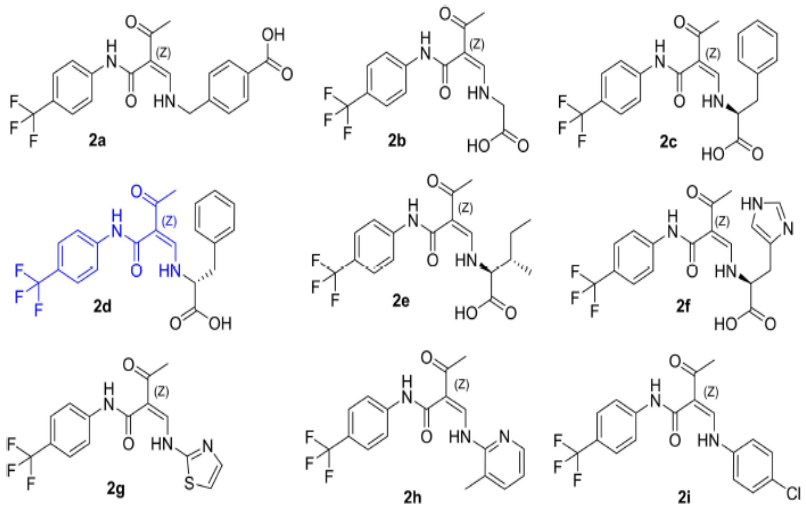

Fig. 3: The structure of (Z) - enaminones (amide substituted)

The two compounds novel enaminone (PFA) and Cadmium complex (PFA-Cd), were prepared and the results of the measurements were very consistent with their composition through their diagnosis with various devices: FT-IR, UV-Vis, ICP/AES, TGA, ^{13}C,^{1}H/NMR and MS. In addition, the ligand and its complex were examined to determine their toxicity against (MCF-7). As an anti-cancer agent compared to PFA-Cd, it was found that PFA was

more active. To find the dominant binding pattern of the synthesized compound in the vicinity of the DNA double helix structure, molecular docking studies were performed. By calculating its toxicity to (MCF-7), the anticancer potential of the new enaminone and its cadmium compound was estimated **[36]**, **Fig. 4**.

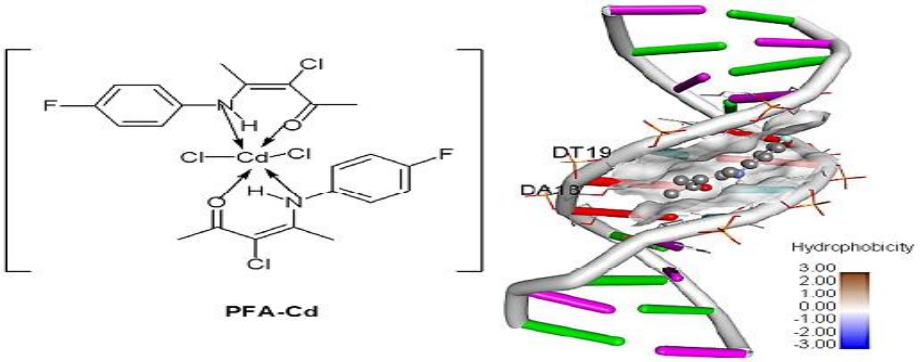

Fig. 4: synthesis of the Enaminone complex PFA-Cd

Metal complexes were prepared through the interaction of the new ligand [3- chloro -4- ((4-methoxy phenyl) amino) pent -3- en -2- one (PA)] with metal ions Co (II), Cd(II) and Mo(0), which were diagnosis by various devices such as ^{1}H, ^{13}C / NMR, UV/Vis, FAB-MS, TGA, ICP-OES and FTIR. The ligand binds to metal ions through the N atom of the NH_2 group and O of the CO group, i.e., it behaves like a bi-dentate. Tests of cytotoxic and urease inhibition activities were also conducted for the prepared compounds, where the metal complexes showed an octahedral geometric shape. The Co (II) compound (PA-Co) is additionally important compared drug thiourea as a reference, as the results of the studies showed. When studying the cobalt complex on MCF-7, Toxicity analysis showed that the compound has a higher toxicity result than the enaminone compound and the other complexes. To find out the putative binding mode within the target protein, molecular docking simulations were performed **[37]**, **Fig. 5**.

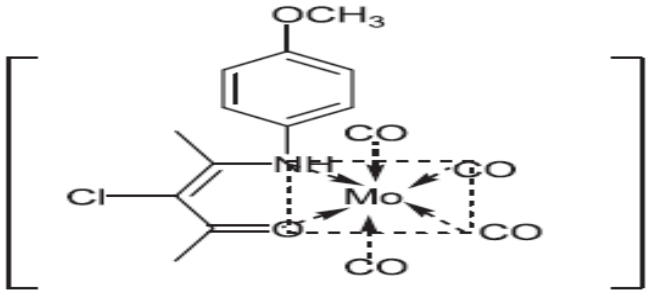

Fig. 5: Synthesis of Metal Complexes

The amount of education investigating the anti-cancer actions of (NPEs) N – propargylic-peta-enaminones is incomplete despite enaminone being a significant structural metal created in a change of pharmacologically active compounds. On human breast cancer cells the cytotoxic

and apoptotic properties of twenty-three diverse NPEs were studied. By MTT assay, cytotoxicity was measured, and by flow cytometry, cell cycle distributions and apoptosis were studied. It showed positive deliveries in cancer cell (breast) identified by ADME and NPEs analysis which means low unfractionated values, good lipophilicity values and high bioavailability **[38]**, **Fig. 6**.

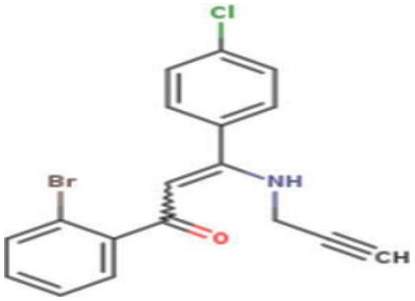

Fig. 6: Strucure of β-enaminones (NPEs 9)

3.2. Anti-urease activity

New ligands (enaminone) were synthesized: (Ac-PCA)= 3-chloro-4-(4-chloro phenyl) aminopent – 3 - en- 2 - one and (Ac-BA)= 4- (benzyl amino) -3- chloro pent – 3 - en- 2 - one with Cu (II), Co (II) and Cd (II) complexes. The antiacetylcholinesterase (AChE) and anti-urease actions of these recently synthesized compounds were explored further. The (Ac - BA) - Cu(II) complex was effective against AChE, but the $(Ac - BA)_2$ - Co(II) complex was effective towards urease. The compounds had slight or no enzyme inhibitory action. To assess their likely binding mechanism, the chemica1s were docked into acety1cho1inesterase enzymes **[39]**, **Fig. 7**.

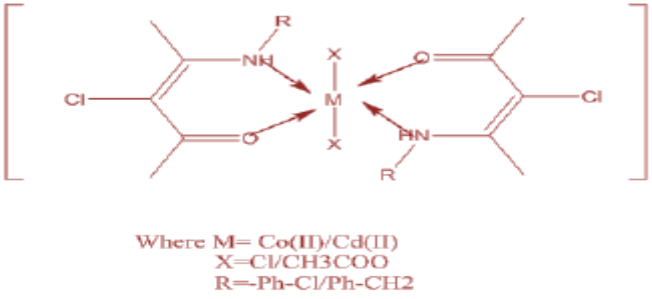

Fig. 7: Proposed structure of 6-coordinated enaminone complexes

3.3. Antimicrobial activity

The compound enaminone 2, (E)-3-(dimethylamino)-l-(8-phenyl-8H-[l,2,4]triazo1o **[4, 3-a]** pyrimidine-10-y1) prop -2- en-l-one was synthesized, and reactions of enaminone 2 with various kinds of hydrazine hydrate or hydrazonoyl chlorides yielded new substituted pyrazoles. Enaminone was also reacted with 6- amino-2- thioxo pyrimidin -4- one to create 2-thioxo pyrido

pyrimidinone derivative. Pyridotriazolopyrimidines are formed when the 1atter thione derivative combines with hydrazonoy1 ch1orides. The reaction of enaminone 2 with hydroxylamine yielded 5-(8-Pheny1-8*H*-[l,2,4]triazo1o[4,3-a]perimidin-10-yl) isoxaz ole. The structure of the new perimidine-derivatives was validated using spectroscopic and CHNS. The anti-bacterial activity of enaminone and freshly synthesized compounds was examined, and the findings indicated that certain derivatives are more effective than the reference medications uti1ized **[40]**, **Scheme l4**.

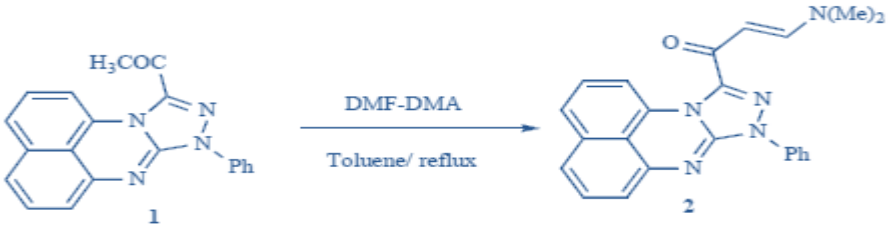

Scheme 14: Synthesis of enaminone 2

Several pyrazoles generated from alternative enaminones were synthesized and tested for antibacterial activity. The antibacterial effectiveness of the produced compounds was originally tested against ATCC- 6538, NCTC- 10418, NCTC- 10400 and ATCC- 27853. Compounds (P1, P11 and P6) showed considerable antibacteria1 activity in the disc diffusion experiment during first screening. These compounds were tested for anti-bacterial effectiveness at various time periods and offered considerable action for 6 hrs. Gram-positive bacteria were found to have higher +e activity. At 24 hrs., however, the activity was only identified against (G+) bacteria, except (P11), which demonstrated antibacterial effectiveness towards kinds of bacteria. P11 had the greatest antibacteria1 efficacy alongside both (G+) and (G-) bacteria **[41]**, **Scheme 15**.

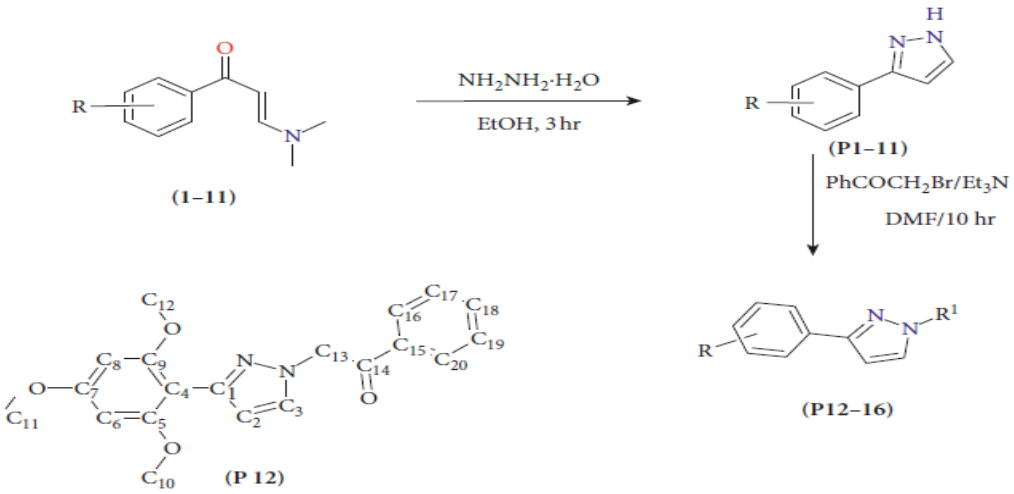

Scheme 15: Synthesis of products (P1–P16)

Complexes (mixed ligand) [M(L_1)(Q)] and [M(L_1)(Q)Cl_2] were prepared where (L_1) represents a new ligand of β-enaminone and (Q) represents (8-Hydroxyquinoline) and (M) represents the ions of the following transition elements; Ni (II), Co (II), Pt (IIII), Cd (II) and Pd (II). The prepared products were diagnosed by various devices, including FT / IR, (^{1}H / ^{13}C NMR, UV / Vis, and CHNS), and through the results of the measurements, it was concluded that the complexes octahedral geometry except Pd (II) complex was square planar. The effectiveness of the prepared compounds was studied against specific types of microorganisms, such as Escherichia coli, Staphylococcus aureus, and Candida albicans, where the complexes showed higher effectiveness than the prepared ligand **[42]**, **Scheme l6**.

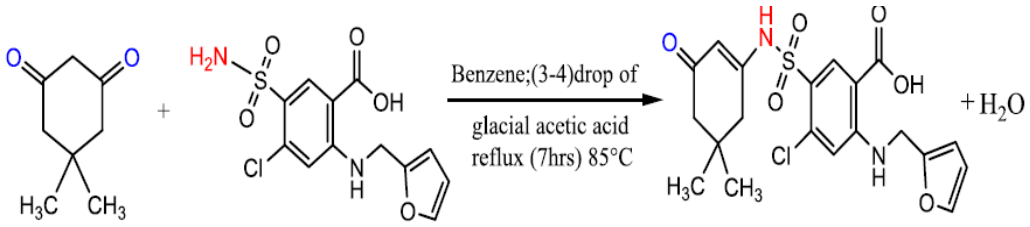

Scheme 16: Synthetic route for the ligand [H_2L_1]

Complexes (mixed ligand) [(M)(L_1)(3ph)] were prepared where (L_1) represents a new ligand of β-enaminone and (3ph) represents (3-amino phenol) and (M) represents the ions of the following transition elements [Co (II), Ni (II), Cu (II), Zn (II), and Cd (II)]. The prepared compounds were characterized by various devices, including (FT/IR, ^{1}H / ^{13}C NMR, Uv / Vis and CHNS), and through the results of the measurements, it was concluded that the ligand binds to the metal ions through the oxygen and nitrogen atoms, that is, it behaves like a tetra-dentate ligand. The prepared compounds were compared with the antibiotic ciprofloxacin after their effectiveness towards microorganisms, as the biological activity of these compounds was good **[43]**, **Fig. 8**.

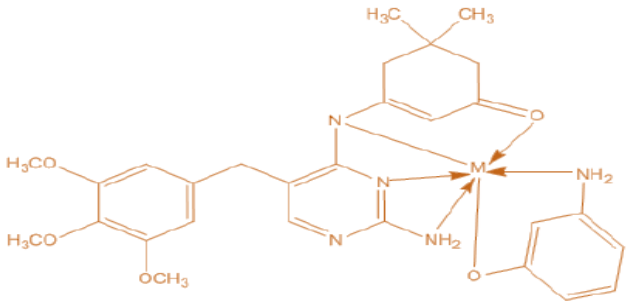

Fig. 8: Proposed structures of complexes

3.4. Anti-malarial activity

A new range of side chain-modified beta-aminaminone quinolines have been synthesized in good to excellent yields. The geometry of all the prepared compounds was inferred through

spectroscopic, X-ray crystallographic, and analytical data. The effectiveness of the prepared compounds against malaria was tested against the chloroquine-sensitive strain $^{3}D_{7}$ and the chloroquine-resistant strain K_1. Using ivermectin as a positive control, the prepared products were calculated aimed at their in vitro effect on microfilariae & adulticide towards adult helminths and B. malayi microfilariae **[44]**, **Scheme l7**.

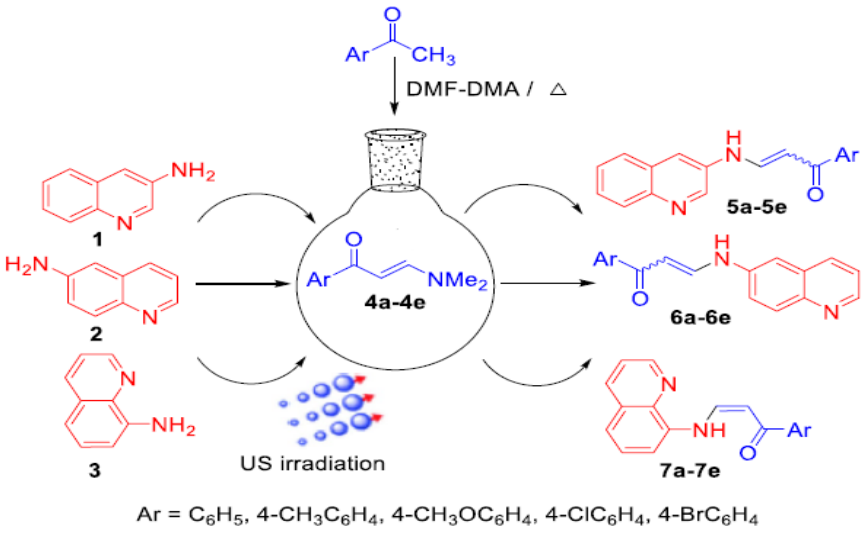

Scheme 17: Synthesis of quinoline β-enaminones

3.5. DFT Studies

Via thermally activated O-quinomethide, the study shows the preparation of enaminone-resorcin. All enaminone units in the state (solid) share a uni-directional line of twelve intra-molecular H-bonds that form about the cavity shown in the crystal structure. Control by temperature and solvent in the solution where the enaminone-resorcin arene is present as a mixture of substances conforming to the distribution. Using the DFTB / GFN2 –x TB method and the fast semi-empirical DFT B3LYP/6-31G (d, p) method in different solvents, the results of theoretical calculations were compared with experimental data **[45]**, **Fig. 9**.

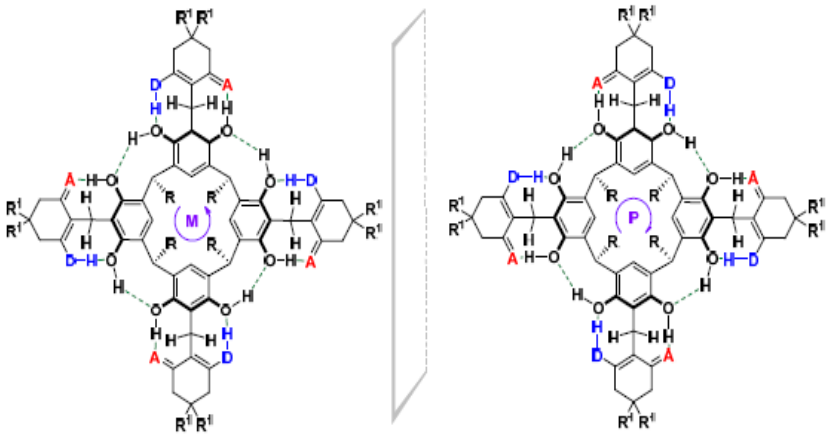

Fig. 9: Enantiomers (P and M) of β-enaminone derivatives

3.6. Optically luminescence

By the method of the condensation reaction of four aromatic amines with acetylacetone in acidic media, β-enaminone compounds were prepared. To explore the luminescent emission on organic solids, optically stimulated luminescence was used. B-Enaminones from the type of organic crystals showed good sensitivity to beta radiation. Optically stimulated luminescence was also recorded for these crystals **[46]**, **Scheme 18**.

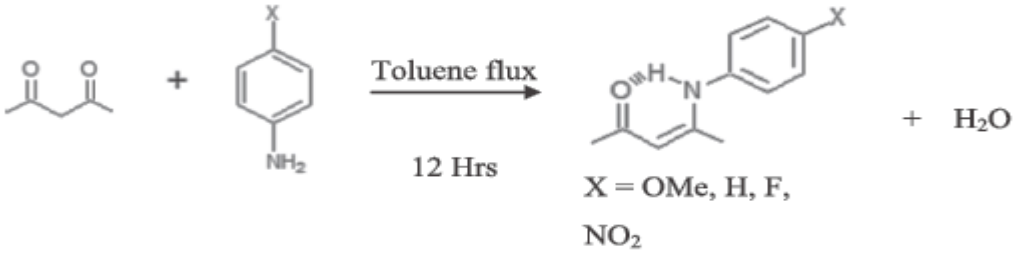

Scheme 18: Synthesis of organic crystals-enaminones

Pyridinium y1ides are widely known as cyc1oaddition reaction dipoles. In turn, instead of a l,3-dipolar cycloaddition, the microwave-abetted collaboration of N - (cyanomethy1)-2-alkyl pyridinium - salts with β-enaminones incomes as a chain (domino) of cyc1oisomerization and cyc1ocondensation processes. The reaction occurs in the existence of a base (NaC_2H_5) and uses safe solvents. The optical characteristics of the resultant pyrido [2, 3 -b] indo-lizines were investigated, and it was discovered that they emit green light with high fluorescence quantum yields **[47]**, **Scheme l9**.

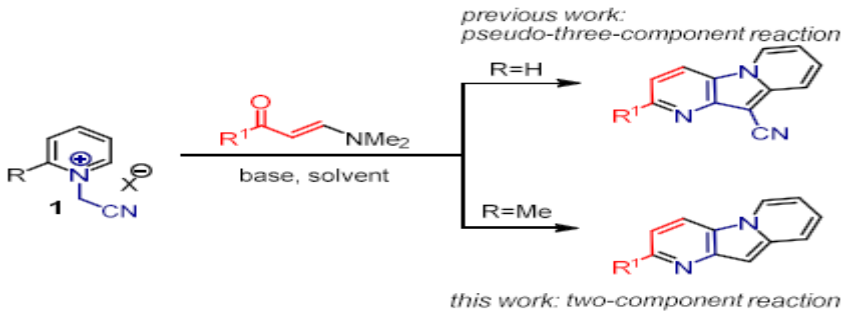

Scheme 19: General plan of work

By luciferase assay, the activity of fifteen quinolin beta-enaminone derivatives towards amastigotes and promastigotes (Leishmania) was studied. By Giemsa staining in hamsters and BALB/c mice infected with L. donovani, reduction of organismal parasite burden was assessed. By means of scintillation and fluorescence assays, the level of intracellular ATP and Ca^{2+} was determined in the activated 3D-treated promastigotes. The 3D compound could be nominated as a promising therapeutic candidate for visceral leishmaniasis due to its inhibition of the L. donovani mitochondrial complex to the extent of apoptosis **[48]**, **Fig. 10**.

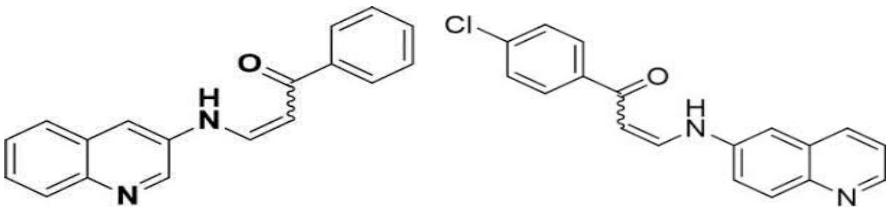

Fig. 10: Structure of quinolinyl β-enaminone derivatives

3.7. Corrosion inhibition

Through the reaction of (dimedone) and (1,2-phenylenediamine), the β-enaminone ligand was prepared, which in turn reacted with the ions of the transition elements Mn (II), Cd (II), Co (II), Ni (II), Cu (II), and Zn(II) to prepare complexes with the general formula $M(L)]Cl_2$. The prepared compounds were characterized by several spectroscopic methods, including From the results of the measurements, it was found that the ligand is tetra dentate CHNS, TGA, FTIR, UV-Vis, ^{1}H, ^{13}C /NMR. The study demonstrated the ability of the ligand to inhibit corrosion-ordinary steel in tap water by losing weight. In addition, the effectiveness of the prepared compounds against selected types of bacteria and fungi was studied by diffusion method **[49]**, **Fig. 11**.

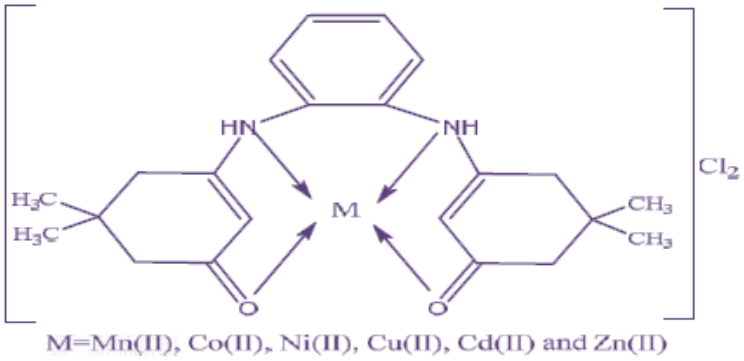

Fig. 11: The suggested chemical structure of the complexes

3.8. Nano Studies

β-enaminones and the compounds derived from them are among the most important compounds with high biological activity. By treating aliphatic and aromatic amines substituted with acyclic/cyclic 1,3-diketones over magnetically separable $CoFe_2O_4$NPs, high yields of several β-enaminones (86-97 %) were obtained. The latter was created as a result of co-precipitation. examination validated its purity, fine crystallinity, elemental distributions, morphology, magnetic characteristics, and thermal stability. Thus, $CoFe_2O_4$ NPs were a superb green heterogeneous nano-catalyst to produce -enaminones, with strong recyclability and little activity loss **[50]**, **Scheme 20**.

Scheme 20: Synthesis of b-enaminones catalyzed by $CoFe_2O_4$ NPs

4. Conclusions

Through this article, β-enaminone ligands and their metal complexes were identified, with a study of their different applications in terms of their role in biological activity, as antioxidants, anticancer, urease, as catalysts for some reactions, and as corrosion inhibition for some metals in acidic, alkaline, or neutral mediums, as fluorescence sensors, and DFT, Nano studies.

Acknowledgment

To the Deanship of the Faculty, the authors extend their sincere thanks and the Head of the Department for their continuous support during the research.

5. References

[1] Olmsted J, III, Kearns DR. Mechanism of ethidium bromide fluorescence enhancement on binding to nucleic acids. Biochem. 1977;16(16):3647-54.

[2] Vashchenko BV, Grygorenko OO, Stepaniuk OO. Heterocyclizations of β-alkoxy, β-diaminoalkyl, and related β-functionalized enones (enals) with NCN-binucleophiles. Ukrainica Bioorganica Acta. 2022;17(1):56-71.

[3] González-Soria MJ, Alonso F. Substrate-Controlled Divergent Synthesis of Enaminones and Pyrroles from Indolizines and Nitroso Compounds. Advanced Synthesis Catalysis Communications 2019;361(21):5005-17.

[4] Kumbhar HS, Gadilohar BL, Shankarling GS. Synthesis and spectroscopic study of highly fluorescent β-enaminone based boron complexes. Spectrochimica Acta Part A: Molecular Biomolecular Spectroscopy. 2015;146:80-7.

[5] Chopin N, Novitchi G, Medebielle M, Pilet G. A versatile ethanolamine-derived trifluoromethyl enaminone ligand for the elaboration of nickel (II) and copper (II)–dysprosium (III) multinuclear complexes with magnetic properties. J Fluorine Chem. 2015;179:169-74.

[6] Mabkhot YN, Aldawsari FD, Al-Showiman SS, Barakat A, Soliman SM, Choudhary MI, et al. Novel enaminone derived from thieno [2, 3-b] thiene: Synthesis, x-ray crystal structure, HOMO, LUMO, NBO analyses and biological activity. Chem Cent J. 2015;9(1):1-11.

[7] Hortelan CRW, da Silveira IOMF, de Souza SM, Beatriz A, da Silva Gomes R, de Campos Domingues NL. Synthesis of β-enaminones catalyzed by nanoparticles of Fe2O3 in ultrasound and solvent-free approach. Blucher Chemistry Proceedings. 2013;1(2):159-.

[8] Andreiadis ES, Gauthier N, Imbert D, Demadrille R, Pecaut J, Mazzanti M. Lanthanide complexes based on β-diketonates and a tetradentate chromophore highly luminescent as powders and in polymers. Inorg Chem. 2013;52(24):14382-90.

[9] Mahmud T, Rehman R, Gulzar A, Khalid A, Anwar J, Shafique U, et al. Synthesis, characterization and study of antibacterial activity of enaminone complexes of zinc and iron. Arabian J Chem. 2010;3(4):219-24.

[10] Zhang M, Abdukader A, Fu Y, Zhu CJM. Efficient synthesis of β-enaminones and β-enaminoesters catalyzed by gold (I)/silver (I) under solvent-free conditions. 2012;17(3):2812-22.

[11] Koduri ND, Scott H, Hileman B, Cox JD, Coffin M, Glicksberg L, et al. Ruthenium catalyzed synthesis of enaminones. Org Lett. 2012;14(2):440-3.

[12] Samantaray MK, Dash C, Shaikh MM, Pang K, Butcher RJ, Ghosh P. Gold (III) N-heterocyclic carbene complexes mediated synthesis of β-enaminones from 1, 3-dicarbonyl compounds and aliphatic amines. Inorg Chem. 2011;50(5):1840-8.

[13] Hassaneen HM. Chemistry of the enaminone of 1-acetylnaphthalene under microwave irradiation using chitosan as a green catalyst. Molecules. 2011;16(1):609-23.

[14] Kidwai M, Bhardwaj S, Mishra NK, Bansal V, Kumar A, Mozumdar S. A novel method for the synthesis of β-enaminones using Cu-nanoparticles as catalyst. Catal Commun. 2009;10(11):1514-7.

[15] Shendage S, Nagarkar J. Ultrasound assisted synthesis of enaminones using Nickel oxide. Current Chemistry Letters. 2013;2(3):145-52.

[16] Beckmann U, Eichberger E, Lindner M, Bongartz M, Kunz PC. Modular Routes Towards New N, O-Bidentate Ligands Containing an Electronically Delocalised β-Enaminone Chelating Backbone. Wiley Online Library; 2008.

[17] Amaye IJ, Haywood RD, Mandzo EM, Wirick JJ, Jackson-Ayotunde PL. Enaminones as building blocks in drug development: Recent advances in their chemistry, synthesis, and biological properties. Tetrahedron. 2021;83:131984.

[18] Shi Y-C, Cheng H-J, Zhang S-H. Syntheses and crystal structures of copper mixed-ligand complexes of multidentate enaminones and acetate anions. Polyhedron. 2008;27(16):3331-6.

[19] Cacchi S, Fabrizi G, Filisti E. N-propargylic β-enaminones: Common intermediates for the synthesis of polysubstituted pyrroles and pyridines. Org Lett. 2008;10(13):2629-32.

[20] Vicente J, Chicote MaT, Martínez-Martínez AJs, Abellán-López A, Bautista D. Reactivity of ortho-β-Enaminone-phenyl Palladium Complexes. Insertion of CO into the Pd− C Bond to Give the First Acyl C, N, O-Pincer Complexes. Sequential Insertion of Dimethylacetylenedicarboxylate into the Enaminone C− H Bond and of Isocyanide into the Pd− C Bond. A New Photooxigenation/Cyclization Process. Organometallics. 2010;29(21):5693-707.

[21] Al-Khazraji AMA. Synthesis of Co (ll), Ni (ll), Cu (ll), Pd (ll), and Pt (lV) Complexes with 1^4,1^5,3^4,3^5-Tetrahydro-1^1 *H*, 3^1 *H*-4, 8-diaza-1,3(3,4)-ditriazola-2,6 (1,4)-dibenzenacyclo octaphane-4, 7-dien-1^5, 3^5-dithione, and the Thermal Stability of Polyvinyl Chloride Modified Complexes. Indones J Chem. 2023;23(3):754 - 69.

[22] Hadi MK, Rahim NAHA, Sulaiman AT, Ali RMHJRJoP, Technology. Synthesis, characterization and preliminary antimicrobial evaluation of new schiff bases and aminothiadiazole derivatives of N-substituted phthalimide. Research Journal of Pharmacy Technology. 2022;15(9):3861-5.

[23] FIRINCI EJJotIoS, Technology. Synthesis and Characterization of Enaminone Derivatives of Barbituric Acid. 2019;9(2):993-1003.

[24] Filkale AE, Pathak C. Dinuclear cobalt complexes supported by biphenol and binaphthol-derived bis (salicylaldimine) ligands: synthesis, characterization and catalytic application in β-enaminone synthesis from 1, 3-dicarbonyl compounds and aliphatic amines. New J Chem. 2020;44(35):15109-21.

[25] Li H, Shu H, Wang X, Wu X, Tian H, Tong H, et al. Solid-state fluorescence enhancement of bromine-substituted trans-enaminone derivatives. Organic Materials. 2020;2(01):033-40.

[26] Shiri M, Heydari M, Zadsirjan V. Efficient synthesis of novel functionalized pyrazolo-pyranoquinoline and tetrahydrodibenzo-[1, 8] naphthyridinone derivatives. Tetrahedron. 2017;73(15):2116-22.

[27] Mart M, Trzeciak A. The synthesis of β-enaminones using trialkylamines and a Pd/DNA catalyst. Molecular Catalysis. 2021;502:111365.

[28] Cui X, Chen Y, Wang W, Zeng T, Li Y, Wang X. Chemoselective synthesis of β-enaminones from ynones and aminoalkyl-, phenol-and thioanilines under metal-free conditions. Chemical Papers. 2021;75:3625-34.

[29] Ciber L, Požgan F, Brodnik H, Štefane B, Svete J, Grošelj U. Synthesis and Catalytic Activity of Organocatalysts Based on Enaminone and Benzenediamine Hydrogen Bond Donors. Catalysts. 2022;12(10):1132.

[30] Rao K, Chai Z, Zhou P, Liu D, Sun Y, Yu F. Transition-metal-free approach to quinolines via direct oxidative cyclocondensation reaction of N, N-dimethyl enaminones with o-aminobenzyl alcohols. Frontiers in Chemistry. 2022;10:1008568.

[31] Shanak QA, Alasli NJ, Numan AT. Preparation and Characterization, of ligand Complexes of Di-beta-Enamino with some Metals. Vegueta Anuario de la Facultad de Geografía e Historia. 2022;22:8.

[32] Zhang K-L, Yang J-C, Guo Q, Zou L-H. Transition Metal-Free Synthesis of 3-Acylquinolines through Formal [4+ 2] Annulation of Anthranils and Enaminones. Catalysts. 2023 13(4):778.

[33] Wang Q, Li Y, Sun J, Chen S, Li H, Zhou Y, et al. Rh-Catalyzed C–H Activation/Annulation of Enaminones and Cyclic 1, 3-Dicarbonyl Compounds: An Access to Isocoumarins. J Org Chem. 2023;88(9):5348-58.

[34] Mohamed FA-S, Numan AT. Synthesis and characterization of some mixed ligands complexes of β-enaminone with some metal ions. Materials Today: Proceedings. 2023;80:1683-90.

[35] Subramamiam P, Ramasubbu C, Athiramu S, Arumugam S, Alagumuthu M. Pharmacological explorations of eco-friendly amide substituted (Z)-β-enaminones as anti-breast cancer drugs. Arch Pharm. 2019;352(1):1800244.

[36] Huma R, Mahmud T, Munir R, Awan SJ, Iftikhar K. Cytotoxicity and Molecular Docking Studies of a Novel Enaminone and its Cadmium (II) Complex. Pakistan Journal of Zoology. 2019;51(2).

[37] Huma R, Mahmud T, Awan SJ, Ashraf M, Khan SU, Rasheed H, et al. Thermal and spectroscopic studies of some metal complexes with a new enaminone ligand 3-chloro-4-((4-methoxyphenyl) amino) pent-3-en-2-one and their investigation as anti-urease and cytotoxic potential drugs. Arabian J Chem. 2022;15(3):103640.

[38] Ilhan S, Atmaca H, Yilmaz ES, Korkmaz E, Zora M. N-Propargylic β-enaminones in breast cancer cells: Cytotoxicity, apoptosis, and cell cycle analyses. Journal of Biochemical Molecular Toxicology. 2023;37(4):e23299.

[39] Huma R, Mahmud T, Mitu L, Ashraf M, Iqgal A, Iftikhar K, et al. Synthesis, Characterization, Molecular Docking and Enzyme InhibitionStudies of Some Novel Enaminone Derivatives and Their Complexes with Cu (II), Cd (II) and Co (II) Ions. J Rev Chim. 2019;70:3564-9.

[40] Masaret GS, Farghaly TA. Synthesis of 8, 10-disubstituted-triazoloperimidines from (e)-3-(dimethylamino)-1-(8-phenyl-8h-[1, 2, 4] triazolo [4, 3-a] perimidin-10-yl) prop-2-en-1-one and their antimicrobial activity. Curr Org Synth. 2018;15(1):126-36.

[41] Bhat MA, Al-Omar MA, Naglah AM, Khan AA. Enaminone-derived pyrazoles with antimicrobial activity. Journal of Chemistry. 2019;2019:1-10.

[42] Abdulsalam MB, Numan AT. Synthesis, Characterization, and Biological Activity of Mixed ligand Complexes from 8-Hydroxyquinoline and new Ligand for β-Enaminone. Pakistan Journal of Medical Health Sciences. 2022;16(08):614-.

[43] Sardar B, Srimani DJT. Concept and progress on the de (hydrogenation) and hydrogenation reactions using transition metal integrated layered double hydroxides (LDHs). Tetrahedron. 2023:133414.

[44] Khanikar S, Kaping S, Helissey P, Joshi P, Shaham SH, Mishra S, et al. Efficient synthesis, structure elucidation, and anti-parasitic activities of novel quinolinyl β–enaminones. Monatshefte für Chemie-Chemical Monthly. 2021;152(6):665-78.

[45] Szafraniec A, Grajda M, Jędrzejewska H, Szumna A, Iwanek W. Enaminone Substituted Resorcin [4] arene—Sealing of an Upper-Rim with a Directional System of Hydrogen-Bonds. Int J Mol Sci. 2020;21(20):7494.

[46] Lara-Camilo A, Villafañe-Bautista Y, de León-Alfaro M, Guzmán-Mendoza J, Quintana-Zavala D, García-Salcedo R, et al. Optically stimulated luminescence in enaminones. Radiation Physics Chemistry. 2020;167:108165.

[47] Sokolova EA, Festa AA, Subramani K, Rybakov VB, Varlamov AV, Voskressensky LG, et al. Microwave-assisted synthesis of fluorescent pyrido [2, 3-b] indolizines from alkylpyridinium salts and enaminones. Molecules. 2020;25(18):4059.

[48] Rani A, Khanikar S, Dutta M, Katiyar S, Qamar T, Seth A, et al. Quinolinyl β-enaminone derivatives exhibit leishmanicidal activity against Leishmania donovani by impairing the mitochondrial electron transport chain complex and inducing ROS-mediated programmed cell death. 2023;78(2):359-72.

[49] Ahmed AA, Waheed EJ, Numan AT, editors. Synthesis, Characterization, Antibacterial study and Efficiency of Inhibition of New di-β-enaminone Ligand and its Complexes. J Phys Conf Ser; 2020: IOP Publishing.

[50] Eidi E, Kassaee MZ, Cummings PT. β-Enaminones over recyclable nano-$CoFe_2O_4$: a highly efficient solvent-free green protocol. Res Chem Intermed. 2018;44:5787-99.

Al-Kitab Journal for Pure Sciences (2023); 7(2):153-172.
https://doi.org/10.32441/kjps.07.02.p12

Al-Kitab Journal for Pure Sciences
ISSN: 2617-1260 (print), 2617-8141(online)
https://isnra.net/index.php/kjps

Petrography and diagenesis of the Middle to Upper Jurassic succession from Sargelu section, northeastern Iraq

Rebwar H. Rasool[1*], Sarmad A. Ali[1,2], Ali I. Al-Juboury[3]

[1]Department of Applied Geology, College of Science, Kirkuk University, Iraq
[2]GeoQuEST Research Centre, School of Earth, Atmospheric and Life Sciences, University of Wollongong, Wollongong, Australia
[3]Petroleum Engineering Department, College of Engineering, Al-Kitab University, Kirkuk, Iraq

*Corresponding Author: rebwar.hussain19@gmail.com

Citation: Rasool RH, Ali SA, Al-Juboury AI. Petrography and diagenesis of the Middle to Upper Jurassic succession from Sargelu section, northeastern Iraq. Al-Kitab J. Pure Sci. [Internet]. 2023 Nov. 30 [cited 2023 Nov. 30];7(2):153-172. Available from: https://doi.org/10.32441/kjps.07.02.p12.

Keywords: Jurassic succession, Northeastern Iraq, Sargelu area, Petrographic components, Diagenesis, Dolomitization.

Article History
Received 12 Oct. 2023
Accepted 27 Nov. 2023
Available online 30 Nov. 2023

Abstract:

Petrographic and diagenetic analysis of the Middle-Upper Jurassic successions (Sargelu, Naokelekan, and Barsarin) formations and boundaries between them in the Sargelu area, Kurdistan region, N.E. Iraq was conducted based on the lithologic description, thin section analysis, and scanning electron microscopy .The study aims to define the petrographic components and diagenetic processes that affect the carbonate rocks of Jurassic succession in the studied section. Thirty-eight thin sections have been prepared, with five samples selected using the S.E.M. technique to reveal the petrographic components and diagenetic processes. The Jurassic succession is composed mainly of carbonates (limestone and dolostone) interbedded with shale units. Petrographically, the Sargelu, Naokelekan, and Barsarin formations are composed of skeletal grains (pelagic pelecypods, radiolaria, calcispheres, planktonic and benthonic foraminifera such as miliolid, ostracods, bioclasts, and stromatolites) which are the most common, in addition, non-skeletal grains such as poloids, micritic groundmass, and recrystallized micro spars, Many diagenetic processes affected the studied carbonate rocks such as micritization, dolomitization compaction and stylolite formation, authigenic minerals (pyrite), cementation, neomorphism, dissolution and porosity formation as represented by moldic, vuggy, channel and fracture porosity.

Keywords: Jurassic succession, Northeastern Iraq, Sargelu area, Petrographic components, Diagenesis, Dolomitization.

الصخرية و العمليات التحويرية لتتابعات الجوراسي الأوسط ـ الأعلى في مقطع سركلو شمال شرقي العراق

ريبوار حسين رسول[1]، سرمد عاصي علي[2،1]، علي إسماعيل الجبوري[3]

[1] قسم علوم الأرض التطبيقية، كلية العلوم، جامعة كركوك، كركوك، العراق

[2] مركز أبحاث جيوكويست، كلية علوم الأرض والغلاف الجوي والحياة، جامعة ولونجونج، ولونجونج، أستراليا

[3] قسم هندسة النفط، كلية الهندسة، جامعة كتاب، التون كوبري، العراق

rebwar.hussain19@gmail.com, sarmad@uokirkuk.edu.iq, alialjubory@yahoo.com.

الخلاصة:

تم إجراء دراسة للبتروغرافية والعمليات التحويرية لتتابعات الجوراسي المتوسط – الأعلى لتكوين (ساركلو، ناوكيلكان وبارسرين) ومناطق التماس بينهم في منطقة ساركلو، إقليم كردستان، شمال شرقي العراق اعتمادا على الوصف الصخري والشرائح الرقيقة وكذلك التحليل بالمجهر الماسح الإلكتروني. تهدف الدراسة الى التعرف على المكونات الصخرية والعمليات التحويرية المؤثرة على صخور الكربونات ضمن التعاقب الجوراسي للتكاوين المدروسة. تم تحضير ودراسة ٣٨ شريحة رقيقة مع ٥ عينات تم اختيارها وتحليلها باستخدام تقنية المجهر الماسح الإلكتروني لوصف المكونات الصخرية وكذلك العمليات التحويرية، تتكون تتابعات الجوراسي بشكل رئيسي من الكربونات (الحجر الجيري والدولوستون) المتداخلة مع التسجيل. من الناحية البتروغرافية ، تتكون تكاوين ساركلو وناوكيليكان وبارسرين من المكونات الهيكلية (الرخويات البحرية، فاسية القدم، الشعاعيات، الكريات الكلسية، الفورامنيفرا الطافية و القاعية (ميليوليد)، الاوستراكودا، الفتات الأحيائي والستروماتوليت) وهي الأكثر شيوعًا، بالإضافة إلى الحبيبات الغير الهيكلية مثل الدمالق، والأرضية المكراتية وكذلك السبار الدقيق معاد أتبلور، أثرت العديد من عمليات التحويرية هذه التتابعات الصخرية مثل المكرتة، الدلمتة، المعادن موضعية النشاءة مثل (البايرايت)، الانضغاط , و تكوين الستايلولايت، التشكل الجديد، والإذابة وتكوين المسامية مثل المسامية القالبية، المسامية بين الحبيبات، القنوات والشقوق المجهرية .

الكلمات المفتاحية: تتابعات الجوراسي، منطقة ساركلو، المكونات الصخرية، الراديولاريا، العمليات التحورية، الدلمته.

1. Introduction:

The Jurassic successions of Iraq have great importance in terms of their petroleum system characteristics [1-3]. Most of the petroleum exposed in Iraq was sourced from Jurassic rocks and trapped in the Cretaceous- and Tertiary-age reservoirs of the Mesopotamian Basin and the Zagros Basin/Zagros Fold Belt [4]. Other Jurassic rocks have been considered essential reservoirs, especially in the central and northern parts of Iraq [5]. These successions lack detailed studies on their mineralogical and petrographic characteristics that are widely affected by the reservoir properties of the Jurassic rocks. The petrographic study is one of the essential means for determining the depositional environments of carbonate rocks based on microfacies analysis. It is also used to investigate diagenesis and other factors affecting sedimentation, such

as climate, tectonic setting, and the nature of the source rocks (provenance), particularly for the clastic rocks [6].

The lithological composition of the Middle to Upper Jurassic successions, including Sargelu, Naokelekan, and Barsarin formations from northeastern Iraq, consists of thin to medium bedded, black, bituminous limestone, dolomitic limestone, and black papery shale, with narrow beds of black chert in the upper part of the successions. The current study examines the petrographic description using a traditional polarizing microscope supported by the SEM-EDS (Scanner Electron Microscope, energy-dispersive X-ray spectroscopy) techniques for the carbonate units in the studied succession to determine their petrographic components and the main diagenetic events affecting on them.

2. Geological Setting

The study area is in Sargelu village near Dokan town, northeastern of Sulaymaniyah city in the High Folded Zone of the Unstable Shelf of Iraq at the coordinates (35° 86' 75" N- 45 ° 16' 37" E) (**Figures 1**, **2**). The Jurassic rocks existed in isolated patches at eroded cores and limbs of anticlines [7, 8]. The studied middle-late Jurassic formations in Iraq were deposited during the isolation of the central intra-shelf basin of Mesopotamia from the Neo-Tethyan Ocean time, possibly due to renewed rifting along the N.E. margin of the Arabian Plate [8,9]. The Neo-Tethys reached its maximum width of 4000 km during the Late Triassic to Middle Jurassic periods [10]. Thinly and thick-bedded, bituminous black limestones, dolomitic black limestones, stromatolitic limestones, and black papery shale beds with thin streaks of black chert in the top part is primary lithology of the middle Jurassic Sargelu Formation in the studied area and the Formation thicknesses about 103m as shown in **Figure 3**, Where The late Jurassic Naokelekan Formation is about 16m composed in the lower unit of laminated argillaceous bituminous limestone alternating with bituminous shale and fine-grained limestone, middle unit is consisting of thin-bedded fossiliferous dolomitic limestone referred to as the (mottled beds) and an upper unit is consists of thin-bedded, highly bituminous dolomite and limestone with beds of black shale (coal horizons). The lower and upper contacts of the Naokelekan Formation are conformable and gradational with the underlying Sargelu Formation and the overlying Barsarin Formation [12]. Stomatolitic limestone and dolomitic limestone alternating shales, contorted and brecciated beds, and some secondary gypsum and anhydrite form the main component of about 18m thickness in the Barsarin Formation of the studied section. The studied formations were deposited in tidal flats (supratidal), restricted lagoons, and shallow marine to bathyal depositional environments [13,8].

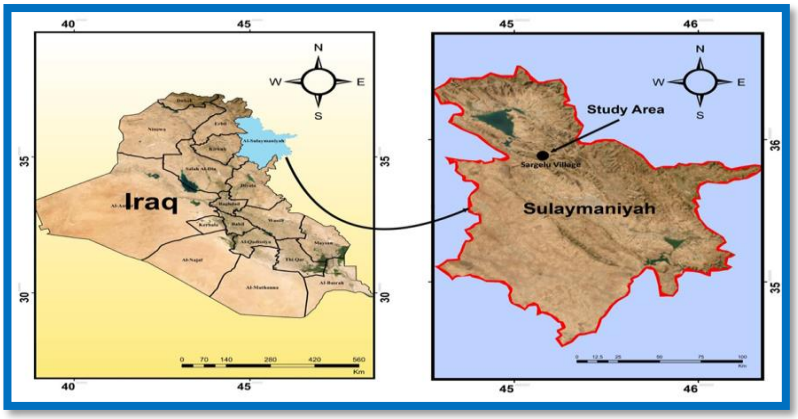

Figure 1. Location map of the study area (Sargelu village)

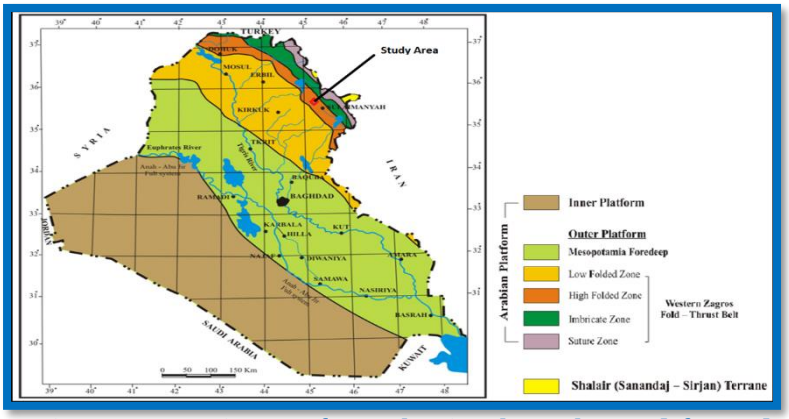

Figure 2. Tectonic map of Iraq showing the study area [after, 14]

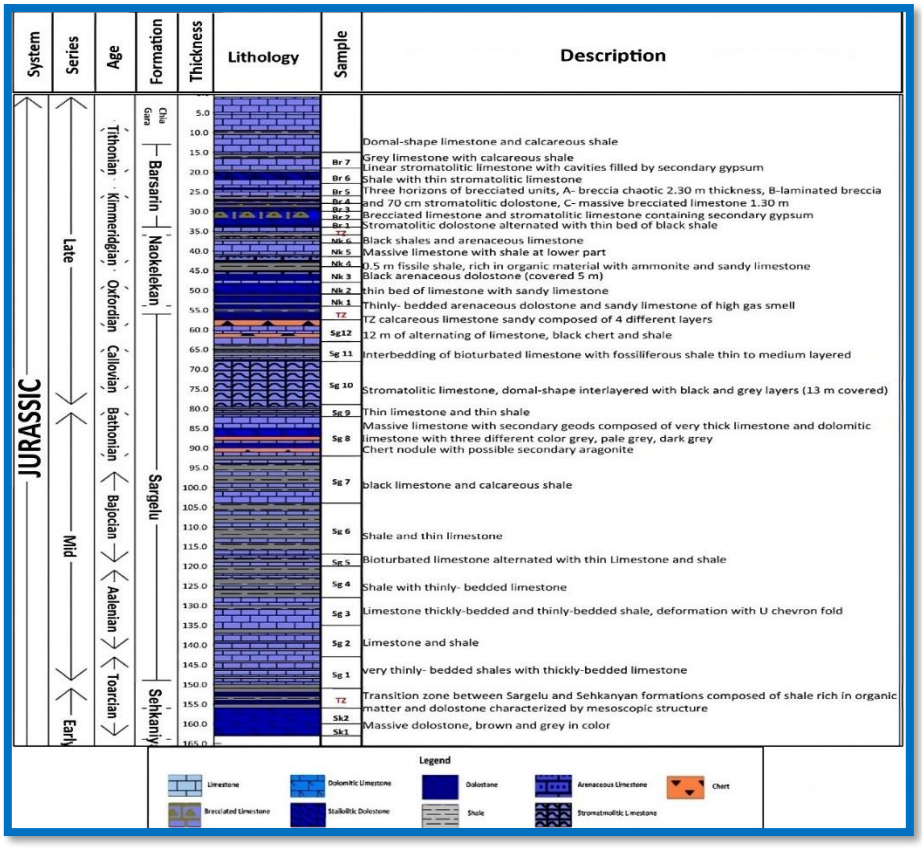

Figure 3. Lithologic section with description and sample numbers of the studied formations

3. Materials and Methods

The samples prepared for the thin section were selected from the carbonate units in the studied Jurassic formations, which are comprised mainly of limestone, dolomitic limestone, and dolomite. The petrographic study is carried out on 38 thin sections prepared from all the studied formations, including 13 slides from the Sargelu Formation, ten slides from the Naokelekan Formation, nine slides from the Barsarin Formation, four slides from the formation's contacts of the buildings and two drops from Sehkanyian Formation. The petrographic description was done at the Department of Geology and Petroleum, College of Science, Salahaddin University, Erbil, Iraq.

At the same time, imaging was achieved at the Department of Applied Geology, College of Science, Kirkuk University, Iraq.

The Scanning electron microscopic study (S.E.M.) was performed on five selected samples at Premier Corex Laboratories in Houston, U.S.A., using an F.E.I. Quanta FEG 650 FE-SEM instrument equipped with two Bruker E.D.S. XFlash 5030 energy dispersive X-ray spectroscopy (E.D.S.) detectors and an FEI R580 Everhart-Thornley (ETD) electron detector.

4. Results

4.1 Petrographic Description

Carbonate rocks consist mainly of grains and groundmass, which are essential for finding depositional environments and texture types. The grains have been divided into skeletal grains, which include fossils and their clasts, and no-skeletal grains, which include lithoclasts, grain aggregates, and peloids **[6]**.

4.2 Petrographic component

The ratio of the skeletal grains is varied between the studied formations. They dominate the Sargelu Formation while are less abundant in the Naokelekan Formation and almost disappeared from the Barsarin Formation.

The Jurassic carbonate rocks were highly affected by diagenetic processes such as dolomitization, dissolution, and compaction **[15-17]**. The identified skeletal grains include mainly fossils and fossil shells; below is a brief description of each of these components:

4.3 Pelagic pelecypods

These skeletal grains predominate in the middle and upper parts of the Sargelu Formation in the study area. They commonly exist in shallow or deep marine environments **[18]** and are the most abundant in the basinal facies from the Late Triassic-Middle Jurassic ages **[19,20]**. Two types of pelecypods have been diagnosed: single valve (Halobia sp. (**Figure 4a**) and class

Bivalvia (Posidonia Sp, Bositra Sp.) (**Figure 4a, b**), which is widely spread in the Sargelu Formation.

4.4 Radiolaria

It is a single-celled marine organism with rigid structures, spherical shapes, and serrated, spiny perforated walls containing lateral protrusion **[21]**. It generally presents in a small proportion and is affected by diagenetic processes. It exists typically in less than 1 mm and frequently between 0.1 and 0.2 mm in size. Radiolaria are recorded in the upper part of the Sargelu Formation (**Figure 4c**) and in the lower and middle parts of the formation, where calcispheres accompany them. It is also presented in the central part of the Naokelekan Formation (**Figure 4d**). Radiolaria was found in pelagic limestones, and they are planktonic organisms living in open marine environments **[22,20]**.

4.5 Calcispheres

The calcareous balls or spheres belong to the group of *Pithonella* and are formed of minute calcareous spherical shells devoid of openings; they belong to the Upper Jurassic-Cretaceous in age **[23]**. The sizes of calcispheres range from 100-200 microns **[24]**. The walls consist of a single layer of lamellar form consisting of homogeneous calcareous crystals **[23,25]**. Calcispheres are common in open marine environments; they are indicators for the environment of marine settings from the edge of the continental shelf to the slope **[21,26]**. In the present work, calcipheres have been found in the Sargelu and Naokelekan formations, which are absent in the Barsarin Formation (Figure 4d, e). it was observed in the Naokelekan Formation as coccolithophores, which is in shape that has been pointed out in the S.E.M. image.

4.6 Foraminifera

They are dominantly marine protozoa, mainly of microscopic size **[6]**. They are the most significant type of microfossils because they are common in rocks. Therefore, they are useful for dating and reconstructing sedimentary environments **[27]**. Petrographic study has revealed different types of planktonic foraminifera in the Sargelu and Naokelekan formations, while miliolid is common in the Barsarin Formation (**Figure 4f**), most of them are difficult to distinguish due to the effect of diagenesis (**Figure 4g**). In the Sargelu limestones, planktonic foraminifera are often tiny, consolidated spherical chambers that are filled with calcite or pyrite. Most of them are affected by the recrystallization process and leaching, like the previous study by **[28]**.

4.7 Ostracods

They have been found in almost all sorts of aquatic environments and have been known since the Late Cambrian **[26]**. Ostracods are useful for stratigraphic investigations because they can

be found in a wide variety of depths and depositional settings, including marine, transitional, and fresh waters [24,29]. Ostracods are recognized in the Sargelu Formation, especially in the upper parts. They are commonly affected by diagenetic processes such as cementation and compaction, resulting in filling chambers with spay calcite cement and elongation and distortion of the shells (**Figure 4h**).

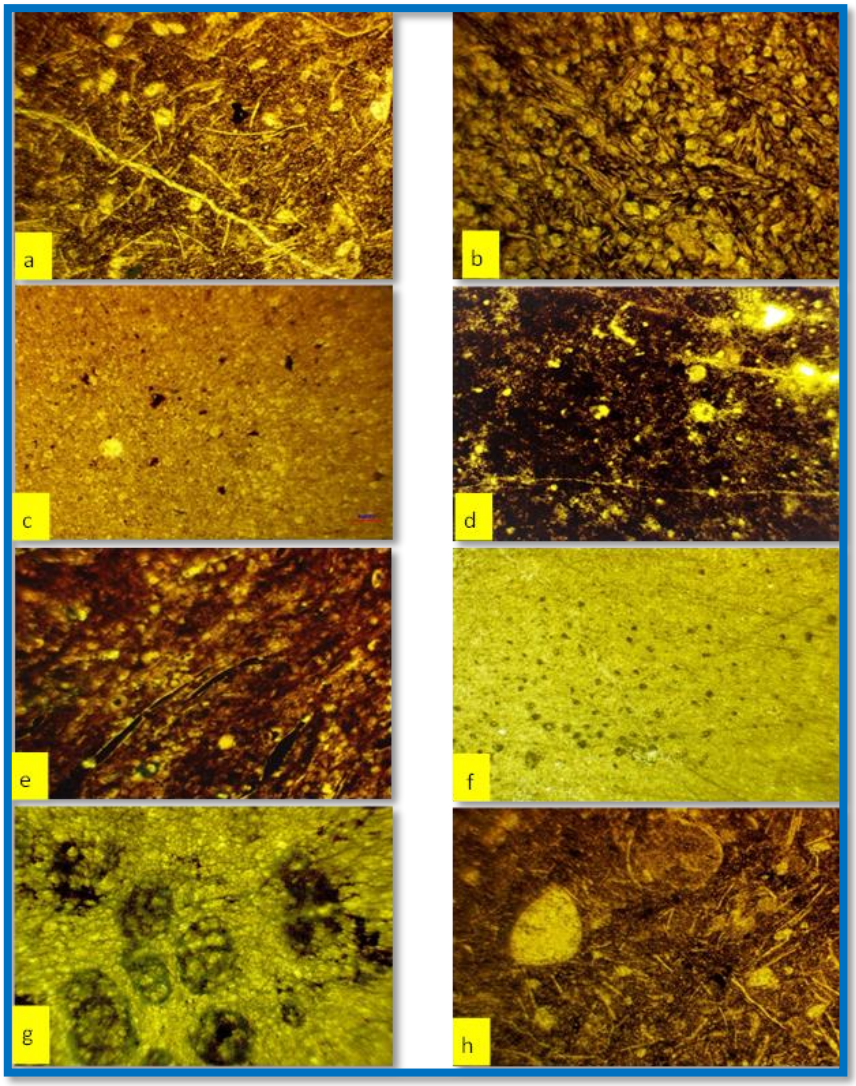

Figure 4. Photomicrograph illustrating

Figure 4 (a) Pelecypod's single valve long curved Halobia (red arrow) in the upper part of the Sargelu Formation in sample (Sg-9B) Magnification, 4X, N.L**. (b)** Thin shelly class bivalve pelagic pelecypod *Bositra (blue arrow)* in metamorphosed and dolomitized limestone in middle part of the Sargelu Formation in sample (Sg-8B), Mag. 4X, N.L. **(c)** Calcitized radiolaria (white arrow) affected by dissolution and filled with sparry calcite cement within a micritic matrix in the lower part of the Sargelu Formation IN Sample (Sg-3B), Mag. 4X, N.L. **(d)** Radiolarian (white arrow) affected by dissolution and filled with sparry calcite cement preserved as moldic

porosity associated with calcispheres (red arrows) and authigenic pyrite in the middle part of the Naokelekan Formation in Sample (Nk-4B), Mag. 4X, N.L. **(e)** walled and un-walled calcispheres filled by granular cement (red arrow) with chert (white arrows) embedded in micrite groundmass, the upper part of the Sargelu Formation in a sample (Sg-12B), Mag. 4X, N.L. **(f)** Different types of foraminifera (planktonic, benthonic) (red arrows) highly affected by diagenesis in the lower part of the Barsarin Formation in a sample (Br-1B) Mag., 4X, N.L. **(g)** Miliolid shell highly affected by dissolution in the middle part of the Barsarin Formation in a sample (Br-4B), Mag., 10X, N.L. **(h)** Spindle ostracoda (red arrow) filled with sparry calcite cement and pelagic pelecypod with authentic pyrite in shape of black spots (white arrow), in micrite ground mass in upper part of the Sargelu Formation in sample.

4.8 Bioclasts

They are remains of fossils that are created by the action of waves and currents in the depositional basin, and they may provide information about the water energy, where the rounded bioclasts denote a high energy level and flattened ones a low energy level [30,26]. The varying ratios of their presence may be caused by the fluctuation of the current energy created by changes in sea level [26]. In the current study, reworked bivalve skeletons and other unidentified mollusks, some of which are phosphatized, are represented in the Sargelu Formation (**Figure 5a**). They are also found in different intervals in the Naokelekan and Barsarin formations.

4.9 Stromatolite

It is sedimentary carbonate structures of inorganic origin that developed because of biological and chemical sedimentary processes associated with the growth and development of benthic assemblies such as blue-green algae and anaerobic bacteria through the deposition of calcium carbonate inside the ground or algal mats [31]. In the current study, stromatolites are observed in the limestones of the lower and upper parts of the Sargelu Formation with braze eye shapes (**Figure 5b**). It's more common in Barsarin Formation as parallel stromatolites (laminated limestone) in the upper part of the formation and planer and crinkled (wavy) stromatolitic limestone in the middle and lower parts of the formation (**Figure 5b-c**). Microscopically, they are observed in the Barsarin Formation, which is filled by calcite cement and organic maters (**Figure 5d**).

4.10 Non-skeletal grains

Peloids are inorganic grains of different shapes and sizes; they are characterized by their fine carbonate grains of size (0.1-0.5) mm, spherical, cylindrical, or angular, without internal structures and dark color [26]. They are frequently considered to be by-products of ooids or

microscopic processes involving bioclast fragments [32,33]. In the current study, peloids were found in the Naokelekan and Barsarin formations (Figure 5d).

4.11 Micrite

According to [34], micrite is a microcrystalline calcite crystal with grains typically smaller than four m. Micrite is characterized by its brown to dark color, according to its content of impurities, organic materials, clay minerals, and iron oxides, in addition to other factors such as the nature of the transformational processes, sedimentation rate, and oxidation and reduction factors [35,26]. The micritic groundmass is common in the Sargelu and Naokelekan formations Figure (5e, f) Spray calcite cement of various sorts, such as drusy, granular, and blocky calcite cement, have also been identified in the samples of the current study.

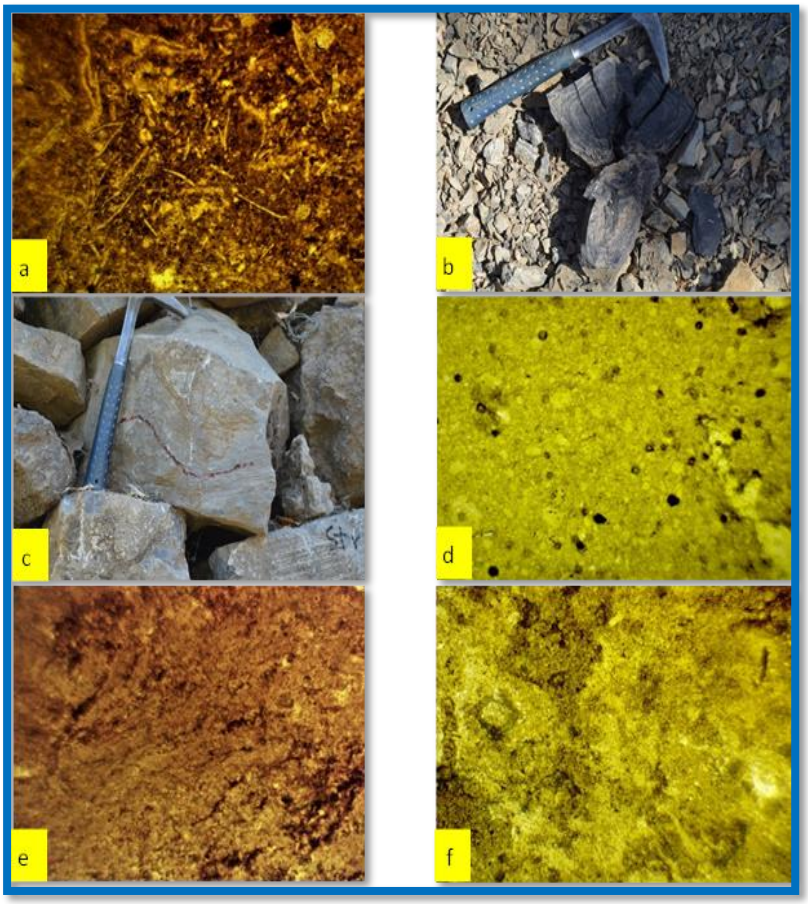

Figure 5. photomicrograph illustrating

Figure 5 (a) Bioclastic fragments (blue arrows) in the Sargelu Formation in a sample (Sg-4B), 4X, N.L. **(b)** field photo of stromatolitic limestone with braze eyes observed in the upper and lower parts of the Sargelu Formation. **(c)** Field photo of the wavy (red arrow) and parallel (blue arrow) stromatolitic limestone in the upper part of the Barsarin Formation in sample Br-6. **(d)** Peloids (red arrows) highly affected by diagenesis chemical compaction (pressure

solution) in the upper part of Naokelekan Formation in sample (Nk-5B), 4X, N.L. **(e)** Micrite groundmass with organic material filled microfracture and pores in the Lower part of Sargelu Formation in sample Sg-2B. 4X, N.L**. (f)** Micrite groundmass with bioclasts in the lower part of Barsarin Formation sample (Br-2B). 4X, N.L.

5. Diagenesis

Diagenetic processes are defined as all biological, chemical, and physical changes affecting sediments after deposition and before reaching the metamorphism stage **[36]**. There were some important factors that affect the diagenesis processes on carbonate rocks, such as changes in sea level levels associated with tectonic events and climate changes **[37]**. Carbonate minerals are metastable minerals, and therefore, they are more highly affected by diagenesis than clastic rocks **[38]**. Therefore, they rapidly respond to diagenetic processes such as cementation, dissolution, porosity, and neomorphism that lead to the destruction of the sedimentary textures, skeletal grains, and groundmass **[35]**. In the current study, the limestone, dolomite, and dolomitic limestone of the studied Sargelu, Naokelekan, and Barsarin formations have suffered from various types of diagenetic processes in different degrees, but it seems that severe effects have occurred on the carbonates of the Naokelekan Formation. The main diagenetic processes that affected the formations under study include.

5.1 Micritization

Micritization is an early diagenetic process that affects skeletal grains **[39],** Where the micrite envelopes the skeletal grains or bioclasts. In marine diagenesis, micritization is a basic process that takes place at the sediment-water interface **[40]** and under low-energy conditions. Micritization is observed in all formations of the study area (**Figure 6a, b**).

5.2 Dissolution and porosity formation

Dissolution is considered one of the types of histochemically destructive diagenetic processes. Dissolution is controlled by the stability of a particular mineral, the degree of fluid saturation with the targeted mineral, fluid pressure, and temperature **[24]**. Melodic pores are formed when grains dissolve completely to leave pores with shapes like the dissolved grains, while vuggy pores are those that have irregular shapes and are formed by a dissolution process that affects the components of the texture, as shown in (**Figures 4g, h and 6b**). Pore systems in sedimentary carbonates are often complicated in terms of shape and origin **[41]**. Porosity decreases by cementation and compaction, whereas it is acquired through solution, dolomitization, and tectonic cracks. Porosity is controlled by a group of factors, the most important of which are climate, fluctuation in sea level, the rate of gravity of sedimentary accumulation, sedimentation, and compression. and cementation **[42,43]**. Primary and

secondary porosity were noted in the carbonates of Jurassic succession in the study area. The primary porosity includes only interparticle porosity, whereas secondary porosity is revealed by moldic, vuggy, channels, and fracture porosity **[26]**, as shown in (**Figure 6b, c, d**) and (**Figure 7A, B, C**).

5.3 Chemical compaction and stylolite formation

Compaction is one of the destructive processes that commonly occurs in carbonate rocks. The process reflects the compaction caused by the severe lithostatic load, leading to a reduction in the porosity. According to **[21]**, compaction is divided into two types: physical compaction and chemical compaction. Dissolution surfaces and stylolites are formed because of the pressure solution **[24]**. Stylolites result from increasing overburden sedimentation or tectonic pressure, which affects the grains within the carbonate rock, promotes dissolution, and propagates seams **[44]**. This process is noted in the Sargelu, Naokelekan, and Barsarin formations in the form of low and high-amplitude peaks stylolite (**Figure 6c, d**) and (**Figure 7E**).

5.4 Cementation

Cementation is the diagenetic process by which voids and pores are filled by calcite cement. The cementation process is one of the chemically similar structural processes. According to **[38,45]**, there are many factors that control the cementation process, which include temperature, mechanical stress, pH, carbon dioxide pressure, type of dissolved elements, and their concentration in the solution. In the current study, several types of cement were distinguished based on the classification of [26], including granular, drusy, and blocky cement. This type of cement dominantly fills the fossil's mold, pores, and fractures (**Figure 6c, d**).

5.5 Neomorphism

Neomorphism includes both recrystallization and inversion processes. The recrystallization process is defined as a change in the size and shape of the crystal, which results in an increase or decrease in the crystalline size without any change in the chemical composition **[36]**. It has been recorded in the form of transformation of the fine micritic groundmass with a size of (4) microns to a microsite with a size greater than (4) microns (**Figure 6g**) and (**Figure 7F, G**). The occurrence of dissimilar parts of recrystallized dolomite crystals is evidence of neomorphism (**Figure 6h**). Inversion is the transformation of an unstable mineral, such as aragonite, into a stable mineral (calcite) without any change in the chemical composition. The inversion process was observed in the three studied formations, as shown in (**Figure 8a**). Neomorphism was also noted within the dolomites of the Sargelu and Naokelekan formations in the form of the creation of dolomite crystals (i.e., aggrading neomorphism) (**Figure 8b, c**).

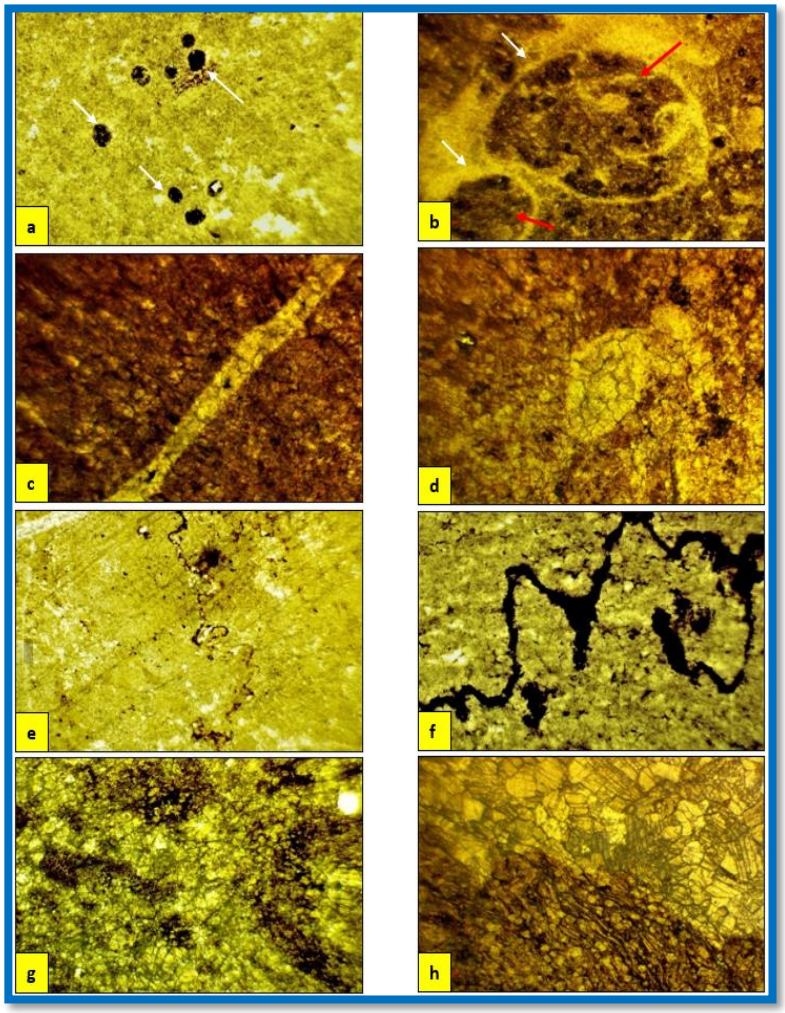

Figure 6. Photomicrograph illustrating

Figure 6 (a) Micritization of skeletal grains (white arrows) in the lower part of the Naokelekan Formation sample (Nk-2B), 4X, N.L. **(b)** Micrite envelop (rim) (white arrow) surrounding Ostracoda in the middle part of the Sargelu Formation in the sample (Sg-7B), note high effect by dissolution process leaving melodic porosity (red arrow). Authigenic pyrite in the shape of black spots also exists, 4X, N.L. (c) Chemical compaction led to stylolite formation in low and high amplitude types and filled by organic material in the middle and upper parts of the Barsarin Formation in sample (Br-3B), 4X, N.L. (d) Chemical compaction and stylolite formation of high amplitude type filled by organic material in the upper part of the Naokelekan Formation in the sample (Nk-5B), 4X, N.L. (e) Fracture filled by drusy calcite cement in the lower part of the Naokelekan Formation within micrite groundmass in the sample (Nk-2B), 4X, N.L. (f) Sparry calcite cement (blocky cement) (red arrow) filled an ostracoda within micrite groundmass in the upper part of the Sargelu Formation in sample (Sg-12B), 4X, N.L. (g) Neomorphism (recrystallization) of micrite groundmass and transformation to microsite in the middle part of the Barsarin Formation in the sample (Br-3B), 4X, N.L. (h) Neomorphism

(recrystallization) of micrite groundmass and transformation to separate in the middle part of the Sargelu Formation with dolomitization and compaction processes in the sample (Sg-8B), 4X, NL.

5.6 Dolomitization

Dolomitization is one of the important diagenetic processes in Jurassic formations in the studied area, with extensive and pervasive dolomitization with a variety of crystal sizes, especially in the Naokelekan Formation, leading to the disappearance of the main skeletal and non-skeletal grains. Different kinds of dolomites were observed in the examined samples, such as scattered fine-grained dolomite rhombs, floating rhomb fabric, and sutured mosaic fabric dolomite (**Figure 7H**) and **(Figure 8b, c, d, e, f**).

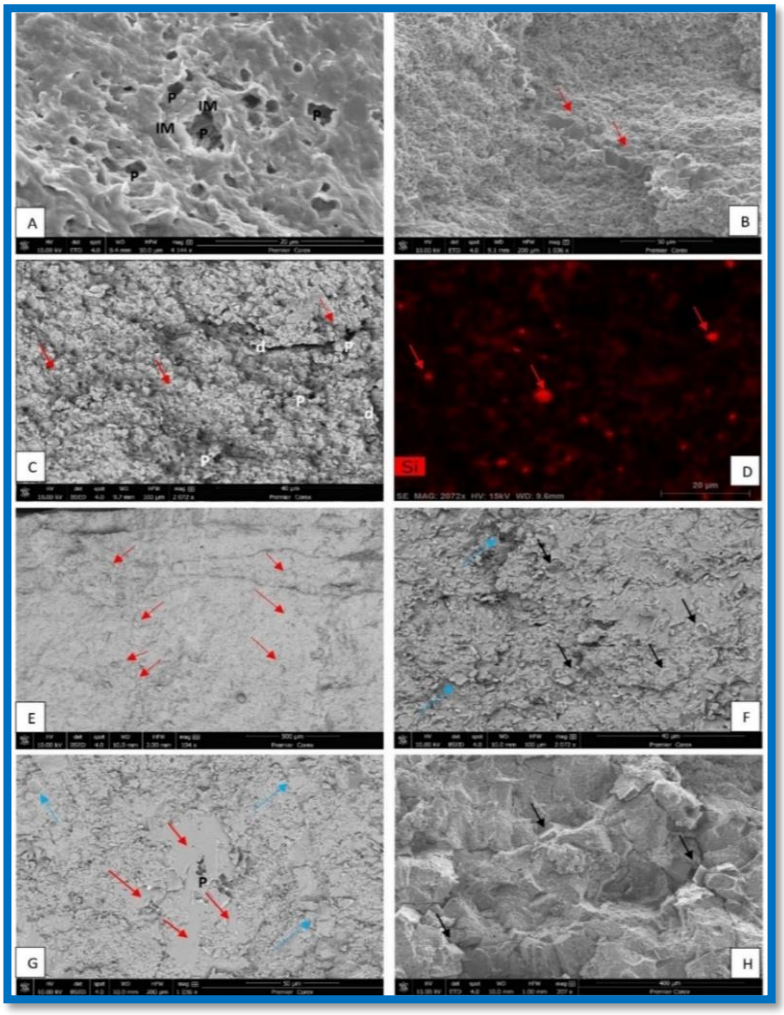

Figure 7. Scanning electron micro images (S.E.M.) illustrating

(A) Common pores (P) referring to the dissolution process and illite-mica (I.M.) with common carbonate (c) in sample TZ-1A**. (B)** Micro vein (red arrows) filled by a cluster of calcite crystals, euhedral hexagonal and columnar crystals relating to the cementation process and embedded in the micritic groundmass, sample Sg4A**. (C and D)** S.E.M. and E.D.X.

microimages for sample Sg4A show common radiolarian shells in different sizes with fine fractures (f) and pores (p). In D, the same locations of red arrows refer to silica content (Si), the main composition of the radiolarian shell. **(E)** Chemical compaction and stylolite formation (red arrow) in sample Br-5A**. (F)** Cementation in nannofossil shell (coccolith shell) and other different types with recrystallization of fine calcite grain in sample Nk-4A **(G)** cementation of fossil shell (red arrows) with recrystallization of fine calcite grain, dissolution and porosity formation of fossils (p) and in sample Br-5A. (**H)** Dolomitization in very fine dolomite rhombs (black arrows), with fracturing in sample Nk-1

5.7 Anthogenesis

Authigenic minerals are created in many of the studied rocks. These minerals are formed diagenetically by local chemical reactions **[26,27].** Pyrite is the common authigenic mineral in the studied rocks; this mineral is formed when dissolved sulfide from microbial sulfate reaction reacts with detrital iron-bearing minerals in anoxic marine sediments **[46]**. Pyrite is common in the Sargelu and Barsarin formations as patches and framboidal pyrite (**Figure 8g, h**), which are composed of tightly packed spherical or sub-spherical clusters of pyrite crystals **[47]**.

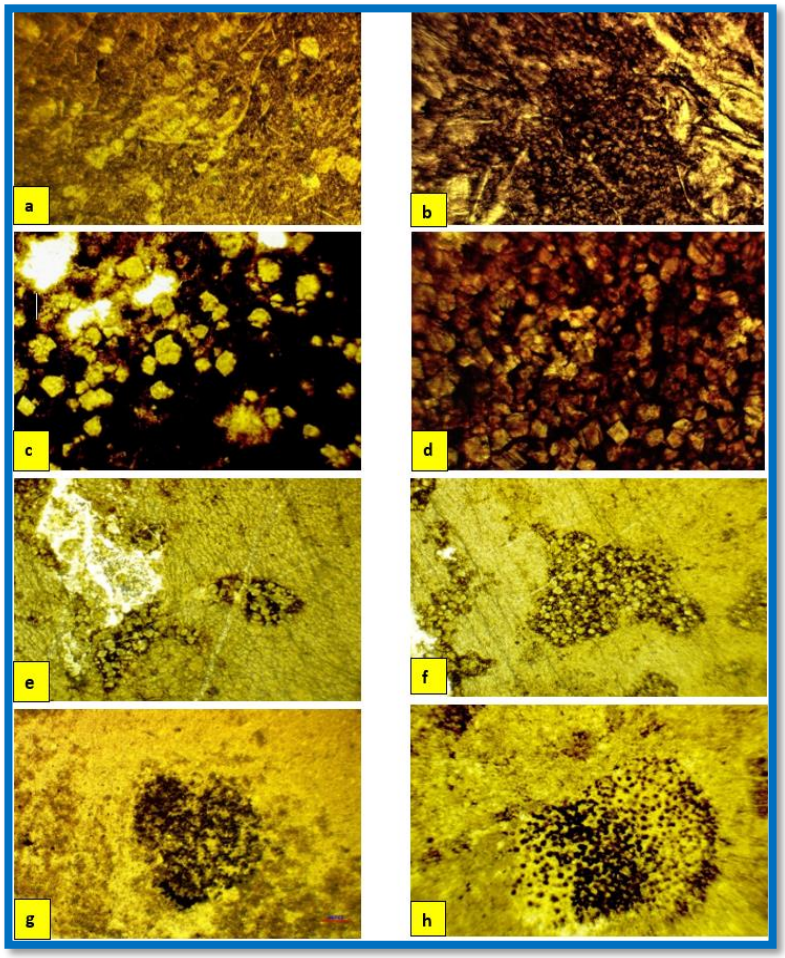

Figure 8. Photomicrograph illustrating

Figure 8 (a) Neomorphism, authigenic pyrite, and dolomitization in the upper part of the Sargelu Formation in the sample (Sg-9B), 4X, N.L. **(b)** Selective dolomitization, scattered fine-grained dolomite rhombs dolomitization neomorphism process affected the micrite matrix in the upper part of the Sargelu Formation in the sample (Sg-10B), 4X, N.L. **(c)** Floating rhomb dolomite fabric in the lower part of the Naokelekan Formation, neomorphism embedded in micritic groundmass in the sample (Nk-1B) 4X, N.L. (d) Subhedral-euhedral dolomite rhomb in the middle part of the Naokelekan Formation in sample (Nk-3B), 4X, N.L**. (e)** Dolomitization in the middle part of the Barsarin Formation affecting skeletal grains filled with organic material in sample (Br-4B), 10 X, NL. **(f)** Dolomitization in the middle part of the Barsarin Formation affects skeletal grains filled with organic material in the sample (Br-4B),10 X, NL**. (g)** Pyritized radiolarian shell in the middle part of the Sargelu Formation in the sample (Sg-6B), 10 X, NL. **(h)** Packed spherical or sub-spherical clusters of pyrite crystals in the lower part of the Barsarin Formation in the sample (Br-2B), 10 X, NL.

6. Discussion

The Sargelu Formation lithological is made up of thin-bedded, bituminous black limestones, dolomitic black limestones, and black papery shales with thin black chert streaks in the top part. The depositional environment was primarily anoxic marine [8]; this is supported by the recognized petrographic components, including pelagic pelecypods, radiolarian, and calcipheres organisms. Naokelekan Formation consists of argillaceous bituminous limestone and dolostone alternating with bituminous shale and fine-grained limestone, while Barsarin Formation is composed of stromatolitic limestones and evaporite layers [11]; according to [48], the Naokelekan Formation was deposited in restricted tidal flats and lagoons, marshes, and euxinic saline swamps. This suggestion can be supported in this study by the presence of peloids, which are commonly present in protected environments such as lagoons, tidal flats, and other quiet environments [24]. On the other hand, the overall characteristics of the Naokelekan microfacies indicate that formation was deposited in two different environments: the shallow marine subtidal environment in the lower and upper parts and the outer shelf in an euxinic environment in the middle part [16, 49]. The upper part of the Barsarin Formation was deposited in an intertidal environment, whereas the lower part of the formation was deposited in the shallow subtidal environment [50].

Mineralogically, variation in the composition of the middle to upper Jurassic Sargelu, Naokelekan, and Barsarin formations from northeastern Iraq demonstrates the influence of the source area, the depositional environment, and the paleoclimatic conditions [51], the presence

of calcite and dolomite reflect the deposition in such restricted and evaporative conditions **[52,53]**. The predominance of illite-mica and kaolinite clay minerals with other components such as quartz and feldspars reflect the contribution of felsic igneous rocks and the prevalent environment, which can be recognized by variation between hot, arid, and humid climates, where the development in quartz and feldspars in the area which are both related to felsic igneous rocks, may be associated to a provenance where felsic rocks from the Rutba Uplift and/or Arabian Shield predominate **[51,54]**.

The petrographic study revealed the variation in the petrographic components reflects the range of the diagenetic processes that affected the studied formations, leading to difficulty in identifying them due to the destruction of most of the skeletal grains as in Naokelekan Formation, which is highly affected by diagenesis.

The detected skeletal grains in the studied formations primarily consist of fossils and fossil shells, including radiolaria, calcispheres of different sizes, benthonic foraminifera such as (Milioliad) and different types of unrecognized planktonic due to diagenetic effect, ostracods, bioclasts, pelagic pelecypods (Bositra and Halobia) and two types of stromatolites parallel and wavy stromatolites all these components are embedded in a groundmass of micrite and microsparite. Where the non-skeletal grains only recognized peloids.

The diagenetic processes that affected these components occasionally had a very strong impact on these components, making it harder to recognize the grain or such as micritization, dissolution and porosity formation, cementation, compaction (pressure solution), neomorphism, dolomitization, and authigenic minerals.

7. Conclusions

The Jurassic succession in the Sargelu section comprises petrographic constituents represented by skeletal grains, which are very common, especially in the Sargelu Formation; these include pelecypod, radiolaria, planktonic foraminifera, benthonic foraminifera, bioclasts, and calcispheres and stromatolites as well as non-skeletal grains, such as peloids. All these components are in two recognized types: micrite and microsite groundmass. Dissolution and porosity formation, cementation, neomorphism, dolomitization, compaction and stylolite formation, and authigenic minerals such as (pyrite) are mainly the kinds of diagenetic processes that had a significant effect on the carbonates of these formations.

8. References

[1] Al-Ameri TK, Zumberge J. Middle and Upper Jurassic hydrocarbon potential of the Zagross Fold Belt, North Iraq. Mar Pet Geol [Internet]. 2012;36(1):13–34. Available from: http://dx.doi.org/10.1016/j.marpetgeo.2012.04.004

[2] Al-Juboury AI, McCann T. Petrological and geochemical interpretation of Triassic-Jurassic boundary sections from northern Iraq: TRIASSIC-JURASSIC BOUNDARY OF NORTHERN IRAQ. Geol J [Internet]. 2015;50(2):157–72. Available from: http://dx.doi.org/10.1002/gj.2537

[3] Abdula RA, Soran University. Source rock assessment of naokelekan formation in Iraqi Kurdistan. J Zankoy Sulaimani - A [Internet]. 2016;19(1):103–24. Available from: http://dx.doi.org/10.17656/jzs.10589

[4] Pitman JK, Steinshouer D, Lewan MD. Petroleum generation and migration in the Mesopotamian Basin and Zagros Fold Belt of Iraq, results from abasin-modeling study, GeoArabia, Gulf PetroLink. Vol. 9. Bahrain; 2004.

[5] Al-Naqib SQ, Al-Juboury AI. A new look on the Jurassic formations of the western part of Iraq. Arab J Geosci [Internet]. 2014;7(2):559–88. Available from: http://dx.doi.org/10.1007/s12517-012-0820-2

[6] Tucker ME. Sedimentary petrology, an introduction, Blackwell Scientific publications. Blackwell Scientific publications. 1981;

[7] Numan NMS. Cretaceous tectonic events in Iraq. Rafidain Jour Sci. 2000;11(3):32–54.

[8] Jassim, S.Z. and Goff, C. Geology of Iraq. Dolin, Prague and Moravian Museum, 2006. Brno.

[9] Ali SA, Buckman S, Aswad KJ, Jones BG, Ismail SA, Nutman AP. The tectonic evolution of a Neo-Tethyian (Eocene-Oligocene) island-arc (Walash and Naopurdan groups) in the Kurdistan region of the Northeast Iraqi Zagros Suture Zone. The Island Arc. 2013;22:104-e125.

[10] Ali SA, Nutman AP, Aswad KJ, Jones BG. Overview of the tectonic evolution of the Iraqi Zagros thrust zone: Sixty million years of Neotethyan ocean subduction. J Geodyn [Internet]. 2019;129:162–77. Available from: http://dx.doi.org/10.1016/j.jog.2019.03.007.

[11] Bellen VRG, Dunnington HV, Wetzel R, Morton DM. Lexique Stratigraphic International, V.3, Asie Fascicule loa-Iraq. Vol. 333. Paris; 1959.

[12] Sharezwri AO, Nourmohammadi MS, Abdula R.A. Facies Analysis and Depositional Environment of the Upper Jurassic Naokelekan Formation in Two Selected Outcrop Sections from Kurdistan Region, Ne Iraq. Iraqi Bulletin of Geology and Mining. 2019;16:1–14.

[13] Omar N, McCann T, Al-Juboury AI, Franz SO, Zanoni G, Rowe H. A comparative study of the paleoclimate, paleosalinity and paleoredox conditions of Lower Jurassic-Lower Cretaceous sediments in northeastern Iraq. Mar Pet Geol [Internet]. 2023;156(106430):106430. Available from: http://dx.doi.org/10.1016/j.marpetgeo.2023.106430.

[14] Fouad S.F. Tectonic Map of Iraq. Iraqi Bulletin of Geology and Mining. 2015;1:1–8.

[15] Balaky SM. Sequence stratigraphic analyses of Naokelekan Formation (Late Jurassic), Barsarin area, Kurdistan region—Northeast Iraq. Arab J Geosci [Internet]. 2015;8(8):5869–78. Available from: http://dx.doi.org/10.1007/s12517-014-1638-x.

[16] Abdula R.A. Stratigraphy and lithology of Naokelekan Formation in Iraqi Kurdistan Review. TheInternational Journal of Engineering and Sciences. 2016;5:7–17.

[17] Omar N, Mccann T, Al-Juboury AI, Franz SO. Petrography and geochemistry of the Middle- Upper Jurassic Banik section, northernmost Iraq - Implications for palaeoredox, evaporitic and diagenetic conditions. Neues Jahrbuch für Geologie und Paläontologie Abhandlungen. 2020(2):125–52.

[18] Molina JM, Reolid M, Mattioli E. Thin-shelled bivalve buildup of the lower Bajocian, South Iberian paleomargin: development of opportunists after oceanic perturbations. Facies [Internet]. 2018;64(3). Available from: http://dx.doi.org/10.1007/s10347-018-0532-5.

[19] P. J. B. J. L. Wilson 1975. Carbonate Facies in Geologic History. xiv + 471 pp., 183 figs, 30 pls. Springer-Verlag, Berlin, Heidelberg, New York. Price DM 90.00 ISBN 3 540 07236 5. Geol Mag [Internet]. 1976;113(6):584–5. Available from: http://dx.doi.org/10.1017/s0016756800041406.

[20] Kuhry B, Declercq SWG, Dekker L. Indications of current action in Late Jurassic limestones, Radiolarian limestones, Saccocoma limestones, and associated rocks from the Subbetic of SE-SPAIN. Jour Sed Geology. 1976;15:235–58.

[21] Flugel E. Microfacies Analysis of Limestones. Heidelberg: Springer; 1982.

[22] Bishop BA. Petrography and origin of Cretaceous limestones, Sierra de Picachos and vicinity, Nuevoleon, Mexico. Jour Sed Pet. 1972;42(2):270–86.

[23] Hart MB. The Late Cenomanian Calcisphere global bioevent, Ussher, Soc. J. 1991;(7):413–7.

[24] Flugel, E., Microfacies of carbonate rocks: analysis, interpretation and application, 2 and. Edition: Springer- Verlage, Berlin, 2010.

[25] Scholle PA, Ulmer - Scholle DS. A Color Guide to the Petrography of Carbonate Rocks: Grains, Textures, Porosity, Diage nesis, A.A.P.G. Memoir - 77. Vol. 474. Tulsa, Oklahoma, U.S.A.; 2003.

[26] Flugel, E. Microfacies of carbonate rock, analysis, interpretation and application, Springer-Verlag, Berlin; 2004, 976.

[27] Edgar K, Bohaty S, Gibbs S, Sexton P, Norris R, Wilson P. Symbiont "bleaching" in planktic foraminifera during the Middle Eocene Climatic Optimum. Geology. 2013;41(1):15–8.

[28] Balaky S.M.H. Stratigraphy and sedimentology of Sargelu formation (Middle Jurassic) in selected sections in Erbil and Duhok Governorates-Iraq Kurdistan. M. 2004.

[29] Awadeesian A.M.R., Al-Jawed S.N.A., Saleh AH, Sherwani G.H. Mishrif carbonates facies and diagenesis glossary, South Iraq microfacies investigation technique: types, classification, and related diagenetic impacts. Arab J Geosci [Internet]. 2015;8(12):10715–37. Available from: http://dx.doi.org/10.1007/s12517-015-1954-9.

[30] Maikliem WR, Bebout DG. Glaister Classification of anhydrite: A practical approach. Bull Can Pet Geol. 1969;17(2):194–233.

[31] Bosak T, Knoll AH, Petroff AP. The meaning of stromatolites. Annu Rev Earth Planet Sci [Internet]. 2013;41(1):21–44. Available from: http://dx.doi.org/10.1146/annurev-earth-042711-105327.

[32] Zadeh, P.G., Adabi, M.H., Sadeghi, A., Microfacies, geochemistry and sequence stratigraphy of the sarvak formation (mid cretaceous) in the kuh-e siah and kuh-e mond, fars area, southern Iran. J. Afr. Earth Sci, 2019, 160, 103634.

[33] Ahmad F, Quasim MA, Ahmad AHM. Microfacies and diagenetic overprintsmin the limestones of middle Jurassic fort member (jaisalmer formation), western Rajasthan, India: implications for the depositional environment, cyclicity, and reservoir quality. Geol J. 2021;56(1):130-151.

[34] Folk, R.L., Practical petrographic classification of limestone. A.A.P.G, Bull. 1959;43(1):1-38.

[35] Boggs SJ. Principles of Sedimentology and Stratigraphy. Pearson Prentice - Hall; 2006.

[36] Larsen G, Chillinger GV. Diagenesis in sedimentary rocks. Development in Sedimentology. 1979;25:1–29.

[37] Blatt, H. Sedimentary Petrology, Freeman, San Francisco, 1982, 564.

[38] Bathurst R.G.C. Carbonate Sediment and Their Diagenesis, Development in Sedimentology 12. Development in Sedimentology. 1975;12.

[39] Tucker ME. Black well scientific publ. An introduction. 1985;3.

[40] Samankassou E, Tresch J, Strasser A. Origin of peloids in Early Cretaceous deposits, Dorset, South England. Facies [Internet]. 2005;51(1–4):264–74. Available from: http://dx.doi.org/10.1007/s10347-005-0002-8.

[41] Choquette PW, Pray LC. Geologic nomenclature and classification of porosity in sedimentary carbonates. Pettijohn, F J. 1970;54.

[42] Tucker ME. Sedimentary petrology: an introduction to the origin of sedimentary rocks. Blackwell Science, Oxford, and Northampton. 2001;262.

[43] Machel HG. The geometry and petrogenesis of dolomite hydrocarbon reservoirs. Brathwaite C.J.R., Rizzi G, Darke G, editors. Vol. 235. Geo. Soc. Lond. Spec; 2004.

[44] Sadd J, Alsharhan AUAE, Embry AF, Klovan J. A late Devonian reef tract on northeastern Banks Island. Bulletin of Canadian Petroleum Geology. 1971;19(4).

[45] Lingman, M.W., Carboante diagenetic textures from upper near surface diagenetic environment. A.A.P.G. Bull, 1980; 64(4):461-486.

[46] Berner RA. Principles of Chemical Sedimentology. Mc Graw Hill Book Company; 1971.

[47] Wilkin RT, Barnes HL. Formation processes of framboidal pyrite. Geochim Cosmochim Acta [Internet]. 1997;61(2):323–39. Available from: http://dx.doi.org/10.1016/s0016-7037(96)00320-1.

[48] Al-Badry AM, Stratigraphy G, Of J. Selected Sections-North Iraq. Ph.D. dissertation (unpublished). Vol. 183. Baghdad, Iraq; 2012.

[49] Dohan AH, Kadhim LS, Hassan FN. Microfacies and Diagenetic Processes of the Late Jurassic Naokelekan Formation in selected wells at Balad, Ajil and Baiji Oilfields, Central Iraq. Central Iraq Tikrit Journal of Pure Science. 2022(4):60–9.

[50] Daoud HS, Karim KH. Types of Stromatolites in the Barsarin Formation (Late Jurassic). Iraqi Bulletin of Geology and Mining. 2010;6–7.

[51] Rasool RH, Ali SA, Al-Juboury AI. Mineralogy of the middle to upper Jurassic succession from Sargelu section, northeastern Iraq. Iraqi National Journal of Earth Science. 2023.

[52] Warren J. Occurrences, evolution and economically important association. Earth Science reviews. 2000;1–81.

[53] Asaad IS, Al-Juboury AI, Bal Akkoca D, Jha P. Petrography and mineralogy of rinded ferrous-carbonate concretions in the Middle Eocene carbonate rocks: A case study from the Avanah Formation in north-east Erbil City, northern Iraq. Geol J [Internet]. 2022;57(8):3021–32. Available from: http://dx.doi.org/10.1002/gj.4463.

[54] Ali SA, Ismail SA, Nutman AP, Bennett VC, Jones BG, Buckman S. The intra-oceanic Cretaceous (˜108 Ma) Kata-Rash arc fragment in the Kurdistan segment of Iraqi Zagros suture zone: implications for Neotethys evolution and closure. Lithos. 2016;260:154–63.

Al-Kitab Journal for Pure Sciences (2023); 7(2):173-183.
https://doi.org/10.32441/kjps.07.02.p13

Al-Kitab Journal for Pure Sciences
ISSN: 2617-1260 (print), 2617-8141(online)
https://isnra.net/index.php/kjps

Simultaneous determination of Guaifenesin, codeine phosphate, phenylephrine hydrochloride, and sodium benzoate in syrup pharmaceutical form by RP-HPLC

Ali E. Karim[1], Muthana S. Ali[2] , Maiser Z. Mohye[1], Azza M. Al-metwali[3], Salah N. Ibrahim [1]

[1]Department of Physiology and Biochemistry, College of Veterinary Medicine, Diyala University, Baquba, Iraq
[2]Department of Science, College of Basic Education, Diyala University, Baquba, Iraq
[3]Department of Chemistry, College of Education for Pure Science, University of Diyala, Baquba, Iraq

*Corresponding Author: basicsci18@uodiyala.edu.iq

Citation: Ali MS, Karim AE, Mohye MZ, Al-metwali AM, Ibrahim SN. Simultaneous determination of Guaifenesin, codeine phosphate, phenylephrine hydrochloride, and sodium benzoate in syrup pharmaceutical form by RP-HPLC. Al-Kitab J. Pure Sci. [Internet]. 2023 Dec 13 [cited 2023 Dec 13];7(2):173-183. Available from: https://doi.org/10.32441/kjps.07.02.p13.

Keywords: (RP-HPLC, method validation, Guaifenesin, codeine phosphate, phenylephrine, sodium benzoate.

Article History

Received	23 Oct. 2023
Accepted	01 Dec. 2023
Available online	13 Dec. 2023

Abstract:

This work describes the development of the RP-HPLC method for the simultaneous estimation of Guaifenesin, codeine phosphate, phenylephrine, and sodium benzoate. This method separates Guaifenesin, codeine phosphate, phenylephrine, and sodium benzoate nicely. This RP-HPLC method uses the Shimadzu HPLC instrument with Chromegabond WR C18 column 5 µm 120 A 30 cm * 3.9 mm. The mobile phase is a mixture of 1% o-phosphoric acid, methanol: acetonitrile (80 : 10: 10), and the pH was adjusted to 3.1. Isocratic elution mode was used with 1 ml/min as the flow rate. The detection for all compounds is carried out at 254 nm. The retention time of Guaifenesin, codeine phosphate, phenylephrine, and sodium benzoate was 14.11, 5.75, 3.9, and 20.52, respectively. The method has been validated concerning accuracy, linearity, and precision. This method is simple, accurate, and reproducible. This validated method was used to estimate these drugs in syrup pharmaceutical form.

Keywords: RP-HPLC, method validation, Guaifenesin, codeine phosphate, phenylephrine, sodium benzoate.

طريقة لتقدير كوايفنيسين، وفوسفات الكوديين، والفينيليفرين، وبنزوات الصوديوم في شراب صيدلاني بواسطة كروموتغرافيا السائل عالي الأداء ذات الطور المعكوس

علي إسماعيل كريم[١]، مثنى علي سعيد[٢]، ميسر زيد محي[١]، عزة منعم المتولي[٣]، صلاح نوري ابراهيم[١]
ali.i@uodiyala.edu.iq, basicsci18@uodiyala.edu.iq, maiser.z@uodiyala.edu.iq, Azzaalmetwali3@gmail.com, salah.nooriaz@gmail.com

[١] فرع الفسلجة والكيمياء الحياتية –كلية الطب البيطري– جامعة ديالى – بعقوبة العراق
[٢]قسم العلوم، كلية التربية الأساسية، جامعة ديالى، بعقوبة – العراق
[٣]قسم الكيمياء –كلية التربية للعلوم الصرفة – جامعة ديالى – بعقوبة العراق

الخلاصة:

يصف هذا العمل تطوير طريقة لكروموتغرافيا السائل عالي الأداء ذات الطور المعكوس لتقدير كوايفنيسين، وفوسفات الكوديين، والفينيليفرين، وبنزوات الصوديوم في وقت واحد. تفصل هذه الطريقة بين الكوايفنيسين وفوسفات الكوديين والفينيليفرين وبنزوات الصوديوم بشكل جيد. تستخدم هذه الطريقة جهاز *Shimadzu HPLC* مع عمود *Chromegabond WR C18 5* . لطور المتحرك يتكون من خليط من ١٪ حمض الفوسفوريك: ميثانول: أسيتونتريل بنسبة (٨٠: ١٠: ١٠) وتم ضبط الرقم الهيدروجيني إلى ٣,١. تم استخدام زمن الجريان ١ مل/دقيقة كمعدل التدفق. يتم الكشف عن جميع المركبات عند ٢٥٤ نانومتر. وجد أن زمن الاحتجاز بالكوايفنسين، فوسفات الكوديين، الفينيلفرين وبنزوات الصوديوم، ١٤,١١، ٥,٧٥، ٣,٩، و٢٠,٥٢ على التوالي.

تم التحقق من صحة الطريقة فيما يتعلق بالدقة والاستقامة الخطية والاستردادية. وقد وجد أن هذه الطريقة بسيطة ودقيقة وقابلة للاستخدام المستمر. تم استخدام هذه الطريقة المعتمدة لتقدير هذه المواد الفعالة الموجودة في شكل شراب دوائي.

الكلمات المفتاحية: كروموتغرافيا السائل عالي الأداء، الكوايفنيسين، فوسفات الكوديين، الفينيليفرين، وبنزوات الصوديوم.

1. Introduction:

Guaifenesin, 3-(2-methoxyphenoxy)-propane-1,2-diol, is used as an expectorant for the symptomatic relief of respiratory problems. Its formula is $C_{10}H_{14}O_4$. Its molecular weight is 198.21. It is white or slightly crystalline with a grey color [1]. Codeine phosphate is known as 7,8-dihydro-4, 5-epoxy-3-methoxy-17-methylmorphinan-6-ol dihydrogen phosphate hemihydrate. It is used as a narcotic analgesic [2]. Phenylephrine hydrochloride is 1-(3-hydroxyphenyl)-2-methylamino-ethanol hydrochloride. The formula is C9H13NO2HCl. P.H.E. decreases nasal congestion and improves drainage of sinus cavities [2-4]. Sodium benzoate is a chemical that is used in pharmaceutical preparation as a preservative [2, 3] to decrease the microorganism development [5-7]. The literature review reveals many HPLC methods are reported for the determination of Guaifenesin, codeine phosphate, phenylephrine, and sodium benzoate individually and in a mixture of Guaifenesin alone and in combination with other drugs [8-12]. Phenylephrine hydrochloride alone and mixing with other drugs [13-14] Codeine phosphate alone and in combination with other drugs [15-18]. The combination of

Guaifenesin, codeine phosphate, phenylephrine, and sodium benzoate has not been published in U.S. and B.P. pharmacopeia. No RP-HPLC method has been published for the simultaneous estimation of Guaifenesin, codeine phosphate, phenylephrine, and sodium benzoate. Therefore, it is necessary to come up with a rapid method for the analysis of these drugs in liquid pharmaceutical formulations. Two main aspects that are important in the determination of the shelf life of the drug are the concentration of the active ingredient and the stability study. A stability test sample was done using this method, according to the guidelines of the International Conference on Harmonization (ICH) **[19]**. This method will be used to separate Guaifenesin, codeine phosphate, phenylephrine, and sodium benzoate from each other. This method has been validated and successfully applied for quantification of the active ingredient and the preservative in liquid pharmaceutical form. The aim of this research is to develop an RPHPLC method for the simultaneous determination of Guaifenesin, codeine phosphate, phenylephrine hydrochloride, and sodium benzoate.

2. Experimental

2.1 Chemicals and reagents

The working standards are obtained from Wadi al- rafidain for pharmaceutical products – Iraq- Baghdad. Guaifenesin purity is (99.93%). Codeine phosphate purity is (99.51%). Phenylephrine HCl purity is (99.34%). Sodium benzoate purity is (99.58%). O-phosphoric acid was purchased from Sigma Aldrich. Acetonitrile and methanol were purchased from ISOLAB GmbH, Germany. All chemicals were purchased HPLC grade.

2.2 Instrumentation

The HPLC instrument has been used in SHIMADZU, Japan, with a diode array detector. The spectrophotometer was UV-Vis Spectrophotometer Shimadzu 1800 with U.V. probe software. Analytical balance was used by Shimadzu. pH meter was used by W.T.W. Germany. All the glass wares used were from ISOLAB.

2.3 Standard solution

A Standard Stock Solution of Guaifenesin was prepared by using 200 mg and dissolving it with mobile phase in a 50 ml volumetric flask to obtain a concentration of 4 mg/ml. A stock solution of sodium benzoate was prepared by dissolving 100 mg with mobile phase in a 50 ml volumetric flask to obtain a concentration of 2 mg/ml. Standard Stock Solutions for Codeine phosphate and Phenylephrine HCl were prepared using mobile phase to obtain concentration (1mg/mL). A standard solution of 2 mg/mL Guaifenesin, 0.2 mg/mL codeine phosphate,0.1 mg/mL Phenylephrine HCl, and 0.5 mg/mL sodium benzoate was prepared from the stock

solutions. Calibration standards solutions at five different concentrations have been prepared by diluting stock standard solutions with a concentration range of 0.25 mg/mL –4 mg/mL for Guaifenesin, 0.05 mg/mL - 1 mg/mL Codeine phosphate, 0.025 mg/mL -0.5 mg/mL Phenylephrine HCl, and 0.125 mg/mL - 2 mg/mL for sodium benzoate. Samples in triplicates have been made for each concentration. The calibration curve was prepared by plotting the peak areas versus the concentrations.

2.4 Assay Procedure for Syrup

10 ml syrup equivalent to 200 mg guaifenesin, 20 mg codeine phosphate, 10 mg Phenylephrine HCl, and 50 mg sodium benzoate were dissolved in a 100 volumetric flask using mobile phase. The solution was sonicated for 10min and filtered using 0.45μm syringe filter. The solution was injected, and peak areas were measured.

3. RESULTS AND DISCUSSION

3.1 Method Development

Several chromatographic conditions were changed in each experiment to achieve the best efficiency. Parameters like wavelength, column, mobile phase, and pH have been optimized. Different proportions of buffer and solvents have been experimented with to achieve the best mixture of the mobile phase. The mixture of 1% o-phosphoric acid: methanol: acetonitrile (80: 10: 10) and pH adjusted to 3.1 has been selected to be the mobile phase. Isocratic elution mode was used with a flow rate of 1 mL/min. The optimum wavelength was selected at 254 nm, which is the best detector response that has been achieved for all drugs.

3.2 Selectivity

The result shows that drugs have been separated from the excipients nicely, as shown in **Figure 1**. This HPLC method has been found to be selective.

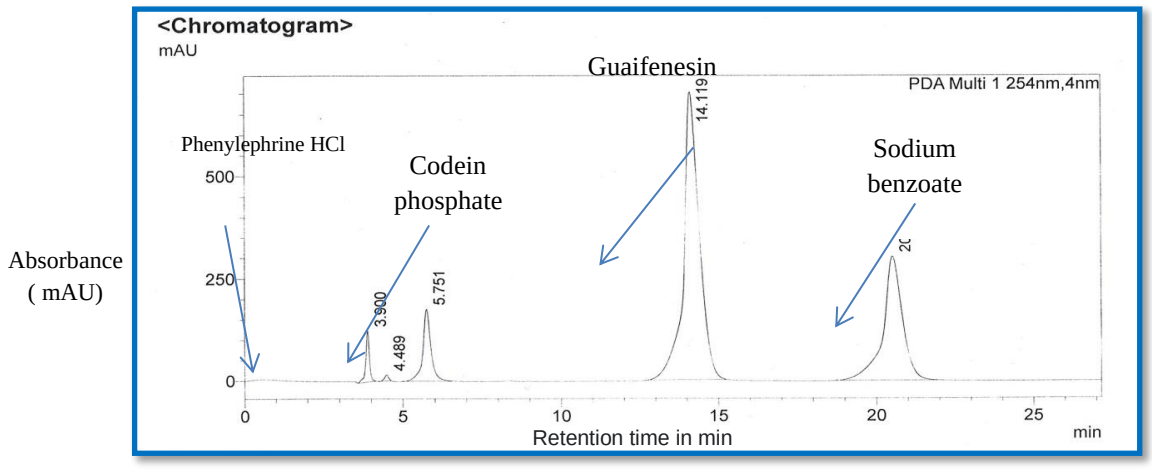

Figure1. RPHPLC chromatogram of Guaifenesin, Codeine phosphate, Phenylephrine HCl, and sodium benzoate.

3.3 Linearity

The linearity of calibration curves was checked in the ranges of 0.25 –4 mg/ml for Guaifenesin, 0.05 - 1 mg/ml Codeine phosphate, 0.025 -0.5 mg/ml Phenylephrine HCl, and 0.125 - 2 mg/ml for sodium benzoate. Results in **Figure** (**2**,**3**,**4**,**5**) show that the calibration curves have been linear in the tested range.

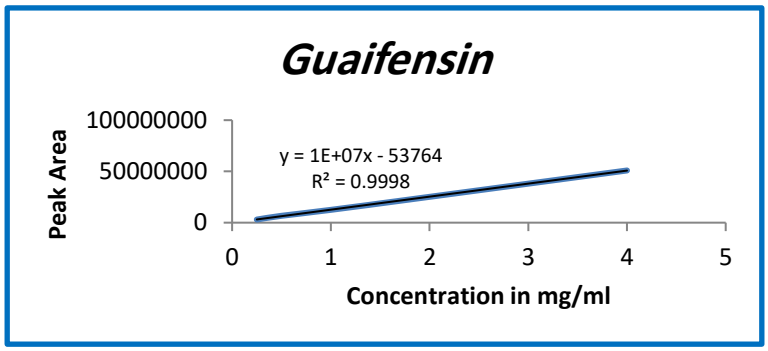

Figure2. Calibration curve of Guaifenesin

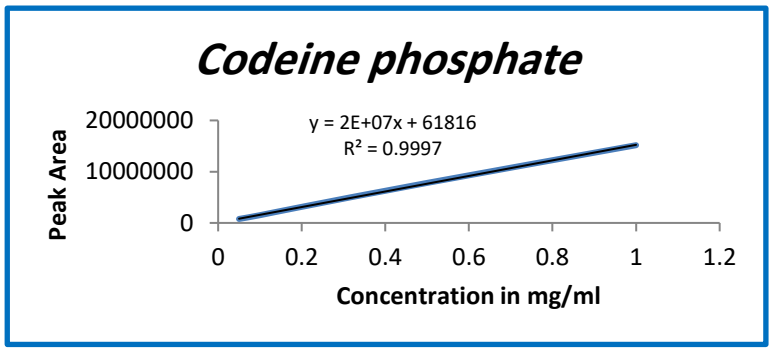

Figure3. Calibration curve of Codeine phosphate

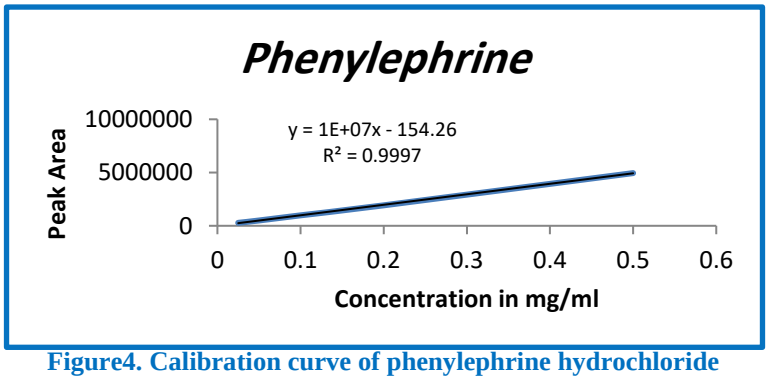

Figure4. Calibration curve of phenylephrine hydrochloride

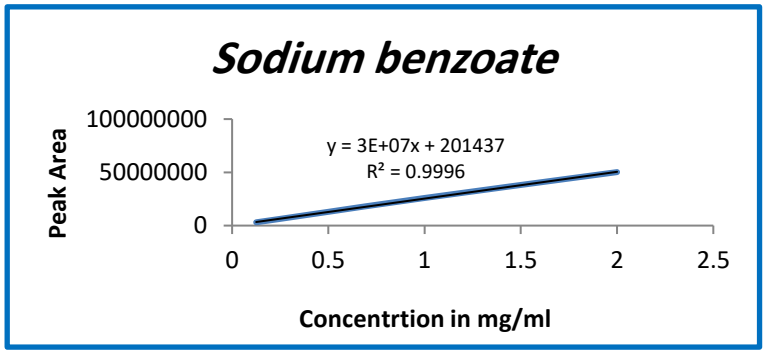

Figure5. Calibration curve of sodium benzoate.

3.4 Accuracy

The accuracy of this reported method has been validated using recovery studies. Results in **Tables 1,2, 3**, and 4 show that this method is significant.

Table 1: Accuracy for Guaifenesin.

Concentration mg/mL	Calculated Conc in mg/mL	Recovery	A.V.R. Recovery%
1.6	1.588	99.25	99.675
1.6	1.592	99.50	
1.6	1.590	99.375	
1.6	1.596	99.75	
1.6	1.608	100.5	
2	1.995	99.75	100.06
2	2.011	100.55	
2	2.006	100.30	
2	1.996	99.80	
2	1.998	99.90	
2.4	2.396	99.833	100.058
2.4	2.412	100.5	
2.4	2.394	99.75	
2.4	2.397	99.875	
2.4	2.408	100.333	

Table 2: Accuracy for codeine phosphate.

Concentration mg/mL	Calculated Conc in mg/mL	Recovery	A.V.R. Recovery%
0.16	0.1596	99.75	100.046
0.16	0.1611	100.68	
0.16	0.1593	99.56	
0.16	0.1607	100.43	
0.16	0.1597	99.81	
0.2	0.1992	99.6	99.86
0.2	0.1996	99.8	
0.2	0.2014	100.7	
0.2	0.1991	99.55	
0.2	0.1993	99.65	
0.24	0.2386	99.41	99.73
0.24	0.2406	100.25	
0.24	0.2391	99.62	
0.24	0.2396	99.83	
0.24	0.2389	99.54	

Table 3: Accuracy for phenylephrine hydrochloride.

Concentration mg/mL	Calculated Conc in mg/mL	Recovery	A.V.R. Recovery%
0.08	0.07982	99.77	99.63
0.08	0.07936	99.2	
0.08	0.07932	99.15	
0.08	0.08016	100.2	
0.08	0.07988	99.85	
0.1	0.1012	101.2	99.96
0.1	0.09964	99.64	
0.1	0.09982	99.82	
0.1	0.09924	99.24	
0.1	0.09992	99.92	
0.12	0.1191	99.25	99.51
0.12	0.1190	99.16	
0.12	0.1196	99.66	
0.12	0.1193	99.41	
0.12	0.1201	100.08	

Table 4: Accuracy for sodium benzoate.

Concentration mg/mL	Calculated Conc in mg/mL	Recovery	A.V.R. Recovery%
0.4	0.3972	99.3	99.27
0.4	0.3968	99.2	
0.4	0.3962	99.05	
0.4	0.3992	99.8	
0.4	0.3960	99	
0.5	0.4992	99.84	99.68
0.5	0.4984	99.68	
0.5	0.5022	100.44	
0.5	0.4972	99.44	
0.5	0.4950	99	
0.6	0.5962	99.36	99.33
0.6	0.5944	99.06	
0.6	0.5988	99.8	
0.6	0.5966	99.43	
0.6	0.5942	99.03	

3.5 Robustness

Robustness was determined using different experimental conditions. The flow rate and the pH were changed on the same day to obtain the best result.

3.6 Specificity

The syrup was analyzed and separated with good resolution. No interferences were shown between the peaks, and that indicates that the method is specific. No interferences are shown between the active ingredients and the excipients.

3.7 Precision

Six injections of the same standard concentration have been injected to check the precision of this method. As shown in **Table 5**, the R.S.D. % for Guaifenesin 0.18 %, codeine phosphate 0.21 %, phenylephrine 0.157, and sodium benzoate 0.314 is not more than 1%, and that indicates that this method is precise.

Table 5. Precision of the method

Repeatability								
Injection number	guaifenesin		codeine phosphate		phenylephrine		sodium benzoate	
	Conc mg/ml	Area	Conc mg/ml	Area	Conc mg/ml	Area	Conc mg/ml	Area
1	2	24692488	0.2	3136006	0.1	980413	0.5	12916302
2	2	24631822	0.2	3129028	0.1	981934	0.5	12816336
3	2	24611646	0.2	3139982	0.1	981906	0.5	12886284
4	2	24682942	0.2	3130116	0.1	979218	0.5	12926269
5	2	24571458	0.2	3134176	0.1	979122	0.5	12906348
6	2	24643064	0.2	3121036	0.1	982802	0.5	12866312
AVR		24638903.3		3131724		980899.1667		12886308.5
SD		45099.9164		6582.24606		1544.433154		40482.20481
RSD%		0.18		0.21		0.157		0.314

3.8 Concentration of active ingredients in syrup form (Pulmocodain Syrup)

Pulmocodain Syrup is syrup produced by The State Company for Drugs Industry and Medical Appliances Samarra/ Iraq. It contains guaifenesin 100 mg/5mL, Codeine phosphate 10 mg/5mL, Phenylephrine HCl 10mg/5mL, and Sodium benzoate 25mg/5mL. This syrup was

injected to check the validation of this method. As presented in **Table 6**, the result shows this method is specific and accurate.

Table 6: Results of Pulmocodain Syrup obtained by using this method.

Active component	Guaifenesin	Codeine phosphate	Phenylephrine HCl	Sodium benzoate
Stated amount	100 mg/5ml	10 mg/5ml	5 mg/5ml	25 mg/5ml
Result found	99.46 mg/5ml	9.92 mg/5ml	4.975 mg/5ml	25.34 mg/5ml
Result Found % ± (S.D.)	99.46 (± 0.32)	99.2 (± 0.18)	99.5 (± 0.54)	101.36 (± 0.44)

4. Conclusion

This work aims to build and validate the HPLC method to determine the concentration of Guaifenesin, codeine phosphate, phenylephrine, and sodium benzoate in liquid pharmaceutical form. The validation result shows good accuracy, precision, and selectivity. This method is easy, and it can be used to determine the assay of four compounds in only one run. This method is rapid, accurate, selective, precise, and robust. It can be used for everyday work in a quality control laboratory. There is no reported method for this mixture of active ingredients in liquid pharmaceutical form.

5. REFERENCES

[1] Dubey N, Sahu S, Singh GN. Development of HPLC method for simultaneous estimation of ambroxol, Guaifenesin, and salbutamol in single dose form.

[2] United States Pharmacopoeia and National Formulary, (22th) Asian Edition, The United States Pharmacopoeia Convention Inc., U.S.A., pp. 427-30, 953-55, 1471-73.

[3] Indian Pharmacopoeia, “Indian pharmacopoeial commission,” Ghaziabad, India, 5th edition 2010, vol 2, pp 1071-72, 1479-83, v 3, pp. 1900.

[4] Tripathi KD. Essentials of Medical Pharmacology, jaypee brothers medical publishers (p) ltd. New Delhi. 2003;5:698-708.

[5] Sankar DG, Rajeswari A, Babu AN, Krishna MV. RP-HPLC method for estimation of flucloxacillin magnesium and sodium benzoate in oral suspension. Asian Journal of Chemistry. 2009 Sep 10;21(8):5843.

[6] Hassouna ME, Abdelrahman MM, Mohamed MA. Validation of a novel and sensitive RP-HPLC method for simultaneous determination of cefixime trihydrate and sodium benzoate in powder for oral suspension dosage form. Journal of Forensic Sciences & Criminal Investigation. 2017 Mar;2(5).

[7] Amer SM, Abbas SS, Shehata MA, Ali NM. Simultaneous determination of phenylephrine hydrochloride, Guaifenesin, and chlorpheniramine maleate in cough syrup by gradient liquid chromatography. Journal of AOAC International. 2008 Mar 1;91(2):276-84.

[8] Jain JK, Prakash MS, Mishra RK, Khandhar AP. Simultaneous determination of multi drug components Theophylline, Etofylline, Guaiphenesine and Ambroxol Hydrochloride by validated RP-HPLC method in liquid dosage form. Pakistan journal of pharmaceutical sciences. 2008 Apr 1;21(2).

[9] Carnevale L. Simultaneous determination of acetaminophen, Guaifenesin, pseudoephedrine, pholcodine, and paraben preservatives in cough mixture by high-performance liquid chromatography. Journal of Pharmaceutical Sciences. 1983 Feb 1;72(2):196-8.

[10] Wilcox ML, Stewart JT. HPLC determination of Guaifenesin with selected medications on underivatized silica with an aqueous-organic mobile phase. Journal of Pharmaceutical and Biomedical Analysis. 2000 Oct 1;23(5):909-16.

[11] Louhaichi MR, Jebali S, Loueslati MH, Adhoum N, Monser L. Simultaneous determination of pseudoephdrine, pheniramine, guaifenisin, pyrilamine, chlorpheniramine and dextromethorphan in cough and cold medicines by high performance liquid chromatography. Talanta. 2009 May 15;78(3):991-7.

[12] Nalini K, Narmada P, Lakshmi GV, Gowtham Y, Jogi KV. simultaneous estimation of paracetamol, guaiphensin, phenylephrine H.C.L., chlorpheniramine maleate and bromohexinehcl in combined tablet dosage form by reverse phase high performance liquid chromatography. International Journal of Pharmaceutical Sciences and Research. 2014 Feb 1;5(2):410-6.

[13] Şenyuva H, Özden T. Simultaneous high-performance liquid chromatographic determination of paracetamol, phenylephrine HCl, and chlorpheniramine maleate in pharmaceutical dosage forms. Journal of chromatographic science. 2002 Feb 1;40(2):97-100.

[14] BOBBARALA DV. ANALYSIS OF COUGH AND ANALGESIC RANGE OF PHARMACEUTICAL ACTIVE INGREDIENTS USING RP-HPLC METHOD USENI REDDY MALLU1, VARAPRASAD BOBBARALA2 AND SOMASEKHAR PENUMAJJI3.

[15] Manassra A, Khamis M, El-Dakiky M, Abdel-Qader Z, Al-Rimawi F. Simultaneous HPLC analysis of pseudophedrine hydrochloride, codeine phosphate, and triprolidine hydrochloride in liquid dosage forms. Journal of Pharmaceutical and Biomedical Analysis. 2010 Mar 11;51(4):991-3.

[16] Chittrakarn S, Penjamras P, Keawpradub N. Quantitative analysis of mitragynine, codeine, caffeine, chlorpheniramine and phenylephrine in a kratom (Mitragyna speciosa

Korth.) cocktail using high-performance liquid chromatography. Forensic science international. 2012 Apr 10;217(1-3):81-6.

[17] Hu Z, Zou Q, Tian J, Sun L, Zhang Z. Simultaneous determination of codeine, ephedrine, guaiphenesin and chlorpheniramine in beagle dog plasma using high performance liquid chromatography coupled with tandem mass spectrometric detection: application to a bioequivalence study. Journal of Chromatography B. 2011 Dec 15;879(32):3937-42.

[18] International Conference on Harmonization, Validation of Analytical Procedure, Text and Methododlogy Q2 (R1), IFMA, Geneva, Switzerland, 2005.